学位論文

Precise Measurement of Nanometer Scale Electron Beam Sizes Using Laser Interference by Shintake Monitor

レーザー干渉型新竹モニターによる

ナノメートル電子ビームサイズの精密測定

平成 26 年 12 月博士（理学）申請

東京大学理学系研究科
物理学専攻
ヤン　ジャクリン

Contents

Abstract

The International Linear Collider (ILC) is essential for the precise measurement of the properties of Higgs boson and new physics beyond the Standard Model for particle physics. The current ILC design and physics program requires a high luminosity of about $2 \times 10^{34}\,\mathrm{cm}^{-2}\mathrm{s}^{-1}$ while minimizing power consumption. This calls for the focusing of its electron (e^-) and positron (e^+) beams to nanometer sizes at the interaction point (IP). The Accelerator Test Facility 2 (ATF2) was constructed at KEK as a realistic scaled down test prototype of the final focus system (FFS) of the ILC. The Goal 1 of ATF2 is to focus the vertical e^- beam size (σ_y) to 37 nm, scaled by energy from the ILC design σ_y of 5.9 nm; the purpose is to demonstrate the design of a FFS for the ILC featuring a novel beam focusing method called the Local Chromaticity Correction scheme, whose merits are a shorter FFS beam line and less beam halo compared to preceding designs. The subject of this thesis, the Shintake Monitor, is a beam size monitor installed at the virtual IP of ATF2 for the purpose of measuring its O(10) nm σ_y. Featuring a technique of using laser interference fringes as a probe to scan the e^- beam, the Shintake Monitor is the only existing device that has demonstrated measurement of σ_y below 100 nm. The collision of the e^- beam with a target of laser interference fringes ejects photons by inverse Compton scattering. A modulation pattern is produced in the photon energy by scanning the fringe phase with respect to the electron beam using a piezo-electric stage. The σ_y is calculated from this signal modulation measured by a downstream gamma-ray detector. The laser optics are designed to accommodate a wide range of σ_y from about 25 nm to a few μm with better than 10% precision. The effective beam tuning using the Shintake Monitor contributed essentially to the ATF2 beam focusing progress; by June 2014, the focusing of σ_y to below 45 nm has been demonstrated on repeated occasions with a measurement stability of about 5%.

   This thesis describes the design concepts and performance of the Shintake Monitor, focusing on an extensive study of systematic errors which enabled the precise extraction of σ_y from the measured signal modulation. In particular, an original method was developed for the analysis of one of the most dominant errors, the fluctuation of the relative phase between the laser and the e^- beam. The reliability of the method was demonstrated using simulation assuming realistic ATF2 conditions. Other modulation reduction factors are related to laser properties e.g. polarization, profile, power, and the position alignment precision with respect to the electron beam at the IP. Based on various measurements conducted of laser properties and of the gamma-ray detector response, systematic errors were evaluated for beam time data collected in spring of 2014. Applying the error study results to a set of world record continuous σ_y measurements in June, 2014 gives the full evaluation of $39.7 \pm 0.6(stat.)^{+2.6}_{-4.0}(syst.)$ nm; the beam size resolution is about 10%. This indicates that the ATF2 Goal 1 has been achieved within error ranges. The results of the error studies demonstrate the means to suppress systematic errors so as to allow the precise measurement of the smaller σ_y at the future ILC.

Part I
Introduction

1   The International Linear Collider

1.1   Particle Physics at the Energy Frontier

The current perception of particle physics is based on the "Standard Model", which has explained and in turn been verified by the results of a variety experiments up to the TeV scale. The Standard Model (SM) attributes the fundamental constituents of matter to quarks and leptons, and the interactions between particles to the exchange of gauge bosons. It provides a crucial base for the construction of new models in search of new physics beyond the SM.

The most recently discovered particle in the SM is the Higgs boson, which is responsible for the mass of all elementary particles. In 2012, a new particle consistent with the Higgs boson was discovered at the Large Hadron Collider (LHC), thereby completing the SM particle spectrum.

However there are various unresolved issues in high energy physics which prevent the SM from being a complete theory. For instance, it does not incorporate the gravitational force, account for the cause of electroweak symmetry breaking, or provide a solution to the hierarchy problem. The Higgs boson mass is unstable under quantum corrections, which is a problem that can be cancelled by the introduction of new physics e.g. supersymmetry (SUSY) particles. The lightest SUSY particle is also a strong candidate for dark matter possibly satisfying properties derived from cosmological observations. Intense efforts are being put into the discovery of new physics beyond the SM at LHC, for which there is compelling motivation from theory.

As a synergy with the LHC, the International Linear Collider (ILC), an electron-positron collider, has been proposed as a precision machine essential for the discovery and research of new physics and more accurate measurement of Higgs boson properties. In contrast to proton collisions at the LHC, the ILC collides electrons (e^-) and positrons (e^+), which are point-like particles and anti-particles whose colliding energies are precisely controllable. This realizes clean interactions with much less background than LHC, thus enabling better knowledge of the initial states and particle mass resolution. Electrons and positrons collisions also enable precise prediction of theories, as opposed to proton collisions, for which the precision is limited by higher order QCD effects. Circular electron-position colliders e.g. the 209 GeV LEP are limited from advancing to higher collision energies by the emission of synchrotron radiation as the beam trajectory is bent. Energy loss per one turn scales as $\delta E \propto \frac{1}{\rho} \frac{E^4}{m^4}$, proportional to the fourth power of energy (E) and to the inverse of the fourth power of particle mass (m) for a fixed curvature radius (ρ). The linear ILC does not suffer from energy loss due to synchrotron radiation, and thus can reach TeV scale energies which is much more promising for measuring new physics beyond the Standard Model.

The following sections will describe the ILC, focusing on the final focusing system in relation to the main theme of this thesis.

1.2   The International Linear Collider

This section describes the basic components of the ILC accelerator.

The ILC accelerator design is a result of worldwide effort, and takes into account the possibility of changes in order to accommodate upgrades. The Reference Design Report (RDR)[1], issued in August 2007, was the first detailed technical report of R&D progress and preliminary cost estimates for each accelerator component. This was followed by the Technical Design Report (TDR)[2], issued in June 2012, which provided comprehensive technical and engineering details, and serves as the

final document to be submitted to funding agencies for project approval. The construction of the ILC is anticipated to commence in the Kitakami mountain site in Japan within a few years.

Figure 1.1 shows the current layout of the baseline ILC accelerator with center of mass energy (E_{CM}) = 500 GeV and a total machine length of about 31 km. The major sub-systems consist of:

- a polarized e$^-$ source with a 5.0 GeV linac;

- damping rings (DR) of 5 GeV and 6.4 km circumference for each of the e$^-$ and e$^+$ beams in the center region of the complex;

- 13.6 km beam transport lines from the DRs to the ends of the two main linacs;

- in the linacs (11 km each), each beam is accelerated up to 250 GeV;

- an undulator-based positron source in the middle of the e$^-$ linac;

- a 4.5 km long beam delivery system (BDS) with 14 mrad crossing angle, including the final focusing system (FFS) ; and

- the interaction region with its detectors installed around the interaction point (IP).

The E_{CM} at ILC can be varied from $<$ 250 GeV to 1 TeV by adjusting linac length and the RF power supplies of klystrons. Figure 1.2 shows the structure of beam trains and bunches. There are 1312 bunches with 554 ns spacing are accelerated in a single RF power pulse induced in the 1.3 GHz superconducting radio-frequency accelerating cavities of the main linac, designed to deliver an average accelerating gradient of 31.5 MV/m.
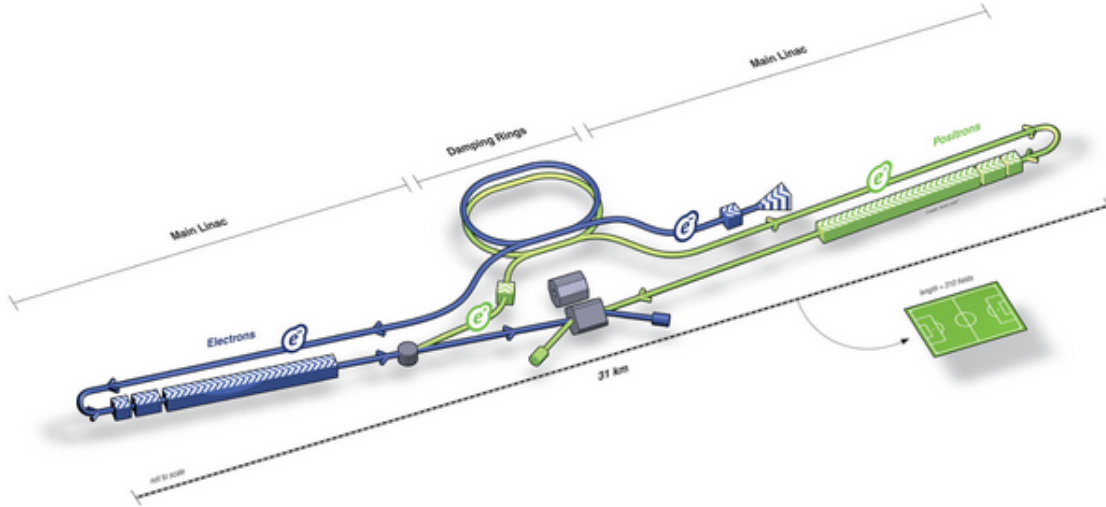
Figure 1.1: The current layout of the ILC accelerator for center of mass energy 500 GeV, according to the TDR baseline design[2].
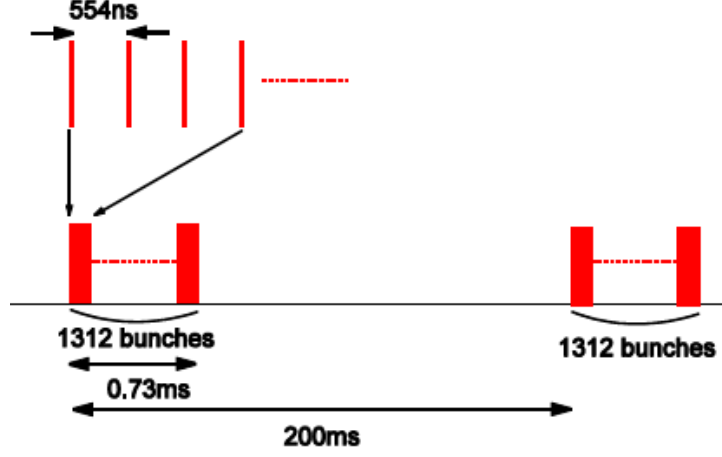
Figure 1.2: The beam train and bunch structure. For the ILC baseline design, there are 1312 bunches in a single train, with bunch spacing of about 554 ns. Since the repetition rate is 5 Hz, the spacing between trains is 200 ms. [3]

1.3 Luminosity and the Final Focus System

The most important parameters for a high energy collider are the center of mass energy (E_{CM}) and the luminosity (L). To deliver the required rate of particle interactions to the detectors for the planned physics program, the ILC baseline design (E_{CM}=500 GeV) demands a high instantaneous luminosity of $2 \times 10^{34}\,\mathrm{cm}^{-2}\mathrm{s}^{-1}$. Luminosity can be expressed as:

$$L = \frac{N_b N_e^2 f_{rep}}{4\pi \sigma_x^* \sigma_y^*} H_D \tag{1.1}$$

Here, N_b is the number of bunches per train, N_e is the number of particles in a bunch, f_{rep} is the repetition rate, H_D is the luminosity enhancement factor, and $\sigma_{x(y)}^*$ is the horizontal (vertical) beam size at the IP. In order to achieve high L within the given limits on power consumption, it is important not only to realize small beam size focusing at the IP, but also to suppress luminosity loss due to beam-beam effects e.g. beamstrahlung. Because energy loss due to beamstrahlung scales inversely with $(\sigma_x^* + \sigma_y^*)$, σ_x^* is chosen to be much larger than σ_y^* by a factor of ~ 80 given the design IP beam sizes at ILC of $(\sigma_x^*, \sigma_y^*) = (474, 5.9)$ nm. Another important issue is nm level beam position stabilization at the IP, for which intra-pulse orbit feedback in the final focus beam line is planned to be utilized.

The beams are focused by the final doublet (FD) quadrupole magnets to a tight waist at the IP (see Fig. 1.3). The FD consists of the upstream quadrupole (QF), which focuses σ_x^* and defocuses σ_y^*, followed by the downstream quadrupole (QD), which focuses σ_y^* and defocuses σ_x^*. One major difficulty in beam focusing arises from the chromaticity generated at the FD. Particles with lower energy are focused more tightly than those with higher energies, similar to how light with longer wavelengths (lower energy photons) receive stronger focusing by a lens in ordinary optics. The beam size growth caused by the energy spread among particles in a bunch reduces the attainable L at the IP, which is critical issue for linear colliders. The beam size at the IP can be represented as the combined contribution from betatron oscillation and momentum spread as :

$$\sigma_y^* \simeq \sigma_{y0}^* \sqrt{1 + (\xi_y \sigma_E)^2} = \sqrt{\varepsilon_y \beta_y^*} \cdot \sqrt{1 + (\xi_y \sigma_E)^2} \tag{1.2}$$

Here, β_y^* is the vertical beta function at the IP, σ_{y0}^* is the "nominal" vertical beam size without chromaticity, σ_E is the relative beam energy spread, and ξ_y is the vertical chromaticity. Section 1.4

describes the methods for correcting the unavoidable chromaticity created in the strong quadrupole fields, referred to as "natural chromaticity". These methods use sextupole magnets arranged in a special configuration with respect to other FFS magnets. This is because the sextupole produces a quadrupole field whose strength is proportional to the horizontal position offset of the particle passing the sextupole. Because the horizontal position offset is generated through the existence of horizontal dispersion, its is necessary to introduce non-zero horizontal dispersion into the correction regions in order to separate particles of different energies.

From Eq. 1.2, it can be seen that a small beam size $\sigma_{y0} \equiv \sqrt{\varepsilon_y \beta_y^*}$ calls for a small vertical emittance ε_y. The Accelerator Test Facility (ATF) at KEK is a DR test facility constructed for this purpose. ATF has demonstrated success in creating beams with $\varepsilon_y \simeq 10\,\mathrm{pm \cdot rad}$. There has also been intense R&D efforts towards realizing a beam delivery system that oversees beam extraction and transportation while preserving a small ε_y, including the FFS for the focusing and dynamic manipulation of the colliding particle bunches. The ATF2 [4] is a prototype FFS constructed as an extension of the ATF with the primary goal of verifying a novel FFS design featuring the "Local Chromaticity Correction" scheme selected for use at the ILC [5]. Details of ATF/ATF2 are found in Sec. 1.5. Table 1.1 shows the major FFS parameters for ILC and ATF2, including the severity of chromatic σ_y^* growth. From the point of view of beam line design, the vertical chromaticity scales approximately with β_y^*, L^* (= distance between FD and the IP), and L_F (= FD quadupole length) as:

$$\xi_y \simeq (L^* + L_F/2)/\beta_y^* \qquad (1.3)$$

In practice, chromaticity is determined by the level of demagnification required of the FFS optics. Equation 1.3 indicates that tighter focusing (realized by a smaller β_y^*) enhances chromatic σ_y^* growth. Smaller beam size requirements also demand more strict control of the placement precision and field strength precision of the FFS beam line magnets in order to suppress higher order errors in the magnetic transport lattice[1]. In the absence of chromaticity correction, $\xi_y \sigma_E$ would blow up σ_y^* by as much as a factor of 10 at ILC/ATF2, even for a relatively mild $\sigma_E \lesssim 0.1\%$. This stresses the importance of chromaticity correction.
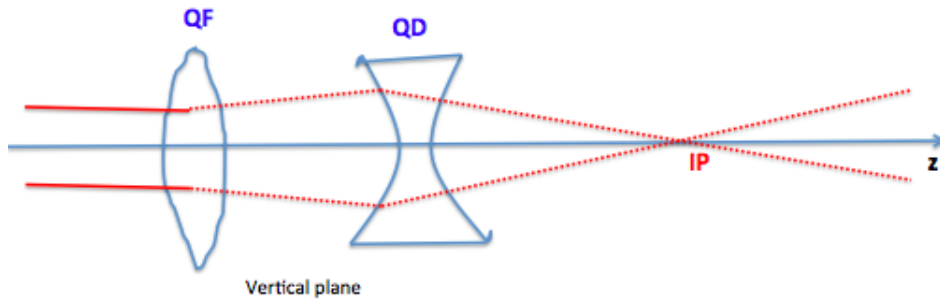
Figure 1.3: Focusing of the e$^-$ beam in the vertical plane. The beam enters parallel into the QF, where it is first defocused, then enter with a large size into the QD, where it receives abrupt focusing to a tight waist at the IP.

---

[1]Before beam tuning begins, the FFS magnets are aligned with a precision of 50-100 μm[4]. When evaluating the effect on beam size, each magnet is required to have O(μm) placement precision and O(10^{-6}) field strength precision[4]. However, in reality tolerance is looser if the optics errors can be cancelled through beam tuning.

parameters	ILC (TDR, $E_{CM}=$ 500 GeV)	ATF2
Beam energy [GeV]	250	1.3
no. of bunches per train N_b	1312	1
repetition rate f_{rep} [Hz]	5	3.12
bunch population N_e	2×10^{10}	1×10^{10}
beam energy spread σ_E [%]	0.07 (e$^+$), 0.12 (e$^-$)	0.07
L^*[m]	4.5	1.0
ε_y [pm·rad]	0.07	12
$\gamma\varepsilon_y$ [nm·rad]	35	31
(β_x^*, β_y^*) [mm]	(11, 0.48)	(4, 0.1)
(σ_x^*, σ_y^*) [nm]	(474, 5.9)	(2200, 37)
$\xi_y \sim ((L^* + L_F/2)/\beta_y^*)$	9400	10000
$\Delta\sigma_y^*/\sigma_y^* \sim \sigma_E \cdot \xi_y$	7 (e$^+$), 11 (e$^-$)	8

Table 1.1: Key design FFS parameters of ILC (TDR, $E_{CM}=$ 500 GeV, ILD detector design) and ATF2[2]. Here, L^* is the distance from QD0 to the IP, ε_y and $\gamma\varepsilon_y$ are the geometric and normalized vertical emittances, respectively, $\beta_{x(y)}^*$ is horizontal (vertical) IP beta function. ξ_y is vertical chromaticity, and $\Delta\sigma_y^*/\sigma_y^*$ indicates the beam size blow-up due to chromaticity (without correction). The values are for the nominal beta function optics, whereas at ATF2 occasionally β_x^* is increased by a factor of 10 for the "10×1" optics.

1.4 Chromaticity Correction Scheme

As mentioned in Sec. 1.3, the "natural chromaticity" generated the FD can be cancelled by the use of correction sextupoles in regions with non-zero horizontal dispersion. However in reality, there are other difficulties; the unavoidable nonlinear fields of correction sextupoles themselves cause higher order aberrations which also blow up the beam size and must be corrected. These consist of "geometrical aberrations" proportional to the quadrature of position and second order dispersion proportional to $\sigma_E{}^2$ (σ_E: beam energy spread). Below, I will describe two chromaticity schemes each featuring its own special magnet configuration which seeks to correct natural chromaticity while also compensating for the higher order aberrations that accompany the use of the nonlinear fields of the correction sextupole; first an older design called the "Global Chromaticity Correction" scheme, then a newer one called the "Local Chromaticity Correction" scheme. The contents are mainly based on [5] and [6].

1.4.1 Global Chromaticity Correction Scheme

Figure 1.4 (top) shows the magnet configuration of the "Global Chromaticity Correction" scheme. The name "global" comes from the fact that the correction sextupoles are placed in regions separate from the FD, the dominant chromaticity source. Here, chromaticity in the horizontal (vertical) planes ($\xi_{x(y)}$) are each corrected in separate dedicated regions, each consisting of a pair of sextupoles. The sextupole strengths are optimized to correct $\xi_{x(y)}$ as well as to enable the downstream sextupole to cancel the nonlinear kick produced by its upstream partner. Because the chromaticity due to sextupoles are proportional to beta function, the $\xi_{x(y)}$ correction regions have high $\beta_{x(y)}$ ($\gg \beta_{y(x)}$). The two sextupoles in a region are linked by a transfer matrix of $-I$, and the beta function and dispersion are equal between their locations. A FFS based on this design was tested at the FFTB project [7] at SLAC. The merit of this beam optics design is its symmetry which allows for relatively simple beam tuning procedures. However the demerits (when compared to the Local Chromaticity Correction scheme) are the limitations on the energy bandwidth of the system, and that the FFS

beam line is longer.

1.4.2   Local Chromaticity Correction Scheme

A major challenge accompanying the aim for higher energies in linear colliders is that their FFS beam lines rapidly become longer, more complex and thus more costly. This is a consequence of the energy errors created inside the FFS amid the chromaticity sources. Some potential energy error sources are wakefield effects and bremstrahlung due to bending by the dipoles. The FFS dipoles would have to be made weak and long. Also, long collimator sections are required to eliminate off-energy particles which would otherwise hit the FD and create background in the detectors at the IP. Energy spread also makes the chromaticity correction ineffective since the sextupole's focusing strength depends on the energy of the beam particles.

To counter these obstacles, a novel FFS optics design was proposed by P. Raimondi and A. Seryi in [5] which features the "Local Chromaticity Correction" scheme. Its name stems from the feature that the natural chromaticity is compensated *"locally"* by placing the downstream sextupoles adjacent to the FD. Figure 1.4 (bottom) shows a simplified configuration of the Local Chromaticity Correction scheme. Here, a pair of sextupoles is interleaved with the FD. Higher order aberrations generated by the sextupoles themselves are cancelled using the necessary chromaticity generated by at least two additional sextupoles placed upstream. The horizontal dispersion necessary for separating particles of different energies is generated throughout the FFS using dipole magnets.

1.4.3   Comparing FFS Designs

The newer Local Chromaticity Correction scheme was chosen over the Global Chromaticity Correction scheme to be used at future high energy lepton colliders such as the ILC. This owes to the following merits [5]:

- The length of the FFS beam line is reduced, while still maintaining beam focusing performance. This is attributed to the fact that chromaticity is corrected locally, in contrast to having to make space for separate ξ_x and ξ_y correction sections upstream of the FD. The overall FFS beam line length now scales slower than linearly with energy, allowing for more flexibility in upgrading to higher collision energies. A compact beam line significantly reduces the number of beam line components and tunnel cost as well.

- The energy bandwidth is wider, i.e. the tolerance for energy errors is looser from the point of view of beam size focusing.

- L^* is increased about two-folds, which enlarges the dynamic aperture of the FD by several orders of magnitude. Although a longer L^* means larger amount of natural chromaticity needs to be corrected (from Eq. 1.3), this one shortcoming is compensated by the following advantages: the background (BG) from synchrotron radiation is reduced; collimation requirements are relaxed; the simplified vicinity of the IP allows for the installation of a larger variety of physical detectors; beam distortion (beam halo) is reduced (see Fig. 1.5).

However, the optics of the local correction method is more complicated since its ξ_x and ξ_y correction sections are overlapped, in contrast to the symmetry and strictly separated sections in the global correction method. This demands more advanced beam tuning procedures, which motivated the construction ATF2, where they have been successfully developed and tested.
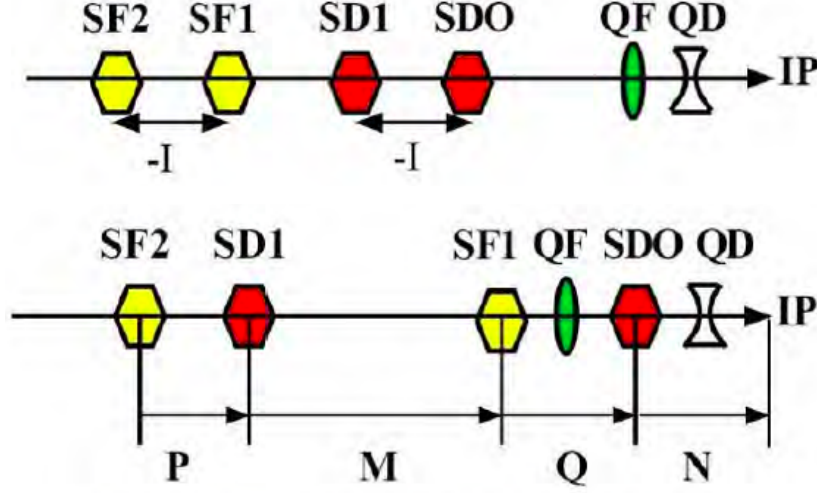
Figure 1.4: Simplified configuration of the Global chromaticity Correction scheme (top) and of the Local Chromaticity Correction scheme (bottom). Here, only the sextupoles (SF1, SF2) and (SD1, SD2) and the FD are shown. In reality other quadrupoles and dipoles co-exist among them. -I, P, M, Q, N represent the transfer matrices linking the magnets [4].
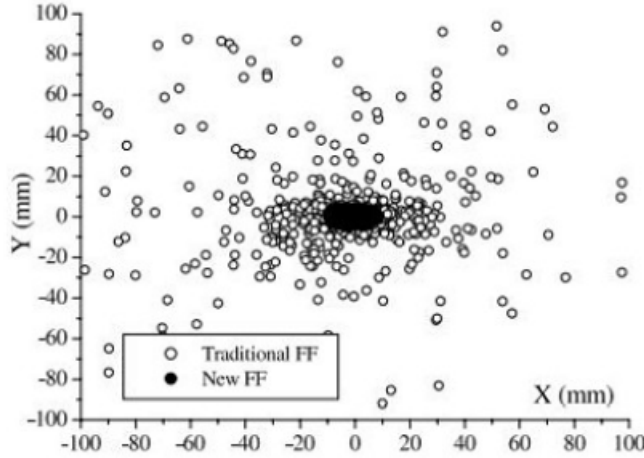
Figure 1.5: The comparison of beam halo particle distribution at the face of the FD between the traditional (= global correction) and the new (= local correction) FFS designs, based on simulation [5].

1.5 ATF / ATF2

1.5.1 Beam Line Layout

As introduced in Sec. 1.3, the ATF was constructed at KEK as a general-purpose accelerator research facility for ILC-like linear colliders. A 70 m S-Band linac accelerates the e^- bunches produced by a RF gun to 1.3 GeV. The beam is fed into a 140 m circumference damping ring (DR). In operation since 1995, the ATF DR has succeeded in realizing single 1.6 nC bunches at 3.12 Hz with an extremely small normalized vertical emittance of $\varepsilon_y \simeq 10\,\mathrm{pm}\cdot\mathrm{rad}$ [8].

The ATF2, consisting of a new extraction beam line and FFS, completed its construction onto

13

the existing ATF DR in December 2008. The extraction line prepares the beam emerging from the DR for injection into the FFS by correcting for residual energy dispersion, cross-plane (x-y) coupling and optics mismatch. Figure 1.6 shows a schematic layout of the ATF2 beam line. The beam orbit is monitored by a system of beam position monitors (BPMs): stripline BPMs (resolution 1-5 μm) and cavity BPMs (resolution 40-200 nm). There are also the "IPBPM" (C-band cavity)[9, 10] featuring O(nm) design resolution installed inside the IP vacuum chamber to provide beam position information nearest to the IP. Various technologies are being developed at ATF/ATF2 by international collaborators, such as kicker magnets, beam profile monitors, polarized positron production, BPMs, and beam position feedback systems.

1.5.2 Goals of ATF2

The ATF2 is designed as an energy-scaled test prototype of the ILC FFS, with basically the same optics, similar beam energy spread, natural chromaticity, and tolerances for alignment and magnet field strengths. This means that a good estimate for the difficulty of ILC beam tuning can be obtained from ATF2 beam operation. The prominent ATF2 beam time results reported in this thesis served to experimentally verify the design feasibility of a FFS featuring the Local Chromaticity Correction method for the ILC. Table 1.1 compares between ILC and ATF2 the basic design parameters, as well as the beam size growth due to chromaticity i.e. $\Delta\sigma_y^*/\sigma_y^* \sim \sigma_E \cdot \xi_y$. Figure 1.7 shows a schematic layout of the ATF2 FFS optics. Figure 1.8 shows the FD magnets and the FFS sextupole magnets used for chromaticity correction at ATF2. The primary goals of ATF2 can be summarized as the following:

- [Goal 1] Demonstrate focusing of σ_y^* to 37 nm, the design size scaled from the ILC by beam energy and β_y^*, and by doing so, verify the Local Chromaticity Correction scheme selected for use at the ILC.

- [Goal 2] Demonstrate O(nm) level IP beam position stabilization under the "Goal 1" beam size.

Regarding Goal 1; using the design parameters of beam energy, ε_y, and β_y^* from Table 1.1, the nominal beam size $\sigma_{y0}^* = \sqrt{\varepsilon_y \beta_y^*}$, is 5.9 nm for ILC and about 35 nm for ATF2. Since FFS chromaticity scales as $\frac{L^*}{\beta_y^*}$, ATF2 's $\beta_y^* = 0.1$ mm and $L^*=1$ m yields nearly the same chromaticity as ILC with $\beta_y^*= 0.4$ mm and $L^*= 4$ m. The official ATF2 σ_y^* milestone is scaled from ILC using both beam energy and β_y^* as 5.9 nm $\times\sqrt{\frac{250\,\text{GeV}}{1.3\,\text{GeV}}} \times \sqrt{\frac{0.1\,\text{mm}}{0.48\,\text{mm}}} \simeq$37 nm. The measurement of O(10) nm beam sizes at ATF2 by a laser interferometer type beam size monitor called the "Shintake Monitor" is essential for achieving Goal 1.

Regarding Goal 2; commissioning and performance studies are ongoing for the high resolution IPBPMs [9, 10] installed around the IP. Furthermore, specialized hardware referred to as "FONT" (Feedback On Nano-Second Timescales) [11] is undergoing tests in the extraction line beam diagnostic region to demonstrate a nm precision intra-pulse orbit feedback system.
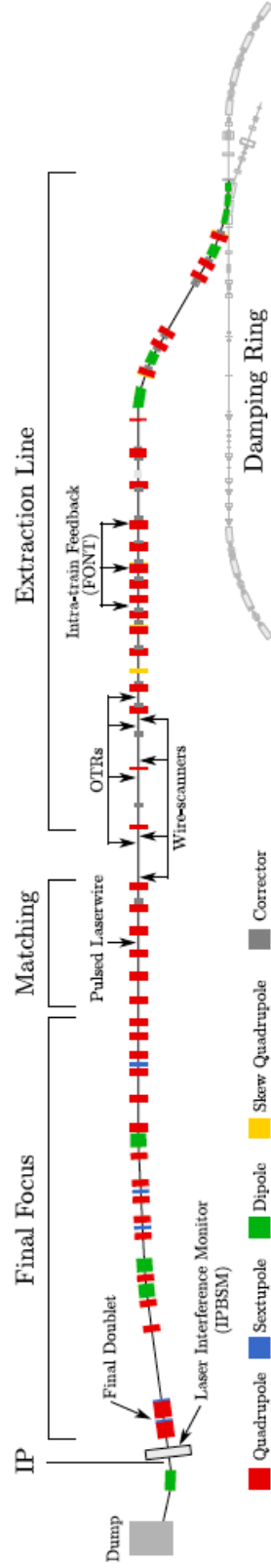
Figure 1.6: The schematic layout of the extraction line and final focus section of ATF2 after extraction from the damping ring. [8]
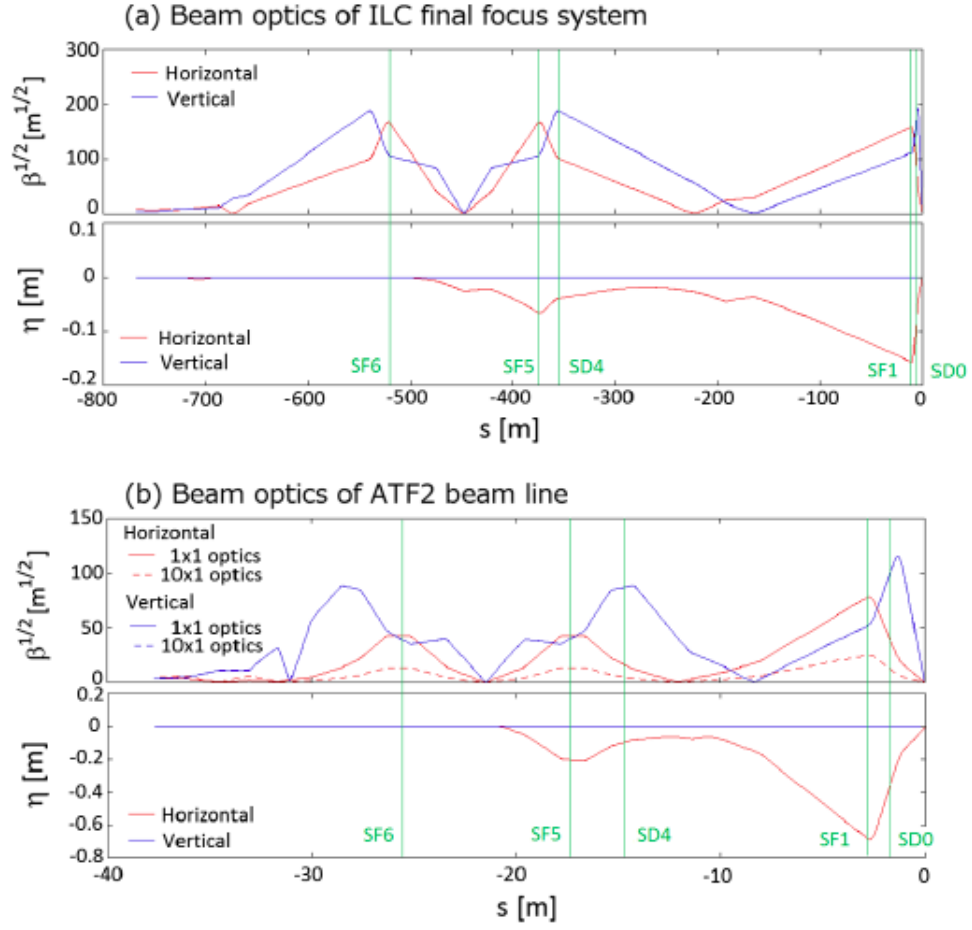
Figure 1.7: Beam optics of (a) the ILC final focus beam line and (b) the ATF2 beam line. For the ATF2, both the 1×1 optics and the 10×1 optics are shown [12]. The beam travels from the initial point (end of the extraction line) on the far left towards the IP on the far right.
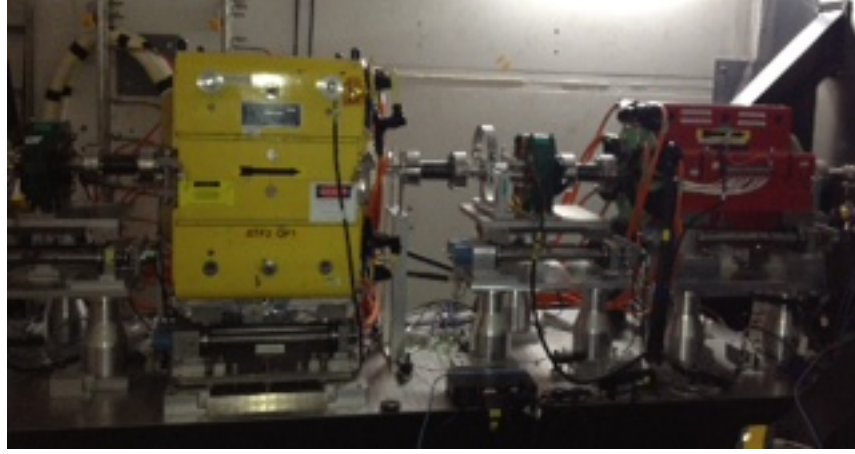
Figure 1.8: (top) the Final Doublet quadrupole magnets at ATF2, QF1 (yellow) and QD0 (red), shown together with the FFS sextupole magnets interleaved with the FD.
(bottom left) A close-up view of the SD0, the sextupole magnet placed next to the QD0. (bottom right) One of the skew setupoles in the FFS for correction of nonlinear errors.

1.6   Beam Size Monitors at ATF2

Throughout the rest of this thesis, the vertical beam size at the IP will be generally denoted without "*", as just "σ_y".

1.6.1   Shintake Monitor

The Shintake Monitor, installed at the virtual IP of ATF2, is the only system at present that has demonstrated the measurement of $\sigma_y < 100$ nm, surpassing conventional beam size monitors described in Sec. 1.6.2. Its stable σ_y measurements are essential for beam tuning and achieving the ATF2 Goal 1. The Shintake Monitor, invented by Dr. T. Shintake [13], was first used at the FFTB (Final Focus Test Beam) experiment (1994-97) at SLAC, where it succeeded in measuring $\sigma_y \simeq 70$ nm with approximately 10% resolution[13, 7]. Section 2.5 describes its upgrade for measuring the even smaller design σ_y of 37 nm at ATF2.

Figure 1.9 shows the location of the Shintake Monitor in the ATF2 beam line. Laser interference fringes are formed at the IP, which is the focal point of both the e$^-$ beam and the laser. The phase

of the interference pattern is scanned with respect to the beam by altering the path length of one arm of the interferometer using a delay line. Beam sizes are inferred from the modulation of the resulting Compton scattered photons as measured by a downstream calorimeter-type gamma-ray detector. The comprehensive description of the Shintake Monitor system is found in Part II. Section 4 explains the use of the Shintake Monitor in beam tuning. The major theme of this thesis is the evaluation of its precision in σ_y measurements.
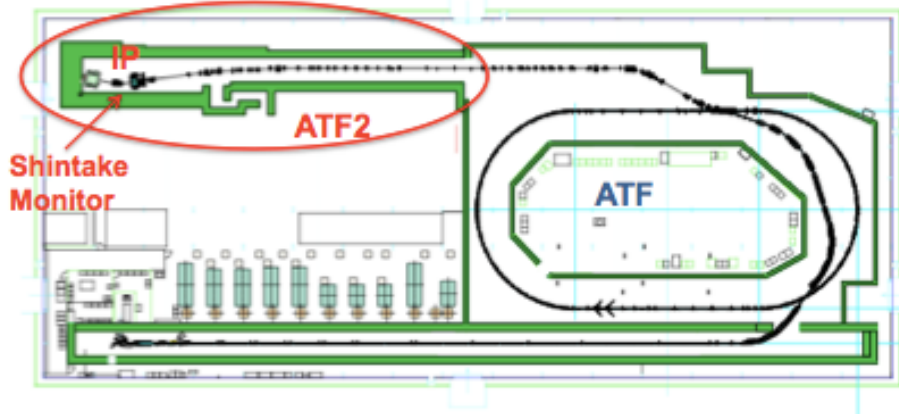
Figure 1.9: The location of the Shintake Monitor in the ATF2 beam line (circled in red)

1.6.2   Other Types of Beam Size Monitors

There are various other types of beam size monitors besides the Shintake Monitor in use at ATF for different purposes. Some, such as wire scanners and laser wires use the "scan" method, while others such as screen monitors, optical transition radiation (OTR) monitors and x-ray synchrotron radiation (XSR) monitors use imaging. Non-destructive methods, such as laser wire and XSR allow repeated measurements and thus can be used for beam tuning at the DR. Wire scanners and OTR monitors measure the beam with destructive methods. This section describes a few systems closely related to the Shintake Monitor. Details on other systems can be found in [15, 16].

Wire Scanner

A wire scanner measures beam sizes by scanning a tungsten or carbon wire across the beam, which causes photon emission due to bremsstrahlung, the dominating process for a highly relativistic beam. The energy of the emitted photons, which extends up to the beam energy, are measured using a gamma-ray detector. If the wire diameter is sufficiently thin compared to the beam size, a Gaussian-like beam profile is obtained by plotting the photon signal as a function of the scanned wire position (see Fig. 1.10). The beam size is inferred from the fitted sigma of the profile after subtracting the wire thickness in quadrature. Beam sizes as small as 1/4 - 1/2 of the wire diameter can be measured. For any beam thinner than this, either correction for wire thickness is difficult, or the wire may be burnt by the high beam intensity. The wire cannot be too thin either since it would not be durable enough. Wire scanners are used at various locations in the ATF(2) beam line. Near the IP, carbon wires of 5 μm diameter are scanned using a mover to measure σ_x and $\sigma_y \gtrsim 1$ μm. The bremsstrahlung photons are measured using a "background monitor" located about 10 cm upstream of the Shintake Monitor gamma-ray detector (see Fig. 3.30). It is a calorimeter made of a 5 mm plastic scintillator with a 10 mm thick lead converter attached to its front surface. Scintillation light is read out by a photomultiplier tube (PMT). The background monitor is installed on a mover which

allows it to be inserted for the wire scanner measurement and removed before using the Shintake Monitor. The IP wire scanners play an important role in initial beam size tuning before σ_y gets small enough to be measured by the Shintake Monitor.

Screen Monitor

The screen monitor is a thin screen made of a fluorescent material. Its collision with the e$^-$ beam releases fluorescent light which is monitored by a CCD camera to observe the beam profile. Its merits are that measurement is simple and not time consuming. However the blurring of the image limits the resolution to a few tens of μms. Screen monitors are installed at a few places in the ATF/ATF2 beam line. At the IP, there is a screen monitor attached together with the IP wire scanners to a complex target system which is slid in and out of the IP using an auto-stage. For example, the IP screen monitor is inserted for the initial position alignment of the Shintake Monitor laser to the e$^-$ beam (see Sec. 4), then ejected before the interference fringe scans.

Laser Wire

The laser wire measurement method is similar to that of the wire scanner, except that the solid wire in the latter is replaced by a laser beam, thus photon emission is due to inverse Compton scattering. A single laser beam path is scanned across the e$^-$ beam, and the energy of scattered photons measured at every laser position forms a distribution of the e$^-$ beam profile convoluted with the laser beam profile. Laser wire can measure beam sizes above 1 μm, smaller than those of wire scanners. The usage of a laser beam as the target for the e$^-$ beam avoids its destruction due to heat. However, it is difficult to maintain sufficient S/N ratio in the gamma-ray detector since photon energy for Compton scattering is low compared to bremsstrahlung. The compensation for signal rate requires high photon density i.e. powerful short laser pulses and strong laser focusing. The laser wire mode of the Shintake Monitor (see Sections 2.4 and 4.2) performs similar functions during preparation for use during beam time.
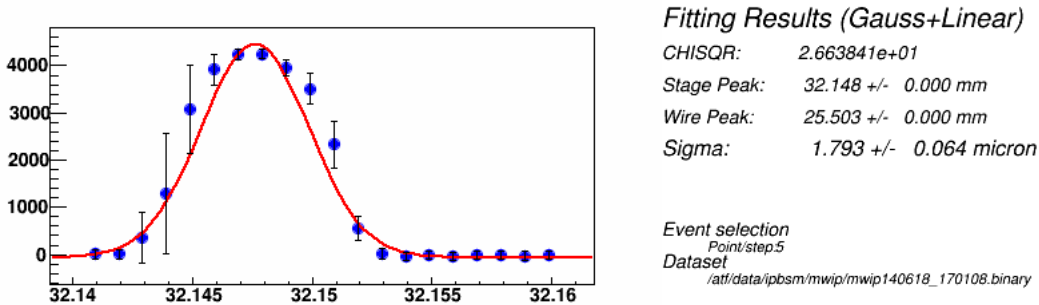
Figure 1.10: An example of the measurement of the vertical beam size by the IP carbon wire scanner. The horizontal axis is the position of the mover stage of the wire scanner (in [mm]). [17]

1.7 Beam Focusing History

Figure 1.11 and Table 1.2 show the important benchmarks in the history of the minimum σ_y stably measured at ATF2 from Dec. 2010 to June 2014. Note that these are the upper bound on σ_y, before correcting for bias factors intrinsic to the Shintake Monitor to be described in Chap. 6. In Dec. 2012, Compton signal modulation corresponding to $\sigma_y \lesssim 70$ nm was detected in fringe scans for the first time. By Mar 2013, $\sigma_y < 65$ nm had been stably measured[8]. By spring of 2014, σ_y close to the Goal 1 size has been routinely achieved. What is remarkable is not only how small a σ_y can

be focused to and measured, but also the reproducibility of beam focusing and measurement. The stable σ_y measurements by the Shintake Monitor enable very efficient beam focusing. For example, as shown in Fig. 1.11 ((b) and (c)), after start-up at the beginning of each "beam ON week", σ_y can be squeezed from a few μm to < 100 nm in a couple of days, then further down to < 60 nm in just half a day. In fact, $\sigma_y \lesssim 65$ nm was achieved during the first week of operation after more than 3 months of shutdown during 2014 summer. The progress in focusing and measuring of small σ_y owes to various improvement made over time on beam tuning methods, the beam line, and instrumentation. The most prominent improvements are grouped into the following two upgrade phases (#1 and #2) in Table 1.2:

Upgrade#1: These played a large part in the achievement of $\sigma_y < 70$ nm.

- A major improvement of the Shintake Monitor laser optics in 2012 summer by the ATF2 group at KEK (see [40]).

- The installation of skew sextupoles in the FFS line and the installation of OTR monitors in the extraction line; these enabled more effective beam tuning.

- The QF1 was replaced to one with a larger aperture which realized better field quality (Nov. 2012); the beam is very sensitive to the higher order multipole magnetic field errors of QF1 since the nominal beta function at QF1 is O(10000) m, i.e. the beam size is large.

- The improvement of tuning knobs (see Sections 4.1.1 and 4.1.2) by exchanging the relevant FFS sextupoles found to have field errors.

Upgrade#2: The items below enabled the achievement of the smallest σ_y ever measured (< 50 nm).

- The stabilization of the Shintake Monitor laser (see Sec. 8.1.1 for details)

- The improvement of tuning knobs (see Sections 4.1.1 and 4.1.2); the sextupole setting of the tuning knobs was recalculated in order to omit one of the FFS sextupoles whose field was found to be abnormally weak (April 2014).

- The stabilization of the e$^-$ beam; the orbit feedback was improved by introducing the use of corrector magnets, which reduced beam orbit drifts.

- The mitigation of wakefield effects: the $\sigma_y < 100$ nm were generally measured with low beam bunch charge ($\lesssim 1 \times 10^9$) to minimize the beam size growth due to wakefield effects. A large fraction of ATF2 beam time has been dedicated to the investigation of wakefield effects since early 2013 (see Appendix G and [18, 20] for details).

(a)

(b)

(c)
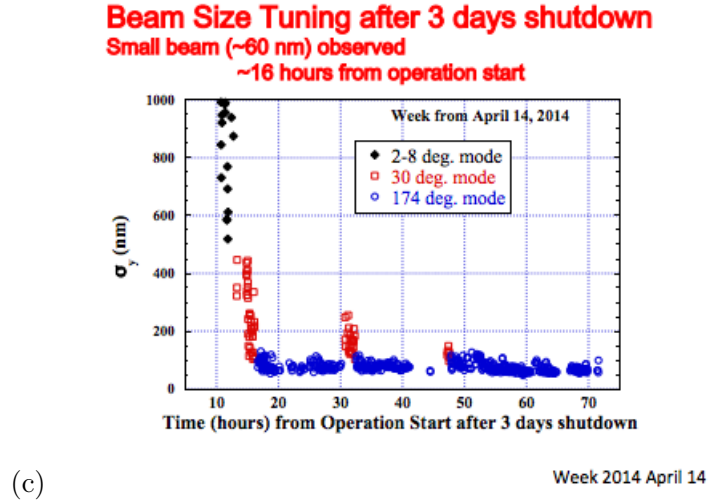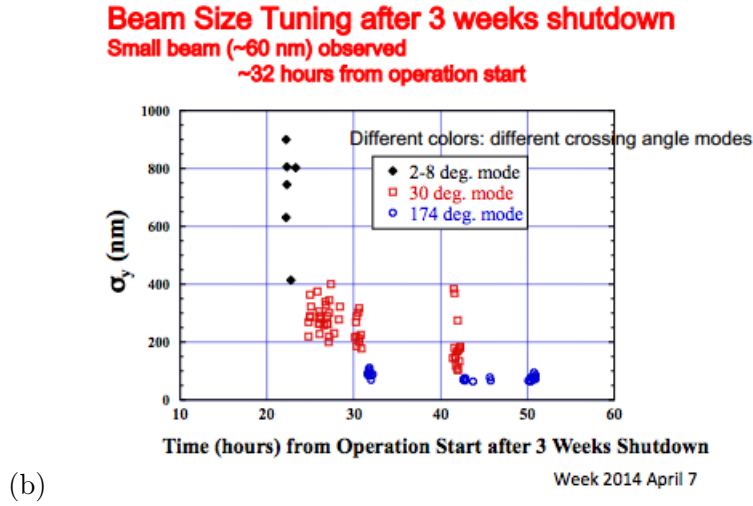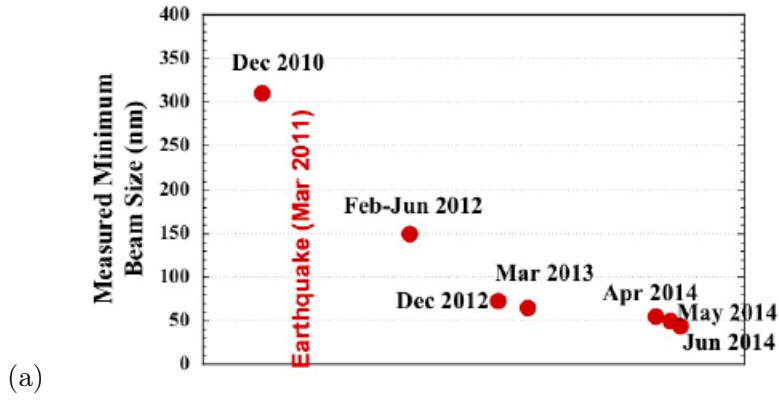
Figure 1.11: (a) The history of stably measured beam sizes (without correction for systematic errors intrinsic to the Shintake Monitor which cause beam size over-evaluation) at ATF2 from Dec 2010 to June 2014.
(b, c) Examples of efficient beam tuning of σ_y from > 1 μm to < 60 nm. The different colors signify different crossing angle modes of the Shintake Monitor system explained in Sec. 4 (b) start-up after 3 weeks of shutdown (c) start-up after 3 days of shutdown [18]

time	stably measured σ_y
Dec., 2010	~ 300 nm
	disturbance due to Mar 2011 earthquake
Feb. -June, 2012	~ 150 nm
	Upgrade#1
Dec., 2012	$\lesssim 70$ nm
Mar., 2013	$\lesssim 65$ nm
	Upgrade #2
Apr., 2014	$\lesssim 55$ nm
May, 2014	$\lesssim 50$ nm
June, 2014	$\lesssim 45$ nm

Table 1.2: The history of stably measured beam sizes at ATF2 from Dec. 2010 to June 2014. The major upgrades contributing to this progress are explained in the main text.

1.8 About this Doctoral Thesis

1.8.1 The Hi-lights of My Personal Contributions

The specialties of my studies in this thesis are that they are the first and only ever to be applied to the measurement of beam sizes < 50 nm, and that they demonstrate a way to achieve the smaller beam sizes at the ILC in the future. My major personal contributions to the research on the Shintake Monitor are the following:

1. I studied and analyzed a wide variety of systematic errors which affect the precision of beam size measurements. In particular, I developed an original method for deriving the dominant systematic error, which is the fluctuation of the relative phase (or equivalently the vertical relative position) between the laser and the e$^-$ beam at the IP. The reliability of this method was verified using simulation. These analysis are based on recent and realistic conditions of the Shintake Monitor system and the ATF2 beam operation.

2. I analyzed the measurement by the Shintake Monitor of world record small beam sizes. These take into account the above-mentioned systematic error studies, which are based on the measurements I conducted of the laser optics and the gamma-ray detector properties. My analysis results indicate that the ATF2 goal beam size has been achieved.

3. I also participated in the following since the first year of my Masters course research ($2010\sim$): the development and improvement of the Shintake Monitor hardware; the regular ATF2 beam tuning shifts during which the beam size measurements by the Shintake Monitor play an essential role.

4. I presented my research results at a number of conferences (international and within Japan), as well as in published papers (some are listed in the bibliography of this thesis).

1.8.2 Structure of Doctoral Thesis

This thesis consists of three major parts:

- In Part I, Chap. 1 begins with an introduction of the ILC, then describes the ATF/ATF2 and the role of the Shintake Monitor.

- In Part II, Chap. 2 describes the measurement scheme of the Shintake Monitor, while Chap. 3 provides the details on each of its components (e.g. the laser optics and the gamma-ray detector); Chap. 4 describes the beam tuning procedures at ATF2 and the preparation of the Shintake Monitor for beam size measurement.

- Part III, about the performance of the Shintake Monitor, is the most important part of this thesis; Chap. 5 evaluates various properties of the laser based on actual measurements e.g. focusing, profile, power, polarization, and angular stability; Chapters 6 and 7 describe an extensive study and analysis of the systematic errors and signal fluctuations affecting beam size measurements; based on these error analysis, Chap. 8 provides the complete evaluation of the smallest beam sizes ever measured. This is followed by the conclusion.

Part II

Concept of Beam Size Measurement by the Shintake Monitor

2 Description of Shintake Monitor

2.1 Measurement Scheme
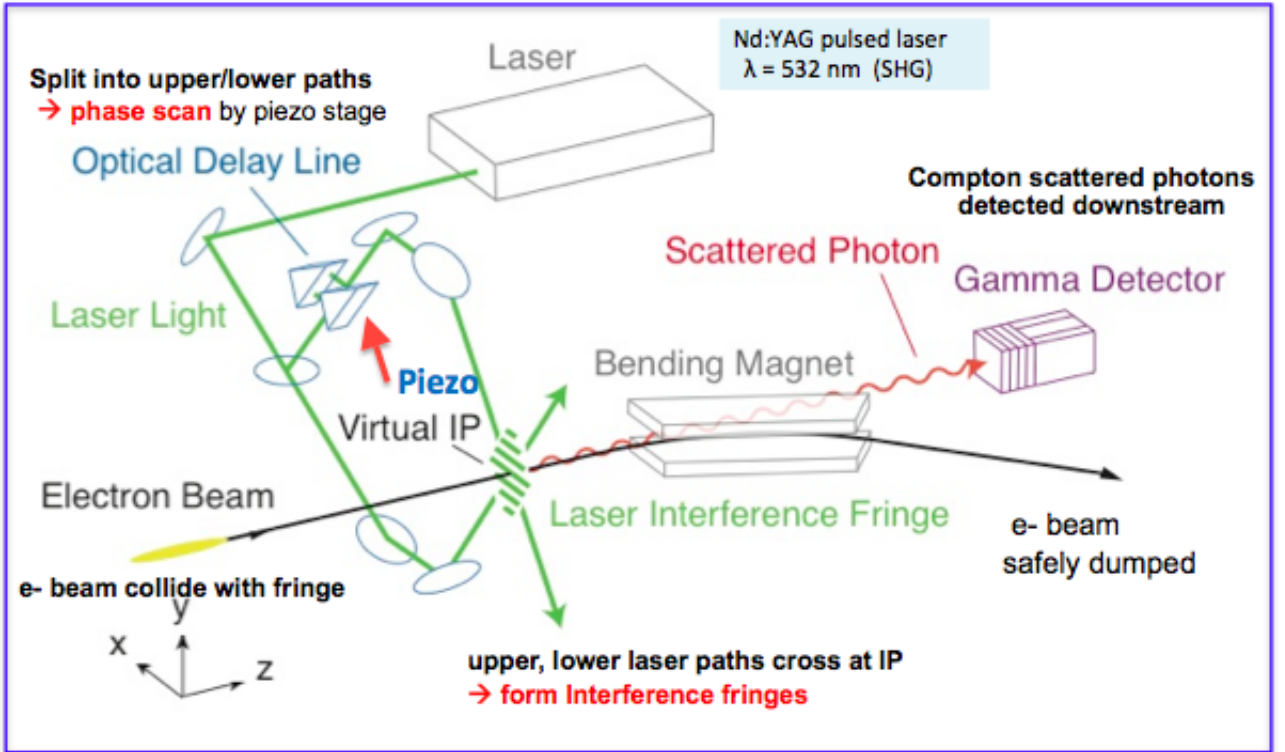
Figure 2.1: The schematic layout of the Shintake Monitor (modified from [22]).

Figure 2.1 shows the schematic layout of the Shintake Monitor system, which consists of laser optics and a gamma detector. The Nd:YAG Q-switch laser source located outside the accelerator tunnel generates laser pulses of wavelength 532 nm, pulse energy of 0.41 J, and FWHM pulse length of 8 ns. The laser pulses are delivered to an upright standing optical table ("vertical table") at the IP through an approximately 20 m transport system containing lenses to adjust the spot size and divergence. On the vertical table, the laser beam is split into upper and lower paths by a 50% beam splitter. The laser paths propagate to lenses which focus them to tight waists at the IP, where they cross to form the interference fringes that the e$^-$ beam collides perpendicularly against. The fringe phase is scanned relative to the beam using a delay line consisting of prisms and a piezoelectric stage. The Compton scattered photons resulting from the laser-beam collision enter a downstream electromagnetic calorimeter-type detector made up of layers of CsI(Tl) scintillators which measures the energy deposited by the photons. The e$^-$ beam is bent by a dipole magnet safely into a dump.

The detector measures the variation in Compton signal intensity as the fringe phase is scanned, called "modulation depth" (denoted as "M"). The M spectrum consists of Compton signal energy

plotted as a function of fringe phase. Figure 2.2 shows the relationship between M and beam sizes. The number of signal photons is large when the beam collides against the fringe peak, and small when it collides against the fringe valley. A well focused beam is more sensitive to this difference. Therefore, M is large if the beam size is small compared to the fringe pitch, whereas M is small for a large beam size.
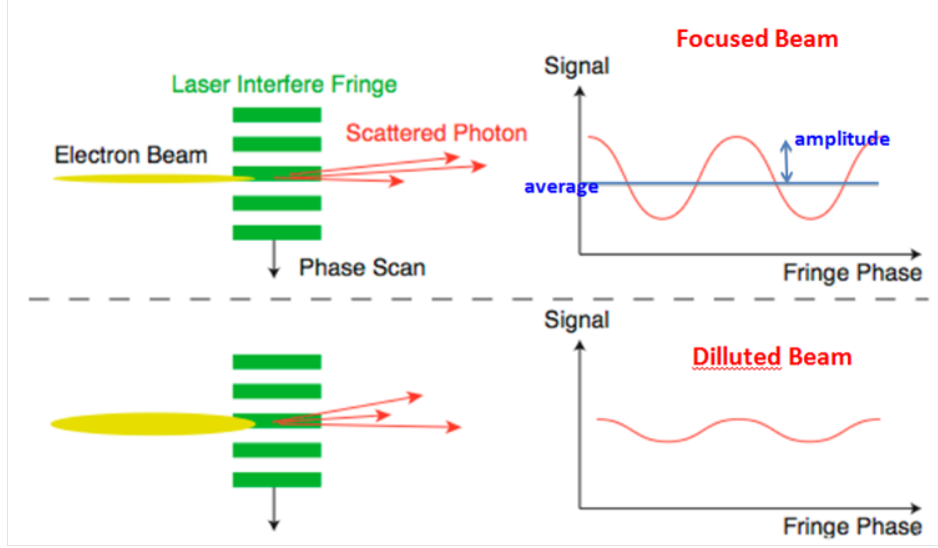
Figure 2.2: Relationship between modulation depth (M) and beam sizes (modified from [22]).

2.2 Beam size Calculation

This section explains how the beam size is derived from the measured modulation. First, the relevant parameters will be defined:

- σ_y : vertical beam size at the IP

- θ : laser beam crossing angle

- $k_y = k\sin(\theta/2)$: wave number component normal to laser fringe

- λ : laser wave length (532 nm for the Shintake Monitor at ATF2)

- y' : vertical relative position at the IP between the laser and the e$^-$ beam

- N : number of Compton scattered photons (= signal intensity)

- α : relative phase between upper and lower laser paths

Figure 2.3 defines the coordinates surrounding the IP. The e$^-$ beam propagates in the z direction in the laboratory frame, while the laser interference fringe is formed in the transverse plane, where x and y are the horizontal and vertical directions, respectively. The wave number vectors of the magnetics fields for the upper and lower laser paths are:

$$\overrightarrow{k_1} = (k\cos(\theta/2), k\sin(\theta/2), 0) \equiv (k_x, k_y, 0) \qquad \overrightarrow{k_2} = (k\cos(\theta/2), -k\sin(\theta/2), 0) \qquad (2.1)$$
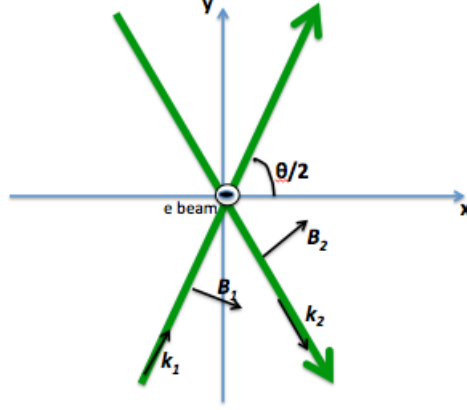
Figure 2.3: Relationship between electromagnetic fields and the propagation of the e$^-$ beam and the two laser paths.

In this experiment, the laser beam is set to be linear S polarization (see Sec. 5.4), for which the electric field of the laser beam is parallel to the surface of the mirrors on the vertical table[2]. The laser spot size is focused by a lens to a waist of about 10 - 15 μm at the IP. Because the laser spot size is much larger than σ_y, the e$^-$ beam is assumed to interact with homogenous planar electromagnetic fields. The electric ($\overrightarrow{E_{elec}}$) and magnetic ($\overrightarrow{B}$) fields of the upper and lower laser paths can be expressed as:

$$
\begin{aligned}
\overrightarrow{E_{elec,1}} &= E_{elec}(0,0,1)\cos\left(\omega t - \overrightarrow{k_1} \cdot \overrightarrow{x} - \tfrac{\alpha}{2}\right) \\
\overrightarrow{E_{elec,2}} &= E_{elec}(0,0,1)\cos\left(\omega t - \overrightarrow{k_2} \cdot \overrightarrow{x} + \tfrac{\alpha}{2}\right) \\
\overrightarrow{B_1} &= B(\sin\left(\theta/2\right), -\cos\left(\theta/2\right), 0)\cos\left(\omega t - \overrightarrow{k_1} \cdot \overrightarrow{x} - \tfrac{\alpha}{2}\right) \\
\overrightarrow{B_2} &= B(-\sin\left(\theta/2\right), -\cos\left(\theta/2\right), 0)\cos\left(\omega t - \overrightarrow{k_2} \cdot \overrightarrow{x} + \tfrac{\alpha}{2}\right)
\end{aligned}
\tag{2.2}
$$

After Lorenz transformation to the rest frame of a relativistic particle, only the field components transverse to the Lorentz boost direction contribute to inverse Compton scattering since these are enhanced by a factor of γ. In the lab frame, the laser fringe intensity can be expressed as the following superposition of magnetic fields from the two laser paths:

$$
\overrightarrow{B} = \overrightarrow{B_1} + \overrightarrow{B_2} = 2B \begin{pmatrix} \sin\left(\theta/2\right)\sin\left(\omega t - k_x x\right)\sin\left(k_y y + \tfrac{\alpha}{2}\right) \\ -\cos\left(\theta/2\right)\cos\left(\omega t - k_x x\right)\cos\left(k_y y + \tfrac{\alpha}{2}\right) \\ 0 \end{pmatrix}
\tag{2.3}
$$

Equation 2.3 shows a traveling wave along the x axis and a standing wave along the y axis. The magnetic field intensity, averaged over time, is expressed as [3]:

$$
\left|\overrightarrow{B}\right|^2 = \left|\overrightarrow{B_1} + \overrightarrow{B_2}\right|^2 = B^2\left(1 + \cos\theta\cos\left(2k_y y + \alpha\right)\right)
\tag{2.4}
$$

Equation 2.4 indicates that the visibility of the interfere pattern depends on the crossing angle θ. It also indicates that the magnetic field intensity changes as $\cos\left(2k_y y + \alpha\right)$, which is a function

---

[2]The electric field of the Shintake Monitor laser is parallel to the e$^-$ beam (longitudinal) direction. The interference fringes form upon a vertical table standing upright perpendicular to the beam direction.

[3]For relativistic energy beams, the fringe intensity can be expressed either using magnetic field in the lab frame or electric field in the e$^-$ rest frame. Averaging the magnetic field intensity over time is valid since the longitudinal e$^-$ beam bunch length ($\sim$8 mm) is much longer than $1/k_x$, and thus the magnetic field oscillates many times along the x axis during the passing of the e$^-$ beam bunch.

of the relative position (y) between the laser and the e$^-$ beam at the IP, and the relative phase α. An optical delay line installed in the upper path is used for changing α during interference fringe scans. The pitch (d) of the interference fringes i.e. the distance between adjacent peaks, depends on the laser crossing angle θ, and is expressed as:

$$d = \frac{\pi}{k_y} = \frac{\lambda}{2\sin(\theta/2)} \tag{2.5}$$

The signal intensity N, which is proportional to the luminosity of collision between the e$^-$ beam and laser fringes, is derived as the convolution between fringe intensity and e$^-$ beam profile as:

$$N \propto \int dx dy' P_{beam}(x, y') \overline{\left|\vec{B}\right|^2} (y') \tag{2.6}$$

Here, y' is the vertical distance between the crossing point of the two laser paths and the e$^-$ beam. Integration in the x plane is equal to 1. Assuming a Gaussian vertical e$^-$ beam profile as: $P_{beam}(y') = \frac{1}{\sqrt{2\pi}\sigma_y} \exp\left(-\frac{y'^2}{2\sigma_y^2}\right)$, Eq. 2.6 can be rewritten as :

$$N \propto \int dy' \frac{1}{\sqrt{2\pi}\sigma_y} \exp\left(-\frac{y'^2}{2\sigma_y^2}\right) \overline{\left|\vec{B}\right|^2} (y') \tag{2.7}$$

$$= B^2[1 + \cos\theta \cos(2k_y y + \alpha)\exp(-2(k_y\sigma_y)^2]$$

Equation 2.7 indicates that the Compton signal intensity changes according to the fringe phase, and that the degree of variation i.e. the "modulation depth" (M), depends on the vertical e$^-$ beam size σ_y. M is related to maximum and minimum signal intensity ($N_\pm = \frac{N_0}{2}B^2[1\pm\cos(\theta)\exp(-2(k_y\sigma_y)^2]$) as:

$$M = \frac{N_+ - N_-}{N_+ + N_-} = |\cos\theta \exp\left(-2(k_y\sigma_y)^2\right)| \tag{2.8}$$

σ_y can then be calculated as a function of M and fringe pitch d as:

$$\sigma_y = \frac{d}{2\pi}\sqrt{2\ln\left(\frac{|\cos(\theta)|}{M}\right)} \qquad \left(d = \frac{\pi}{k_y} = \frac{\lambda}{2\sin(\theta/2)}\right) \tag{2.9}$$

In practice, the Compton energy spectrum measured by the gamma-ray detector is plotted as a function of the fringe phase, and fitted with the following cosine-like function (as in Fig. 2.2) to extract M, E_{avg} (average energy), and φ_0 (initial phase).

$$E(y) = E_{avg}(1 + M\cos(2k_y y + \varphi_0)) \tag{2.10}$$

Examples of fringe scans from actual beam time can be found in Sec. 8.1. From Eq. 2.10, M can be interpreted as $\frac{\text{Amplitude}}{\text{Average}}$ of the measured energy. The contrast, or "visibility" of the laser fringes is defined using the highest and lowest intensity interacting with the beam in the e$^-$ rest frame as $I = \frac{I_{max} - I_{min}}{I_{max} + I_{min}}$. A clear contrast is important for measuring a large M (i.e. a small σ_y), whereas a degraded contrast leads to the under-evaluation of M (i.e. over-evaluation of σ_y).

2.3 Measurable Range

From Eq. 2.9, it can be seen that the measurable beam size range is determined by the fringe pitch d which depends on the crossing angle θ. In order to be able to measure a wide range of σ_y from 25 nm to a few μm with better than 10% resolution, the laser optics is designed to enable the switching

between several θ modes according to e$^-$ beam focusing status. This is explained as follows. Using Equations 2.8 and 2.9, the beam size resolution can be expressed as a function of σ_y/d, the ratio of beam size to fringe pitch, as:

$$\left| \frac{\Delta \sigma_y}{\sigma_y} \right| = \frac{|\Delta M/M|}{2 \ln \left(\frac{|\cos(\theta)|}{M} \right)}$$

$$= \frac{\exp \left(2\pi^2 \left(\sigma_y/d \right)^2 \right)}{4 |\cos \theta| \, \pi^2 \left(\sigma_y/d \right)^2} \cdot |\Delta M| \tag{2.11}$$

Equation 2.11 is plotted in Fig. 2.4 assuming a constant $|\Delta M|$=0.02 and $|\cos \theta| = 1$. From Fig. 2.4, we can observe the following:

- resolution is best when σ_y is around $1/5$ of d.

- resolution worsens suddenly as σ_y exceeds $1/2$ of d; this is because as σ_y approaches the scale of d, the e$^-$ beam loses its sensitivity to the contrast of the interference fringes.

- resolution worsens slowly as σ_y decreases below $1/10$ of d; this is because if d is large compared to σ_y, the fringe loses its sensitivity to the narrow scale of the e$^-$ beam.

The Shintake Monitor has a stricter limit on a larger σ_y for a fixed d. This is why several crossing angle modes are necessary in order to widen the range of measurable beam sizes.

For several representative modes of $\theta = 2$, 8, 30, and 174 deg, Fig. 2.5 shows M (Eq. 2.8), while Fig. 2.6 shows beam size resolution (Eq. 2.11) assuming $|\Delta M|$=0.02, both as a function of σ_y. Table 2.1 shows d and the measurement range for σ_y; the standard for the upper limit ($\sigma_{y,max}$) is based on M=0.1 since the typical amount of signal jitter limits detection of M smaller than this. The standard for the lower limit ($\sigma_{y,min}$) is based on $\Delta \sigma_y/\sigma_y$=10% in Fig. 2.6.

For the larger σ_y, 2 - 8 deg modes (continuously adjustable) are used. As σ_y is focused down smaller (using the tuning procedures in Sec. 4.1), mode is switched to 30 deg, and finally to 174 deg mode. Mode switching is carried out via the remote control of auto-stages carrying actuator-controlled mirrors. In practice, the typical M for each mode is typically 0.1-0.9, with the exception of the upper limit for 30 deg mode, for which $\cos \theta$ comes up to only about 0.86 ($=\cos (\pi/6)$). The lower limit for the measurable σ_y (as M approaches 1), where switching to a larger θ mode is usually carried out, is determined by the bias effects from systematic errors.
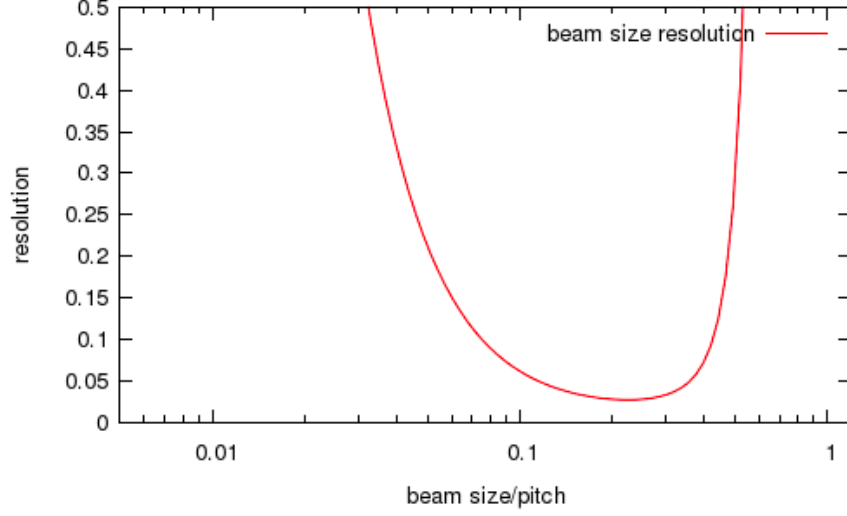
Figure 2.4: The relative beam size resolution $\Delta\sigma_y/\sigma_y$ plotted as a function of σ_y/d i.e. the ratio of beam size to fringe pitch assuming a constant ΔM=0.02 and $|\cos\theta| = 1$.
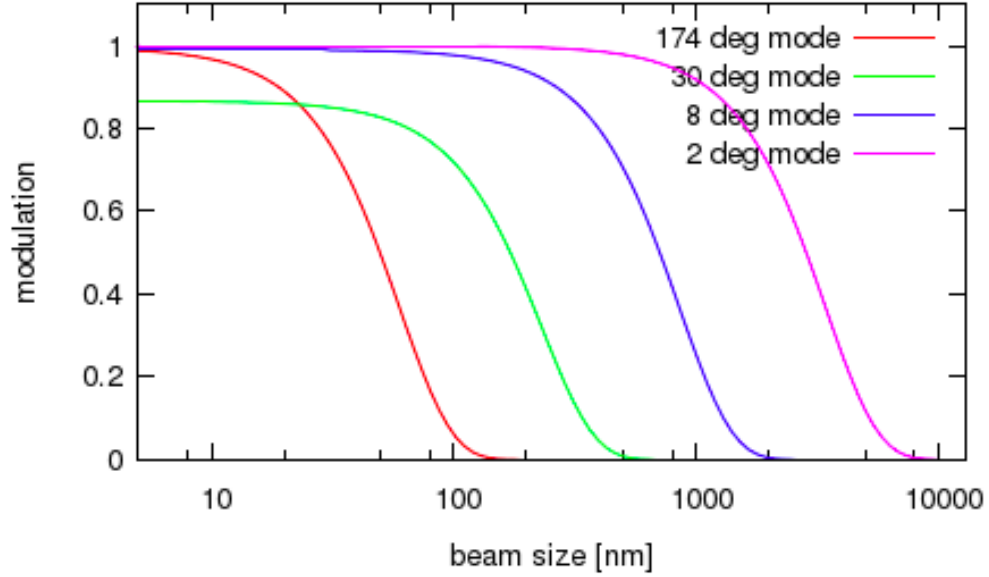
Figure 2.5: For the crossing angle modes of 2, 8, 30, and 174 deg: the relationship between modulation (M) and vertical beam size (σ_y). For a fixed σ_y, M takes on very different values for different modes. The maximum M comes up to $|\cos\theta|$.

29
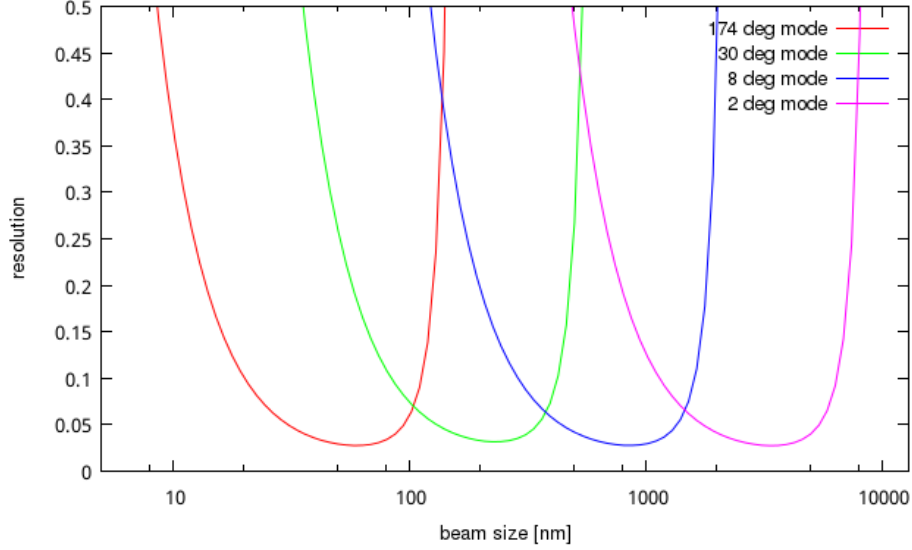
Figure 2.6: For the crossing angle modes of 2, 8, 30, and 174 deg: the relationship between beam size resolution ($\Delta\sigma_y/\sigma_y$) and σ_y, assuming a constant ΔM=0.02.

crossing angle θ	174 deg	30 deg	8 deg	2 deg
fringe pitch d	266 nm	1.028 μm	3.81 μm	15.2 μm
range $\sigma_{y,min}$ / $\sigma_{y,max}$	20 nm / 90 nm	85 nm / 340 nm	290 nm / 1.3 μm	1.2 μm / 5.2 μm

Table 2.1: Beam size measurement range for each crossing angle mode.

2.4 Laser wire mode

In addition to the interference modes in Table 2.1, there is a "laser wire mode" which consists of scanning a single laser path in the transverse plane relative to the e$^-$ beam using mirrors controlled by actuators. This serves to measure σ_x and/or laser spot size σ_{laser}. In this case, the "beam size seen from the laser (σ_{beam})" depends on crossing angles (θ) as:

$$\sigma_{beam} = \sqrt{\sigma_x^2 \sin^2(\theta/2) + \sigma_y^2 \cos^2(\theta/2)} \tag{2.12}$$

Assuming Gaussian profiles for both the laser and the e$^-$ beam, the Compton signal also takes on a Gaussian distribution; its spread is the convolution of σ_{laser} and σ_{beam} :

$$\sigma_{lw} = \sqrt{\sigma_{beam}^2 + \sigma_{laser}^2} \tag{2.13}$$

Equation 2.13 shows that passing the laser horizontally i.e. $\theta \to 0$ deg allows measurement of σ_y, while passing it vertically i.e. $\theta \to 180$ deg makes it sensitive to σ_x. In this way, the horizontal beam size σ_x can be measured using laser wire scan at 174 deg mode. During recent ATF2 operations, σ_x is of similar size to σ_{laser}, and is typically measured using the IP wire scanners (see Sec. 1.6.2). By the time the Shintake Monitor is used in beam tuning, σ_y would already been tuned to be much smaller than σ_{laser}, also using the IP wire scanners. Thus most of the time the Shintake Monitor laser wire mode is used for the following purposes (see Sec. 4.2 for details):

1. Measure laser spot size σ_{laser}. This is subtracted from the 1-σ spread of the measured laser wire scan signal using Eq. 2.12 and Eq. 2.13.

30

2. Align laser position in the transverse plane to enable collision with the e$^-$ beam.

2.5 Upgrades from Use at the FFTB

The Shintake Monitor had first been used at the FFTB experiment (at SLAC), where it had succeeded in measuring $\sigma_y \simeq 70$ nm with approximately 10% resolution[13, 7]. The discrepancy between the 70 nm and the FFTB goal σ_y of 60 nm is possibly attributed to e$^-$ beam jitter and beam size monitor related systematics, and has not been made certain. The measurement of e$^-$ beam jitter at the IP would require the yet to be commissioned O(nm) resolution cavity BPMs. There may also have been some residual non-linear aberrations which blow up σ_y since the Local Chromaticity Correction scheme was developed after FFTB had ended. In the years that followed, various proposals for FFS design in linear colliders prompted the construction of ATF2. This section describes the changes made to the Shintake Monitor to adapt it for achieving goals specific to ATF2. Table 2.2 compares the design parameters between ATF2 and FFTB. Compared to FFTB, the Shintake Monitor at ATF2 faces the following challenges:

[1] Repetition rate is lower for ATF2 (1.56 Hz at first, later 3.12 Hz) than for FFTB (30 Hz) by a factor of about 10. To compensate this limit on signal statistics, precision must be improved by suppressing bunch-to-bunch signal fluctuation factors such as laser power, position, phase, and background. Also, fringe scans at ATF2 are more time consuming, which is unfavorable from the point of view of maintaining stability against slow position drifts of the laser and/or the e$^-$ beam. For instance, at ATF2, typically about 200 pulses are used for a scan taking over 1 min (10 pulses at each of the 20 phases). At FFTB, about 900 bunches can be measured in much shorter scans of about 30 s. The higher FFTB repetition rate enables 10 times more pulses to be used at each phase for the same length of time.

[2] Beam energy is lower for ATF2 (1.3 GeV) than for FFTB (46.6 GeV) by a factor of about 36. Therefore single photon energy is also much lower for ATF2, making signal detection more difficult.

Despite the above-mentioned challenges, the Shintake Monitor realized at ATF2 succeeded in measuring smaller beam sizes than FFTB with similar resolution. This owes to the following improvements:

Laser wavelength: Because a smaller fringe pitch $\left(d = \frac{\lambda}{2\sin(\theta/2)}\right)$ is required for measuring a smaller design σ_y, the laser wavelength (λ) was halved from 1064 nm to 532 nm by second harmonics generation (SHG).

Wider measurement range: The laser optics was upgraded to measure a wider range of beam sizes (25 nm - a few μm) than at FFTB (40 - 720 nm). In particular, continuously adjustable laser crossing angle modes between 2-8 deg were implemented for more effective tuning of large beam sizes during initial tuning stages. This allows the overlap and crosscheck with wire scanner measurements. In addition, a "laser wire mode" (see Sec. 2.4) enables the convenient measurement of the larger horizontal beam sizes using a single laser path.

Scan method: For fringe scans at FFTB, the vertical position of the e$^-$ beam itself is shifted using steering magnets w.r.t. a fixed laser fringe. This method is unsuitable for ATF2 because (a) very slight shifts of the beam are difficult given the low ATF2's beam energy, and (b) it is unfavorable to jeopardize beam position stability from the point of view of the Goal 2 of ATF2, which is nm precision stabilization of e$^-$ beam position at the IP. At ATF2, modulation is produced by scanning the relative phase of the two laser paths using a phase control system (see Sec. 3.3.1) w.r.t. the e$^-$ beam position fixed at the IP. The prevention of e$^-$ beam position instability is more positive for measurement accuracy.

design parameters	FFTB	ATF2
beam energy	46.6 GeV	1.3 GeV
1 photon energy	8.6 GeV	15 MeV
repetition rate	30 Hz	3.12 Hz
(σ_x^*, σ_y^*)	(900 nm, 60 nm)	(7 μm , 37 nm)
(β_x^*, β_y^*)	(10, 0.1) mm	(40, 0.1) mm
$(\gamma\varepsilon_x, \gamma\varepsilon_y)$	$(3 \times 10^{-5}, 3 \times 10^{-6}$) m $\cdot$ rad	$(2.8 \times 10^{-6}, 3.1 \times 10^{-8}$) m $\cdot$ rad
aspect ratio (σ_x^*/σ_y^*)	15	189
N_{bunch}	1×10^{10}	1×10^{10}
energy spread	0.3%	0.7-0.9%

Table 2.2: Comparison between FFTB and ATF2 (status in 2014) of design parameters related to the Shintake Monitor (modified from [7]).

2.6 Physics of Compton Scattering

The physics process of inverse Compton scattering between laser photons and electrons in the beam will be described, with the aim to derive the following in the lab frame:

- total cross section of Compton scattering

- energy and angular distribution of the Compton scattered photons

The following notations are used:

- 4 momentum vector : p for e$^-$, k for photon

- θ : scattering polar angle, $\quad$ ϕ : azimuthal angle, $\quad$ Ω : solid angle

- with ' : "after collision", without ' : "before collision"

- with * : e$^-$ rest frame, without * : lab frame

- γ : Lorentz boost factor, $\gamma = 1/\sqrt{1 - \beta^2}$

- $\vec{\varepsilon}$: photon polarization vector

- m : e$^-$ rest mass

Figure 2.7 shows the diagrams for Compton scattering in the e$^-$ rest frame and the lab frame. Kinematics will be calculated in the comparatively simpler e$^-$ rest frame, then the results will be converted using Lorentz transformation to the lab frame. Assuming that incident photon propagates in the z direction, the following 4 momentum vectors will be used:

$$p^* = (m, 0, 0, 0)$$

$$k^* = (k^*, 0, 0, -k^*)$$

$$k'^* = \left(k'^*, k'^* \sin\theta'^* \cos\phi'^*, k'^* \sin\theta'^* \sin\phi'^*, k'^* \cos\theta'^*\right) \tag{2.14}$$

The differential cross section in the e$^-$ rest frame is:

$$\frac{d\sigma}{d\Omega'^*} = \frac{1}{64\pi^2 m^2} \left(\frac{k'^*}{k^*}\right)^2 \overline{|M|^{*2}} \tag{2.15}$$

The squared matrix element of Compton scattering is [14]:

$$\overline{|M|^2} = 2e^4 \left[\frac{p \cdot k'}{p \cdot k} + \frac{p \cdot k}{p \cdot k'} - 2 + 4\left(\varepsilon \cdot \varepsilon'\right)^2\right] \tag{2.16}$$

Equation 2.16 is based on linearly polarized photons and the gauge $\varepsilon \cdot p = \varepsilon' \cdot p = 0$. It can be shown that after summing over all final polarization states (since the Shintake Monitor detector is not sensitive to polarization) and integrating over all azimuthal angles, this can be expressed as the Klein-Nishina equation [22]:

$$\frac{1}{2\pi} \int_0^{2\pi} d\phi^* \overline{|M|^{*2}} = 2e^4 \left[\frac{k^*}{k'^*} + \frac{k'^*}{k^*} - 1 + \cos^2\theta'^*\right] \tag{2.17}$$

The relationship between parameters in the e$^-$ rest frame and lab frame are obtained from Lorentz transformation as the following:

$$k^* = \gamma k$$

$$\phi^* = \phi$$

$$\cos\theta'^* = \frac{\cos\theta' - \beta}{1 - \beta\cos\theta'}$$

$$d\Omega'^* = \gamma^2 \left(1 + \beta\cos\theta'^*\right)^2 d\Omega' \tag{2.18}$$

From kinematics i.e. conservation of momentum, the energy of the scattered photons is calculated to be Eq. 2.19 and Eq. 2.20 in the e$^-$ rest frame and the lab frame, respectively:

$$k'^* = \frac{mk^*}{m + k^* \left(1 - \cos\theta'^*\right)} \tag{2.19}$$

$$k' \simeq \frac{\gamma mk}{k - k\sin\theta'\cos\left(\phi - \phi'\right) + \gamma m \left(1 - \beta\cos\theta'\right)}$$

$$\simeq \frac{\gamma mk}{k + \gamma m \left(1 - \beta\cos\theta'\right)} \tag{2.20}$$

In Eq. 2.20, the approximation $\sin\theta' \ll 1$ is applied based on the very forward distribution of scattered photons. The maximum and minimum energies of the scattered photons are

$$k'_{max} = \frac{\gamma mk}{k + \gamma m \left(1 - \beta\right)} \simeq 29.5\,\text{MeV} \qquad \left(\theta' = 0\right) \tag{2.21}$$

$$k'_{min} = \frac{\gamma mk}{k + \gamma m \left(1 + \beta\right)} \simeq 1.17\,\text{eV} \qquad \left(\theta' = \pi\right) \tag{2.22}$$

Using Equations 2.15, 2.17, and 2.18, the cross section is distributed in terms of $\cos\theta'$ as :

$$\frac{d\sigma}{d\cos\theta'} = \frac{d\Omega'}{d\cos\theta'} \frac{d\Omega'^*}{d\Omega'} \frac{d\sigma}{d\Omega'^*} = \int d\phi'^* \gamma^2 (1 + \beta\cos\theta'^*)^2 \times \frac{1}{64\pi^2 m^2} \left(\frac{k'^*}{k^*}\right)^2 \overline{|M|^{*2}}$$

$$= \frac{\alpha^2 \pi}{m^2} \left(\frac{k'^*}{k^*} \right)^2 \gamma^2 (1 + \beta \cos \theta'^*)^2 \left[\frac{k^*}{k'^*} + \frac{k'^*}{k^*} - 1 + \cos^2 \theta'^* \right] \qquad \left(\alpha = \frac{e^2}{4\pi} \right) \tag{2.23}$$

Integration over the entire solid angle gives the total cross section for Compton scattering as :

$$\sigma_{\text{total}} = \frac{2\pi\alpha^2}{m^2} \left\{ \frac{1+q}{q^3} \left[\frac{2q(1+q)}{1+2q} - \ln(1+2q) \right] + \frac{\ln(1+2q)}{2q} - \frac{1+3q}{(1+2q)^2} \right\} \tag{2.24}$$

Here, the parameter $q \equiv \gamma k/m$ represents the energy ratio between the incident photon and the electron in the e$^-$ rest frame. In can be seen that σ_{total} declines with the increase of q, i.e. with the increase of e$^-$ beam energy (γ) or incident laser photon energy k. For ATF2, $q \simeq \frac{2544 \times 2.33 \, eV}{511 \, keV} \simeq$ 0.0116, which gives $\sigma_{\text{total}} = 0.65 \, \text{barn}$.

The angular distribution and energy distribution of Compton scattering cross section are calculated as Eq. 2.25 and Eq. 2.26, respectively. Inserting Equations 2.18, 2.19 , and 2.23, these are plotted as in Fig. 2.8, along with the scattered photon energy as a function of scattered angle (Eq. 2.20).

$$\frac{d\sigma}{dk'} = \left(\frac{dk'}{d\cos\theta'} \right)^{-1} \frac{d\sigma}{d\cos\theta'} = \frac{k}{\beta k'^2} \frac{d\sigma}{d\cos\theta'} \tag{2.25}$$

$$\frac{d\sigma}{d\theta'} = \frac{d\cos\theta'}{d\theta'} \frac{d\sigma}{d\cos\theta'} = -\sin\theta' \frac{d\sigma}{d\cos\theta'} \tag{2.26}$$

In Fig. 2.8 (top right), the angular spread of the scattered photons corresponding to 95% of the total number of photons is about 1.7 mrad. This signifies that the photons are nearly all projected along the e$^-$ beam direction. Their angular spread is increased slightly by the divergence of the e$^-$ beam : $\Delta\theta_x^e \simeq 0.17 \, \text{mrad}$, $\Delta\theta_y^e \simeq 0.35 \, \text{mrad}$.
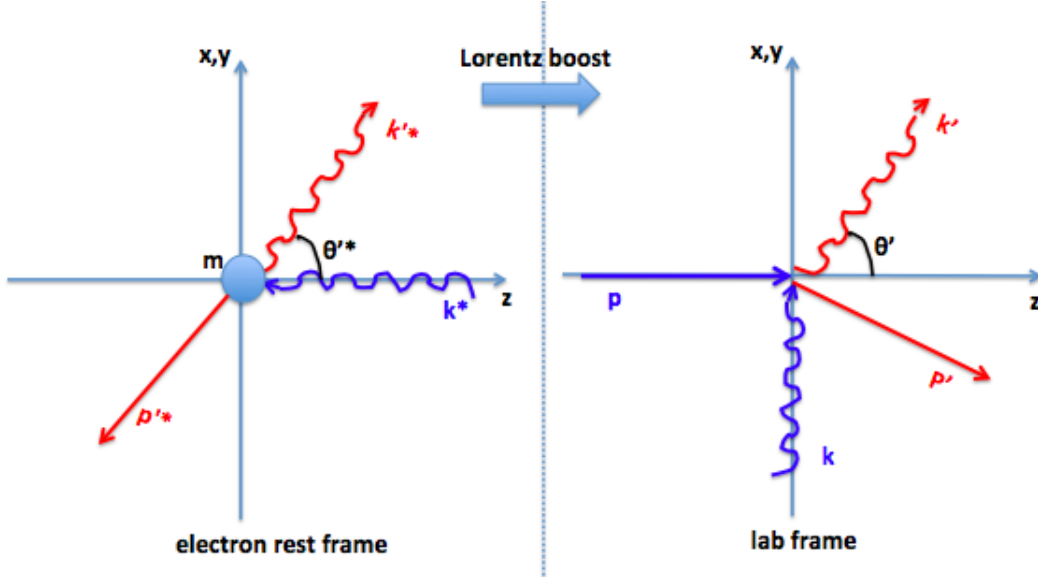
Figure 2.7: Schematics of Compton scattering between laser photons and electrons: (left) in the e$^-$ rest frame {right) in the lab frame.
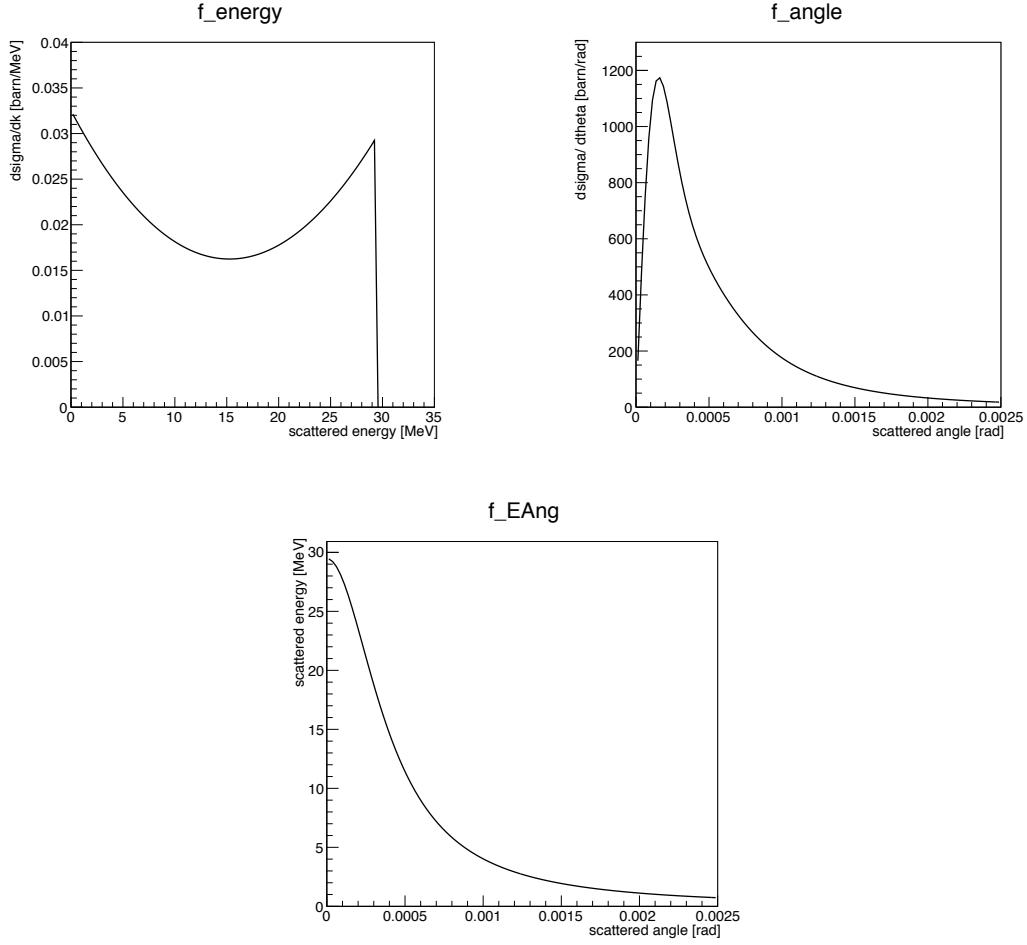
Figure 2.8: (top) The distribution of Compton scattering cross section w.r.t. final state photon energy (left) and final state photon scattered angle (right).
(bottom) The energy of Compton scattered photons plotted as a function of their angle.
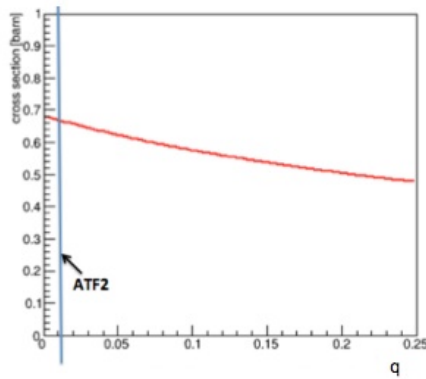
Figure 2.9: The dependence of the total Compton scattering cross section σ_{total} on $q = \gamma k/m$, shown in the range of $q = 0$ - 0.25. The blue line indicates the case of ATF2.

3 Description of Individual Components

3.1 Overall Layout

3.1.1 Laser Transport

Figure 3.1 shows the schematic overview of the laser optics. On a laser table outside the accelerator tunnel, the laser light is generated inside an optical cavity and is transported to the upright standing main optical table ("vertical table") in the IP area. The interference fringes are formed on the vertical table. The transport system ($\sim$ 20 m) shown in Fig. 3.2 consists of a pipe passing over the top of the concrete shield of the accelerator tunnel and mirrors placed inside boxes located beside the optical tables to guide laser beam propagation. Figure 3.3 shows examples of the laser sent up from the laser table, guided through the transport line, and ejected onto the vertical table.
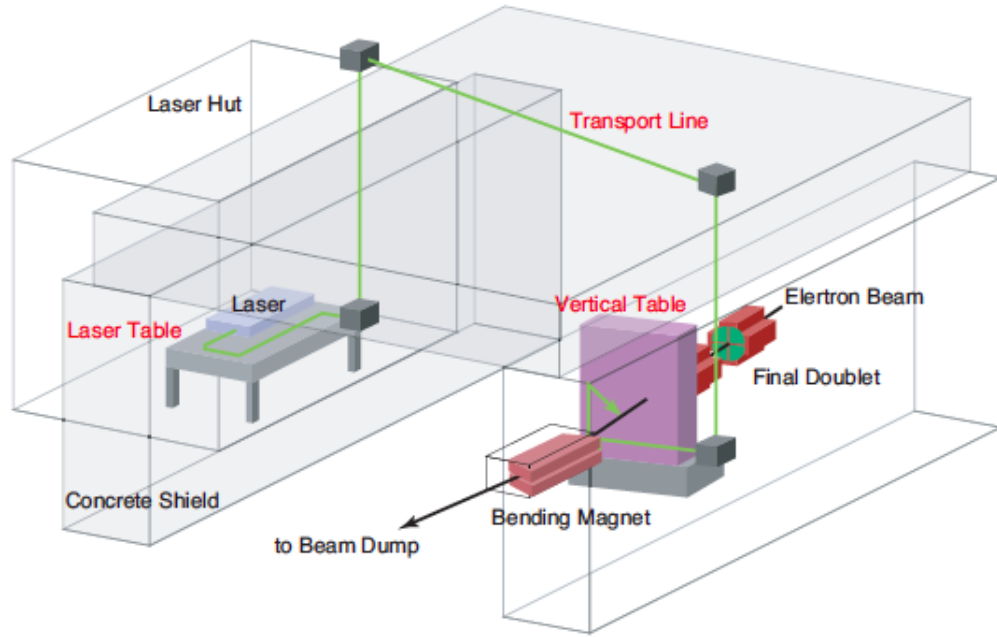
Figure 3.1: The overall layout of the Shintake Monitor system. The laser beam, after being generated and adjusted at the laser table, is transported through a transport line to the main vertical table in the IP area. [22]

Figure 3.2: The transport line sitting on the roof of the accelerator tunnel.
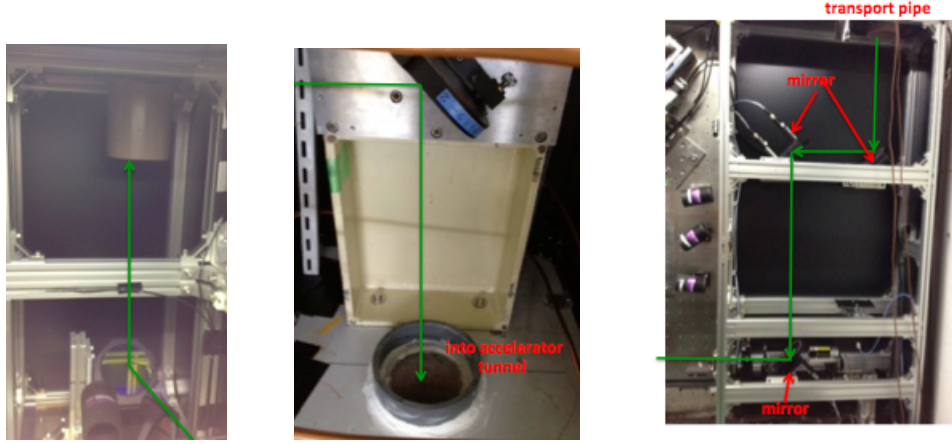
Figure 3.3: (left) The laser reflected up from the laser table through a pipe into the transport pipe line. (center) The laser reflected down into the accelerator tunnel. (right) The laser emerging onto the vertical table.

3.1.2 Expander and Reducer

Prior to transport, the laser spot size (σ_{laser}) is magnified approximately two-folds by the "expander" on the laser table in order to prevent divergence during transport. Magnification by M times is achieved by pairing an upstream concave lens with focal length $-f$ with a downstream convex lens with focal length Mf. After emerging onto the vertical table, σ_{laser} is restored using the "reducer", which consists of the opposite, an upstream convex lens and a downstream concave lens. The coated lenses (Fused Silica) are manufactured by Sigma Koki Inc. (SLSQ-50-(f)PY2 for convex and SLSQ-50-(f)NY2 for concave; f is focal length). In practice, the distance between the lenses receive slight adjustments in order to realize the desired σ_{laser} focusing. More details on σ_{laser} adjustment are given in Sec. 5.1. Figure 3.4 shows the schematics and photos of the expander and the reducer.

Alignment irises (Thorlab) are placed before and after the expander/reducer lenses to ensure that the laser passes precisely through the lens centers. Irises are also used for alignment at several other locations on the optical tables. The laser path is adjusted to pass the center of the irises, which are closed for alignment, then opened again afterwards.
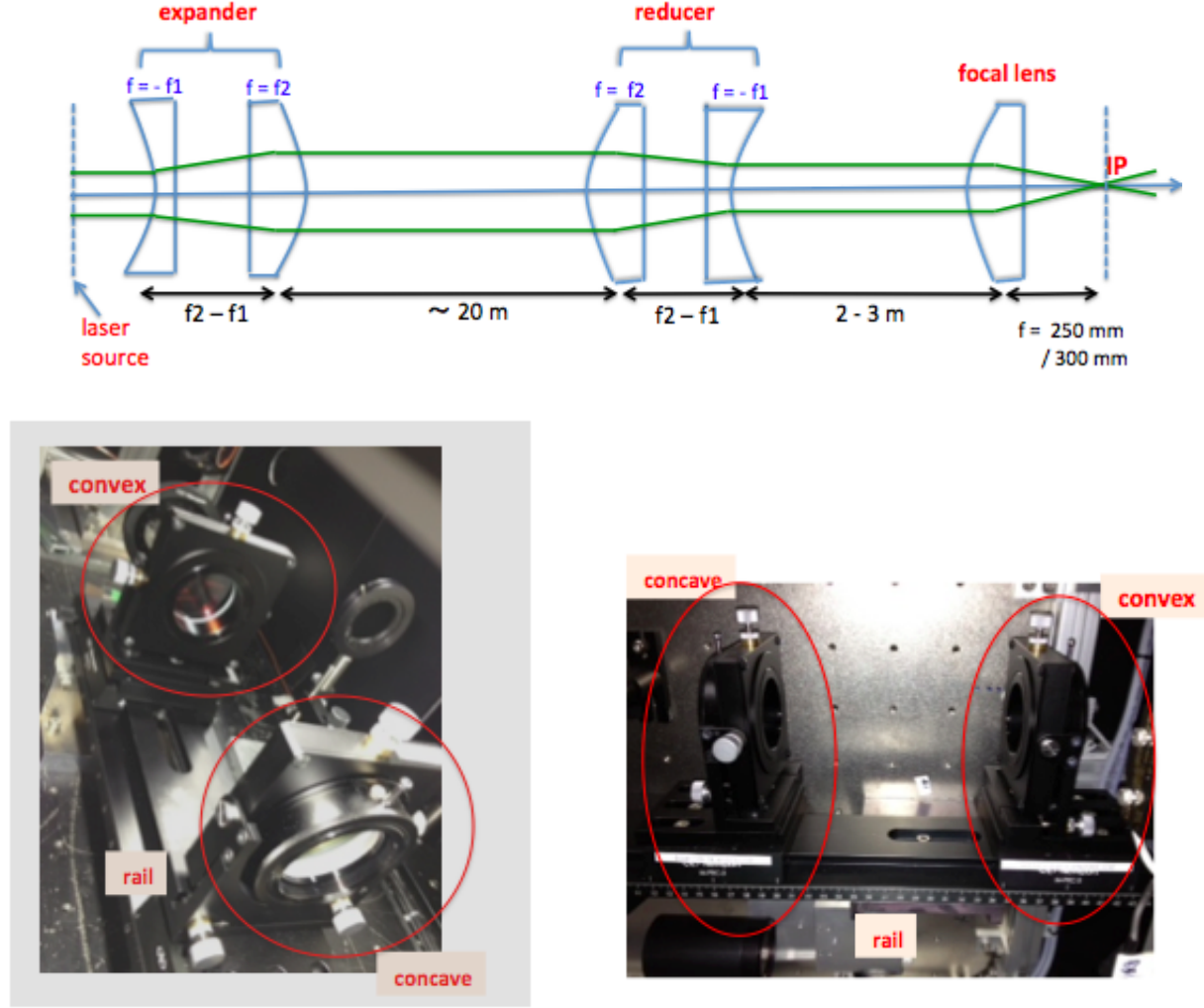
Figure 3.4: (top) The schematics of the expander and the reducer. (bottom left) The expander on the laser table. (bottom right) The reducer on the vertical table.

3.2 Laser Table

Figure 3.5 shows the schematic layout of the laser table in the "laser hut"[4]. The laser cavity and optical components are kept inside a box to maintain a dust-free and temperature stable environment.

Inside the laser cavity, the Nd:YAG Q-switched pulsed laser is generated and amplified at wavelength λ=1064 nm. Then λ is down-converted to 532 nm by second harmonics generation (SHG). The laser pulse output is triggered by an upstream master signal. A laser power attenuator composed of two highly reflective mirrors and beam dumps is inserted and ejected on a motorized stage to switch between low power for diagnostics and alignment, and high power for interference scans. Diagnostic devices monitor various properties e.g. laser timing, power, profile, before transport to the vertical table at the IP. Figure 3.6 shows the photodiode and the PIN-photodiode which are used for monitoring the laser's total power and temporal profile, respectively. The power supply for the laser is also inside the laser hut. The major components on the laser table are described in detail below:

---

[4]Locating the laser hut outside the accelerator tunnel is convenient arrangement for checking on the condition of the laser even during beam time as well as for preventing damage due to radiation
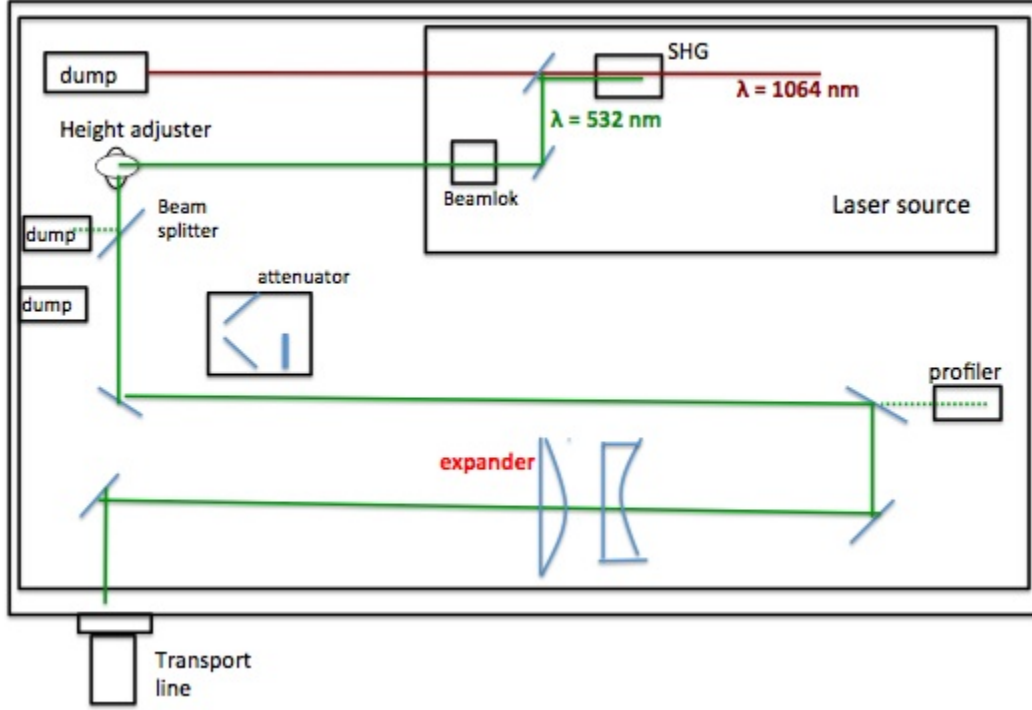
Figure 3.5: The schematic layout of the laser table inside the laser hut
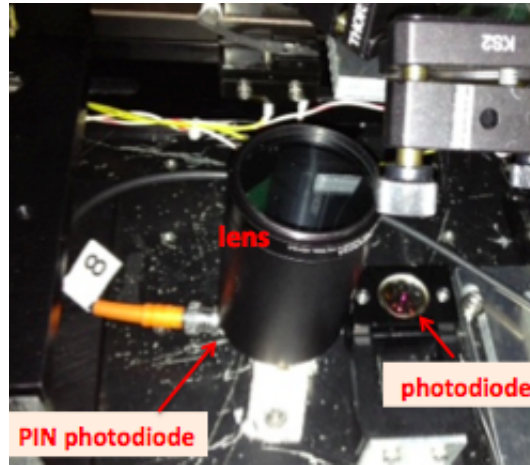
Figure 3.6: The weakened light transmitted by a mirror enters a PIN-photodiode (hidden here under a cylinder carrying ND filters), which monitors the laser timing. Next to it is a photodiode which monitors the stability of total laser power.

3.2.1 Laser Cavity

This section describes the basic properties of the Nd:YAG Q-switched pulsed laser (Quanta-Ray Pro-350, manufactured by Spectra Physics)[24] of the Shintake Monitor. Table 3.1 displays its catalogue specifications. More details are found in Appendix A. Its pulse width is 3.4 ns (RMS), or 8 ns (FWHM), which is more than 100 times longer than the e^- bunch length of about 20 ps. The laser temporal profile is approximately Gaussian (confirmable from Fig. 3.24). Precise beam size

measurements require the laser system to have high stability, good coherence, and the intensity to generate sufficient Compton photons.

Figure 3.7 shows the laser source. The laser beam is initially generated from population inversion in the Nd:YAG medium of the oscillator, then amplified in the resonator cavity. The cavity consists of two mirrors which are coated to reflect photons of a particular wavelength while transmitting others. One mirror (the "high reflector") reflects all light back into the cavity, while the other mirror (the "output coupler") is made to be semi-transparent as to transmit the energy stored in the cavity as the output laser beam. In the amplifier section two pump chambers add energy to the laser beam.

medium	Nd:YAG
wavelength	532 nm (SHG)
peak energy	1.4 J
pulse width	8 ns (FWHM)
repetition rate	6.24 Hz
line width	< 0.003 cm^{-1}
timing stability	< 0.5 ns
energy stability	± 3 %

Table 3.1: The basic design parameters of the Pro-350 Nd:YAG pulsed laser of the Shintake Monitor.

Figure 3.7: (top) The optical components in the laser cavity [23]. (bottom) A photo of the laser cavity.

Q-switching

The Q-switch (Fig. 3.7) is an electro-optic device used for realizing laser emission with short pulse width and high peak intensity. It comprises of a polarizer, a quart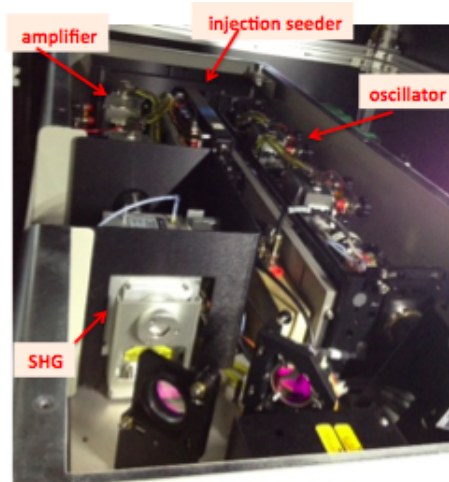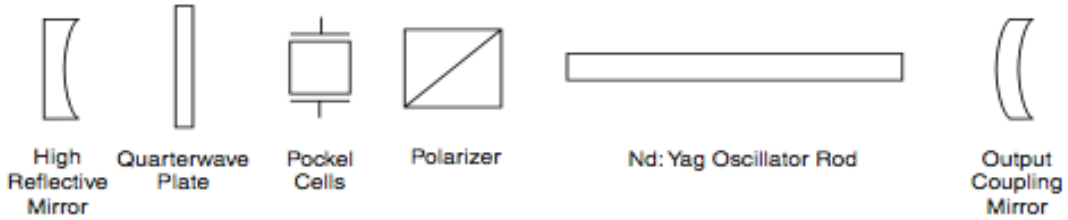er wave ($\lambda/4$) plate, and a Pockels Cell. It allows the abrupt switching between a high loss state in the resonator, during which energy stores up, and a low loss state during which oscillation occurs and energy is released from the cavity as light output. The details of Q-switch mechanism are as follows:

1. Initially the Q-switch is set to a low Q state. Here, no voltage is applied to the Pockels cell crystal, thus it does not affect the polarization of the light passing through it. The light entering the Q-switch is first horizontally polarized by the polarizer, then converted to circular polarization by the $\lambda/4$ plate. After the circular polarized light is reflected back from the high reflector (rear mirror), it is converted to vertical polarization by the $\lambda/4$ plate and remains that way as it passes through the zero voltage Pockels cell crystal. Because the polarizer transmits only horizontal polarized light, light is reflected out of the resonator. In this way, the cavity is kept at a high loss state, thus light feedback is prevented.

2. During Q-switched operation, the flash lamp excites the Nd ions (= pumping) for approximately 200 μs to build up a large population inversion. Here, excitation of the laser crystal energy levels takes place. At the instant of maximum population inversion, a fast and high voltage pulse is applied to the Pockels cell which switches from a high loss to a low loss state in the cavity. When voltage is applied to the Pockels cell, it cancels the polarization retardation by the $\lambda/4$ plate, thus allowing the light to remain horizontally polarized and be transmitted by the polarizer. This sudden switching to a low loss state leads to abrupt increase in oscillation of the light released during the de-excitation of the laser crystal energy levels. The cavity releases the large amount of energy stored up within the resonator during the excitation process all at once in the form of very short and high peak intensity laser light pulses. This amplified light output induced by stimulated emission is coupled out through the "output coupler" mirror.

Injection Seed laser

An injection seeding laser (Model 6350 manufactured by Spectra Physics)[24] is used for achieving oscillation in a single longitudinal mode. For unseeded Q-switch operation, spontaneous noise emission is oscillated in multiple longitudinal modes. For seeded Q-switch operation, a small amount of single-frequency seed laser light is directed on-axis into the host cavity. Because the intensity of the seed laser is higher than that of spontaneous emission by more than 6 orders of magnitude, the Q-switch pulse builds up much faster around the seed light. As a result, the amplification of spontaneous emission is inhibited, and a single frequency light output is achieved. The use of injection seeding reduces the line width by a factor greater than 300, from about 1.03 cm^{-1} to 0.003 cm^{-1}. This enables the smooth temporal coherence required for high quality interference fringes.

One measure of the stability of a Q-switched laser is the "buildup time", defined as the interval between the Q-switch opening and the laser pulse output. For unseeded operation, the buildup time corresponds to the time taken by the weak spontaneous emission light to make many round trips in the oscillator to be amplified up to the intensity of saturation flunk level. For seeded operation, buildup timing is much reduced, as shown in Fig. 3.8.

The stability of the laser output depends on the control of the frequency locking of the host laser to the seed laser. This is done by minimizing the buildup timing. Frequency is directly linked to the length of the host cavity i.e. the distance between its two mirrors. The position of the high reflector is tuned using a feed back loop based on a piezoelectric frequency tuning element (FTE). For each laser pulse, a small offset voltage ("buildup voltage") is applied to the FTE to enable it to provide the mechanical mirror position translation for fast frequency correction. The relationship between

buildup timing and voltage is 0.05 V/ns. Frequency and energy instabilities translates to jitters in Q-switch buildup timing. Therefore, the buildup voltage is read out as a means to monitor buildup timing stability (Fig. 3.9), especially when adjusting the delay of the laser timing triggers.

Laser tuning is conducted regularly by an engineer from Spectra Physics. In practice, the seed laser is tuned to optimize temporal coherence while monitoring the buildup timing and the temporal profile measured by a PIN photodiode. The laser profile is tuned by coarse adjustments of the screws of the rear mirrors by hand, which changes the angle of the laser passing through the components in the cavity.

The feedback correction of the cavity length also compensates for the effects due to temperature changes. Both the seed laser and the main laser are sensitive to temperature. Some potential effects are the changes in the optical length of the laser cavity due to thermal expansion of the support structure, and temperature changes in the laser rods. The stabilization of environmental temperature and the temperature of the internal cooling water supply are important. The laser system is also sensitive to mechanical vibration transmitted through the support structure, the cooling water and its hoses.

The laser table containing the main cavity and seed laser is kept in a laser hut whose temperature is maintained stable at all times. The location of the laser power source (Fig. 3.10), which also carries the cooling water tank, is selected to minimize the effect of vibration from surrounding devices. Thermocouple wire sensors are strung in various locations around the system, and their readout values are logged to monitor temperature stability[29]. Figure 3.11 shows the temperature monitored at various locations in the laser optics. Table 3.2 lists the representative temperature values in June 2014. The temperature of the laser hut is maintained stable using a control unit located immediately outside the hut walls (Fig. 3.10 right). It can be seen that the temperature in the laser box, where stability is most important, remains almost constant between the different months. There are very slight variations of 1-2 deg for the other locations affected by ambient temperature.

Second Harmonics Generator

The wavelength (λ) of the light output from the cavity is changed by the second harmonics generator (SHG) from the primary Nd:YAG λ of 1064 nm to 532 nm. The shorter λ is required for producing the narrower laser fringe pitches required for measuring smaller beam sizes. The crystals in the SHG are arranged in a particular sequence and orientation to generate the second harmonics. A mirror directs the λ= 532 nm light to the Beamlok (see below) for stabilization while transmits the residual λ= 1064 nm light to a beam dump.

Beamlok

The Beamlok system is an optional component installed into the laser system for the purpose of stabilizing the pointing jitter of the laser beam. It consists of a pointing sensor and a control mirror. The pointing sensor detects the deviation of the laser beam position at the far field (the laser beam is reflected many times and transferred about 20 m). Then it provides feedback to the control mirror, which is moved by a piezoelectric element to stabilize the position of the output laser beam. From catalog specifications, pointing stability is smaller than ± 50 μrad and smaller than ± 25 μrad without and with the Beamlok system, respectively[24].
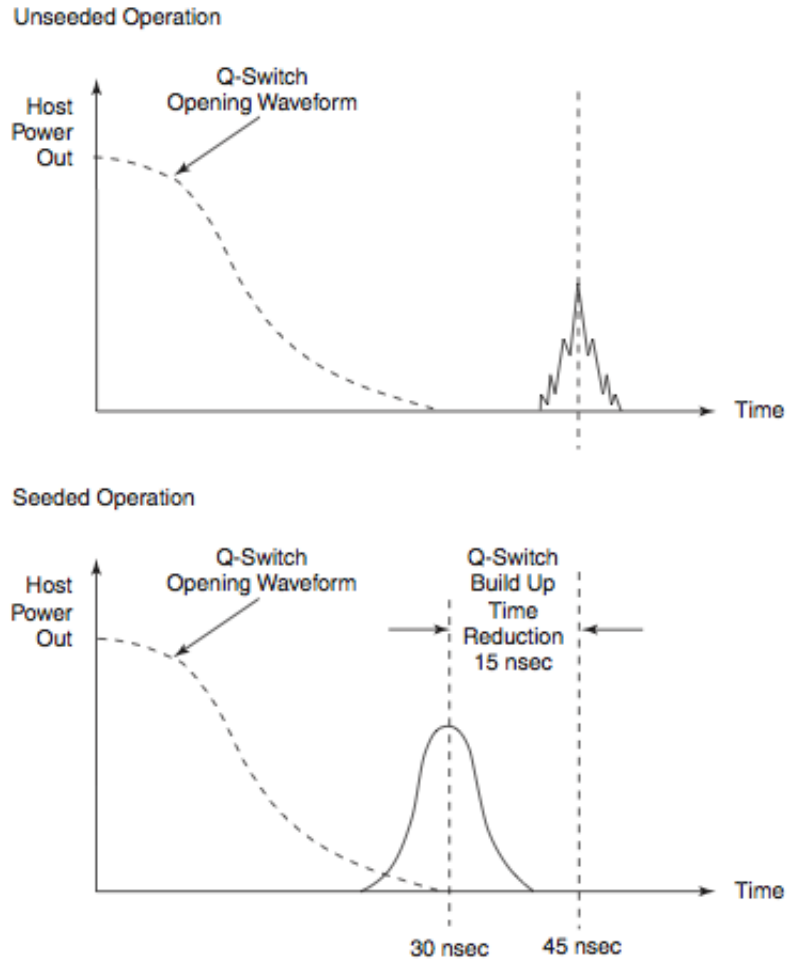
Figure 3.8: The reduction in Q-switch buildup timing as a result of using seeded operation.[24]
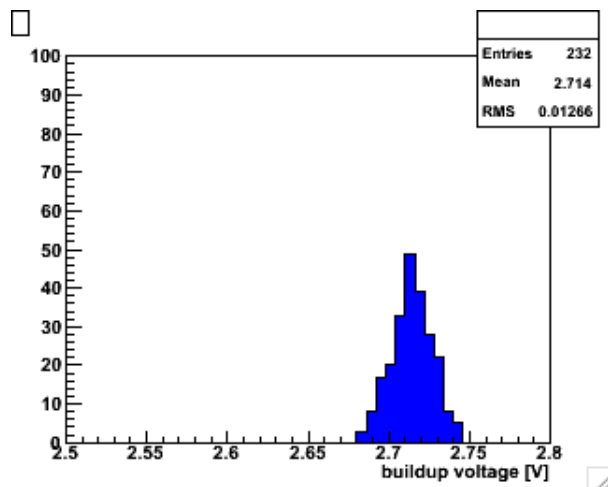
Figure 3.9: The distribution of buildup voltage monitored during a single fringe scan (about 2 minutes) in June, 2014.
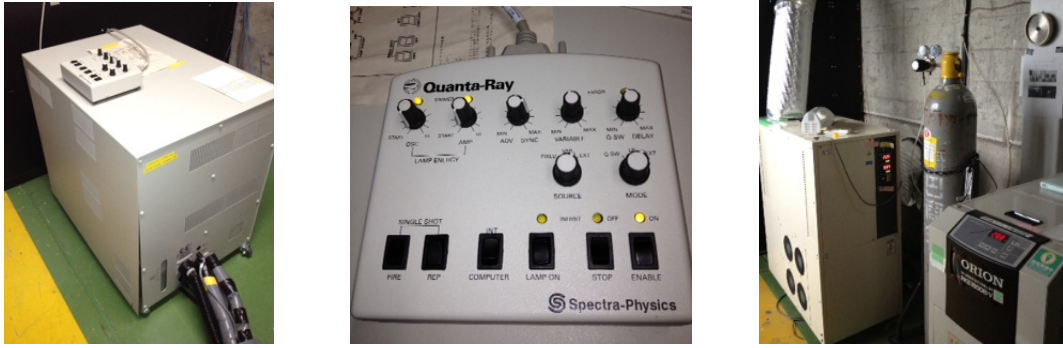
Figure 3.10: (left) The tank containing the power source of the Shintake Monitor laser and the cooling water circulation system. (center) The control panel for the laser oscillation. (right) Going from left to right, the temperature control unit for the laser hut, the nitrogen gas tank with valves to control gas pressure, and the tank for external cooling water

location	temperature [^{o} C]
laser box (bottom)	25.4
above laser box (inside plastic curtains)	21.4 ± 0.1
DAQ room (just outside laser hut)	23.0 ± 0.1
laser transport line	25 - 27
vertical table	26.7
internal cooling water (supply)	29.9
internal cooling water (return after circulation)	32.5

Table 3.2: The temperature measured using thermocouple sensors at various locations in the laser optics for a single scan on June 12, 2014.
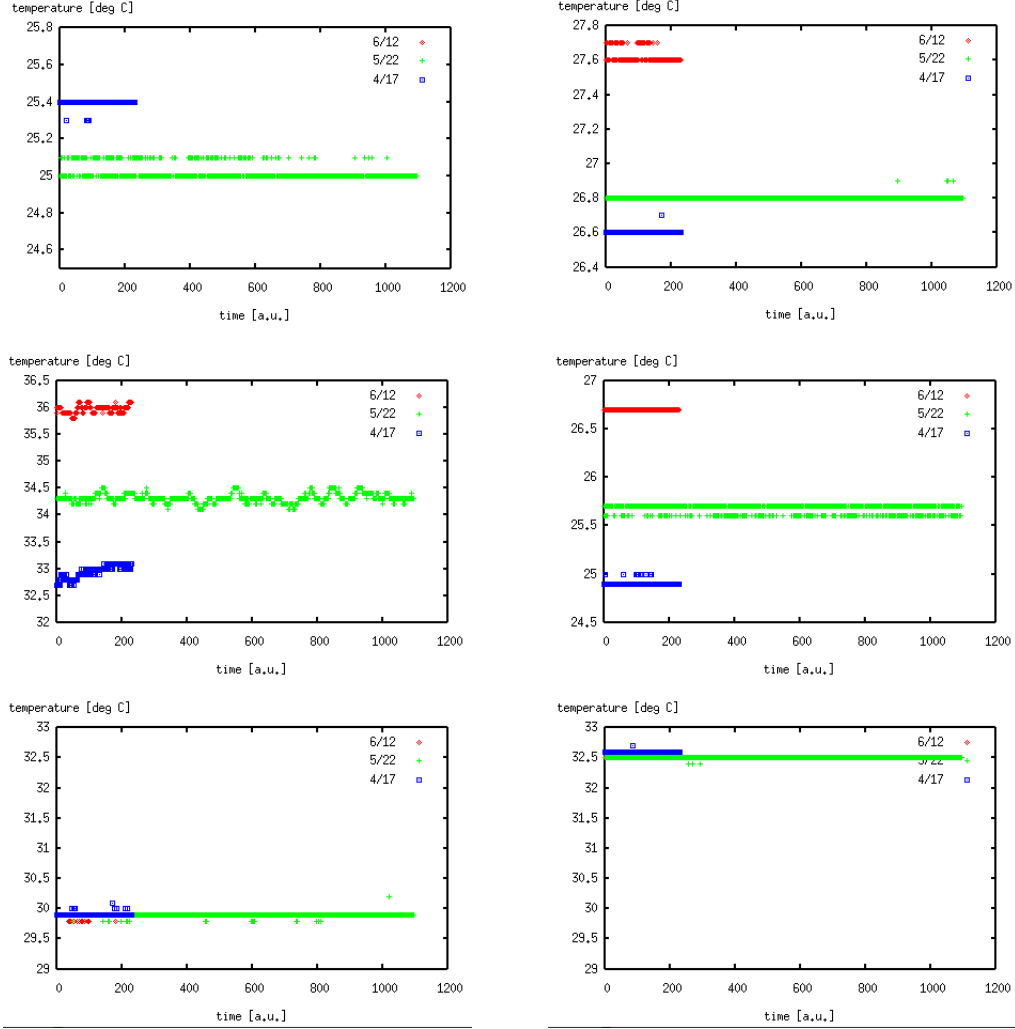
Figure 3.11: The temperature measured by thermocouple sensors during a single fringe scan in April, May, and June of 2014 (vertical axis). The horizontal axis is time during the scan. For some, the red line (June) is overlapped i.e. hidden by the blue line (May).
(top left) Inside of the laser box containing the cavity. (top right) The laser hut.
(middle left) The temperature control unit which works to stablize the temperature of the adjacent laser hut. (middle right) The vertical table.
(bottom left) The internal cooling water supply. (bottom right) The internal cooling water returning to the tank after circulating through the system.

3.2.2 Attenuator

For the protection of human and diagnostic components during alignment, laser power needs to be attenuated while still maintaining laser path accuracy. An "attenuator" composed of two dumps and two highly reflective mirrors is inserted and ejected on a motor stage to switch between low power for alignment and high power for fringe scans. For the "inserted" state, nearly all of the laser power is directed into dumps by mirrors with reflectivity close to 100%. The laser beam is reflected two times and the laser beam is weakened by a factor of R^2 (R : mirror reflectivity $> 99.5\%$). Figure 3.12 shows the schematics and photo of the attenuator, as well as the propagation of the laser emerging from the source until the attenuator.

The two mirrors are placed in opposite directions in order to cancel the position shift of the transmitted laser beam. This position shift (Δx) at the vertical table about 20 m downstream is estimated from the parallelism of the mirrors ($\lesssim 5$ [arcsec]) to be $\Delta x \leq 20\text{m} \times \sqrt{5\,[\text{arcsec}]^2 + 5\,[\text{arcsec}]^2} \leq 140\mu$m. This Δx is sufficiently small for alignment.

Figure 3.12: The attenuator, comprised of two highly reflective mirrors and beam dumps, is inserted and ejected on the laser table to allow selection of high laser intensity for interference scans and low intensity for alignment (modified from [25]). (left) The schematics of the attenuator (right) the actual photo.

3.3 Vertical Table

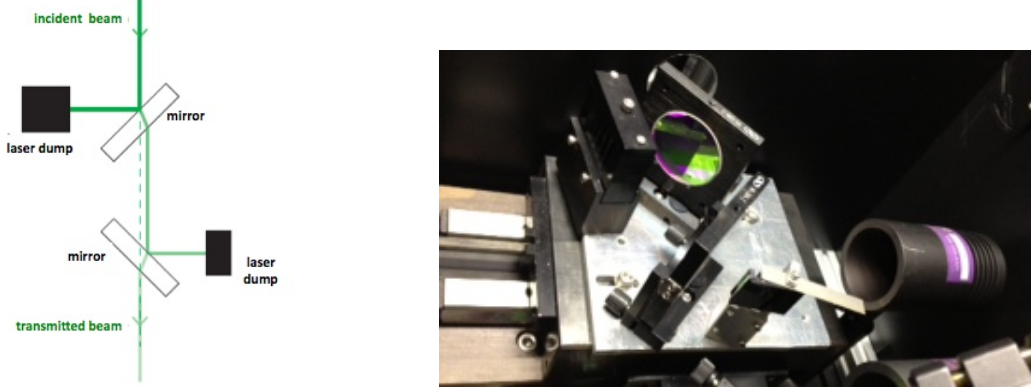Figures 3.13 and 3.14 show the upright standing main optical table, called the "vertical table", where collision between the e^- beam and the laser interference fringes takes place[5]. The transported laser beam emerges from the bottom-right corner, looking from downstream of the IP (also see Fig. 3.2). After the laser spot size is restored by the reducer, it propagates to a 50% beam splitter, called the "half mirror" (Fig. 3.15), into upper and lower paths. These are then focused at the IP by focal lenses and cross to form the interference fringes inside the IP vacuum chamber. The reflectance of the half mirror is measured to be 50.3 % for the S-polarized light of the Shintake Monitor laser. This is consistent with catalog specification.

The mirrors and focal lenses are made from optical glass BK7. The vacuum chamber windows are made of quartz for radiation hardness, since they are not easy to replace [6]. The coating on the mirror surfaces provide the appropriate reflectance of $> 99\%$. The damage thresholds for the mirrors (10-20 J/cm^2@λ=1064 nm and 10 ns pulse width) are confirmed to withstand the intensity density of the laser pulses with λ=532 nm, total energy of about 0.56 J/pulse, pulse width 8 ns (FWHM) and laser spot radius of about 3 mm downstream of the reducer. Appendix C provides the details on damage thresholds. The weak light transmitted through the mirrors is used for diagnostics, such as profile monitors and PIN-photodiodes.

The optical components are aligned using a green continuous wave (CW) Nd:YAG laser (CrystaLaser GCL-005-S, see Fig. 3.16) of λ= 532 nm, spot size 0.36 mm (diameter) and beam pointing

---

[5]The vertical table is made of steel honeycomb and supported by a rigid frame to suppress vibration. It is been confirmed to move synchronized with ground motion.

[6]The mirrors, focal lenses, and vacuum windows are manufactured by Lattice Electro Optics. The model numbers are: for the mirrors: RX-532-45S-B-2038, RX-532-22.5S-B-2038, and RX-532-37.5S-B-2038 for reflection angles 45 deg, 22.5 deg, and 37.5 deg, respectively; for the lenses: B-PX-100-250(300)-532 for focal length $f = 250$ (300) mm; for the vacuum windows: WA2-UF-WP-130mmD×13mmT-532 (174 deg mode), WA2-UF-WP-40mmD×5mmT-532 (30 deg mode), and WA2-UF-WP-60mmD×8mmT-532 (2-8 deg mode).

stability $\lesssim 20$ μrad. Its low output power of 5 mW guarantees safety during alignment. The pulse laser cannot be used for component alignment because of its strong intensity and large spot size (diameter ~ 5 mm).

The following sub-sections explain in detail the mechanisms for optical delay and crossing angle adjustment.

Figure 3.13: An actual photo of the vertical table, looking from downstream of the IP.
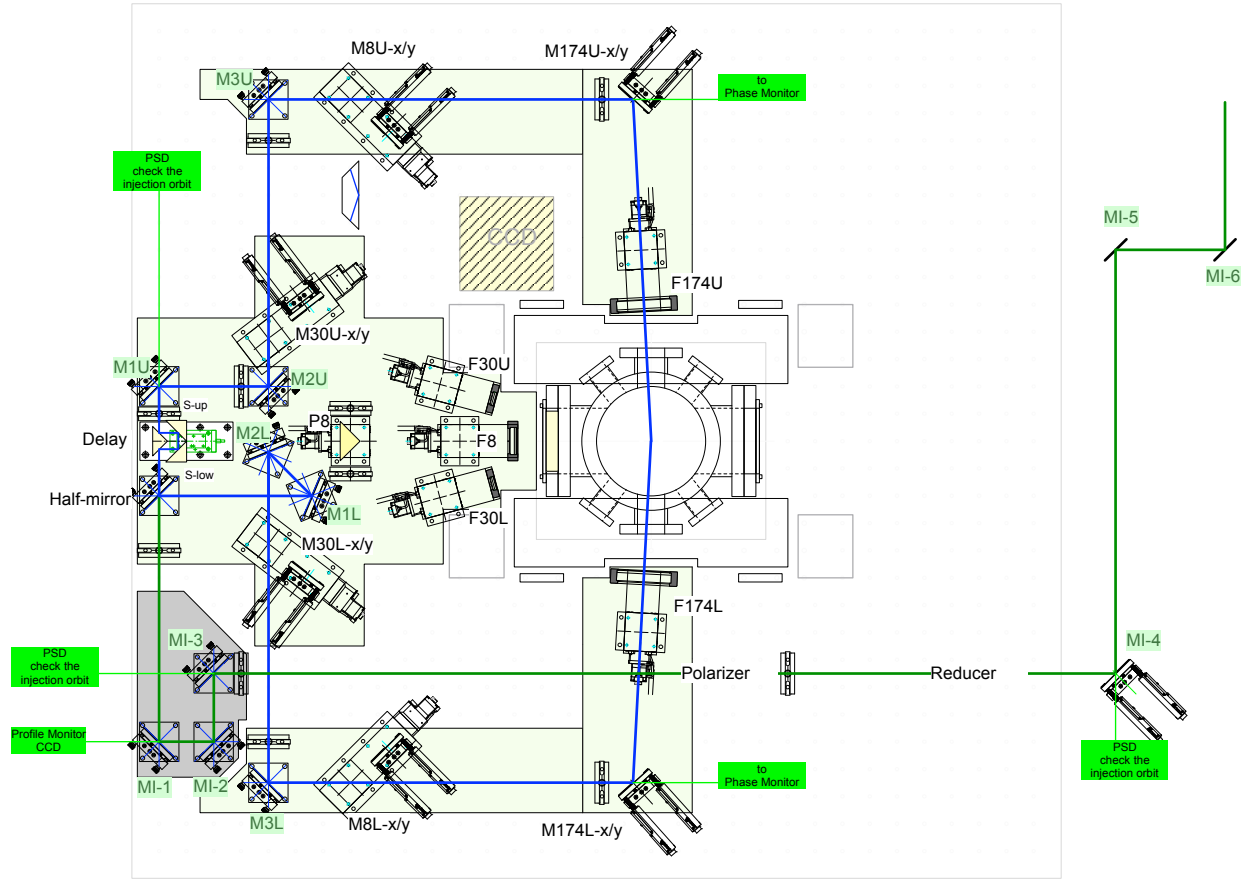
Figure 3.14: The layout of the main optical table, the " vertical table" on which the laser interferometer is formed as a target for the e⁻ beam, including the schematics showing the propagation of the laser beam: the CAD drawing by N. Terunuma[17] for the 174 deg mode path.

Figure 3.15: (left) The half mirror on the vertical table which split the laser beam into upper and lower paths which cross at the IP to form the interference fringes against which the e⁻ beam collides.

Figure 3.16: The CW laser used for alignment on the vertical table.

3.3.1 Optical Delay Control

For the Shintake Monitor at ATF2, signal modulation is produced by scanning the phase of the laser fringes against the e⁻ beam. This is carried out by an optical delay line (Fig. 3.17) installed into the upper path consisting of two triangular prisms, one of which is mounted on a piezoelectric stage (P-752.1C, Physik Instrumente). By adjusting the distance between the prisms (d) using the piezo stage, the phase between the two laser paths (α) changes as:

$$\alpha = 2kd = 4\pi d/\lambda \tag{3.1}$$

Here, $k = \frac{2\pi}{\lambda}$ is laser wave number. Table 3.3 shows the basic specifications of the piezo stage. Its DAC system has design position resolution of 0.2 nm (close loop) and O(10) ms position setting time (response speed), which is sufficient for the ATF2 repetition rate of 3.12 Hz. These meet the demands for controlling α with a precision of a few mrad. The piezo stage position is monitored by a inner capacitance sensor. The set and read voltages are recorded in a fringe scan data set synchronized with the signal energy measurement.

The movement of the piezo stage was tested through measurement using a distance meter (Iwatsu. ST-3541).

While the delay line was moved to scan the fringe phase (α), the readout voltage of the piezo stage was observed to rise in steps of 17 mV per α step of 0.6 rad, and 45 mV per α step of 1.5 rad. From Eq. 3.1, since 1 rad correspond to 42 nm in optical path length, the derived relationship is approximately 15 μm per input voltage of 10 V. Consistent results were reproduced over repeated scans. This test confirms the linear relationship between voltage input and the scanned phase.

stage	Physik Instrument, P-752.21C
controller	Oriental Motors, E-661K005
resolution	0.2 nm (closed loop)
response time	O(10 ms)
conversion time	16 μs maximum
reproducibility	± 2 nm (full range)
input voltage	± 10 V
travel range	30 μm per ± 10 V of input voltage
load tolerance	30 N

Table 3.3: The specifications of the piezoelectric stage [26]
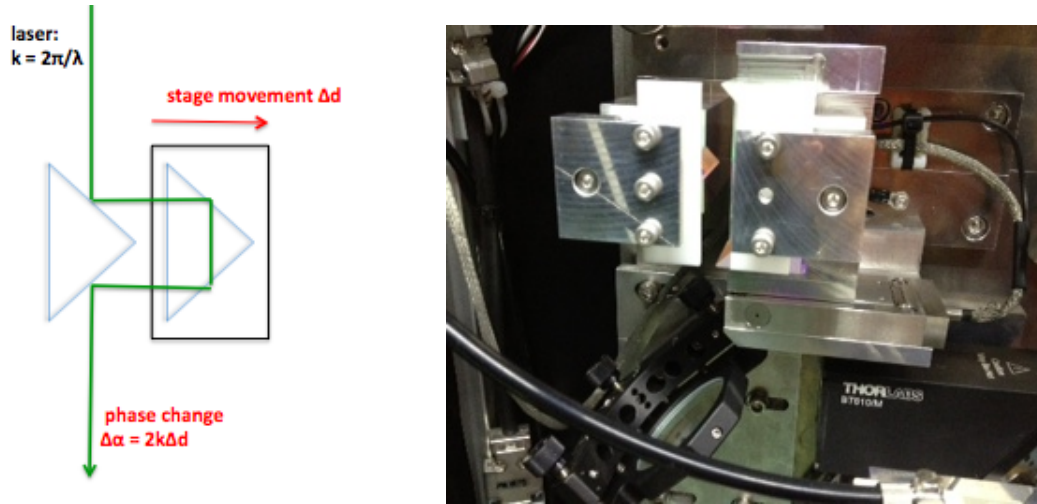
Figure 3.17: [left] The schematics of the delay line for fringe phase scan installed into the upper path. [right] A photo of the piezo stage. Also shown here is the half mirror located below the piezo stage.

3.3.2 Laser Crossing Angle Adjustment

In order to measure a wide range of σ_y, the laser optics is designed to switch between 3 types of optical paths, referred to as "crossing angle (θ) modes": 2-8 deg (continuously adjustable), 30 deg, and 174 deg. Figure 3.18 shows the optics layout for each mode. Precise and effective interchanging between θ modes in accordance to the target σ_y is extremely important for beam tuning. Mode switching is carried out via remote PC control of compact linear stages carrying mirrors. Since there is no need to divide up the laser power into more than pre-determined laser modes, this method retains the full laser power of each of the two paths and thus contributes to a higher S/N ratio.

Continuous mechanical adjustment between 2-8 deg is made possible by a linear stage carrying a prism (Fig. 3.19), whose position is changed continuously. This is desirable because it allows more freedom in the tuning of large σ_y, explained as follows: Measurement resolution depends on the

fringe pitch $d = \frac{\pi}{k \sin(\theta/2)}$, which changes more abruptly as θ gets smaller ($\because \frac{\partial d}{\partial \theta} = -\frac{\pi \cos(\theta/2)}{2k \sin^2(\theta/2)}$). The relationship between θ, the focal length of the 2-8 deg lens (f=250 mm), and the distance (h) between the two paths on the prism is [7]:

$$\theta = 2 \arctan \left(\frac{h}{2f} \right) \tag{3.2}$$

The mirrors (Fig. 3.20) on the linear stages are also responsible for extremely precise alignment of laser paths. The angles of the mirrors are steered by a pair of rotating actuators (Thorlab Optics, ZST13) that move in X and Y controlled by stepping motors with 10 nm resolution. This allows mirror angles to be controlled within O (1) mrad precision. The mirror angle ϕ changes as :

$$\Delta\phi = 2\Delta d/D \qquad (\Delta d \ll D) \tag{3.3}$$

Δd is the change in actuator length. D (=61.9 mm) is the distance from the actuator to the mirror rotation axis i.e. the kinematic mount support. The resulting shift in laser position at the IP (Δx_{IP}) is:

$$\Delta x_{IP} = f\Delta\phi = (2f/D)\,\Delta d \tag{3.4}$$

Equation 3.4 can be rewritten as $\Delta x_{IP} = C\Delta d$. The table below summarizes the scaling factor C is for each θ mode: C = 8.08 for the 2-8 deg and 174 deg modes, and by C = 9.7 for the 30 deg mode. This scaling relationship is applied when calculating Δx_{IP} from the actuator movement Δd, as well as when estimating the laser spot size from the measured sigma of a laser wire scan, where a single laser path w.r.t. the e$^-$ beam at the IP using the X actuator (see Sections 2.4 and 4.2.1).

mode: θ [deg]	$C = \Delta x_{IP}/\Delta d$
2-8, 174	8.08
30	9.7

---

[7]The theoretical calculation for θ assumes parallel propagation from the prism to the focal lens. The realistic laser beam may have a slight divergence. Although prism is also set via remote PC control, we sometimes confirm the precision in θ by measuring by hand the distance between laser spots on the final lens . The $\pm$1mm precision of this measurement correspond to error of $\Delta\theta/\theta$ ~ 10 %.
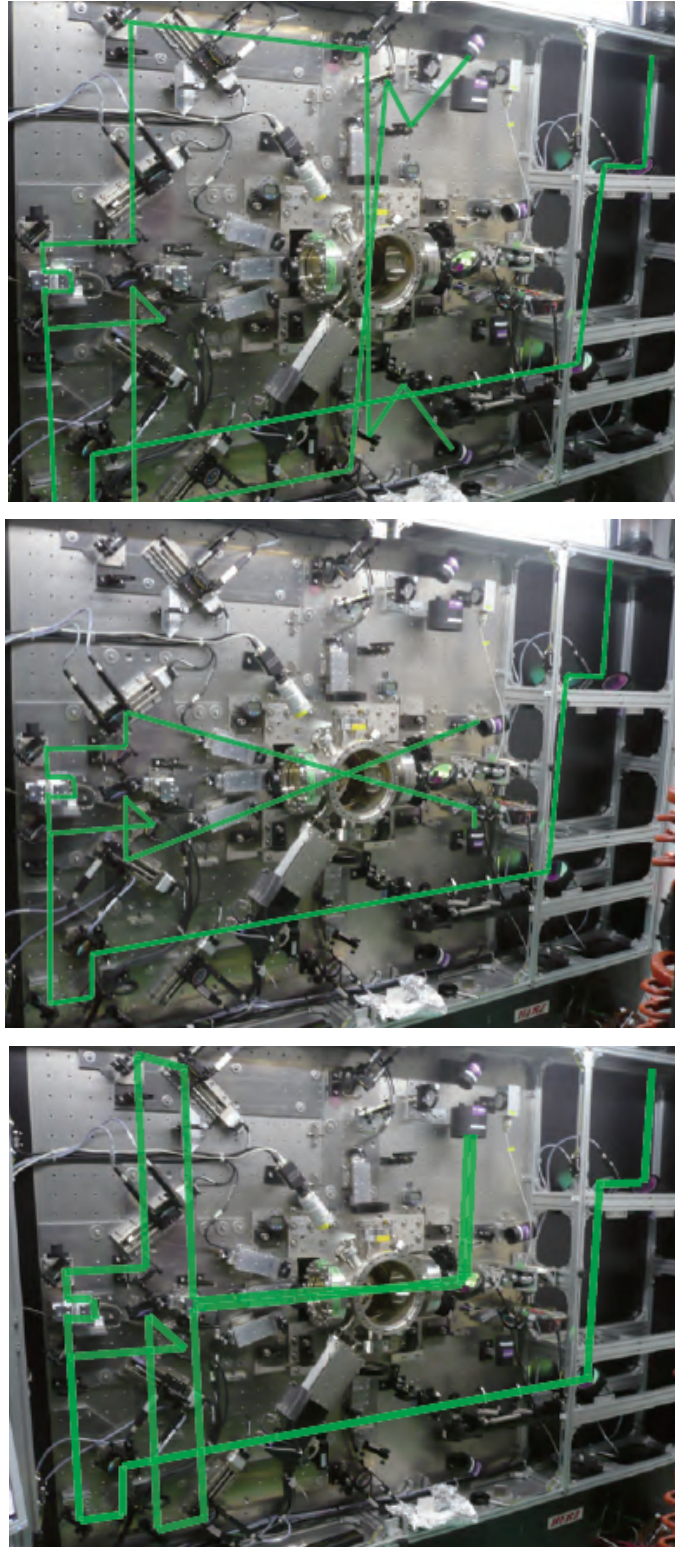
Figure 3.18: The optical path (in green) for each crossing angle mode. From top to bottom: 174 deg mode, 30 deg mode, 2-8 deg mode.
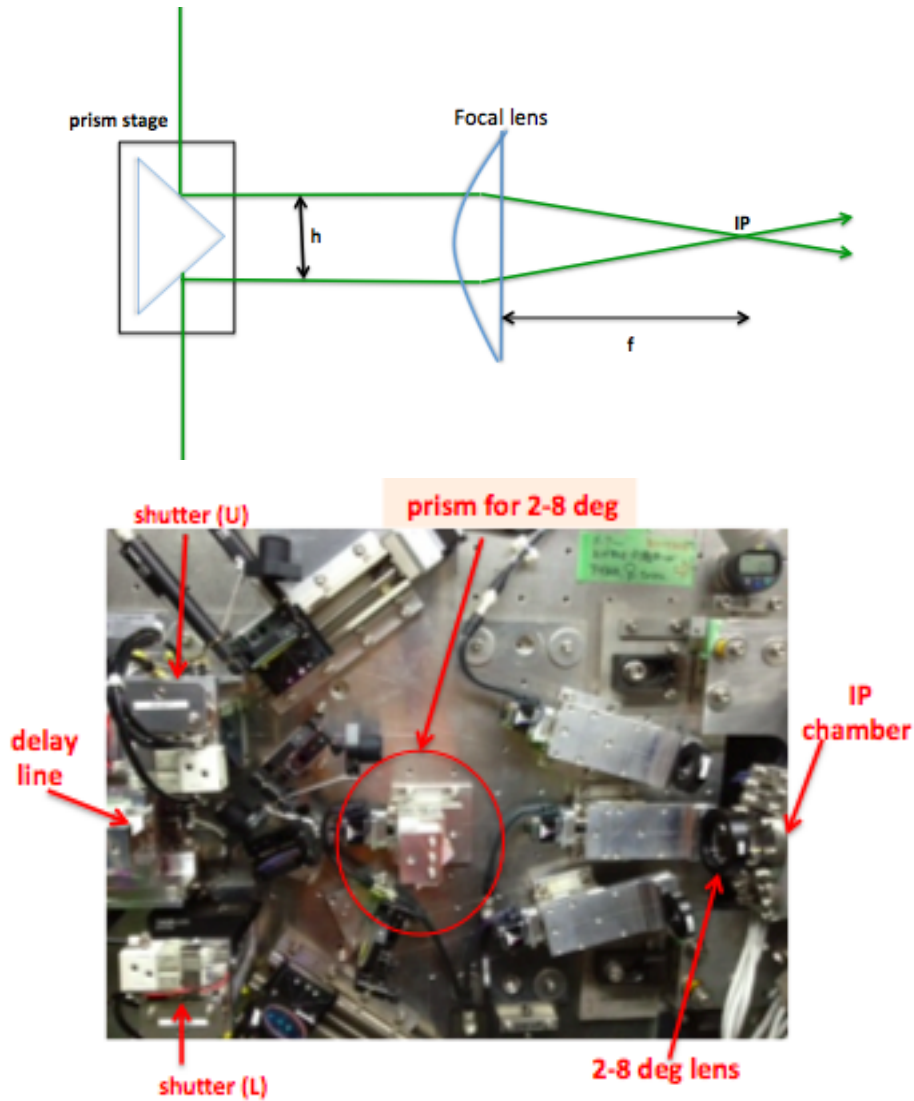
Figure 3.19: (top) The schematics of the prism stage for continuous mode adjusting between 2 and 8 degrees.
(bottom) The area of the vertical table surrounding the prism (circled in red). Also shown here are the delay line, the laser shutters for the upper and lower paths, and part of the focal lenses.
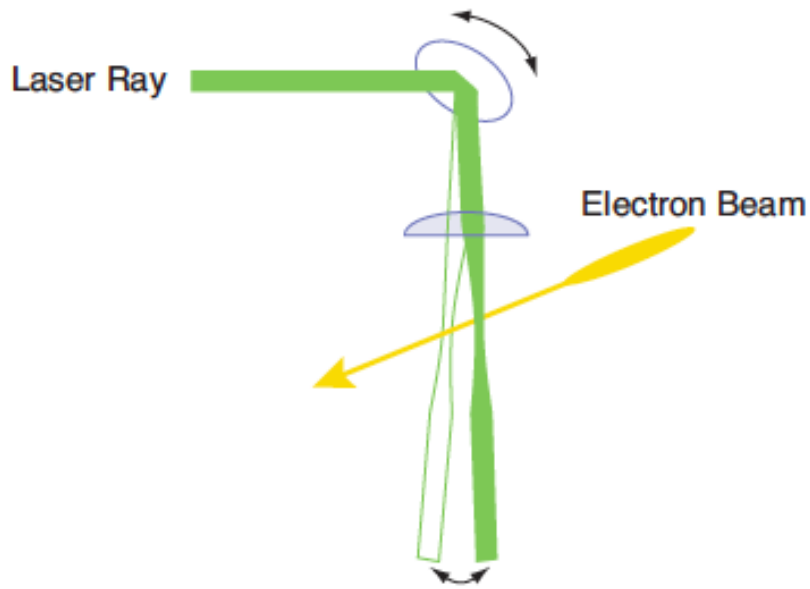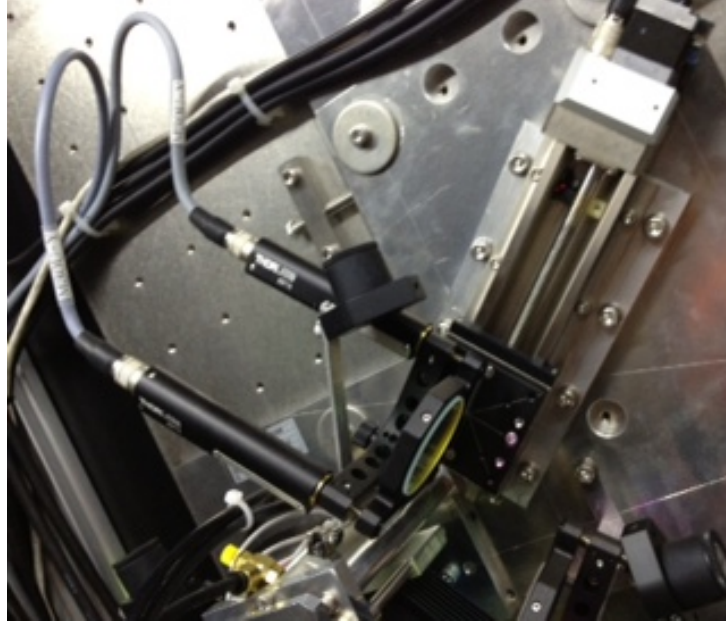
Figure 3.20: (top) One of the mirrors in the Shintake Monitor optics mounted on an linear motorized stage that is slid in and out during mode switching. Mirrors have actuators attached to them for precise adjustment of laser beam position and angle. (bottom) The schematics of adjusting the laser position at IP by rotating the mirrors using actuators [22]

3.4 Laser Timing System

3.4.1 Q-switch Timing and Laser Pulse Output

Figure 3.21 shows the logic diagram of the laser timing system. The laser output timing is determined by inputting a properly delayed trigger signal into the Q-switch. The timing trigger inputs for the e^- beam and for the pulse laser are generated and adjusted using digital modules called event generators "EVG" and event receivers "EVR" (Micro-Research Finland Oy; VME-EVG-230 and

VME-EVR-230RF). Because the trigger signals for the e$^-$ beam and the laser are made from a common upstream master signal generated by a synthesizer, they are synchronized with each other. In Fig. 3.21, the "LAMP" and "Q-SW" represent the start of flash lamp excitation and Q-switch, respectively. These are made to be 6.25 Hz to match the laser repetition rate. "BEAM" represents the trigger signal for the e$^-$ beam timing. The frequency of "BEAM" is halved from the laser trigger to 3.12 Hz. The EVRs are scanned in sub-ns steps in order to carry out the fine timing delay adjustment for the following purposes:

1. optimize the proper relative delay between laser timing and e$^-$ beam timing for Compton scattering.

2. optimize the timing interval between "LAMP" and "Q-SW" in order to achieve stability of the buildup timing, which directly affects the stability of laser output timing and power.

Figure 3.22 shows the timing relationship between flash lamp trigger, flash lamp light pulse, Q-switch trigger, and laser light output. The flash lamp creates a laser light pulse after it receives a TTL level input signal. If the Q-Switch is triggered within the proper delay from flash lamp trigger ((Q-SW)- (LAMP) interval $\sim$ 180 μs), maximum laser power is extracted 100 ns later. This process is important for achieving high Compton signal intensity. Occasionally e.g. after laser oscillator tuning, the flashing interval needs to be re-optimized by adjusting the EVR while monitoring the buildup timing. The distribution of buildup voltage was shown in Fig. 3.8.
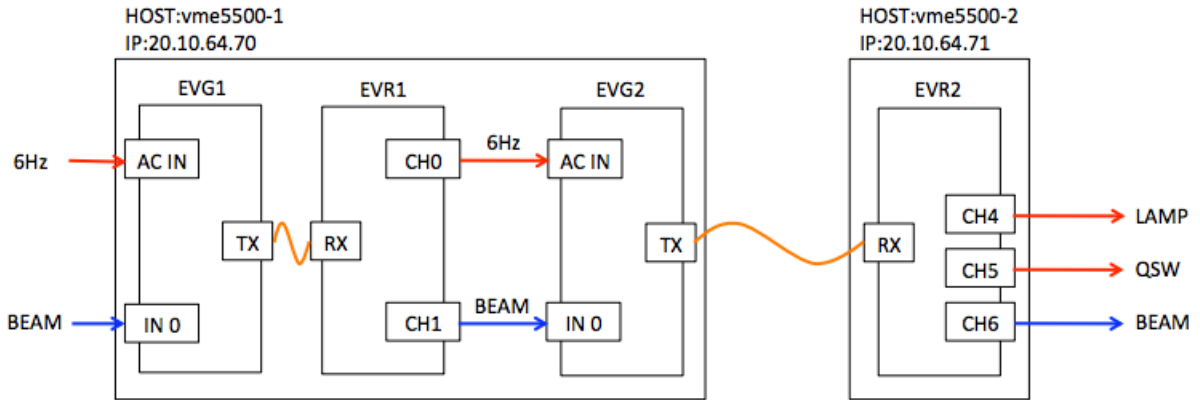
Figure 3.21: The schematic layout of the timing control system. The trigger signals for the e$^-$ beam timing and laser oscillation timing are generated and controlled using event generators (EVGs) and event receivers (EVRs). The trigger signals are made from a common upstream master signals, thus are synchronized with each other. "BEAM" represents the trigger signal for the e$^-$ beam timing. "LAMP" and "Q-SW" represent the start of flash lamp and Q-switch, respectively. The EVRs are scanned in sub-ns steps in order to precisely adjust the relative timing between the laser and the e$^-$ beam, as well as for the timing interval between "LAMP" and "Q-SW".[17]
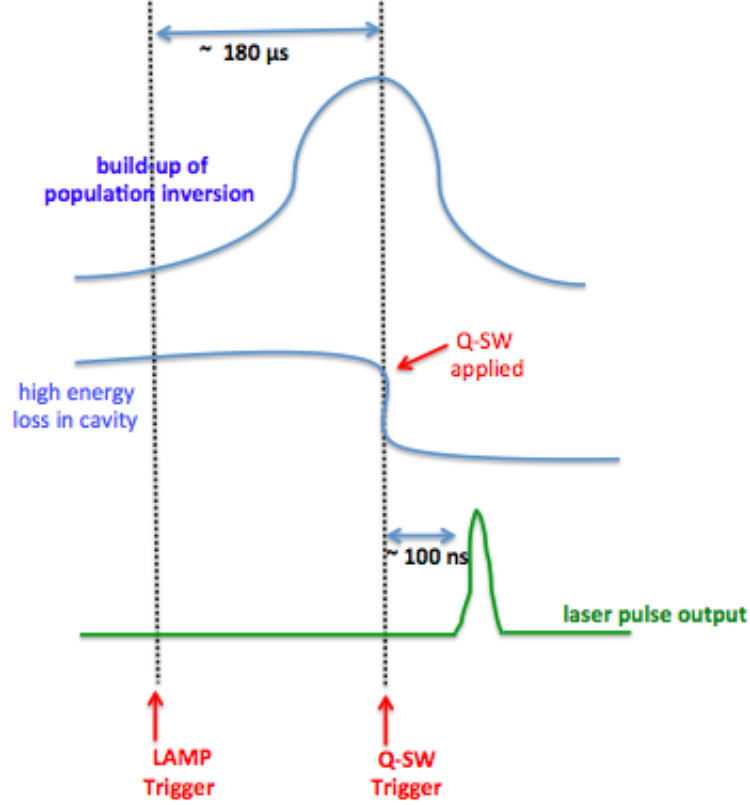
Figure 3.22: The timing relationship between flash lamp trigger, flash lamp light pulse output, Q-switch trigger, and laser light output. The flash lamp creates a laser light pulse after it receives a TTL level input signal. If the Q-Switch is triggered within the proper delay from flash lamp trigger ($\sim 180~\mu$s), maximum laser power can be extracted another 100 ns later.

3.4.2 Monitoring of Relative Timing

This section describes the process for monitoring and adjusting the relative timing between the laser and the e^- beam. More details are found in Sec. 4.2.5.

Laser timing is monitored by fast response Si:PIN photodiodes (PIN-PD) (see Fig. 3.6). A PIN-PD is a semiconductor photodiode with an insulator "i-layer" sandwiched between the P layer and N layer of a typical PN junction diode. When incident light hits the deletion layer, which is also the sensitive area, charge carriers are generated. An inverse bias voltage is applied to the diode effectively widens the depletion layer. The resulting reduction in the junction capacitance increases the bandwidth i.e. enables faster response. The PIN-PD for the Shintake Monitor optics (Thorlab, DET025A) has a fast rise time and fall time of 150 ps each, and a frequency bandwidth of 2 GHz. There is one PIN-PD for each of the laser table and the vertical table.

The electron beam timing is monitored using the signal taken from an electrode extending from a stripline BPM into the beam pipe. As the beam pass through the beam pipe, output signals with short rise times are triggered in the electrode.

Figure 3.23 shows the PIN-PD and the stripline BPM located next to an upstream quadrupole magnet.

Fluctuation in relative timing leads to Compton signal energy jitters in fringe scans (see Sec. 7.1.4). Timing jitter is generally suppressed to $\lesssim 1$ ns (from observing the PIN-PD waveform), which contributes $< 5\%$ to Compton signal energy jitters. However there are also much finer zig-zagged

structures with a time scale of O(10) ps which may cause pulse by pulse fluctuations in the laser intensity colliding with the e$^-$ beam.

First, in order to trigger initial collision between the laser pulses and the e$^-$ beam, their timing signals are matched with O(ns) precision while observing the signals from a PIN-PD and a stripline BPM electrode using an oscilloscope (see Fig. 3.24). Next, fine sub-ns timing adjustment is conducted in order to maximize Compton signal intensity and minimize the signal jitters due to timing jitters. This is done by scanning the EVR delay setting in steps of 0.4 ns while colliding one of the laser paths with the e$^-$ beam. The LAMP delay is also scanned to optimize the interval between LAMP and Q-SW for stable buildup voltage.
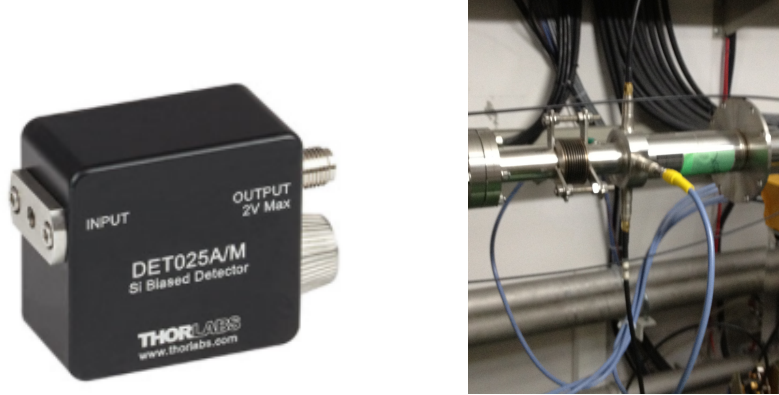
Figure 3.23: (left) The PIN-PD (Thorlab, DET025A) which is used for measuring the timing of the laser. (right) The stripline BPM next to an upstream quadrupole magnet, whose signal is used for monitoring e$^-$ beam timing.
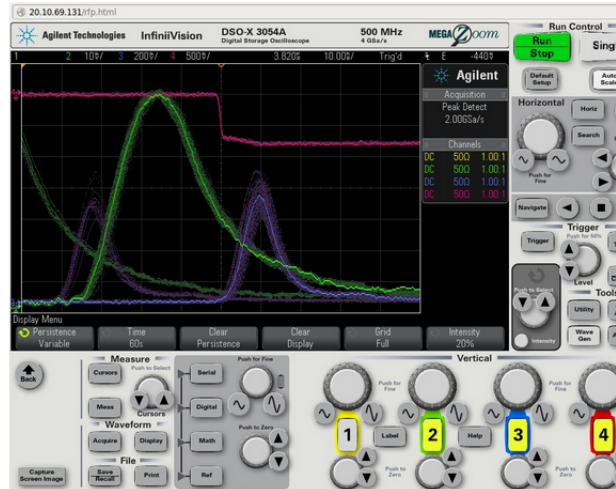
Figure 3.24: Relative timing of the laser and the beam observed on an oscilloscope. Red shows the beam timing (BPM), green shows the laser hut PIN-PD. Blue shows the vertical table PIN-PD. The PIN-PD waveform corresponding to Laser ON timing is shown to the left, while those for Laser OFF timing is shown to the right, 40 ns ahead. The distance between the peaks of each waveform indicate the appropriate relative timing delay between the beam and the laser at the time (Photo taken by N.Terunuma[17]).

3.5 Detector

3.5.1 Detector Layout

The Shintake Monitor uses a calorimeter-type detector to measure the total energy of photons from Compton scattering. Figure 3.25 shows the beam line components surrounding the detector positioned 6.2 m downstream of the IP. The energy deposit from the electromagnetic showers triggered by the incident photons is transformed into scintillation light in layers of CsI(Tl) scintillators, which then enters photomultiplier tubes (PMTs) coupled to the scintillators to be processed. Tables 3.4 and 3.5 list the basic specifications of the scintillators and the PMTs (Hamamatsu Photonics, R7400U), respectively.

Figure 3.26 shows the structure of the detector. The transverse dimension is (100 mm ×50 mm). The longitudinal length is 330 mm, which is about 17.7 times of the CsI(Tl) radiation length of 18.6 mm. It is composed of five layers of scintillators: the front four layers are each 10 mm thick. The fifth "bulk layer" is 290 mm thick and is divided into three transverse sections. Doping CsI with Tl increases light output. However, CsI(Tl) is slightly hygroscopic (as opposed to pure CsI), therefore the scintillators are enclosed in Al housing purged with nitrogen gas for protection. The housing walls are 10 mm thick, with the exception of the front surface through which photons enter, which is only 1 mm thick to minimize energy loss. Each layer is wrapped with fluorocarbon polymer sheet and alumimylar to prevent optical cross talk and improve light collectivity.

Figure 3.27 shows the naming of the PMTs (12 in all) which are coupled to the scintillators through cylindrical light guides. Two PMTs (left and right) are attached to each of the front four layers. For the fifth layer, two are attached to the large center section, and one to each of the side sections. The compactness of the PMTs (50 mm long, 8 mmϕ) is favorable for attaching to the thin scintillators and for fitting into the tight space among the collimator blocks. The PMTs operate under positive HV applied to their anodes, while their photocathode surfaces are grounded to prevent electrical discharge due to direct contact with the Al housing.
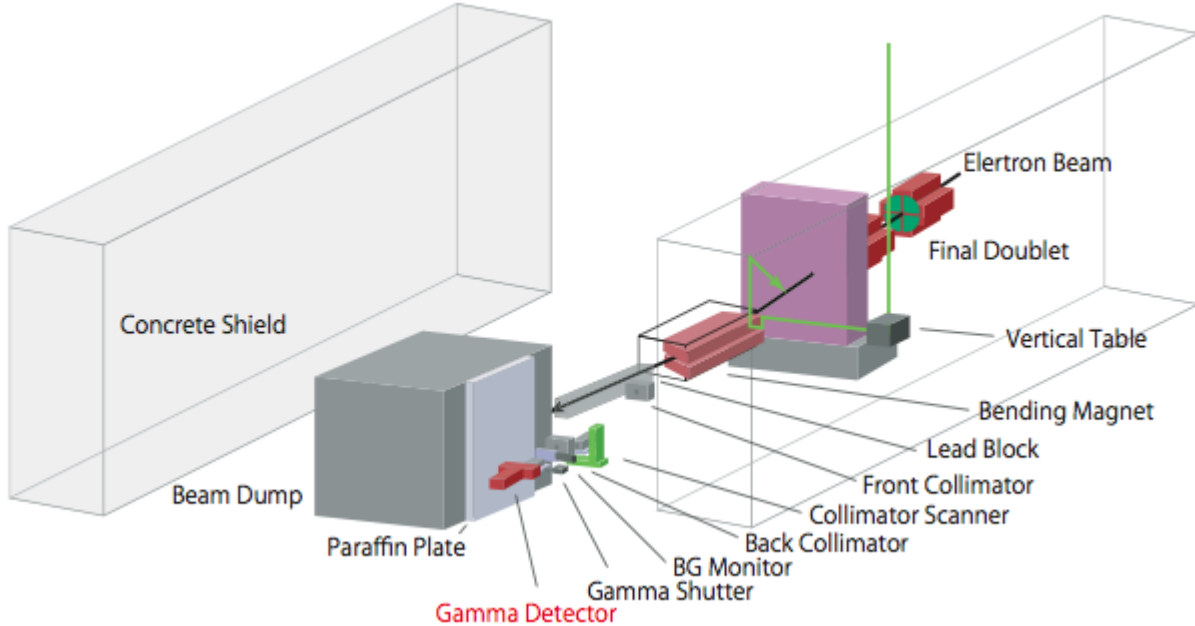

Figure 3.25: The layout of the beam line components surrounding the Shintake Monitor gamma-ray detector. [22]
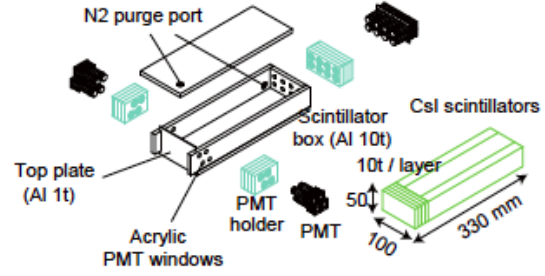
Figure 3.26: The structure of the Shintake Monitor gamma-ray detector. [25]
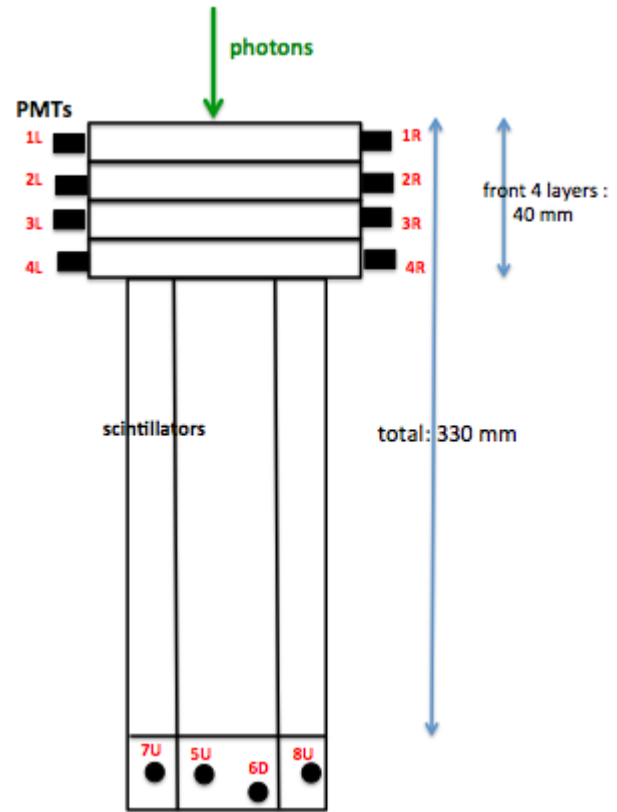
Figure 3.27: (left) The photo of one of the PMTs of the detector[25] (right) The naming and arrangement of the 12 PMTs coupled to the left and right of each scintillator.

density	4.51 g/cm^2
radiation length	1.86 cm
photon emission	59000 / MeV
decay constant	1 μs
reflective index	1.79
photon wavelength at max. intensity	565 nm

Table 3.4: Basic specifications of the CsI(Tl) scintillators of the Shintake Monitor gamma-ray detector.

dynode	metal channel, 8 stages
photocathode	Bialkali
outer / effective diameter	16 / 8 mm
length (PMT + socket)	50 mm
nominal gain	7×10^5 at 800 V
max. / standard voltage	1000 / 800 V
rise time	0.78 ns (typical)
electron transit time	5.4 ns (typical)
spectral range	300-650 nm
dark current (after 30 min.)	0.2 nA (typical)
quantum efficiency	25% (at 420 nm)

Table 3.5: Basic specifications of the Hamamatsu Photonics (R7400U) PMTs of the Shintake Monitor gamma detector [27].

3.5.2 Separation of Signal and Background

The multi-layer detector design had originally been intended for separating signal and BG by taking advantage of the significant difference in their shower development with energy[28]. The mean energy of a single photon is inferred from simulation to be about 15 MeV for Compton signal, and about 50 MeV for BG (see Table 3.6)[22]. Analysis methods were developed accordingly for optimizing S/N ratio and the tolerance for BG fluctuation.

The incident photon energy is estimated by measuring the energy deposit in the scintillators. Figure 3.28 shows the longitudinal distribution of energy deposit in the detector for signal and BG photons, generated by GEANT4 simulation[22]. Higher energy photons deposit more energy in the deeper layers because the depth of electromagnetic shower maximum is logarithmly proportional to energy. The shower development of signal photons is concentrated to the front layers, peaking in the second layer. About half of the total energy deposit is in the front four layers. In contrast, most ($\sim$80%) of the BG energy is deposited into the thick fifth layer. The sufficiently large number of incident Compton photons (O(100) per bunch) maintains the statistical fluctuation of shower shape to a negligible level.

BG from Bremsstrahlung

The majority of BG comes from bremsstrahlung photons emitted due to the collision of the beam halo with the beam pipe. The beam pipe wall is more than a few sigmas away from the beam halo. However, in order to focus to a tight waist at IP, the beam size is first abruptly defocused immediately before the FD. In particular, the expansion of σ_x to as large as 3 mm before entering QF1 enhances the interaction between the beam halo and the beam pipe at that location. Figure 3.29 shows the

energy spectrum of bremsstrahlung BG photons, from the simulation of interaction between the beam and the beam pipe at the FD. Plotted together is the energy spectrum of Compton signal photons calculated in Sec. 2.6. The energy distribution of signal photons show a sharp "Compton edge" (around 30 MeV for ATF), while the BG energy distribution has a tail extending up to the e^- beam energy (1.3 GeV for ATF).

Another major source of bremsstrahlung BG photons is the post-IP dipole magnet for bending the e^- beam into its dump (see Fig. 3.30).
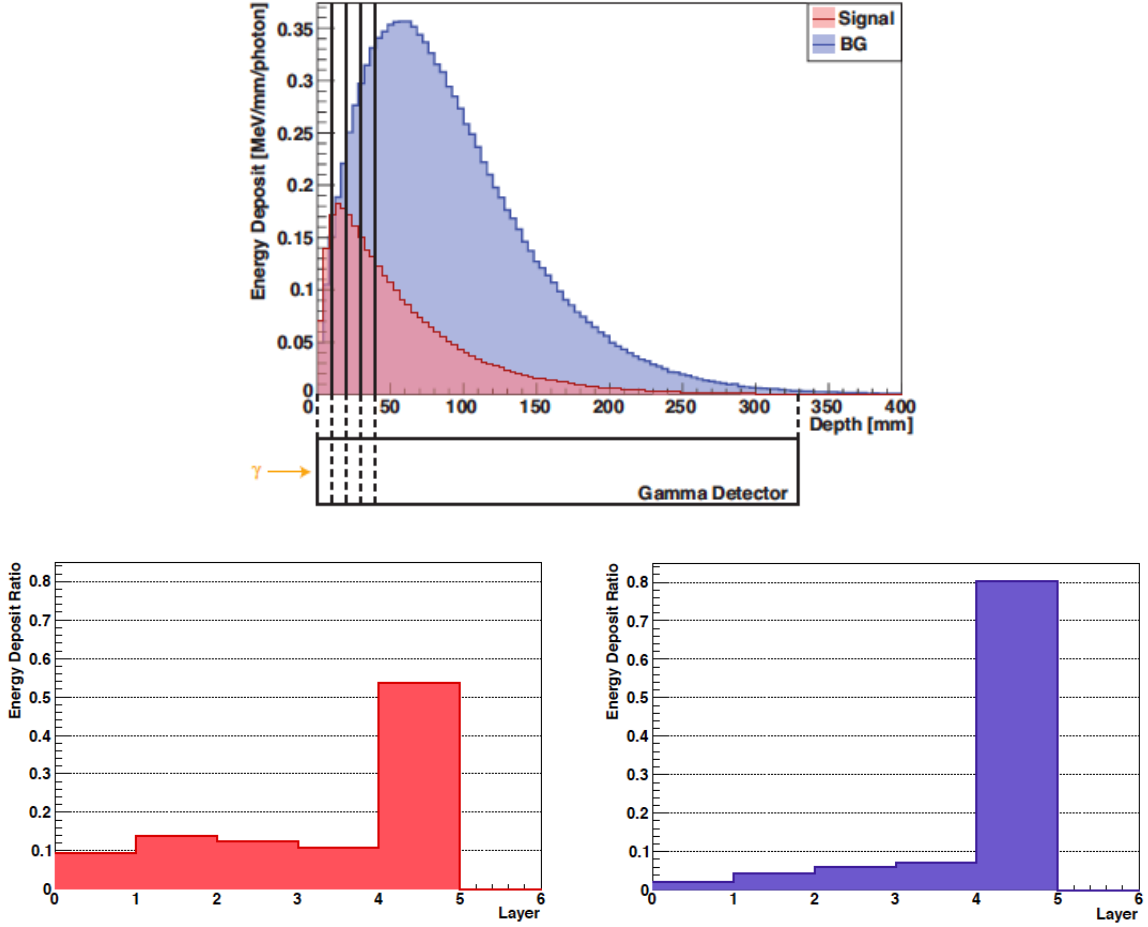
Figure 3.28: (top) The distribution of energy deposit per unit distance per photon in each scintilator layers for Compton signal and bremsstrahlung BG, from GEANT4 simulation[22]. The amount of BG is input according to the status in 2010 operation, for which the S/N ratio of $\lesssim 1$ is lower than 1/25 of that in 2014.

(bottom) From the GEANT4 simulation results [22]: the ratio of energy deposit in each detector layer (1, 2, 3, 4, 5) is (0.093, 0.139, 0.125, 0.107, 0.535) for Compton signal photons (left), and (0.021, 0.045, 0.061, 0.071, 0.802) for bremsstrahlung BG photons (right).
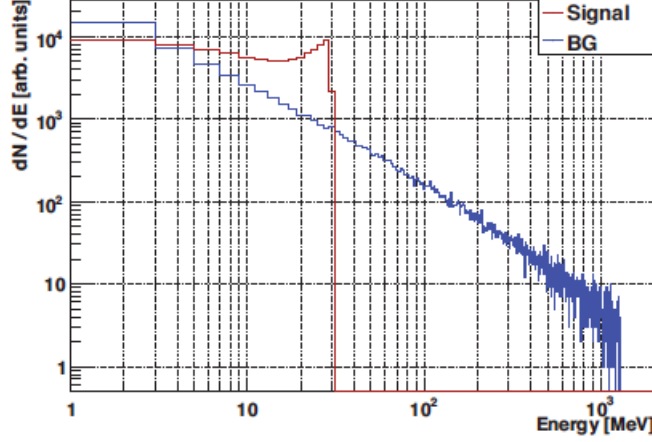
Figure 3.29: The energy spectrum of bremsstrahlung BG photons (blue) from the simulation of interaction between the beam and the beam pipe at the FD[22]. Plotted together is the energy spectrum of Compton signal photons (red) calculated in Sec. 2.6.

	average [MeV]	RMS [MeV]
signal	14.7	9.3
background	53.0	14.7

Table 3.6: The average and RMS of the energy of signal and BG photons from simulation[22]

Slow Neutron BG

Most of the hadrons produced in the post-IP beam dump (about 50 cm to one side of the detector) are absorbed by the dump itself. However, some neutrons, being long-lived and neutral, leak out and deposit energy in the detector. Paraffin absorber plates are inserted between the dump and the detector to block these neutrons (see Fig. 3.30). The high H atom content (close to neutron in mass) in the inexpensive paraffin effectively absorbs the neutrons' kinetic energy through elastic scattering. Since BG neutrons are slower than signal photons, they can also be separated by adjusting the detector's ADC gate timing. The "slow BG" was confirmed to be indeed neutrons by observing the change in signal on an oscilloscope when the paraffin plates were inserted and removed.

Negligible BG Sources

Some minor sources of BG photons are synchrotron radiation when the beam passes the FD and the bremsstrahlung from scattering with the residual gas in the vacuum pipe.

The critical energy for synchrotron radiation is about $E_{C,SR}\,[\text{keV}] = 0.665\,(E\,[\text{GeV}])^2\,B\,[\text{T}]$. This is about 1.1 keV for the beam energy (E$\sim$1.3 GeV) and the FD magnet field (B$\sim$1 T) at ATF2. Thus the energy loss due to synchrotron radiation is at the most a few keV. This is more than three orders of magnitude smaller than the average signal energy of about 15 MeV. Almost all SR photons should lose their energies inside the ATF2 beam pipe which is made from stainless steel (SUS304) of thickness 1.6 mm. Therefore, BG from synchrotron radiation is negligible.

The vacuum inside the FFS beam pipe at ATF2 has been measured to be better than 10^{-6} Pa [8]. The cross section for the production of bremssstrahlung photons > 1 eV due to residual gas

---

[8]The IP beam chamber has a larger volume per length, thus the vacuum in the beam pipe at IP should be even better than this value.

scattering is $\sigma_{gas} < 1.5 \times 10^{-23}\,\mathrm{cm}^{-2}$. From these, the estimated density of residual gas particles is $n_{gas} < 2.7 \times 10^{10}/\mathrm{cm}^3$. Assuming a beam bunch charge of $N_e \sim 10^9$, the number of bremsstrahlung BG photons due to residual gas scattering produced after traveling L=50 m through the beam pipe is estimated to be $N_{\gamma-gas} \sim \sigma_{gas} n_{gas} N_e L < 2/\mathrm{bunch}$. Since average energy is about 15 MeV and 53 MeV for signal and BG photons, respectively, this correspond to $\lesssim 1$ % in energy for every 1000 signal photons, and is thus negligible.
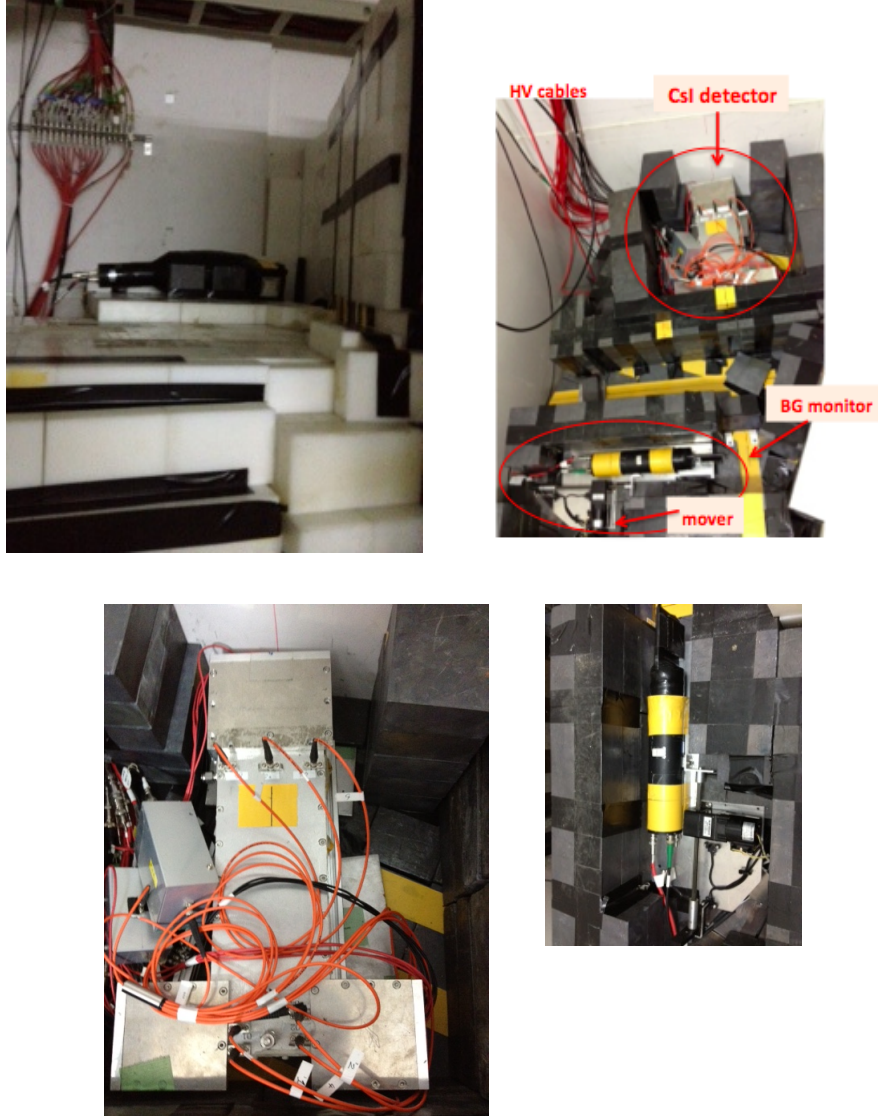
Figure 3.30: The area surrounding the "Gamma Detector" in Fig. 3.25:
(top left) The Pb blocks to cut breamstrahlung BG photons and parafine shielding (in white) placed around the detector to cut BG neutrons backscattered from the beam dump.
(top right) The CsI(Tl) gamma detector (upstream) and the BG monitor (downstream) shown sitting amid the Pb blocks after the top of the shielding has been removed.
(bottom) The close up view of the CsI(Tl) detector (left) and the BG monitor (right).

3.5.3 Collimation

There are in general three types of collimators installed in the beam line between the IP and the Shintake Monitor gamma-ray detector sitting 6.2 m downstream of the IP (see Fig. 3.31):

1. To cut the bremsstrahlung BG generated at the FD, there are two types of lead collimators installed; a collimator of 20 mmϕ aperture fixed at just 340 mm upstream of the detector, and a movable collimator of 10 mmϕ aperture is installed further upstream at about 3200 mm from the detector, immediately after the exit of the final bending magnet.

2. To cut the bremsstrahlung BG generated at the post-IP dipole magnet, an intermediate collimator was installed into the beam chamber there in summer 2012[29]. This significantly reduced the amount of BG photons and increased the S/N ratio in fringe scans.

The position of the movable collimator in 2. is scanned using a movable stage (Sigma Koki, SGSP26-100(X)) during beam time with the purpose of optimizing signal acceptance in accordance with slight shifts in signal photon path which result from e$^-$ beam orbit tuning. More on "collimator scans" are found in Sec. 4.2.4. The relative position between the movable collimator and fixed collimator is calibrated using an alignment laser. The table below lists their aperture, distance, and polar angle acceptance when looking from the IP.

	movable collimator	fixed collimator
distance from IP	~ 3000 mm	5860 mm
aperture (radius)	5 mm	10 mm
polar angle acceptance[9]	1.67 mrad	1.71 mrad

Assuming perfect alignment w.r.t. the center of the signal photon distribution, the aperture of the entire collimator system yield a signal acceptance of 94% for the number of photons and $> 99\%$ for signal energy. Because the bremsstrahlung BG photons generated at the FD propagate nearly parallel to the signal photons projected from the IP, it is difficult to collimate a sufficient amount of BG while still maintaining signal acceptance. Thus bremsstrahlung photons remain the major source of BG in the detector. This is compensated by separating signal from BG in analysis.

The detector is surrounded by additional Pb blocks to reduce any residual BG photons. Also inside this barrier is the BG monitor (see Sec. 1.6.2) about 10 cm upstream of the main detector. The BG monitor is inserted on a mover to measure the energy of bremsstrahlung photons for the IP wire scanner, and is removed afterwards.
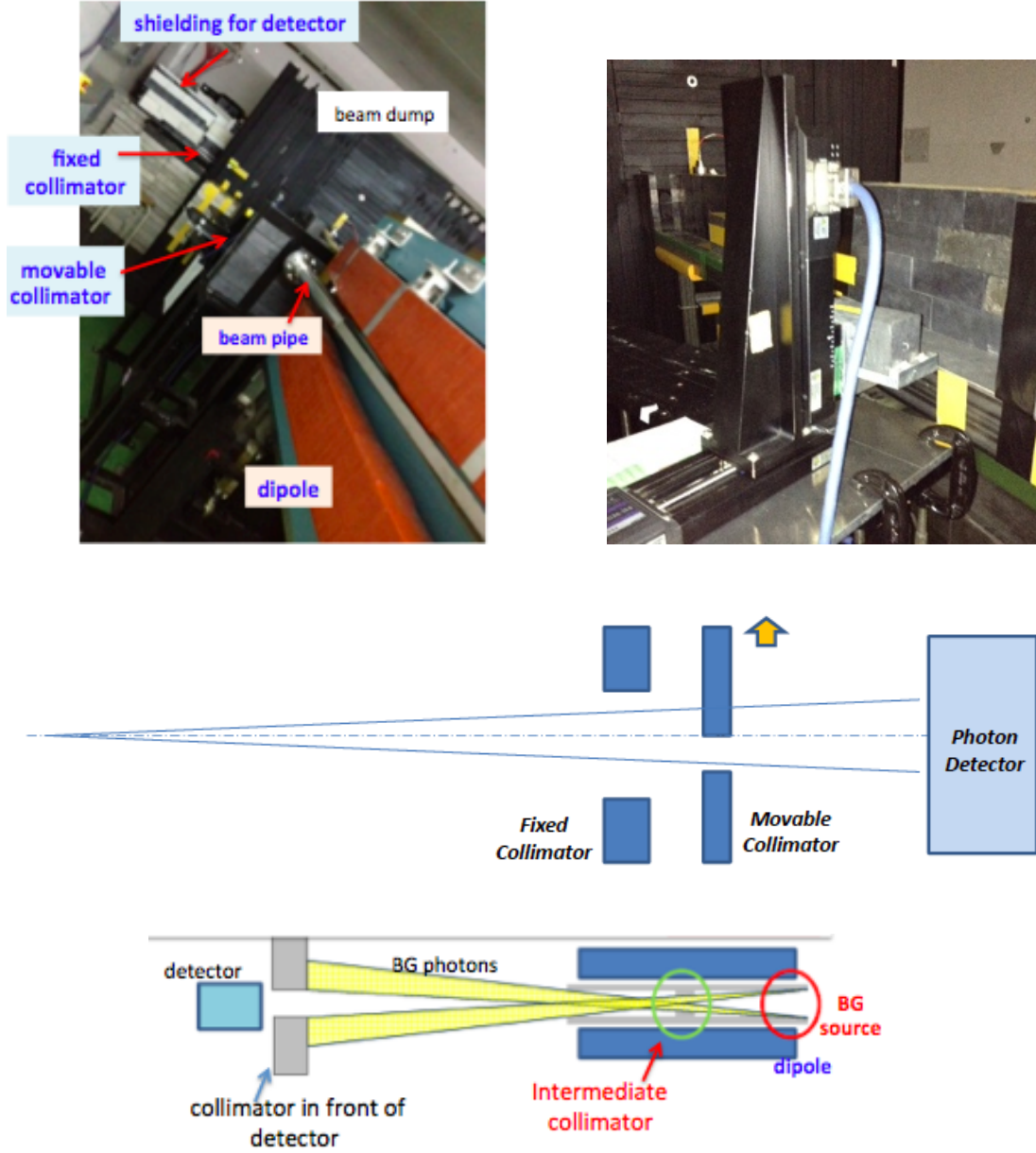
Figure 3.31: (top left) A photo of the beam line leading up to the CsI(Tl) gamma-ray detector. (top right) The movable collimator scanned during beam time to maximize signal. It has 10 mmϕ aperture and dimension of (50 mm × 50 mm × 200 mm). (middle) The schematics of the movable collimator which is scanned to maximize the amount of signal passing to the gamma-ray detector.[30] (bottom) The schematics of BG photons generated at the final bending dipole, and the "intermediate collimator" inserted into the beam pipe to cut this BG (modified from [31]).

3.5.4 Methods for Analysis and Signal Digitization

The measured Compton signal energy is analyzed using the "ON/OFF" method. The energy of "ON events" (E_{ON}) are measured with collision between laser and e$^-$ beam. The energy of "OFF events" (E_{OFF} = BG energy) are measured without collision by shifting the laser trigger timing away by about 40 ns. The total signal energy is calculated as $E_{sig} = E_{ON} - E_{OFF}$. At each fringe scan phase,

1 OFF event is measured, followed by subsequent "N_{av}" pulses of ON events. The energy deposit for the i-th detector layer is defined as the average of the left and right PMTs : $E_i = (E_{iL} + E_{iR})/2$ (i = 1-4) [10] . Typically, the sum of ADC counts in only the front 4 layers is used in analysis. This custom is meant for accommodating any S/N ratios since under high BG circumstances, the last bulk layer is dominated by BG [11].

In the past, another more sophisticated analysis method called the "shot by shot method" had been used. This had been developed in accordance to the multi-layer design of the detector. The information of all layers are used, and BG is separated from signal shot by shot by fitting their shower shapes. Compared to the "ON-OFF" method, the "shot-by-shot" method has the merit of being more robust against BG fluctuation; however there are more ambiguities and complexities, such as systematic errors due to unexpected changes in the shower shape of BG photons due to beam angular jitter. Thus the "ON-OFF" method became the recent choice for analysis. The details of both methods are found in [22][32].

The detector signals are digitized using a charge sensitive ADC (Hoshin, v005), shown in Fig. 3.32. In order to suppress the effect of e$^-$ beam intensity jitters, the measured energy is normalized by the beam bunch charge (N_e) measured using an "integrated current transformer (ICT) monitor". An ICT monitor consists of cables wrapped around a toroid ferrite core (Fig. 3.34). The variation in the magnetic field induced by the beam pulse passing through the core results in a voltage output signal directly proportional to N_e. The beam current of multiple pulses is integrated over about 70 ns, and bunch charge is measured as the area under the signal pulse. The signals are then amplified and digitized by the charge sensitive ADC (RPV-171), whose gate signal is synchronized with that for the ADC measuring energy. Figures 3.32 and 3.33 show the schematics of DAQ (inputs of signal and gate triggers) of the ADCs. Table 3.7 shows the ADC specifications.

---

[10]In recent operation, an equal weighting is applied to all PMTs. This should not cause a significant miscalibration effect since the measured PMT gains are not very different[25].

[11]The S/N ratio was improved from < 5 before 2014 to > 50 due to improvements in beam tuning and collimation. The custom of using only the front 4 layers has continued. Some alternative methods are to use the ADC counts from all 5 layers, or to use the 2nd layer only, as it has the highest S/N ratio. It has been confirmed that the fitted beam size is consistent within the fitting errors regardless of which method is used. It has also been confirmed that there is less than 1 % additional statistical fluctuation due to sampling from only the front 4 layers as opposed to using all 5 layers.
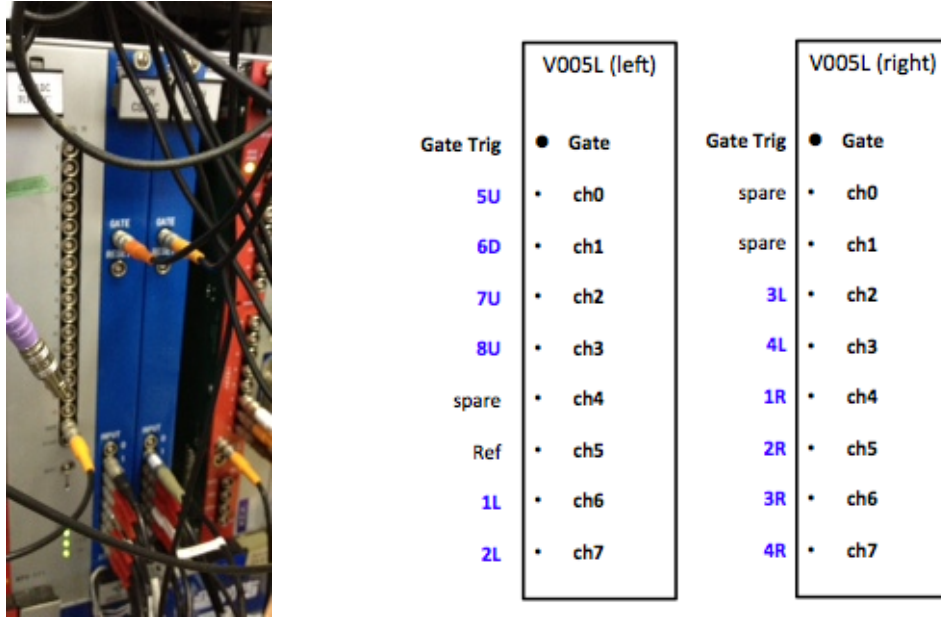
Figure 3.32: (left) The two charge sensitive ADCs (v005) for the gamma-ray detector. (right) Input of PMT output signal and gate trigger signals into the ADC. "Ref" is a reference PMT for calibration.
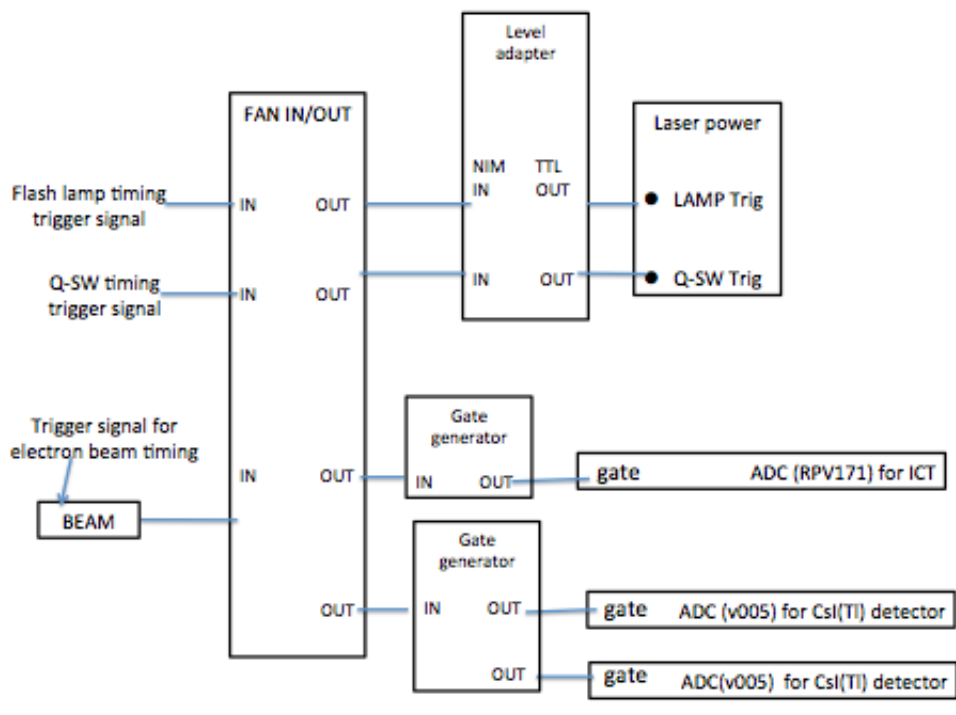
Figure 3.33: The schematics of gate trigger signal input into the ADC v005 for digitizing Compton photon energy measured by the gamma-ray detector and the ADC RPV-171 for digitizing beam intensity measured by the ICT monitor. The trigger signals for laser timing are shown together here.
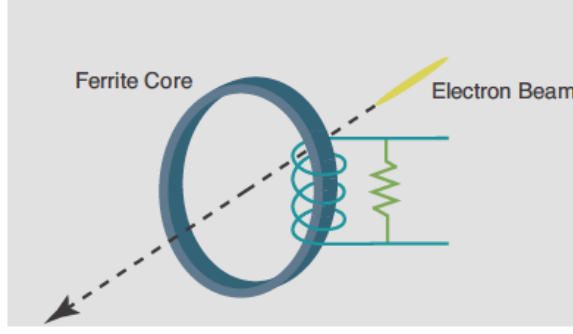
Figure 3.34: The schematics of an ICT monitor used for measuring e$^-$ beam intensity at ATF2[22].

product	v005, Hoshin
no. of channels	8
full range	0-1000 pC
resolution	14 bit
gate width	30 - 1000 ns

product	RPV-171, Repic Corporation
no.of channels	16
full range	0-1000 pC
resolution	12 bit
gate width	100 - 1000 ns

Table 3.7: Basic specifications for the charge sensitive ADCs (VME modules) of the Shintake Monitor: (left) v005 for the photon energy measured by the gamma-ray detector[33] (right) RPV-171 for the beam intensity measured by the ICT monitor.

3.6 Estimation of Statistical Fluctuations

The gamma-ray detector measures the total energy of Compton signal photons bunch by bunch. The statistical error of the measured energy depends on Compton photon statistics, collimation and detector response.

3.6.1 Compton Photon Statistics

The number of Compton scattered photons N_{sig} entering the gamma detector is calculated as :

$$N_{sig} = N_e \cdot \Sigma_{laser} \cdot \sigma_c \cdot (\text{collimator acceptance}) \tag{3.5}$$

N_e is e$^-$ beam bunch population. σ_c is total Compton cross section ($= 0.65$ barns). Σ_{laser} is the surface density of laser photons interacting with the beam, and is calculated as :

$$\Sigma_{laser} = \frac{E_{laser}}{2\pi\varepsilon_{laser}\sigma_{laser}c\sigma_t} \tag{3.6}$$

Inserting the values of the relevant laser parameters in Table 3.8 gives $\Sigma_{laser} = 1.7 \times 10^{22}/\text{m}^2$. Since the e$^-$ beam pulse ($\sim$20 ps) is much shorter than the laser pulse (3.4 ns), it is assumed to interact with constant laser photon density.

1-photon energy	laser pulse energy	laser spot size	laser pulse width (RMS)
ε_{laser}	E_{laser}	σ_{laser}	σ_t
2.33 eV	0.41 J ^{12}	10 μm	3.4 ns

Table 3.8: The realistic values of the laser related parameters used in the calculation of N_{sig}

The collimators upstream of the detector are optimized as to cut as much BG as possible while maximizing signal acceptance. Assuming perfect alignment w.r.t. the center of the Compton photon trajectory, the signal angle acceptance of the collimation system is about 1.67 mrad based on the geometry given in Sec. 3.5.3. From integration of the angular distribution in Fig. 2.8 (top right), this corresponds to 94% of all photons.

Furthermore, the power loss during the transport from the laser source to the IP is estimated to be about 57%. This assumes the reflectivity R∼99% of each of the 20 mirrors, and the transmittance (T∼90%) of each of the 5 lenses and the vacuum chamber viewport window [13]. In addition, because there are multiple (2∼3) non-Gaussian modes observed in the laser profile[14] (see Sec. 5.2), it is possible only 30-70% of the total laser energy contributes to the collision with the e^- beam.

From all of the above and Eq. 3.5, N_{sig} is calculated to be 100-350/bunch for the relatively low $N_e = 1.0 \times 10^9$ in recent ATF2 beam operation. From this, the statistical fluctuation due to Compton photon statistics (without detector effects) is evaluated using simulation as follows:

1. N'_{sig} photons from Compton scattering are generated according to a Poisson distribution with the mean changed in the range of 100-350.

2. Each photon is randomly assigned an energy from the energy distribution in Fig. 2.8 (top left). The sum is taken of the energy of the N'_{sig} photons.

3. The above is repeated for 10000 pseudo experiments. The relative energy fluctuation is evaluated as $\Delta E / E_{mean}$, where E_{mean} and ΔE represent the mean and standard deviation of the 10000 events. Figure 3.35 shows a histogram for the case of N_{sig}=200, for which $\Delta E / E_{mean} \simeq 7\%$. For the N_{sig}=100-350/bunch estimated above, the statistical fluctuation is estimated to be 5-10% .

---

[13]The catalog R of the mirrors (Lattice Electro Optics) is >99%. The T of the lenses and vacuum windows (also Lattice Electro Optics) take into account their thickness and the properties of their materials (BK7 and Fused Silica, respectively). In addition, a margin is included for possible deviation from catalog specifications due to radiation damage and/or dust on the component surfaces.

[14]There are typically 2∼3 high intensity spots, among which one spot has the apparently highest intensity. Before fringe scans, the laser position is adjusted to allow the location with the highest intensity to collide with the e^- beam.
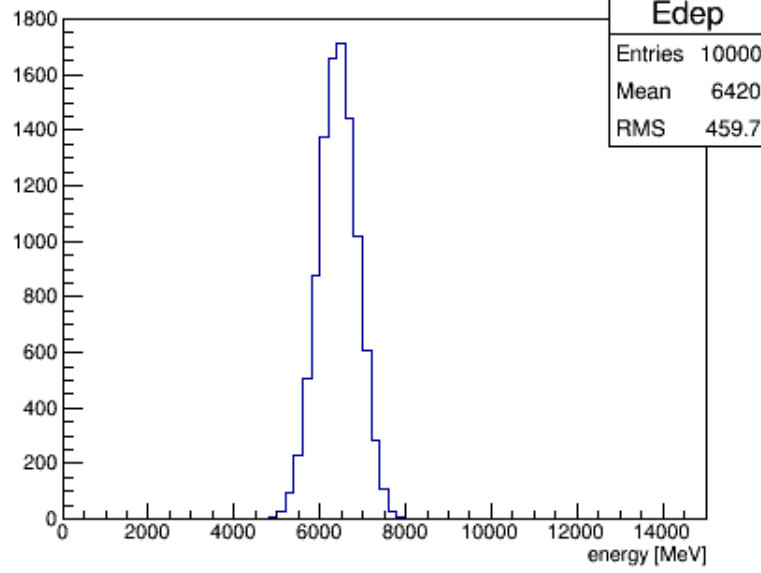
Figure 3.35: The sum of the energy of N_{sig}=200 Compton signal photons generated by simulation for 10000 pseudo experiments. Each photon is randomly assigned an energy from the energy distribution in Fig. 2.8 (top left).

3.6.2 Detector Response

When a photon deposits an energy of E MeV into the detector scintillators, the number of photo-electrons emerging from the PMT photocathode is:

$$N_{pe} = N_{sig} \times E \times \varepsilon_{sci} \times \varepsilon_{coll} \times Q.E. \tag{3.7}$$

Here, ε_{sci} is scintillation efficiency. ε_{coll} is light collectivity between the scintillators and the PMTs, and $Q.E.$ is PMT photocathode quantum efficiency. The final output charge from a PMT and the corresponding ADC counts can be expressed as Eq. 3.8 and Eq. 3.9, respectively.

$$Q_{out} = N_{pe} \times (\text{PMT gain}) \times e \tag{3.8}$$

$$ADC = Q_{out} \times \frac{ADC_{max}}{Q_{max}} \tag{3.9}$$

Here, e is the elementary charge = 1.6×10^{-19} [C]. Q_{max} and ADC_{max} are the maximum charge and maximum ADC count of the charge sensitive ADC module (see Sec. 3.5.4) used for the detector. The factors affecting statistical fluctuation are estimated as follows:

The N_{pe} emerging from the photocathode is estimated to be about 10^4 using Equations 3.8 and 3.9, the PMT gain of 4×10^4 for the typically applied HV of 500 V [27], $ADC \sim 1000$ (from observation), and Q_{max}= 1000 pC and ADC_{max}=2^{14} (from ADC specifications). The contribution to signal fluctuation, scaling as $1/\sqrt{N_{pe}}$, is $\lesssim 1\%$.

In Sec. 3.6.1, the statistical error due to photon counting statistics i.e. the fluctuation of N_{sig} was estimated to be 5-10%. However, from the GEANT4 simulation results in [22] about 10% of the total Compton signal energy leaks out of the detector without being detected. Most of this leakage is from the top and bottom of the detector, since the vertical dimension of 50 mm is not sufficiently long compared to the CsI(Tl) Moliere radius of 37.5 mm. Furthermore, from Fig. 3.28, only about 50% of the total energy is deposited into the front four layers. Therefore only about

90%×50%=45% of the total incoming signal energy ends up as energy deposit to be used in the typical analysis (see Sec. 3.5.4). When combined with shower development fluctuation, this detector sampling effect leads to statistical fluctuation, estimated as follows. From the GEANT4 simulation in [22], the mean and rms. of the energy deposit of a single photon in the first detector layer are 1.2 MeV and 3.2 MeV, respectively. When N_{sig} photons enter the detector, the resulting statistical fluctuation is approximately $\left(3.2\,\mathrm{MeV} \times \sqrt{N_{sig}}\right)/\left(1.2\,\mathrm{MeV} \times N_{sig}\right)$. From the observation of the signal in each PMT, the difference in fluctuation between the sum of the front four layers and that in a single layer is generally $< 15\%$ [15]. When taking into account the correlation between layers, the statistical fluctuation due to shower development fluctuation for a single layer can be considered a pessimistic evaluation for the sum of the front four layers: 27% and 14% for N_{sig}=100 and N_{sig}=350, respectively. Convoluting this with the fluctuation from photon counting statistics, the total statistical fluctuation is estimated to be 15-28%.

3.6.3 Signal Acceptance

There are additional factors that may change the N_{sig} and photon energy (E_{sig}) reaching the detector. The two major factors are:

1. The angular jitter of the e$^-$ beam directly leads to the angular jitter of Compton photons. This causes shot by shot fluctuations in E_{sig}.

2. The misalignment of the movable collimator reduces signal acceptance. This may occur if the collimator is not re-optimized after unexpected changes in the e$^-$ beam trajectory and thus the signal photon path.

Regarding 1: the angular jitter of the e$^-$ beam is generally about 30% of its divergence. Based on recent ATF2 design parameters, the horizontal and vertical divergences are about $\sqrt{\varepsilon_x/\beta_x^*} = \sqrt{1.1\,\mathrm{nm}/40\,\mathrm{mm}} \simeq 0.17$ mrad and $\sqrt{\varepsilon_y/\beta_y^*} = \sqrt{12\,\mathrm{pm}/0.1\,\mathrm{mm}} \simeq 0.35$ mrad, respectively. These yield angular jitters of $(\delta\theta_{ex},\ \delta\theta_{ey}) \simeq (0.05$ mrad, 0.1 mrad). The resulting shot by shot signal fluctuation depends on the collimator alignment precision in 2.

Regarding 2: from experience, the movable collimator could be misaligned by as much as 2-3 mm. A misalignment of 2 mm in either X or Y could reduce N_{sig} by about 10% and E_{sig} by about 1%, w.r.t. the case when photons pass exactly through the collimator centers.

Figure 3.36 (top left) shows the spatial distribution of N_{sig} generated from the angular distribution in Fig. 2.8 (top right). Figure 3.36 (top right) shows the distribution of E_{sig} with each event weighed by the distribution of N_{sig}, based on the angle-energy correlation of the scattered photons in Fig. 2.8 (bottom).

A simulation was conducted to evaluate the effect on signal acceptance (N_{sig} and E_{sig}) from the combination of collimator offset and beam angular jitter. The input conditions assume the actual geometry of the collimator and the beam line, as well as the following:

- The spatial projections in Fig. 3.36 (top).

- Collimator offsets (X,Y) are changed in 1 mm steps over a range of 0-3 mm.

- Photon angular jitter with a Gaussian distribution whose sigmas are $(\delta\theta_{ex}, \delta\theta_{ey}) \simeq (0.05$ mrad, 0.1 mrad).

Figure 3.36 (bottom) shows the results of 1000 pseudo experiments in the form of $N_{sig}/N_{sig,0}$ ($E_{sig}/E_{sig,0}$), defined as the ratio of the N_{sig} (E_{sig}) that made it past the collimators to the detector

---

[15]The difference in signal fluctuation between different detector layers is also generally $< 15\%$.

w.r.t. total angular coverage. Table 3.9 lists the results for a few particular collimator offset scenarios. A perfectly aligned collimator i.e. $(X, Y) = (0, 0)$ yields $N_{sig}/N_{sig,0} = 94.1\%$ and $E_{sig}/E_{sig,0} = 99.6\%$. For a pessimistic case of $(X, Y) = (3\ mm, 2\ mm)$, N_{sig} and E_{sig} are reduced to 87% and 95% w.r.t. the case of no collimator offset; this would increase statistical fluctuation by $\lesssim 1\%$ [16].
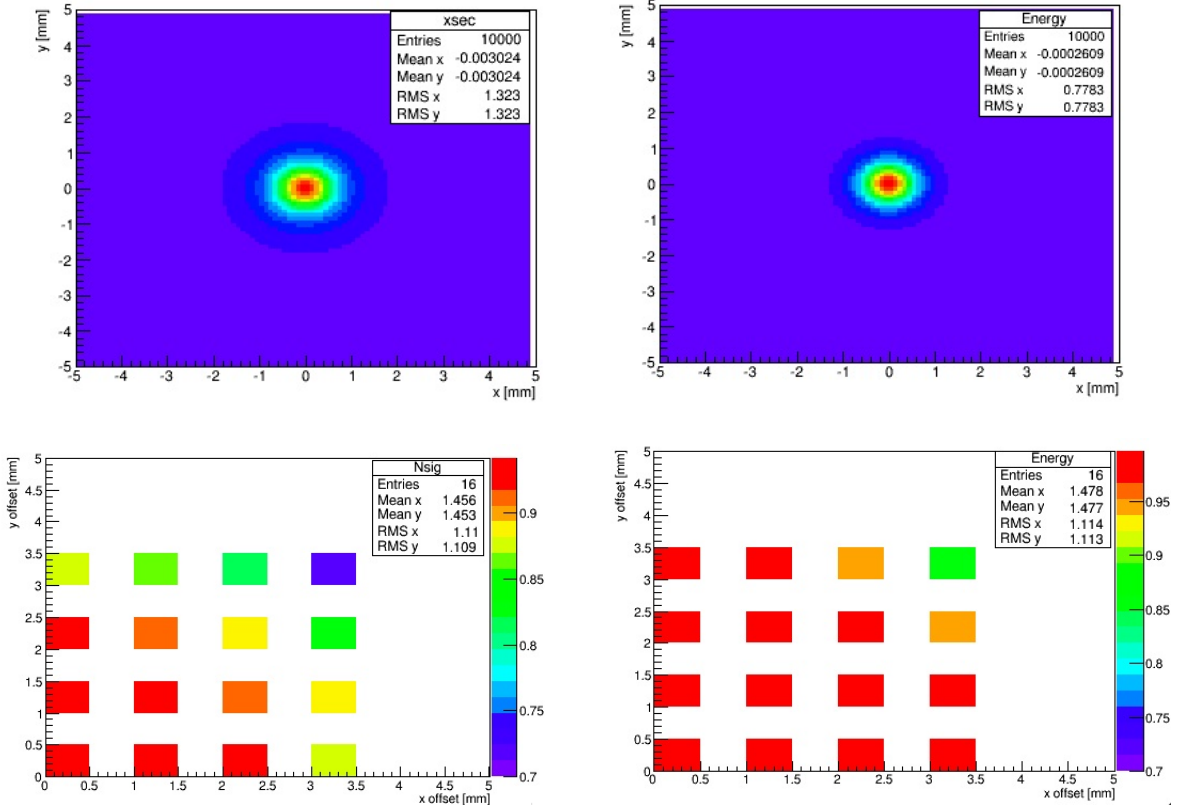
Figure 3.36: [top] (left) The spatial distribution of N_{sig} generated from the angular distribution of Compton scattering cross section in Fig. 2.8. The origin represents the photon path center. This does not take into account beam angular jitter. (right) The distribution of the scattered photon energy (E_{sig}) generated from the plot of angle vs energy in Fig. 2.8 (bottom). Each event is weighed by the distribution of N_{sig}.

[bottom] Simulation is carried out using the projections above. The inputs are: actual beam line geometry, X and Y collimator offsets in 1 mm steps over a range of 0-3 mm, and Gaussian distributed photon angular jitter with the sigma being $(\delta\theta_{ex}, \delta\theta_{ey}) \simeq (0.05\ mrad, 0.1\ mrad)$. The plots show the results of 1000 pseudo experiments in the form of $N_{sig}/N_{sig,0}$ and $E_{sig}/E_{sig,0}$ as a function of X-Y collimator offsets. N_{sig} (E_{sig}) is the number (energy) of signal photons that reach the detector. $N_{sig,0}$ ($E_{sig,0}$) is the number (energy) of signal photons for total angle acceptance.

---

[16]This assumes that the stochastic term in relative signal jitter scales approximately as $1/\sqrt{E_{sig}}$. In this case, the angular acceptance is reduced by as much as 1 mrad on one side. Although $\delta\theta_{ex} \neq \delta\theta_{ey}$, the distribution in Fig. 3.36 (top) is almost symmetrical between X and Y, since the effect of angular jitter is small compared to that of the collimator offsets. In addition, when the Compton photon angular distribution is smeared with e$^-$ beam divergence, the effect on E_{sig} is less than a few % even for a pessimistic case of collimator offset.

X [mm]	Y [mm]	$N_{sig}/N_{sig,0}$	$E_{sig}/E_{sig,0}$
0	0	94.1%	99.6%
1	1	93.0%	99.4%
2	2	88.4%	98.1%
3	2	82.1%	94.8%

Table 3.9: A few cases for the simulated plots in Fig. 3.36 (bottom).

4 Procedures of Beam Size Measurement

This chapter briefly describes the procedures of beam tuning and beam size measurement at ATF2. Section 4.1 explains about the e$^-$ beam orbit tuning both in the upstream sections of the beam line and at the IP. Section 4.2 describes the process of preparing the Shintake Monitor for use in IP beam tuning.

4.1 Beam Tuning at ATF2

ATF2 beam tuning begins in the extraction line upstream of the FFS. First, the beam is steered into a straight trajectory through the magnetic field centers of the beam line magnets using correction dipole magnets and quadrupole magnets while referring to the beam position measured by BPMs. Then dispersion incoming into the FFS is measured by changing the RF frequency in the DR, and comparing the BPM orbit readings to energy. The dispersion is matched into the FFS using two quadrupoles and two skew quadrupoles. In the diagnostic section, the multi-OTR (Optical Transition Radiation) monitor system [34] provides fast shot-by-shot measurements of beam profile, emittance, and Twiss parameters [17]. Based on these, the FFS optics is adjusted to the measured Twiss parameters using quadrupoles at the FFS entrance and x-y coupling is corrected using 4 skew quadrupoles. All FFS magnets are placed on movers which allow their positions and roll angles in the transverse plane to be changed by remote control.

The first-order correction for the errors at the IP e.g. horizontal and vertical waist offset, dispersion, and x-y coupling is performed by changing the field strength and rotation angles of the FD quadrupoles. Figure 4.1 shows an example of a "QD0 scan". This stage in tuning typically yields $\sigma_x^* \sim 10$ μm and $\sigma_y^* \lesssim 3$ μm, which are measured using carbon wire scanners.

Then more precise correction of residual linear aberrations is performed using the "linear tuning knobs" (see Sec. 4.1.1) calculated as the horizontal and vertical motion of the FFS sextupole magnets. The combination of sextupoles for each knob can be orthogonized i.e. chosen independently of each other. Usually linear knob tuning is first done using beam size measurements by wire scanners, then repeated using measurements by the Shintake Monitor after σ_y^* has been tuned down to $\lesssim 2$ μm.

In the final stage of beam tuning, higher order aberrations may be corrected using the "non-linear knobs" (see Sec. 4.1.2), which are calculated as the combination of the strength of normal and skew sextupoles. The alternate reiteration of linear knobs and non-linear knobs enabled σ_y^* to be focused to $\lesssim$40 nm in 2014 operation [18]. The descriptions of tuning knobs in this thesis are mainly based on [12] and [35].

4.1.1 Linear Optics Tuning Knobs

The linear tuning knobs are calculated as orthogonal sets of the horizontal and vertical offsets of the FFS sextupoles. There are five sextupoles (SF6, SF, SD4, SF1 and SD0) in the ATF2 beam line (similar to the ILC FFS) whose transverse positions can be scanned using magnet movers. The field potential of magnets [36] can be represented in the form of $V_n^* = V_n + iV_{sn}$, where the normal field component V_n and the skew field component V_{sn} are expressed as:

$$V_n = -\frac{k_n}{n!}r^n \cos n\theta \tag{4.1}$$

---

[17]The Twiss parameters α_i, β_i, γ_i (i=x, y) describe the shape and orientation of the phase space ellipse for a single particle. Their adjustments can be expressed by the transfer matrices of the particle trajectory for a particular beam line lattice. The Twiss parameters are related to emittance ε as $\varepsilon = \gamma x^2 + 2\alpha xx' + \beta x'^2$, where x and x' are the position and angle of a single particle, respectively.

[18]In 2014, an "10×1" optics was used, for which β_x^* is increased to 40 mm, by a factor of 10 larger than the nominal 4 mm. The purpose was to reduce the effect of the multipole errors of QF1.

$$V_{sn} = \frac{k_{sn}}{n!} r^n \sin n\theta \tag{4.2}$$

Here, $n = 1$, 2, 3 represent dipole, quadrupole, and sextupole, respectively. For example, for a normal quadrupole: $V_2 = -\frac{k_2}{2}\left(x^2 - y^2\right)$; for a skew quadrupole: $V_{s2} = k_{s2}xy$; for a normal sextupole: $V_3 = -\frac{k_3}{6}\left(x^3 - 3xy^2\right)$; for a skew sextupole: $V_{s3} = \frac{k_{s3}}{6}\left(3x^2y - y^3\right)$.

For the case of a normal sextupole, a horizontal offset $x \rightarrow x + \Delta x$ changes the field potential as:

$$V_3 \rightarrow -\frac{k_3}{6}\left[(x + \Delta x)^3 - 3(x + \Delta x)y^2\right]$$

$$= -\frac{k_3}{6}\left(x^3 - 3xy^2\right) - \frac{k_3 \Delta x}{2}\left(x^2 - y^2\right) + \mathrm{O}\left(\Delta x^2\right) \tag{4.3}$$

The last term represents higher order dispersion effects. A vertical offset $y \rightarrow y + \Delta y$ changes the field potential as:

$$V_3 \rightarrow -\frac{k_3}{6}\left[x^3 - 3x(y + \Delta y)^2\right]$$

$$= -\frac{k_3}{6}\left(x^3 - 3xy^2\right) + k_3 \Delta y \cdot xy + \mathrm{O}\left(\Delta y^2\right) \tag{4.4}$$

The second term in Eq. 4.3 can be rewritten as $\frac{k_2}{2}\left(x^2 - y^2\right) = \frac{k_2}{2}r^2 \cos 2\theta$. This indicates that the horizontal movement of a sextupole generates a quadrupole field whose strength $k_2 = k_3 \Delta x$ is proportional to the horizontal motion Δx. This changes the horizontal and vertical beam waist positions (W_x and W_y), the horizontal dispersion at the IP (η_x) and its derivative (η'_x) w.r.t. the longitudinal coordinate. The linear knobs AX, AY, EX, and EPX, calculated as orthogonal sets of the horizontal offsets, change W_x, W_y, η_x, and η'_x, respectively.

Similarly, the second term in Eq. 4.4 can be rewritten as $k_{s2}xy = \frac{k_{s2}}{2}r^2 \sin\theta$. This indicates that the vertical movement of a sextupole generates a skew quadrupole field whose strength $k_{s2} = k_3 \Delta y$ is proportional to the vertical motion Δy. This changes the vertical dispersion at the IP (η_y), its derivative (η'_y), and coupling components between the x and y plane. The linear knobs EY, EPY, and Coup2, calculated as orthogonal sets of the vertical offsets, change η_y, and η'_y, and x'-y coupling respectively. The σ_y at the IP is sensitive to W_y, η_y, and x'-y coupling. Therefore linear knob tuning typically comprises of the knobs AY, EY, and Coup2. Their contribution to σ_y can be expressed as:

$$\sigma_y^2 = \sigma_{y0}^2 + C_{\alpha y}^2\left(AY\right)^2 + C_{\eta y}^2\left(EY\right)^2 + C_{x'y}^2\left(Coup2\right)^2 \tag{4.5}$$

Here, $\sigma_{y0} = \sqrt{\beta_y \varepsilon_y}$ is the nominal vertical IP beam waist size. The functions of each knob are listed below:

- AY: the deviation from 0 of the Twiss parameter α_y, which represents the shift of the vertical beam waist along the beam direction;

- EY: the deviation from 0 of η_y;

- Coup2: the deviation from 0 of x'-y coupling.

The effect represented by each coefficient $C_{\alpha y}$, $C_{\eta y}$, and $C_{x'y}$ are listed below:

- $C_{\alpha y}$: the effect of waist position; depends on vertical beam divergence;

- $C_{\eta y}$: the effect of η_y ; basically constant; depends on momentum spread;

- $C_{x'y}$: the effect of x'-y coupling; depends on horizontal beam divergence.

At locations away from the waist, σ_y is sensitive to the vertical divergence angle $\sigma_{y'} = \sqrt{\frac{\epsilon_y\left(1+\alpha_y^2\right)}{\beta_y}}$. If the knobs are independent, the measured modulation (M) is expressed using the response of each knob by:

$$M = C_{\text{total}}|\cos\theta|\exp\left(-2k_y^2\sigma_y^2\right)$$

$$\begin{aligned} = \quad & C_{total}|\cos\theta|\exp\left(-2k_y^2\sigma_{y0}^2\right) \\ & \cdot\exp\left(-2k_y^2C_{\alpha y}^2\left(AY\right)^2\right)\exp\left(-2k_y^2C_{\eta y}^2\left(EY\right)^2\right)\exp\left(-2k_y^2C_{x'y}^2\left(Coup2\right)^2\right) \end{aligned} \qquad (4.6)$$

Here, θ is the crossing angle of the Shintake Monitor laser. $|\cos\theta|\exp\left(-2k_y^2\sigma_{y0}^2\right)$ indicates the maximum achievable M (corresponding to the minimum achievable σ_y). C_{total} (<1) is the total systematic error intrinsic to the Shintake Monitor which acts to under-evaluate M (see Chap. 6). The orthogonality of the linear knobs has been tested by particle tracking simulation using SAD [12].

4.1.2 Nonlinear Tuning Knobs

The strengths of the FFS sextupoles are set so as to cancel the chromaticity generated at the FD. However, the presence of sextupole field errors causes additional higher order aberrations. In order to correct second order optics errors, "nonlinear tuning knobs" are applied in the final stage of IP beam size tuning. There are six nonlinear knobs in use: {Y22, Y44, Y66, Y26, Y24, and Y26}, calculated as the strengths of the FFS sextupoles. Y24 and Y46 correct normal sextupole field errors. Y22, Y44, Y66, and Y26 correct skew sextupole errors. Here, the indices 2, 4, 6 represent x', y', and energy, respectively. For example, Y66 is effective for 2nd order dispersion. The nonlinear knobs are almost orthogonal to each other, but not completely so. Because there are cross terms, the knob settings are optimized through reiteration. Reiteration is sometimes also carried out between linear knobs and nonlinear knobs.

Figure 4.2 (shows an example of linear knob tuning and nonlinear knob tuning using measurements by the Shintake Monitor. The response of M to the knob strokes is fitted with a Gaussian function. The setting of each knob is optimized so as to yield the Gaussian peak.
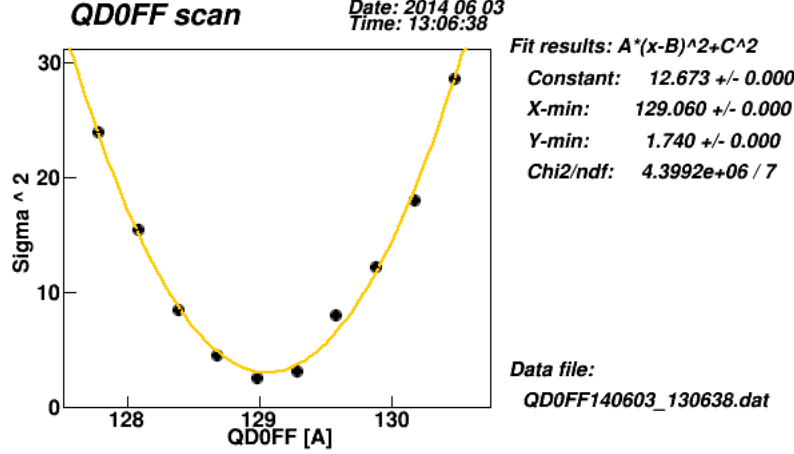
Figure 4.1: An example of a QD0 scan [17]. Here, σ_y is measured using the IP wire scanner as a function of the scanned strength (current) of the vertically focusing quadrupole QD0, and fitted with a parabolic function.
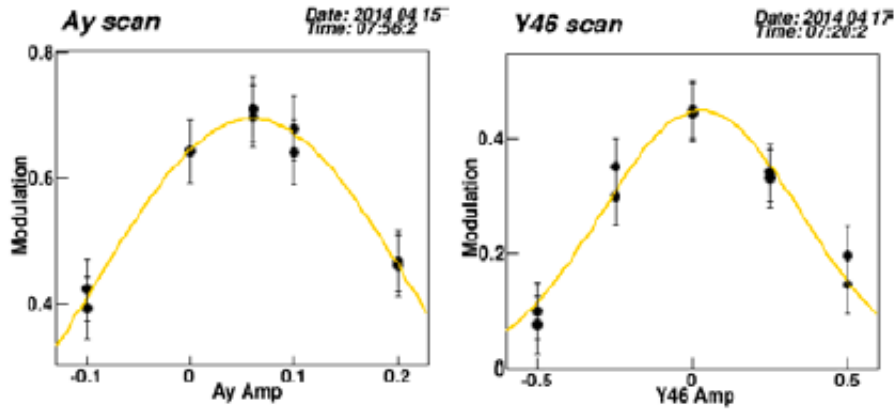
Figure 4.2: An example of multi-knob tuning [17]: (left) linear knob AY (right) non-linear knob Y46. The horizontal axis indicates the strengths of the knobs. Here, M is measured using the Shintake Monitor as a function of the knob amplitudes, then fitted with a Gaussian function.

4.2   Setup Procedure for the Shintake Monitor

This section describes the process of preparing the Shintake Monitor system for use in beam tuning. This comprises of the adjustment of the laser timing and position w.r.t. those of the e$^-$ beam at the IP, the adjustment of the focal lenses, and the optimization of collimation. After these preparations have been completed, the Shintake Monitor stably measures beam sizes as part of the e$^-$ beam tuning process described in Sec. 4.1. The laser crossing angle mode is switched in accordance to the beam focusing status.

4.2.1   Transverse Laser Position Alignment

The laser position must be kept constantly under strict alignment relative to the e$^-$ beam at the IP in order to measure M precisely. This section describes the routinely performed position alignment

process, which is repeated throughout the beam tuning process to compensate for drifts in the position of either laser or beam over time.

Preliminary Alignment by Screen Monitor

First, the laser paths are made to overlap with the beam using a CCD camera to monitor their positions on a screen (see Sec. 1.6.2) which allows a simultaneous view of both laser spots and the e$^-$ beam spot. The screen is mounted on the "IP target" mover and inserted into (out of) the IP before (after) this process. The CCD camera views the e$^-$ beam by the fluorescent light generated when it passes through the screen, and the laser spots by the light reflected from the screen. To prevent the screen from being burnt, the laser intensity is first weakened by the attenuator before the screen is inserted. The laser paths are aligned one at a time to the center of the e$^-$ beam spot by adjusting the angles of the actuator-attached mirrors. This is capable of alignment precision of $\lesssim 1 \times \sigma_{t,laser}$. Figure 4.3 shows the IP target and an example of alignment on the screen.
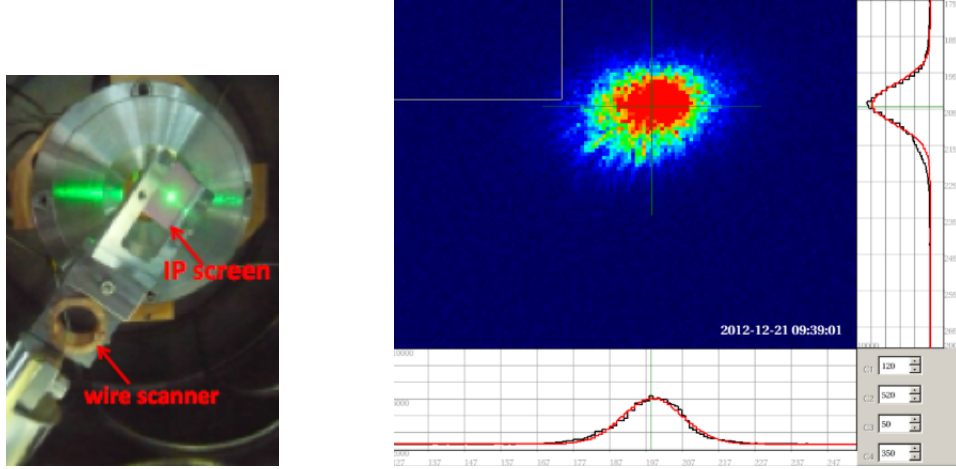

Figure 4.3: (left) The complex IP target system carrying the wire scanner and the screen. The weakened laser light (in green) is shown hitting the screen monitor.
(right) An example of laser position alignment using the IP screen monitor. The bright spot is the laser profile while the marker in its center indicates the e$^-$ beam position. The grey panel on the bottom right shows the mirror actuator settings being adjusted.

Fine Alignment by Laser Wire Scan

After the alignment using the IP screen monitor, finer position alignment with precision of about $1/10$ of $\sigma_{t,laser}$ is carried out using collision between high power laser and the e$^-$ beam. In the transverse plane, alignment is carried out by the "laser wire scan" introduced in Sec. 2.4. The position of one path at a time is scanned in the horizontal (x) direction w.r.t the beam by scanning the mirror actuators in fine steps of typically 0.5 μm, corresponding to a laser position shift at the IP of about $1/2$ of $\sigma_{t,laser}$. The range of the scan is typically wider than $\pm 5 \times \sigma_{t,laser}$. The primary purpose is to locate x_0, the position that yields the peak in the Gaussian-like laser wire signal. This is obtained by plotting the Compton signal energy resulting from collision as a function of position x, then fitting it by the following Gaussian function:

$$E\left(x\right) = E_0 \exp\left(-\frac{(x - x_0)^2}{2\sigma_{t,laser}^2}\right)$$

(4.7)

Here, E_0 is the peak energy, which ideally corresponds to $1/2$ of E_{avg} in a fringe scan. The accuracy in determining x_0 depends on the fitting precision, and is typically about $1/10$ of $\sigma_{t,laser}$. Figure 4.4 shows the effect of transverse laser position misalignment and an example of a laser wire scan. Another laser wire scan with 50 pulses measured at each x is shown in Fig. 5.5. The Gaussian-like signal is a convolution of the laser spot size $\sigma_{t,laser}$ and e^- beam size (mostly just σ_x, since $\sigma_y \ll \sigma_x$), and is expressed as :

$$\sigma_{lw} = \sqrt{\sigma_{t,laser}^2 + \sigma_{x,rel}^2} = \sqrt{\sigma_{t,laser}^2 + \sigma_x^2 \sin^2{(\theta/2)} + \sigma_y^2 \cos^2{(\theta/2)}} \qquad (4.8)$$

Here, $\sigma_{x,rel} \equiv \sqrt{\sigma_x^2 \sin^2{(\theta/2)} + \sigma_y^2 \cos^2{(\theta/2)}}$, interpreted as the "e^- beam size seen by the laser", approximately equals to just σ_x for the 174 deg mode. The horizontal beam size is inferred from wire scanner measurements (see Fig. 1.10), and is typically 9-12 μm during operation in 2014.
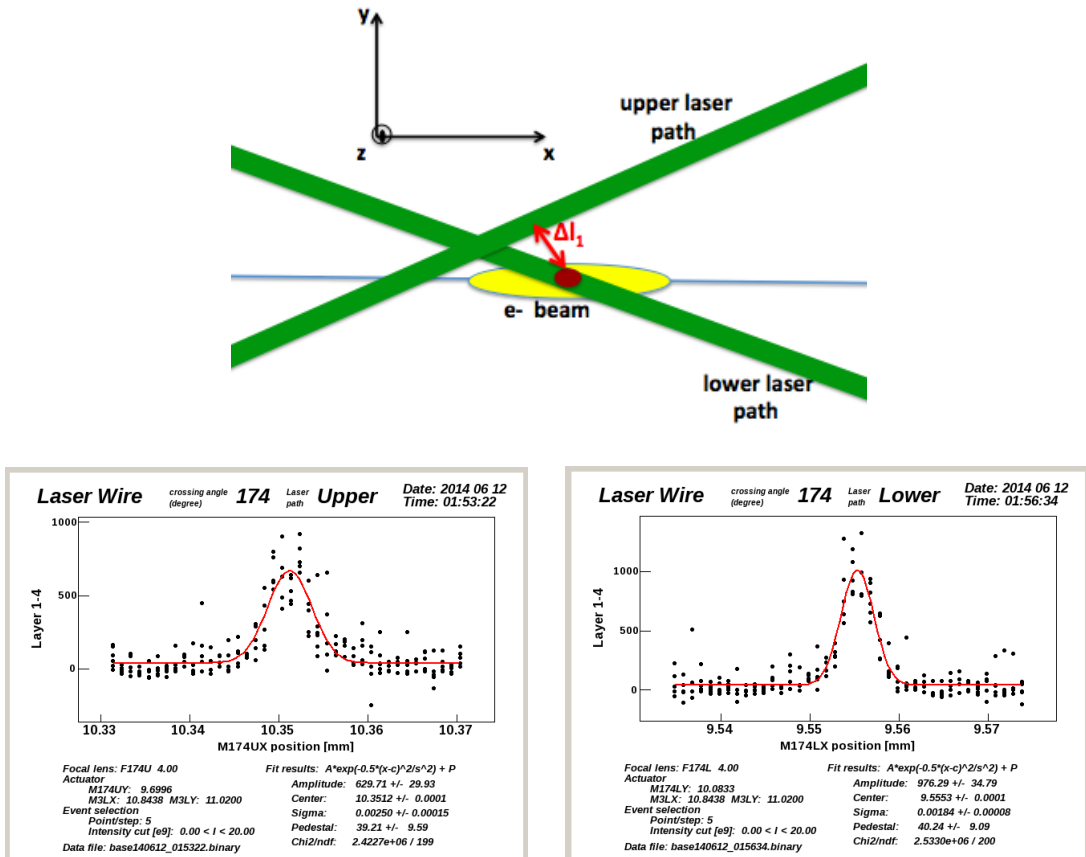
Figure 4.4: (top) The schematics of transverse laser position misalignment at the IP. Here, the upper path is assumed to be offset w.r.t. the e^- beam center by Δl_1, while the lower path is assumed to be precisely aligned. (bottom) A set of upper and lower path laser wire scans conducted in the 174 deg mode [17].

4.2.2 Longitudinal Position Alignment

The laser wire scan enables the laser to collide with the beam. However, fringe contrast would be degraded if the two laser paths are offset in the longitudinal (i.e. e^- beam) direction. Precise longitudinal alignment is done using the "z-scan". Figure 4.5 shows the effect of longitudinal offset and an example of z-scan. The "Y" actuator of the lower laser path is scanned with about the same

steps and as the laser wire scan. Fringe scan is conducted at each step. The M response is fitted with the following Gaussian function:

$$M\left(z\right) = M_0\exp\left(-\frac{(z-z_0)^2}{8\sigma_{z,laser}^2}\right) \tag{4.9}$$

Here, $\sigma_{z,laser}$ is the longitudinal laser spot size. z is the lower path's longitudinal position being scanned, z_0 is the optimum position which yields zero offset and thus realizes the sharpest fringe contrast, i.e. largest M. The actuator is set to align the laser to z_0 with a precision of typically $1/10$ of $\sigma_{z,laser}$ ($\sigma_{z,laser} \simeq \sigma_{t,laser}$). The 1-sigma of the Gaussian-like signal corresponds to $2 \times \sigma_{z,laser}$.
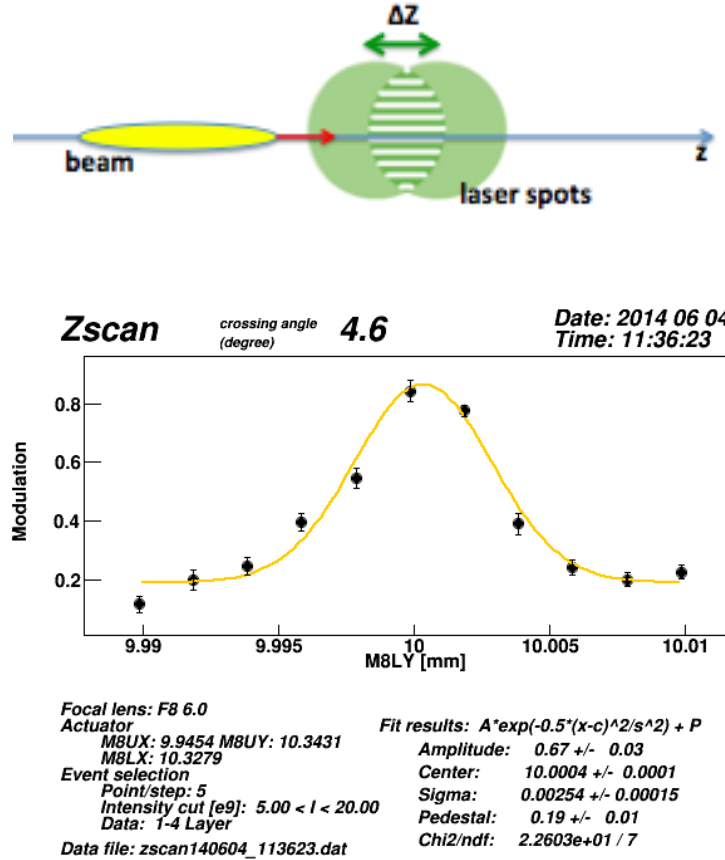
Figure 4.5: (top) The schematics of longitudinal laser position misalignment. The two paths are assumed to be offset by Δz in the e$^-$ beam direction. (bottom) An example of a z-scan conducted at the 4.6 deg mode; here, five pulses are measured at each step of the mirror actuator being scanned [17].

4.2.3 Focal Lens Scan

The focal lenses are able to be scanned in the laser beam propagation direction by placing them on movers of resolution 0.1 μm and stroke 30 mm (Figures 4.6 and 4.7). The "focal lens scan" is conducted during the setup of the Shintake Monitor for the following purposes:

- To optimize the laser profile balance between upper and lower paths; profile imbalance would cause bias of fringe contrast. (see Sec. 6).

- To realize a well focused laser spot size at the IP to maximize Compton signal intensity [19].

The procedures are as follows: the lens position is scanned in the laser beam propagation direction. Laser wire scan is conducted at each step while recording σ_{lw}, the sigma obtained from fitting the laser wire scan signal. The laser spot size ($\sigma_{t,laser}$) is calculated from σ_{lw} by subtracting the e$^-$ beam size as $\sigma_{t,laser} = \sqrt{\sigma_{lw}^2 - \sigma_x^2 \sin^2(\theta/2) + \sigma_y^2 \cos^2(\theta/2)}$ (modified from Eq. 4.8). The focal lens position (z) is set to the waist position (z_0) which yields the minimum $\sigma_{t,laser}$. The lens should be scanned over a wide range e.g. more than one Rayleigh length away from z_0. Figure 4.8 shows an example of a "focal lens scan" conducted using the 174 deg mode upper laser path. Here, the measured laser spot radius $\omega \simeq 2 \times \sigma_{t,laser}$ is plotted as a function of focal lens position. The waist spot size is $\omega_0 = 25.9 \pm 2.2$ μm (at $z_0 = 6$ mm). Section 5.1.2 gives a detailed evaluation of laser focusing status.
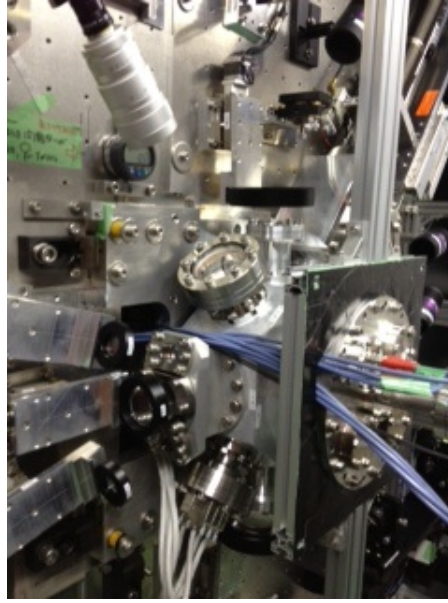
Figure 4.6: The vacuum chamber with viewports facing the focal lenses of the Shintake Monitor.

---

[19]Usually, the laser spot size is focused to the smallest possible while checking the status of signal jitters. Because a very small laser spot size may lead to larger pointing jitters at the IP, the focal lens position may be adjusted to slightly enlarge the laser spot size.
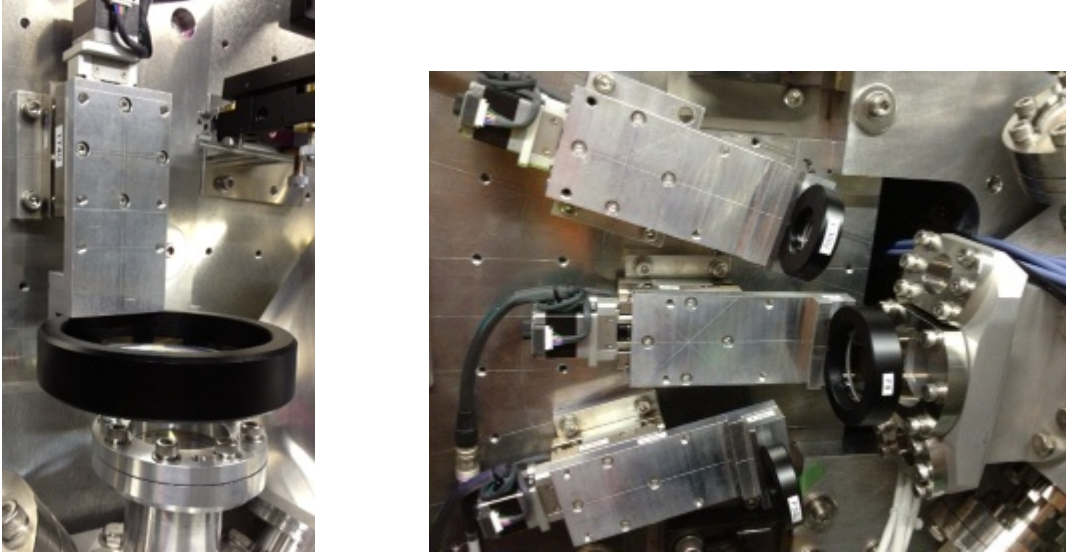
Figure 4.7: (left) The focal lens of the 174 deg mode upper path. (right) The focal lenses of the 30 deg mode upper and lower paths on either side of the 2-8 deg mode focal lens.
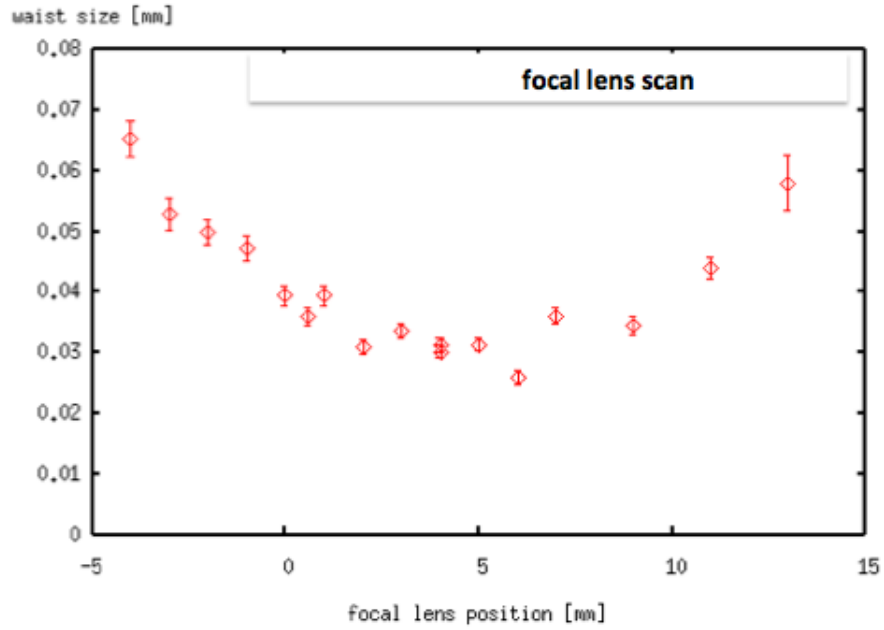
Figure 4.8: A focal lens scan conducted in the 174 deg mode (in May 2014).

4.2.4 Collimator Scan

The tuning of the e^- beam trajectory affects the path of Compton signal photons, possibly causing them to lose energy by brushing against the collimators on their way to the detector. There may also be an increase in BG energy fluctuation due to unpredicted changes in the location of BG sources.

Section 3.5.3 introduced two types of collimators for cutting bremsstrahlung BG generated at the FD: a downstream fixed collimator, and an upstream movable collimator which is scanned via remote control using an automatic stage for the following purposes:

1. To maximize the amount of signal entering the detector; this re-adjustment is necessary when signal path is altered along with the e$^-$ beam orbit. Figure 4.9 shows an example of the results of a collimator scan. Here, signal intensity is measured by the detector while the collimator is scanned in X and Y directions.

2. To detect sudden changes in the e$^-$ beam trajectory; in Fig. 4.9, if the peak of the measured signal intensity i.e. the photon distribution center is significantly deviated from the initial collimator center, it may be a sign that the e$^-$ beam orbit needs re-adjustment.
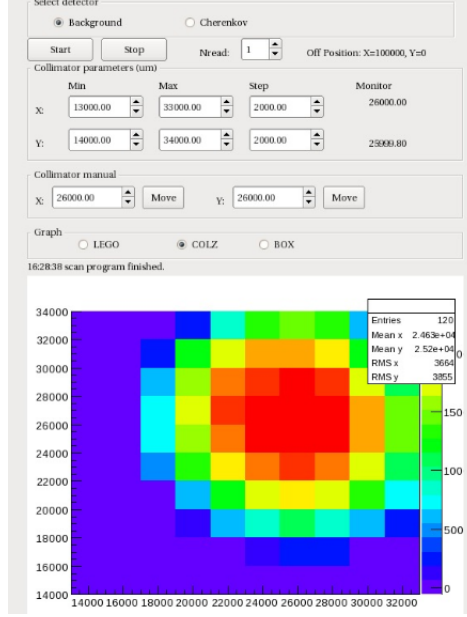
Figure 4.9: The result of a collimator scan conducted in June 2014, shown on the online ATF panel as a 2D histogram: The horizontal and vertical axis indicate the X and Y positions of the movable collimator stage, respectively. The center of the collimator was adjusted to the red area, which indicates the peak of signal intensity measured by the detector. [17]

4.2.5 Relative Timing Adjustment

Section 3.4.2 explained the monitoring of the timing of the laser and the e$^-$ beam using the signals of a PIN-PD and strip line BPM, respectively, and timing control using digital modules (EVR). The laser-beam relative timing require fine adjustment of precision better than 1 ns in order to maximize signal intensity and suppress Compton signal jitters to <5% (see Sec. 7.1.4 for detail). For this, Q-switch timing is changed in steps of 0.4 ns by scanning the delay setting of the EVR, while colliding one laser path against the e$^-$ beam. The online panel of this "timing scan" is shown in Fig. 4.10. The vertical axis is the Compton photon energy measured by the detector. The horizontal axis is the Q-switch timing scanned in sub-ns steps.

The timing scan is typically reiterated with laser wire scans before measuring M in z-scans. Because the laser path length to the IP differs for each crossing angle mode, the laser timing trigger setup must be re-adjusted after mode-switching. This is done automatically by software (timing control panels) using the appropriate recorded values.

Figure 4.10: An example of a timing scan. This was conducted in the 4.6 deg mode, with 3 pulses of Compton energy (vertical axis) measured at each step of the laser trigger timing (horizontal axis) being scanned. [17]
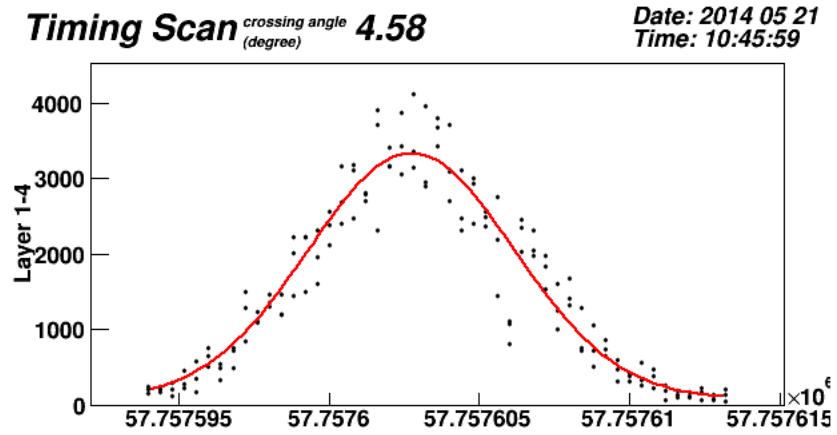
Part III
Performance Evaluation of Shintake Monitor

5 Evaluation of Laser Properties

5.1 Adjustment of Laser Spot Size

5.1.1 Representation of Laser Propagation by Transfer Matrices

When describing the propagation of the laser through a lattice comprised of optical components, it is convenient to use transfer matrices in the following form:

$$\begin{pmatrix} r_2 \\ r_2' \end{pmatrix} = A \begin{pmatrix} r_1 \\ r_1' \end{pmatrix} \tag{5.1}$$

Here, the position r and angle r' of the laser beam are represented by a vector, where the indices 1 and 2 represent the initial and final states, respectively. The 2×2 propagation matrix A is $D(L) = \begin{pmatrix} 1 & L \\ 0 & 1 \end{pmatrix}$ for a drift space of length L, and $F(f) = \begin{pmatrix} 1 & 0 \\ -1/f & 1 \end{pmatrix}$ for focusing due to a thin lens of focal length f; $\det A = 1$ is satisfied based on the conservation of phase space area under linear transformation.

Propagation through the expander/reducer

Section 3.1.2 explained the magnification of the laser spot size (σ_{laser}) by the expander on the laser table, and the restoration of σ_{laser} by the reducer after transportation to the vertical table. Using transfer matrices, propagation through an ideal expander can be expressed as:

$$A_{\text{expander}} = F(f_2) D(f_2 - f_1) F(-f_1)$$

$$= \begin{pmatrix} 1 & 0 \\ -1/f_2 & 1 \end{pmatrix} \begin{pmatrix} 1 & f_2 - f_1 \\ 0 & 1 \end{pmatrix} \begin{pmatrix} 1 & 0 \\ 1/f_1 & 1 \end{pmatrix} = \begin{pmatrix} f_2/f_1 & f_2 - f_1 \\ 0 & f_1/f_2 \end{pmatrix} \tag{5.2}$$

In Eq. 5.2, the degree of magnification of σ_{laser} is $M = f_2/f_1$. Therefore Eq. 5.2 can be rewritten in the form of

$$A_{\text{expander}} = \begin{pmatrix} M & L \\ 0 & 1/M \end{pmatrix} \tag{5.3}$$

Propagation through an ideal reducer with a demagnification of $1/M$ can be expressed by exchanging f_1 and f_2 in Eq. 5.2 :

$$A_{\text{reducer}} = F(-f_1) D(f_2 - f_1) F(f_2)$$

$$= \begin{pmatrix} 1/M & L \\ 0 & M \end{pmatrix} = \begin{pmatrix} f_1/f_2 & f_2 - f_1 \\ 0 & f_2/f_1 \end{pmatrix} \tag{5.4}$$

In practice, the setup of the expander and reducer lenses is more complex. The focal lengths and the drift lengths between the lenses need to be optimized to meet the following requirements:

1. The laser must propagate parallel after emerging from the expander/reducer and pass through the center of mirrors all the way to the focal lens. An angular error when injecting into the lens leads to profile imbalance between the two paths at the IP.

2. The laser spot size must be adjusted as not to cause damage to optical components due to high laser intensity (also see Appendix C).

3. The laser must be focused at the IP to a spot size small enough for a sufficient rate of Compton signal, while not too small as to cause too much laser pointing jitters.

Regarding 1, it is important not to strike the walls of the transport line. The magnification of the expander should be maximized within this limit. The diameter of the transport line is about 100 mm, while the typical laser spot diameter emerging from the laser source is about 10 mm. Therefore, there is a tolerance of about a factor of 5 even after a two-fold magnification.

Propagation through the focal lens

The propagation of the laser beam from the focal lens entrance to the IP can be expressed using $F(f) = \begin{pmatrix} 1 & 0 \\ -1/f & 1 \end{pmatrix}$ for the focusing due to a thin lens of focal length f, followed by $D(f) = \begin{pmatrix} 1 & f \\ 0 & 1 \end{pmatrix}$ for a drift space of length f until the IP as:

$$\begin{pmatrix} r_2 \\ r_2' \end{pmatrix} = \begin{pmatrix} 1 & f \\ 0 & 1 \end{pmatrix} \begin{pmatrix} 1 & 0 \\ -1/f & 1 \end{pmatrix} \begin{pmatrix} r_1 \\ r_1' \end{pmatrix} \tag{5.5}$$

From Eq. 5.5, we obtain:

$$r_2 = f \cdot r_1' \tag{5.6}$$

Equation 5.6 indicates that the position offset at the IP is determined by the initial angular error when injecting into the lens, whereas initial position offset has no effect. Therefore it is important for the laser to propagate parallel from the reducer exit to the focal lens. Otherwise there would be an insufficiently focused laser and/or profile imbalance between the upper and lower paths. However these can be compensated by conducting the focal lens scan for each path (see Sec. 4.2.3).

5.1.2 Laser Focusing at the IP

It is important to focus the laser to a small waist size in order to realize sufficiently high laser intensity for generating Compton signal and maintaining a high S/N ratio. One quantitative measure of whether the laser spot size can be focused sufficiently at the IP is the "M^2 factor"; it defines the deviation of the actual beam from an ideal Gaussian beam (i.e. $M^2 = 1$). The waist size at the IP ω_0 ($= 2 \times \sigma_{t,laser}$ [20]) depends on M^2, the lens's focal length (f), and the spot size injected into the lens (ω_i) as:

$$\omega_0 = \frac{\lambda f M^2}{\pi \omega_i} \tag{5.7}$$

The laser spot size can be expressed as a function of the coordinate in the laser propagation direction (z) w.r.t. the waist position (z_0) as:

$$\omega(z) = \omega_0 \sqrt{1 + \left\{ \frac{M^2 \lambda (z - z_0)}{\pi \omega_0^2} \right\}^2} = \omega_0 \sqrt{1 + \left(\frac{z - z_0}{z_R} \right)^2} \tag{5.8}$$

---

[20]The laser spot radius ω, defined as the width at which intensity falls to $1/e^2$ of the peak, is the parameter typically used in optical calculations. For a perfect Gaussian beam of sigma σ, the beam radius is $\omega = 2\sigma$, and the beam diameter is $2\omega = 4\sigma$.

Here the Rayleigh length z_R, defined as the distance over which $\omega(z)$ increases by a factor of $\sqrt{2}$, is expressed as:

$$z_R \equiv \frac{\pi \omega_0^2}{M^2 \lambda} \tag{5.9}$$

A larger M^2 indicates more sudden focusing, i.e. $\omega(z)$ changes at a faster rate with distance z. This is understandable from the fact that the beam divergence $\Theta = \omega_0 z_R = \frac{\lambda M^2}{\pi \omega_0}$ is proportional to M^2. Figure 5.1 shows the dependence of laser beam divergence on M^2.

In reality ω_i can be adjusted using reducer lens setup. The initial spot size immediately before the focal lens was observed to be $\omega_i \sim 2.5$ mm in 2014 spring (see Sec. 5.2). If we assume a perfect Gaussian profile ($M^2 = 1$) and parallel injection into the focal lens with $\omega_i = 2.5$ mm, the waist size at the IP is calculated to be:

$$\omega_0 = \frac{\lambda f}{\pi \omega_i} = \begin{cases} 16.9\,\mu\text{m}: & 2 - 8\,\text{deg}, 174\,\text{deg}\ (f = 250\,\text{mm}) \\ 20.3\,\mu\text{m}: & 30\,\text{deg}\ (f = 300\,\text{mm}) \end{cases} \tag{5.10}$$

Using the focal lens scan shown in Fig. 4.8 (Sec. 4.2.3), M^2 is evaluated as follows. The waist spot size ω_0 is measured to be $25.9 \pm 2.2\ \mu$m (at $z_0 = 6$ mm). Using this, the observed $\omega_i = 2.5$ mm, and Eq. 5.7, M^2 is calculated to be 1.5 ± 0.1. The Rayleigh length z_R is calculated using Eq. 5.9 to be 2.6 ± 0.2 mm, which is approximately consistent with the distance observed in Fig. 4.8 over which ω increases by a factor of $\sqrt{2}$. For this measurement, $\sigma_{t,laser}$ at the waist is $= 13.0 \pm 1.1\ \mu$m. The $\sigma_{t,laser}$ inferred from laser wire scans in 2014 is typically 10-15 μm. From Sec. 3.6.1, the number of Compton signal photons (N_{sig}) is proportional to the inverse of $\sigma_{t,laser}$. At the low e$^-$ bunch charge of $N_e = 1 \times 10^9$, $\sigma_{t,laser}$ should be focused to $< 16\ \mu$m in order to obtain sufficient N_{sig} to suppress the statistical errors due to photon statistics to $< 7\%$. The typical $\sigma_{t,laser}$ meets this expectation. In reality, $\sigma_{t,laser}$ varies with occasional slight adjustments of the focal lenses or the reducer lenses. In 2014 spring, the reducer lenses were adjusted as to yield a very relaxed focusing; a smaller spot (ω_i) was injected into the lens in order to realize a larger waist size so as to mitigate effects from laser pointing jitter. The resulting long z_R serves to reduce the bias from wave-front effects (see Sec. 6.8).
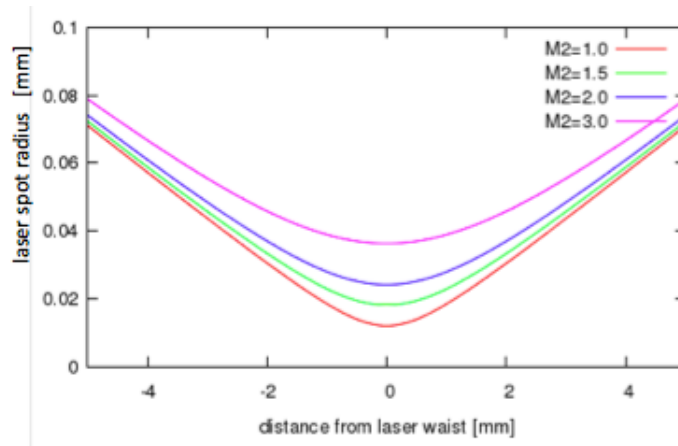

Figure 5.1: Dependence of laser beam divergence on M^2 factor.

5.2 Laser Profile

The spatial laser beam profiles are measured using profile monitors consisting of CCD cameras, lenses, and targets (Fig. 5.2). The CCD camera (JAI, CM-030GE) has 640 (H) ×480 (V) pixels and pixel size 7.4μm × 7.4 μm. It monitors a laser image formed by shining weakened laser light (transmitted from a mirror) upon a paper target. This method is more convenient in terms of visible range given the frequent adjustments of the laser spot size and/or position, as opposed to injecting light directly into the camera lenses.

Figure 5.3 shows images of the laser profiles measured before the expander lenses (left), in the injection line on the vertical table (middle), and next to the most downstream mirror in the 174 deg lower path (right). Round and concentric Gaussian profiles are observed on the laser table. However, after the transportation ($\sim$20 m) to the vertical table, the profile becomes triangular and shows multi-mode characteristics. The causes for the degraded spatial profile are still under investigation. One possibility is that the laser wavefronts become distorted due to complications during the amplification process[21]. The distortion become noticeable after the propagation of each of the higher order modes through multiple mirrors and lenses from the laser source to the vertical table. The multi-components are indicated by the occasionally observed two-peak structure in the laser wire profile. Also, it becomes difficult to overlap the profiles of the two laser paths by z-scan if the focal points in their multi-components differ. These factors affect the peak search precision in laser wire scans and z-scans, and thus lead to fringe contrast reduction due to laser position misalignment. In addition, the interference of multiple transverse modes in the laser profile may lead to further distorted laser wavefronts at the IP.

In the past, the laser wavefronts on the vertical table had been measured using a Shack-Hartmann wavefront sensor (see Thorlabs manual [37]), which measures the deviations from a reference wavefront. The incoming laser beam is divided by a lenslet array into several smaller beams. Each smaller beam is then imaged by a CCD camera placed at the focal plane of the lenslet array. For the case of a uniform plane wave incident on the sensor, a regularly spaced grid of focused spots are formed in the focal plane. For the case of a distorted wavefront, the focused spots are displaced from the optical axis, thus yielding a disrupted formation on the grid. The wavefront can then be reconstructed from the spot displacement information since each spot centroid is proportional to the local wavefront slope at a single lenslet. The measured results[25] indicate neither significantly uneven spot distribution on the grid, nor significantly distortion of the reconstructed wavefronts. However, this measurement was only conducted on the optical tables i.e. the near-field. It is necessary to also conduct it at various other locations, including in the transport line i.e. the far-field. Furthermore, it is suspected that the laser spots size at the time of the measurements may have been slightly too large to fit completely into the camera lens. Thus it is not possible to draw a reliable conclusion about the laser wavefronts from these results. Future measurements need to be conducted in a more systematic method and with better resolution.

The following improvements have been made to improve the quality of the laser profile. A part of these also served to reduce signal jitters and drifts:

- In order to lighten the effect of laser pointing jitters at the IP: (a) the spot size at the focal point was enlarged by injecting a smaller spot size into the focal lens; (b) the reducer lenses were adjusted to realize a longer Rayleigh length i.e. a more relaxed focusing. This appeared to smooth out some of the higher order mode components in the profile.

- In order to reduce profile fluctuation: (a) a window was inserted in the laser transport to reduce air flow; (b) an iris was used on the laser table to clip the outer part of the profile

---

[21]Other possible causes include the offset of the optical axis between the main laser and the seed laser, and either the aging or slight damage of the seed laser and/or main laser YAG rod.

which fluctuates more apparently. After these efforts, the fluctuation of the profiles w.r.t. a fixed reference marker was observed to be $< 5\%$ of the laser spot diameter in all locations.

- The laser spatial profile was tuned by adjusting the angles of the rear mirrors in the laser cavity (also see Sec. 3.2.1). This optimized the angle of the laser passing through the components of the cavity. As a result, the profile emerging from the laser source became rounder and more concentric, and its intensity bias ("hot spots") were reduced.

The laser profile is also observed by the eye at various locations such as by using a concentric paper target to roughly measure the laser spot size. Figure 5.4 shows some examples from April-June of 2014. During this period, the expander lenses had focal lengths f_1 = -150 mm (concave) and f_2 = 350 mm (convex), while the reducer lenses had f_1 = 450 mm (convex) and f_2 = - 150 mm (concave). From this, the magnification by the expander of $|f_2/f_1|$ = 2.3 times followed by the demagnification by the reducer of $|f_2/f_1|$ = 3 times should give a net demagnification of 1.3 times for the spot size injected into the focal lenses. From actual observations, the laser spot diameter before and after the expander were 8 mm and 16 mm, respectively; the diameter of ovalish profile before and after the reducer were 15×17 mm and 5×6 mm, respectively. These direct spot size observations are consistent with the (de)magnification calculated from the focal lengths. The spot size was observed to be preserved all the way from the reducer exit to the focal lens, which indicates parallel propagation.
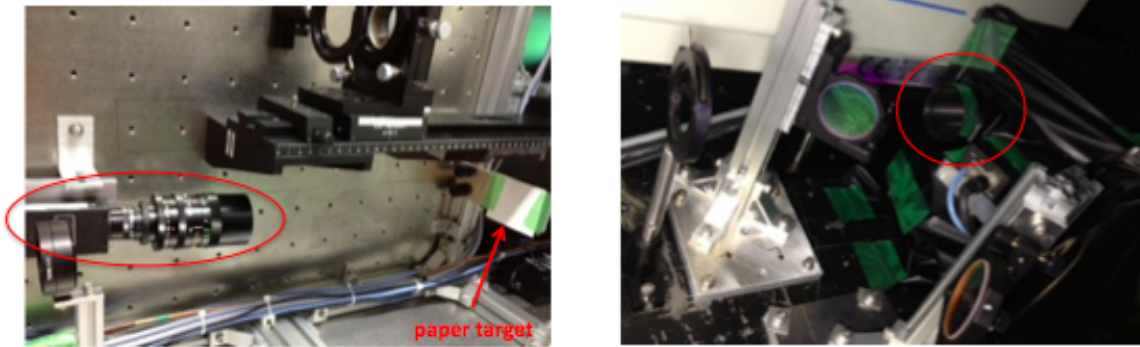
Figure 5.2: Examples of laser profile monitors (circled in red), consisting of CCD cameras and lenses (left) just after injection onto the vertical table (right) at one end of the laser table (surrounded by black-out shading)
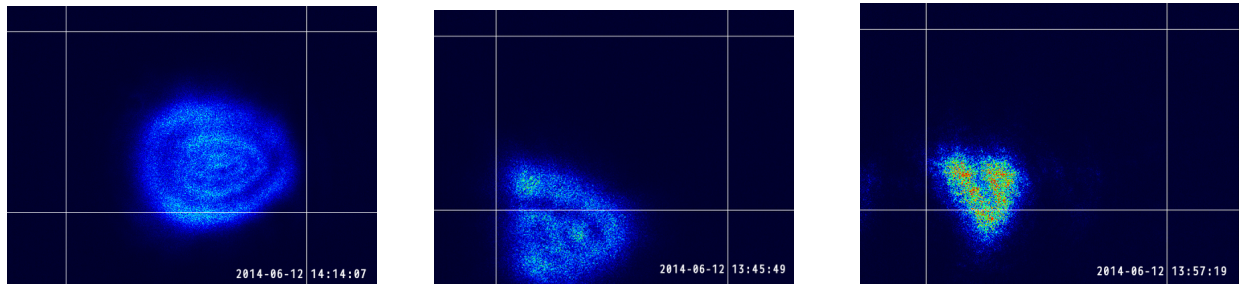
Figure 5.3: Images of laser profile monitored by CCD cameras just in front of the expander lenses on the laser table (left) vertical table , injection line (middle) vertical table, at the mirror M174L closes to the 174 deg mode lower path focal lenses (right). The concentric circular structure can be interpreted as Fraunhofer diffraction.

Figure 5.4: Images of laser profile observed with the eye by shining the laser light on a thin paper, at various locations on the laser table and vertical table. : From left to right: just before expander, just after expander, at an intermediate mirror (M3), at the focal lens of the 30 deg mode upper path.

5.3   Laser Pointing Jitter

Relative position jitter between the laser beam and the e$^-$ beam at the IP causes signal jitters. This section evaluates horizontal relative position jitter ($\sigma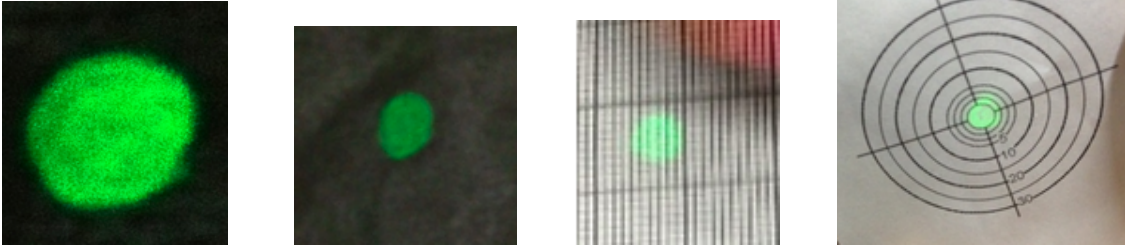_{\Delta x}$) and laser pointing jitter using the upper path laser wire scan shown in Fig. 5.5, which was taken in the 174 deg mode. To improve analysis precision, $N_{av} = 50$ pulses were measured at each mirror position (x), whereas N_{av}=3-5 are measured for the typical alignment.

Using Eq. 4.7, the contribution from $\sigma_{\Delta x}$ to the energy jitter can be expressed in first order approximation as :

$$\Delta E_{rel}(x) = \frac{d}{dx}\left(E_0 \exp\left(-\frac{(x-x_0)^2}{2\sigma_{lw}^2}\right)\right)\sigma_{\Delta x} = -\frac{E_0(x-x_0)\sigma_{\Delta x}}{\sigma_{lw}^2}\exp\left(-\frac{(x-x_0)^2}{2\sigma_{lw}^2}\right) \quad (5.11)$$

Therefore, the relative signal jitter due to relative position jitter $\sigma_{\Delta x}$ at an offset of $|x - x_0|$ away from the laser wire peak position (x_0) is :

$$\left|\frac{\Delta E_{rel}(x)}{E(x)}\right| = \left|\frac{x-x_0}{\sigma_{lw}^2}\right| \cdot \sigma_{\Delta x} \quad (5.12)$$

For example, the jitter expected at 1 sigma from the laser wire scan peak is $\sigma_{\Delta x}/\sigma_{lw}$. Assuming a Gaussian laser wire profile, $\sigma_{\Delta x}$ is derived by the following process: the energy jitter i.e. the standard deviation of the N_{av} is plotted as a function of mirror position (x) (Fig. 5.6), then fitted by a model written as:

$$\Delta E(x) = \sqrt{\Delta E_V^2(x) + \Delta E_{rel}^2(x)} \quad (5.13)$$

Equation 5.13 assumes that ΔE is a convolution of ΔE_{rel} and vertical jitters ΔE_V. Vertical jitter is modeled as :

$$\Delta E_V(x) = \sqrt{C_{const}^2 + \left(C_{stat}\sqrt{E(x)}\right)^2 + (C_{linear}E(x))^2} \quad (5.14)$$

Each component in Eq. 5.14 will be explained in Sec. 7.1. Here, $\sigma_{\Delta x}$, C_{const} and C_{linear} are free parameters, while C_{stat} is fixed according to detector calibration results (see Sec. 7.3). Table 5.1 displays the relevant parameters obtained from fitting, as well as parameters calculated using these.

The laser wire scan sigma σ_{lw} is obtained from the fit in Fig. 5.5. The horizontal e$^-$ beam size σ_x is measured by wire scanner to be 9.1 ± 0.2 μm . Inserting the measured σ_x and σ_{lw} into Eq. 4.8, laser spot size $\sigma_{t,laser}$ is calculated to be 12.2 ± 0.2 μm.

For this data, the horizontal relative position jitter $\sigma_{\Delta x}$ is obtained from the fit in Fig. 5.6 to be $2.4 \pm 0.8\,\mu m$. By subtracting horizontal e^- beam jitter (assumed to be 15% of σ_x[38]) in quadrature from $\sigma_{\Delta x}$, the pointing jitter of the laser only is estimated to be $\sigma_{\Delta x,laser} = 2.0 \pm 0.9\,\mu m$, which is 16 ± 8 % of the laser spot sigma $\sigma_{t,laser}$ [22].

	from laser wire scan (Fig. 5.5)	from jitter plot (Fig. 5.6)
σ_{lw}	$15.2 \pm 0.3\ \mu m$	
$\sigma_{t,laser}$	$12.2 \pm 0.2\ \mu m$	
$\sigma_{\Delta x}$		$2.4 \pm 0.8\ \mu m$
$\sigma_{\Delta x,laser}$		$2.0 \pm 0.9\ \mu m$
$\sigma_{\Delta x}/\sigma_{lw}$		16 ± 5 %
$\sigma_{\Delta x,laser}/\sigma_{t,laser}$		16 ± 8 %

Table 5.1: The analysis results for horizontal relative position jitter and laser pointing jitter.
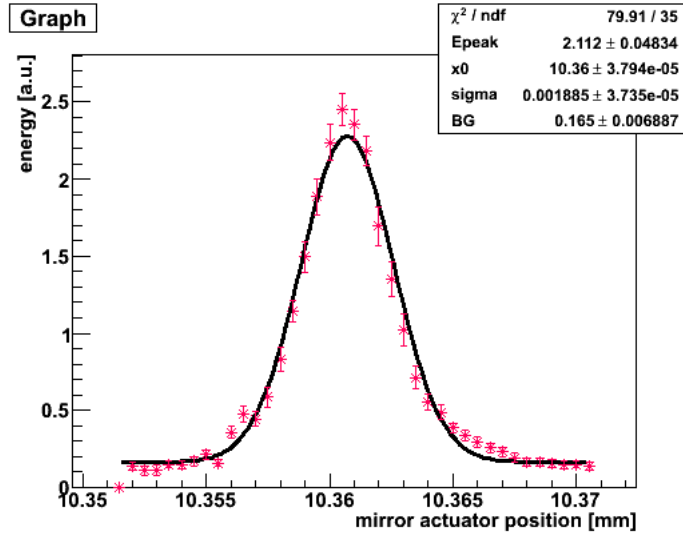
Figure 5.5: A laser wire scan using the upper laser path in the 174 deg mode. The horizontal axis is the position of the mirror M174U being scanned. The vertical axis is the statistical results of the 50 pulses measured at each position of the mirror M174U being scanned. This is fitted with Eq. 4.7 to obtain the peak height and position, and the sigma of the Gaussian-like profile.

---

[22]This is approximately consistent with the laser profile fluctuation observed using CCD cameras upstream of the IP (in Sec. 5.2).
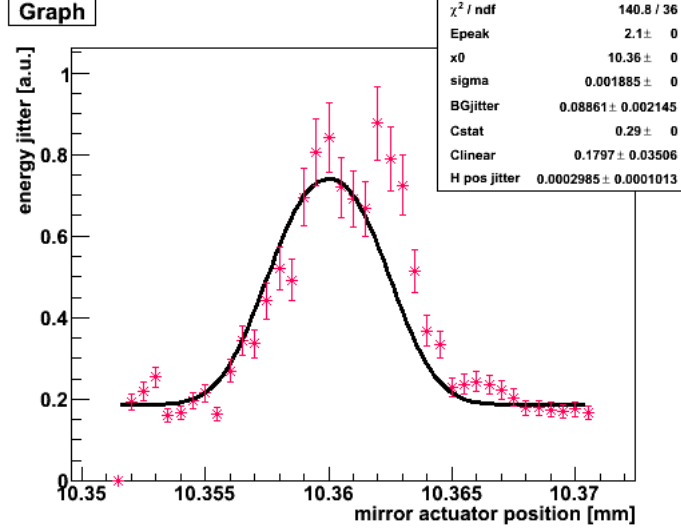
Figure 5.6: The plot used for deriving horizontal relative position jitter using the laser wire scan in Fig. 5.5. The horizontal axis denotes the mirror position being scanned. The vertical axis is the signal jitter, i.e. standard deviation of the 50 pulses measured at each mirror position. This is fitted with Eq. 5.13 to obtain the horizontal position jitter.

5.4 Laser Polarization

The Shintake Monitor optics is designed for purely linearly S polarized laser. Any deviation from this will cause M reduction. This is because the half mirror has a design reflectivity of 50% for S polarized light, thus any "contamination" from elliptical P components will lead to intensity imbalance between the upper and lower paths. P components can mix in through the transportation to the vertical table. Section6.5 explains the M reduction due to polarization and power imbalance [23].

5.4.1 Polarization Measurement

The results of laser polarization measurement indicated the laser to be very close to pure S state. The setup is shown in Fig. 5.7. The location is just after injection onto the vertical table at the IP, at the label "polarizer" in Fig. 3.14 (top)). The polarization of the laser is rotated by a half lambda ($\lambda/2$) plate over a full 360 deg range in fine steps. Rotating the $\lambda/2$ plate introduces a phase shift between the horizontal and vertical electric electric field components. Downstream of this a beamsplitter reflects the S light component upwards into a power meter to be measured, while transmitting the P light component. The $\lambda/2$ plate (rotator: Sigma Koki, SGSP-80YAW) and the beam splitter (Sigma Koki, PBSHP-20-5320) are shown in Fig. 5.8. The power meter (VEGA Ophir Photonics) is shown in Fig. 5.9.

Polarization can be explained using Jones matrix as follows[39]: Assuming light propagates in the z direction, the x (y) components of its electric field, with phase $\phi_{x(y)}$ and amplitude $E_{x0(y0)}$, respectively, are expressed as :

$$\begin{pmatrix} E'_x(t) \\ E'_y(t) \end{pmatrix} = \exp\{i(kz - \omega t)\} \begin{pmatrix} E_{x0}\exp(i\phi_x) \\ E_{y0}\exp(i\phi_y) \end{pmatrix} \tag{5.15}$$

---

[23]On the optical table, polarization is defined with respect to the surfaces of optical components. Therefore special care is taken to align all mirrors.

Here, x and y represents the S and P polarization components, respectively. The phase difference $\phi \equiv |\phi_x - \phi_y|$ is 0 for a linear polarized laser, and $\pm\frac{\pi}{2}$ for a circularly polarized laser.

The Jones matrix for a $\lambda/2$ plate being rotated by θ is represented as $\begin{pmatrix} \cos 2\theta & -\sin 2\theta \\ \sin 2\theta & \cos 2\theta \end{pmatrix}$. The beamsplitter transmits S polarized light with the (1,0) component of its Jones matrix. Using these, the light propagation in Fig. 5.7 (left) can be expressed as:

$$\begin{pmatrix} E'_x(t) \\ E'_y(t) \end{pmatrix} = \begin{pmatrix} 1 & 0 \\ 0 & 0 \end{pmatrix} \begin{pmatrix} \cos 2\theta & -\sin 2\theta \\ \sin 2\theta & \cos 2\theta \end{pmatrix} \begin{pmatrix} E_x(t) \\ E_y(t) \end{pmatrix} \tag{5.16}$$

The optimum settings of the $\lambda/2$ plate which maximizes the ratio of S light will be referred to here as "S peaks". The measured cosine-like power spectrum (Fig. 5.11 (left)) is fitted by the following function:

$$P = \frac{P_0}{2}\left(1 + C_1 cos4\theta + C_2 sin4\theta\right) \tag{5.17}$$

The relationship between field amplitudes and total power is $P_0 = P_s + P_p = E_{x0}^2 + E_{y0}^2$ [$P_{s(p)}$: power of S (P) light]. P_0 is set to 1.12 ± 0.01 W, which is the average of the power measured at several "S-peaks" (0, 90, and 180 deg). The coefficients C_1 and C_2, to be obtained from fitting, are expressed as a function of field amplitudes and ϕ as the following:

$$C_1 = \frac{E_{x0}^2 - E_{y0}^2}{E_{x0}^2 + E_{y0}^2} = \frac{P_s - P_p}{P_s + P_p} = \cos 2\chi \tag{5.18}$$

$$C_2 = \cos\phi \frac{2E_{x0}E_{y0}}{E_{x0}^2 + E_{y0}^2} = \cos\phi \frac{2\sqrt{P_s P_p}}{P_s + P_p} = \cos\phi \sin 2\chi \tag{5.19}$$

Here, the eccentricity χ is defined as the ratio between the long and short axis of the polarization ellipse as:

$$\tan\chi = \frac{E_{y0}}{E_{x0}} = \sqrt{\frac{P_p}{P_s}} \tag{5.20}$$

Table 5.2 shows the fitted results for C_1 and C_2 and using these, the results calculated for ϕ, P_p/P_s, and χ. The small eccentricity angle $\chi = 6.9\pm0.1$ deg and "P contamination" $P_p/P_s < 1.5$ % indicate the laser to be very close to pure S linear polarization [24]. The "S peaks" angles of the $\lambda/2$ plate were cross-checked by confirming that they yield the best power balance. The power of each path was measured as a function of $\lambda/2$ plate rotation angle immediately before the focal lenses (see Fig. 5.10). Additionally, the reflectivity of the 50% beam splitter was measured to be $R_s = 50.3\%$ for S light, well within catalog specifications. $R_p = 20.1\%$ was measured for P light. By setting the $\lambda/2$ plate to the "S peak" angles, any residual P components are prevents from entering the half mirror, thereby eliminating nearly all polarization related systematic errors. This is demonstrated in Sec. 6.5 using beam time fringe scans in which M is maximized while scanning $\lambda/2$ plate angle over a wide range.

Before the above-mentioned measurements, a calibration linking the set values of the rotation angles of the $\lambda/2$ plate and its controller (Sigma Koki, Shot204) was carried out. Figure 5.12 shows the satisfactorily linear relationship.

---

[24]It was confirmed that the lowest power values are well within measurable range of the power meter, and that sensitivity of the measurement is finer than 5 deg.

C_1	C_2	ϕ [deg]	P_p/P_s [%]	$\tan\chi$	χ [deg]
0.971± 0.001	0.013± 0.012	86.8±3.0	1.47±0.06	0.121±0.002	6.9±0.1

Table 5.2: The coefficients from Eq. 5.17 obtained from the fitting of the measured polarization spectrum in Fig. 5.11 and the phase shift and P_p/P_s calculated from these.
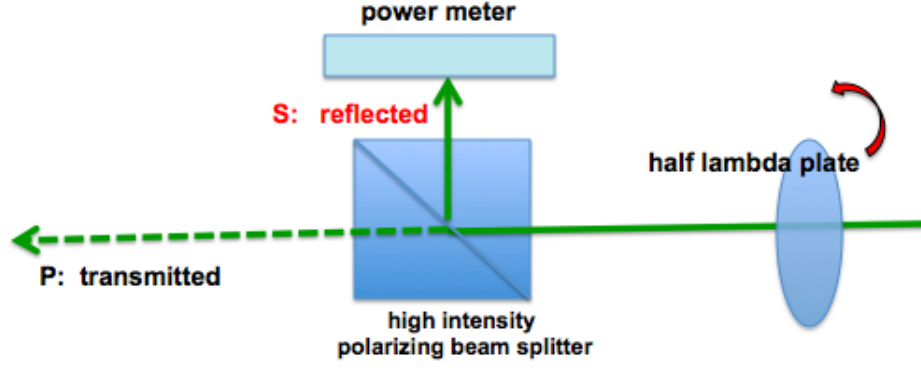
Figure 5.7: Setup for measurement of laser polarization.
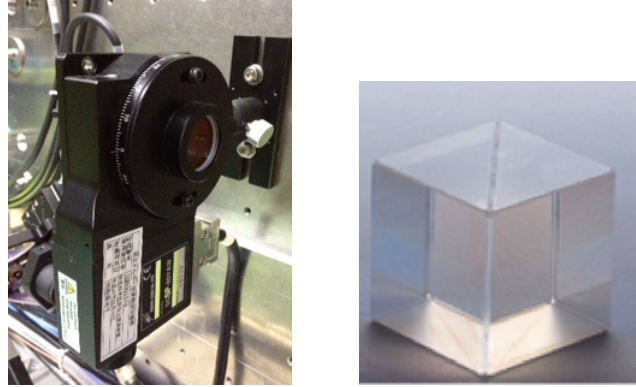

Figure 5.8: (left) The half lambda plate which rotates the polarization state of the laser. (right) The beam splitter for high intensity laser which reflects S light.

Figure 5.9: (left) The power meter (VEGA, Ophir Photonics) used for measuring total laser power. (right) The sensor attached to the power meter.
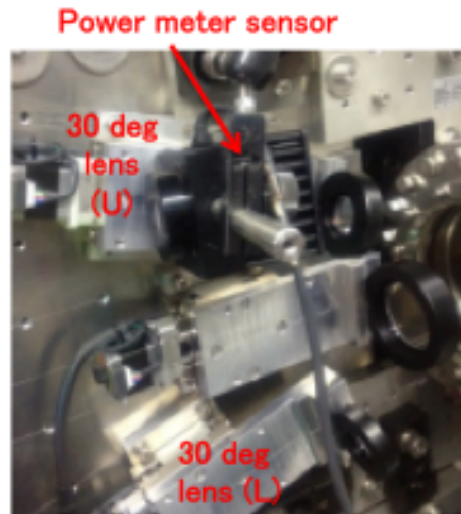

Figure 5.10: Setup for laser power measurement before the focal lenses.
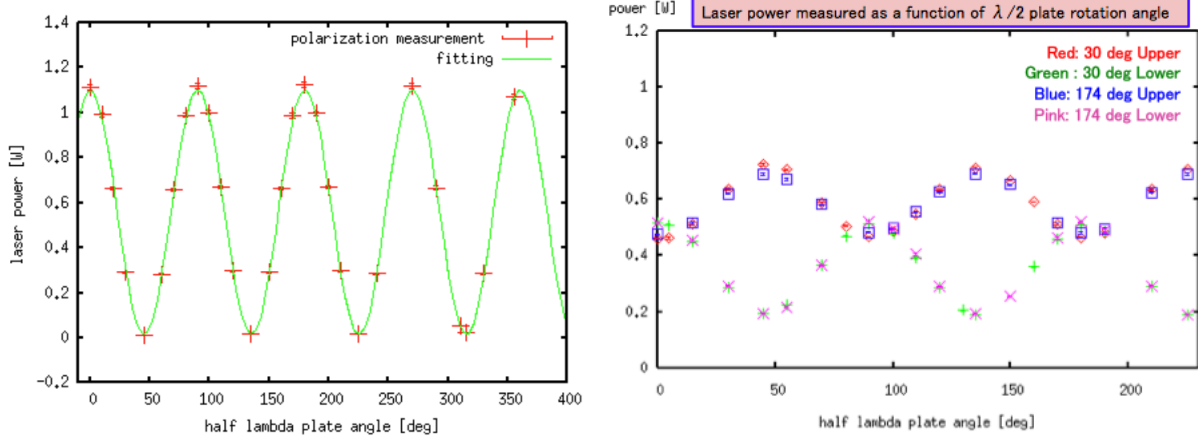
Figure 5.11: (left) laser power spectrum measured as a function of rotated angle of the $\lambda/2$ plate using the setup in Fig. 5.7: Plotted here are the average of 5 points for each step with error bars assuming 1% design resolution of the power meter sensor. The fitted result shows the laser to be very close to S linear polarization. (right) Laser power measured using the setup in Fig. 5.9. This shows that the optimum $\lambda/2$ plate setting, "S peaks" yields the best power balance between the upper and lower laser paths for both 30 deg and 174 deg modes. Meanwhile the "P peak" settings yield the worst balance
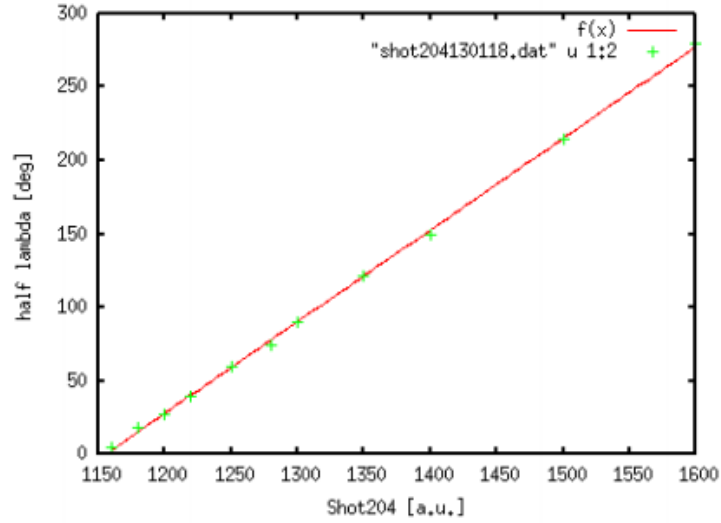
Figure 5.12: The linear relationship resulting from the calibration between $\lambda/2$ plate rotation angle (vertical axis [a.u.]) and set value of its controller Shot204 (Sigma Koki) (horizontal axis).

5.5 Laser Power

The power of the laser was measured using the power meter in Fig. 5.9 in the following locations:

- In the 174 deg mode upper path (174 U), immediately in front of the focal lens

- In the 174 deg mode lower path (174 L), immediately in front of the focal lens

- Before dividing up into two paths on the vertical table, just after the $\lambda/2$ plate in the injection line

96

- On the laser table, before the expander

These measurements were all done within about two hours in 2014 spring when the Shintake Monitor was stably measuring $\sigma_y < 60$ nm. The e$^-$ beam was turned off. The results are shown as histograms in Fig. 5.13 and in the table below. These values are the mean and RMS of 20-30 events read out at each location.

location	174 U	174 L	vertical table	laser table
power [W] (mean±RMS)	0.356±0.002	0.357±0.003	0.799±0.004	0.857±0.005
power jitter = RMS/mean	0.5%	0.8%	0.5%	0.6%

The following observations are made based on the results:

1. The power balance between the upper and lower paths of the 174 deg mode is $P_U/P_L = 95\pm1\%$. This result is important for the analysis of systematic errors in fringe scans (see Sec. 6.6).

2. The power jitter is $< 1\%$.

3. The power retained after transport to the vertical table is 93±1%.

4. The sum of the power measured for the upper and lower paths is 91±1% of the power measured in the injection line.

Some possible causes of the power loss in 3. and 4. are the non-ideal reflectivity (R) of mirrors and/or the non-ideal transmittance (T) of lenses. Under assumption of the design R∼99% and T∼90% for the 6 mirrors and 4 lenses respectively between the measuremet locations on the laser table and the vertical table, the power loss is calculated to be about 10%. Similarly, for the 11 contacts with optical components in each path from the injection line to the focal lens, the power loss is calculated to be about 11%.
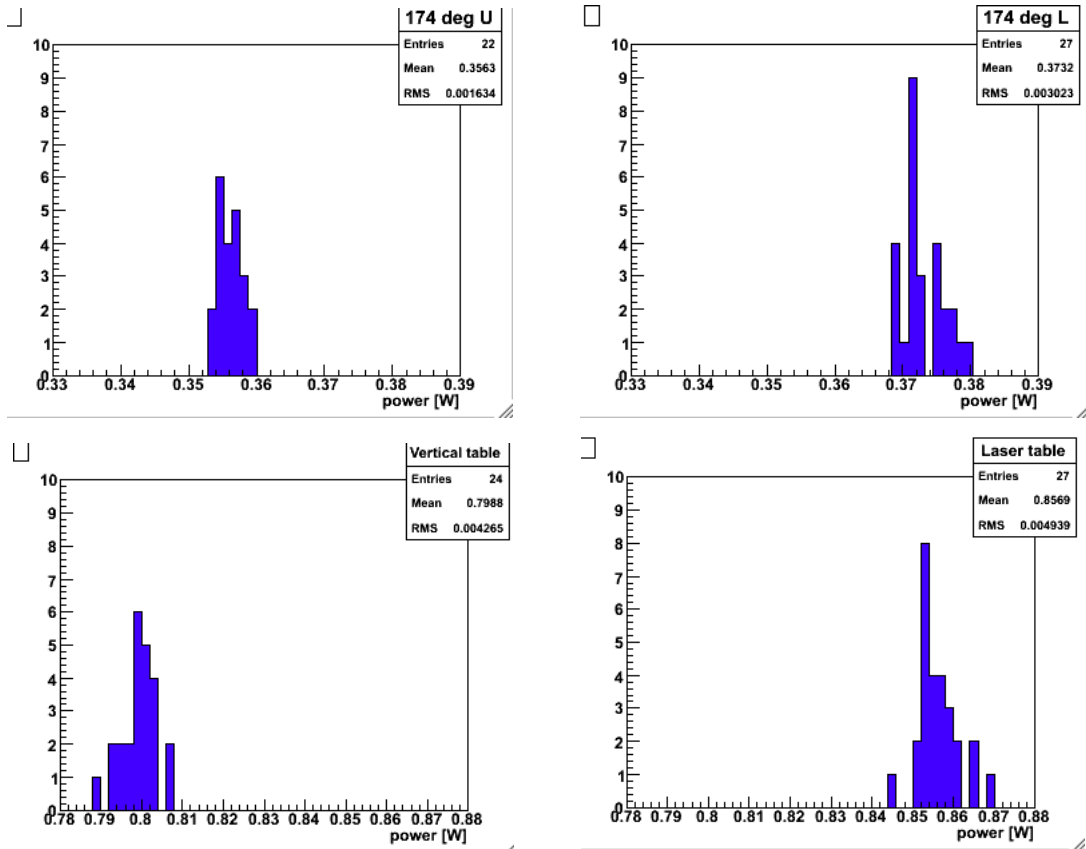
Figure 5.13: Results of power measurement at various locations in the laser optics: Clockwise from top left: 174 deg mode upper path, 174 deg mode lower path, vertical table injection line, laser table. The values in these histograms are read out consecutively by the eye with intervals of 1-2 s from the display panel of the power meter shown in Fig. 5.9.

6   Modulation Reduction Factors

The systematic errors on the measured beam size are interpreted using "modulation reduction factors". These smear the fringe contrast and cause the measured M (M_{meas}) to be smaller than the ideal M:

$$M_{meas} = \left(\prod_i C_i \right) M_{ideal} = C_{total} M_{ideal} \tag{6.1}$$

Here C_i represents the individual M reduction factors. This bias leads to an over-evaluation of the measured beam size $\sigma_{y,meas}$ as:

$$\sigma_{y,meas}^2 = \sigma_{y,ideal}^2 + \frac{1}{2k_y^2} \left| \sum \ln C_i \right| \tag{6.2}$$

Most M reduction factors are laser-related, due to its alignment, profile, power, and polarization. There are also some factors related to the e^- beam position. These will be described in the following subsections, and summarized in Chap. 8.1. Details can also be found in [40][41]. The first priority should be to suppress error sources by improving hardware and/or alignment methods. Then residual systematic errors can be evaluated offline to the best precision possible in order to approach an estimate of the true beam size.

6.1   Methods to Evaluate Modulation Reduction

The correction of $\sigma_{y,meas}$ requires the estimation of the total M reduction factor C_{total}. This can be done using the following two methods:

1. Each individual bias source is quantitatively evaluated, then C_{total} is calculated as their product: $C_{total} \equiv \prod_i C_i$.

2. The total M reduction for a particular θ mode is observed by comparing the inconsistency in $\sigma_{y,meas}$ immediately before and after mode switching.

Method 1 is difficult because for some types of C_i, only the lower limits (i.e. the worst scenario) can be obtained from the available data [25]. In some cases, a theoretical estimation is made based on realistic assumptions and/or simulation.

Regarding Method 2., the σ_y has to be within the measurable range for both the higher and lower θ mode. The fringe contrast at the lower θ mode would have to be clear enough to measure a very large M close to the resolution limit. For example, when comparing results between the 30 deg and 174 deg modes, σ_y must be focused down to $\lesssim 90$ nm in the 30 deg mode in order to be able to detect modulation after switching to the 174 deg mode. Assume that the M measured immediately before mode switching reaches only 0.6, despite that theoretically $\sigma_y = 90$ nm corresponding theoretically to $M = 0.74$ in the 30 deg mode (from Eq. 2.8). This inconsistency indicates a $C_{total} \sim 80\%$ for the 30 deg mode. However, this C_{total} cannot be applied universally to any θ mode because some systematic errors are mode dependent and/or vary over time. After subtracting the effects of mode dependent factors, the residual M reduction due to the common factors can be compared between the two modes. The following Sec. 6.2 shows a detailed example of such a study.

The evaluation of systematic errors is very complex. Nevertheless, the merit of using the Shintake Monitor in beam focusing is that we can observe the relative changes in M (σ_y) regardless of M reduction, provided that e^- beam conditions remain stable.

---

[25]Since multiple types of bias affect M_{meas} at once, it is difficult to single out each type .

6.2 Measurement of Total Modulation Reduction

This section gives an example of the estimation of the total M reduction factor C_{total} using consecutive $N_{av} = 50$ fringe scans immediately before and after switching from 174 deg to 30 deg mode. This study of about 1 hour was conducted under constant condition of the e$^-$ beam and Shintake Monitor setup. M was measured continuously three times in the 174 deg mode, which resulted in $M_{meas} = 0.285 \pm 0.025$ (stat.). After switching to the 30 deg mode, M was again measured continuously three times, which resulted in $M_{meas} = 0.765 \pm 0.006$ (stat.).

Table 6.1 shows the most important M reduction factors evaluated for each mode: C_φ from phase jitter σ_φ (see Sections 6.3 and 7.4) and C_{align} related to laser position alignment (see Sec. 6.7). First, the total M reduction factors $C_{tot} \simeq C_\varphi \cdot C_{align}$ are evaluated independently for each mode as: $C_{tot}(174 \text{ deg}) > 0.655$ and $C_{tot}(30 \text{ deg}) > 0.932$. The apparent difference in C_{tot} is mainly due to σ_φ, which averaged at 0.792 ± 0.047 (stat.) rad for the 174 deg mode, in contrast to 0.265 ± 0.051 (stat.) rad for the 30 deg mode. Section 6.3.1 explains the mode dependence of σ_φ.

Next, the total M reduction for the 30 deg mode is derived using an alternative method, by comparing with the 174 deg mode results as follows:

1. By correcting for $C_{tot}(174 \text{ deg})$, the supposedly "true" M for 174 deg mode is $M_{corr} = M_{meas}/C_{tot} < 0.473$, which corresponds to $\sigma_{y,corr} > 51.6$ nm.

2. Assuming σ_y remains constant (since no beam tuning was conducted), the M expected for 30 deg mode is $M_{exp} < 0.824$.

3. Comparing the M_{exp} in 2. with the actually measured $M_{meas}(30 \text{ deg}) = 0.765 \pm 0.006$, the total M reduction is $C_{tot,exp} = M_{meas}(30 \text{ deg})/M_{exp} > 0.921$.

It can be seen that the worst limits for the indirectly obtained $C_{tot,exp}$ in 3 and the directly estimated C_{tot} (30 deg) are almost the same; their discrepancy is about 1%. This is a demonstration of the precision in evaluating M reduction factors.

174 deg		30 deg	
M_{meas}	0.285 ± 0.025	M_{meas}	0.765 ± 0.006
σ_{meas}	66.9 ± 2.3 nm	σ_{meas}	81.3 ± 2.5 nm
σ_φ	0.792 ± 0.047 rad	σ_φ	0.265 ± 0.051 rad
C_φ	0.731 ± 0.027	C_φ	0.965 ± 0.014
C_{align}	> 0.93	C_{align}	> 0.98
$C_{tot}(174 \text{ deg})$	> 0.655	$C_{tot}(30 \text{ deg})$	> 0.932
M_{corr}	< 0.473	M_{exp}	< 0.824
σ_{corr}	> 51.6 nm	$C_{tot,exp}$	> 0.921

Table 6.1: The measured M and the dominant M reduction factors evaluated for consecutive fringe scans. The results are shown for 3 $N_{av} = 50$ scans before/after switching from the 174 deg mode to the 30 deg mode. The statistical errors are defined as the statistic standard deviation of the N scans divided by $\sqrt{N-1}$, whereas $N =$ the number of scans (in this case 3). These data were collected in Apr., 2014.

The following sections 6.3- 6.9 in this chapter describes and evaluates the individual M reduction factors affecting beam size measurement. These are related to fringe phase fluctuation, the rotation of the fringes and laser path misalignment w.r.t. the beam, laser polarization and power, the spherical laser wave-fronts, and the growth of within the fringes. For phase fluctuation, which is the dominant error source, Chap. 7 is added to provide further details.

6.3 Phase Related Systematic Errors

Because the study of phase fluctuation is one of the most important topics of this thesis, its description will be divided as follows: the following Sec. 6.3.1 introduces phase jitter, while Sec. 6.3.2 estimates the contribution to it from the laser optics. Section 6.3.3 shows the effect from slow phase drift. The following Chap. 7 demonstrates using simulation the precision of a method developed for extracting phase jitter from fringe scans, then applies it to analyzing actual beam time data.

6.3.1 Introduction of Phase jitter

Phase jitter can be interpreted as the relative vertical position jitter between the laser and the e^- beam at the IP. The relationship between the relative position jitter ($\delta\Delta y$) and the phase jitter (σ_φ) is:

$$\sigma_\varphi = 2k_y \cdot \delta\Delta y \tag{6.3}$$

Phase jitter is one of the dominant M reduction factors. Assuming Gaussian jitters, σ_φ reduces M_{meas} as $M_{meas} = M_0 \cdot C_\varphi$. Here, the M reduction factor due to σ_φ is expressed as:

$$C_\varphi = \exp\left(-\sigma_\varphi^2/2\right) = \exp\left(-2\left(k_y \cdot \delta\Delta y\right)^2\right) \tag{6.4}$$

This can be explained through the smearing of the amplitude of the cosine-like modulation curve as follows:

$$C_\varphi \cos\left(2k_y y + \varphi_0\right) = \int d\varphi \cdot \frac{1}{\sqrt{2\pi}\sigma_\varphi} \exp\left(-\frac{\varphi^2}{2\sigma_\varphi^2}\right) \cos\left(2k_y y + \varphi_0 + \varphi\right) \tag{6.5}$$

From the point of view of relative position jitter, the impact on the beam size is:

$$\sigma_{y,meas}^2 = \sigma_{y,0}^2 + \delta\Delta y^2 \tag{6.6}$$

Using the method described in Chap. 7, σ_φ can be extracted from fringe scan data and used to correct the measured M as:

$$M_{corr} = M_{meas}/C_\varphi \tag{6.7}$$

6.3.2 Causes of Phase Jitter

Phase jitter σ_φ (or relative position jitter $\delta\Delta y$) is the convolution of the laser fringe phase jitter and the vertical e^- beam jitter at the IP. It is difficult to distinguish which is dominant given the current lack of the means of independent measurement for either effect[26]. Electron beam jitter is mainly caused by the vibration of beam line magnets, especially the FD quadrupoles. The information from BPMs and FD vibration measurements indicate that the vertical beam jitter is generally $< 40\%$ of σ_y[38, 30]. Future precise measurements of IP beam position by the nm resolution "IPBPMs" under commissioning at ATF2 are anticipated[9, 10]. The laser fringe phase fluctuation (without the e^- beam) had been measured by T.Yamanaka in 2009[32] using a different laser from the current one and a previously installed phase monitor. The measured phase variation pattern is used for simulation in Sec. 7.5[27]. The controller of the piezo stage for fringe scan is ruled out from being a significant σ_φ factor since the jitter of its readout values is monitored, and has been confirmed to be < 40 mrad (see Fig. 6.1).

---

[26]If e^- beam jitter is dominant, real beam size growth issues may need to be addressed.

[27]There is no guarantee that this measured laser phase represents the current condition.
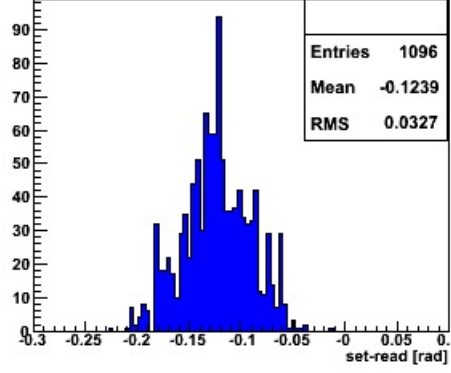
Figure 6.1: An example of the jitter of the piezo stage controller used for phase delay, monitored during a single fringe scan. The horizontal axis is (set value) - (read value) of the piezo controller. The jitter is typically < 40 mrad, thus does not contribute significantly to phase jitter.

The dominant cause of σ_φ related to the Shintake Monitor laser optics is thought to be the angular jitter of the laser (i.e. laser pointing jitter) when injecting into the half mirror. There may also be a small effect from the independent vibration of the mirrors in each path downstream of the half mirror. Assuming (a) a laser angular error of $\Delta\theta$ when injecting into the half mirror, and (b) the rotation $\Delta\Phi_j$ of each mirror "j" (j=1,..., n : n = number of mirrors downstream of the half mirror), the clockwise/counterclockwise angle change of the laser reflected from mirror j is $\theta_{0j} \to \theta_{0j} + 2\sum_{i=1}^{j} \Delta\Phi_i + \Delta\theta$. The schematics of this can be seen in Fig. 6.2. These change the length of each of the upper path ($L_U \to L_U + \Delta L_U$) and/or the lower path ($L_L \to L_L + \Delta L_L$) between the half mirror and the focal lenses. The phase in fringe scan is directly related to the "path length difference" $\Delta L = |L_U - L_L|$. The jitter ($\delta\Delta L$) of ΔL leads to phase jitter at the IP as [28]. :

$$\sigma_\varphi = k \cdot \delta\Delta L = \frac{2\pi \cdot}{\lambda} \delta\Delta L \tag{6.8}$$

---

[28]For the case when each path jitters completely incoherently by δl w.r.t. each other, $\delta\Delta L = \sqrt{2} \cdot \delta l$. Given the lack of a means for measuring the realistic mirror angular error, only a pessimistic estimation can be made as follows: for a pessimistic case of mirror actuator error $\Delta d < 0.0001$ mm (about $1/10 \times \sigma_{t,laser}$ at the IP), and given the rotational axis length $D = 61.9$ mm, the corresponding mirror angular error is $\Delta d/D \simeq 1.5$ μrad; this is still about an order smaller than laser angular jitter.
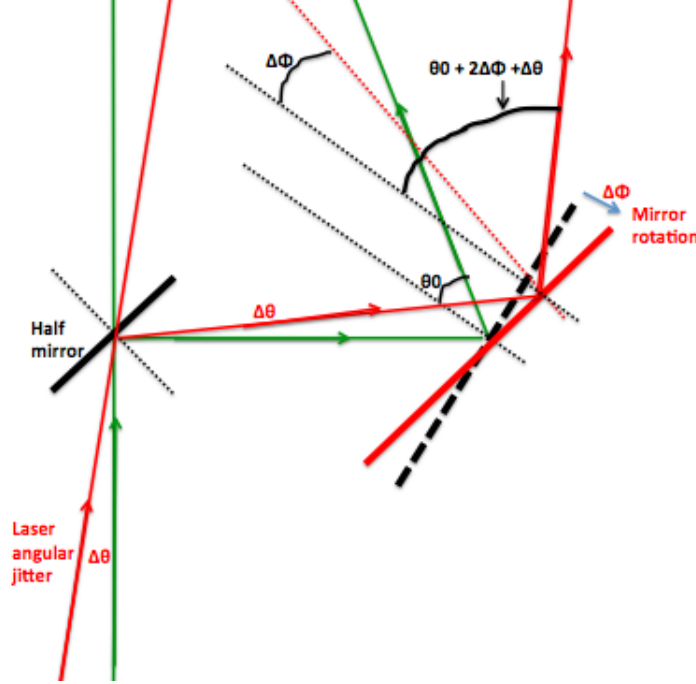
Figure 6.2: The schematics of a combination of (a) a laser angular error of $\Delta\theta$ when injecting into the half mirror, and (b) the rotation $\Delta\Phi$ of a mirror (downstream of the half mirror); the clockwise/counterclockwise angle change of the laser reflected from the mirror (red path) becomes $\theta_0 \rightarrow \theta_0 + 2\Delta\Phi + \Delta\theta$. The green path represents the nominal case i.e. neither laser angular error nor mirror rotation. Here, the injection position offset at the half mirror is ignored for simplicity.

Simulation of laser pointing jitter

Monte Carlo simulation is used to estimate the σ_φ due to laser angular jitter as in Eq. 6.8. Here, the optical components on the vertical table are placed according to the geometry shown in Fig. 3.14[29]. When entering the half mirror, the laser beam is given an angular jitter which follows a random Gaussian distribution i.e. $\Delta\theta = Gauss\,(0, \delta\Delta\theta)$, as well as a position offset in accordance to the actually observed laser profile fluctuation of $< 5\%$ of the profile radius (see Sec. 5.2). Figure 6.3 shows the simulation results of 10000 pseudo experiments for the 174 deg and 30 deg modes. The plot in Fig. 6.3 (top) shows the resulting σ_φ as a function of $\delta\Delta\theta$ which is changed as $\{10, 20, 25, 30, 40\}$ μrad. From catalog specifications, laser pointing jitter is below 25 μrad when the Beamlok is used for pointing stabilization[24]. Figure 6.3 (bottom) shows histograms of path length difference $\Delta L = |L_U - L_L|$ assuming $\delta\Delta\theta$=25 μrad, whose RMS values correspond to the path length jitter $\delta\Delta L$ in Eq. 6.8. For the 174 deg mode, $\delta\Delta L$ is 54 nm, corresponding to σ_φ=0.64 rad. For the 30 deg mode, $\delta\Delta L$ is 39 nm, corresponding to σ_φ=0.46 rad. These can be considered the worst limit for the σ_φ due to the laser optics.

Interpretation

For the same amount of laser pointing jitter, more σ_φ is generated for the 174 deg mode than for the 30 deg mode because of the difference in laser optics design. The total path length ($L_U \simeq L_L$)

---

[29]The path variation after focusing by the lens (with focal length f) is approximately $f\Delta\theta_{out}^2$, where the angular error after emerging from the lens is expressed as $\Delta\theta_{out} = \Delta\theta_{in} - \Delta x_{in}/f$, where $\Delta\theta_{in}$ and Δx_{in} are the incident angular and position error, respectively. This effect is negligibly small (about a few mrad) compared to the angular jitter of O(100) mrad from upstream.

downstream of the half mirror for the 174 deg mode (about 2000 mm) is longer than that of the 30 deg mode (about 1000 mm) by a factor of 2. In each of the upper and lower paths between the half mirror and the focal lenses, there are four mirrors for the 174 deg mode and three mirrors for the 30 deg mode.

The σ_φ resulting from simulation of the 174 deg mode is not significantly different from the phase variation of the previous Shintake Monitor laser measured by T. Yamanaka [32], which also used the 174 deg mode. However, note that the discussion in this section considers only the effect from the laser optics, whereas the phase jitter extracted from actual fringe scan data in Sec. 7.8 is a convolution of the laser fringe jitter and the e$^-$ beam jitter.
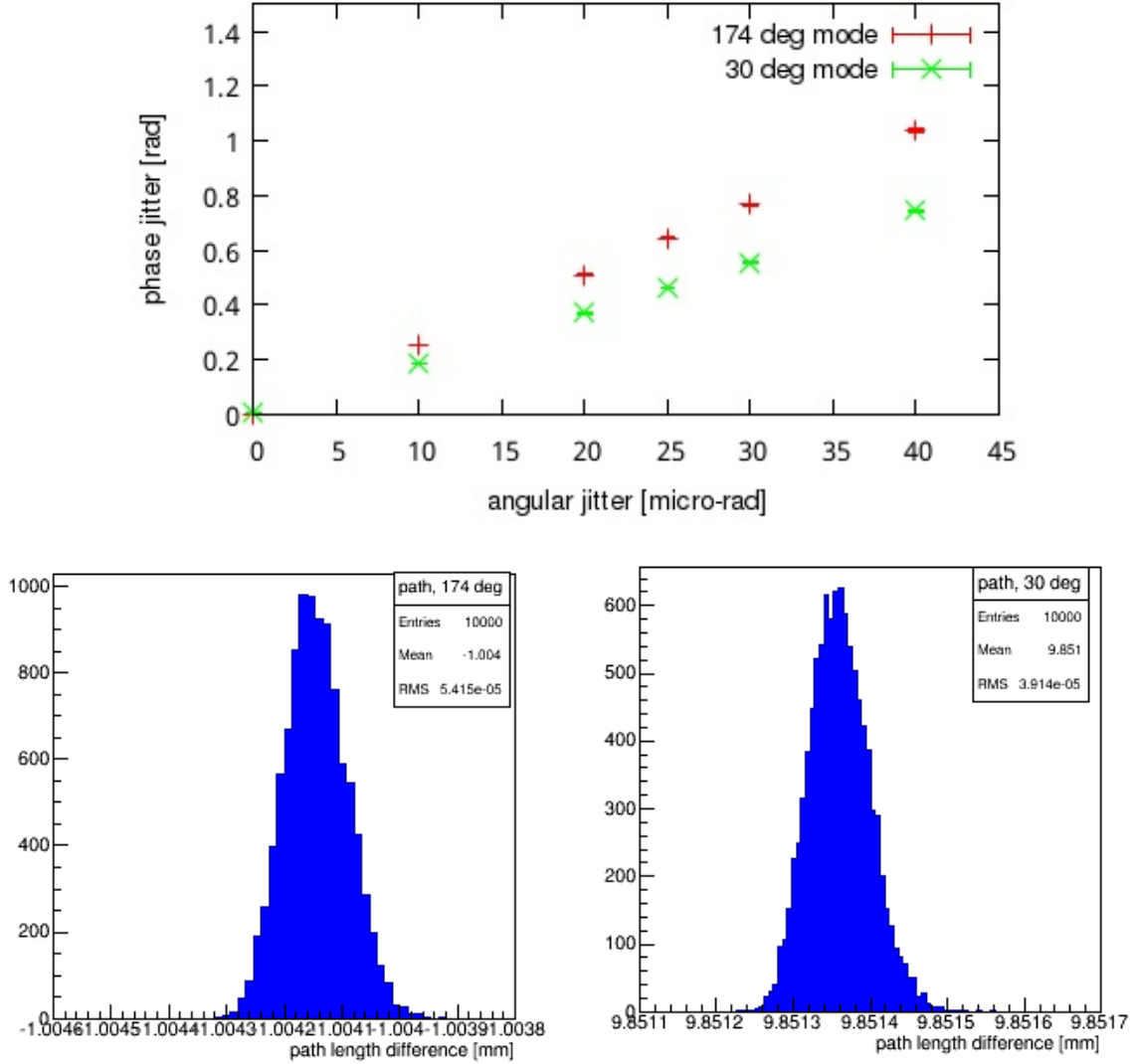
Figure 6.3: Simulation results of the phase jitter due to laser pointing jitter ($\delta\Delta\theta$), shown as the result of 10000 pseudo experiments. [top] σ_φ plotted as a function of $\delta\Delta\theta$. [bottom] Histograms of the path length difference $\Delta L = |L_U - L_L|$ for the 174 deg mode (left) and 30 deg mode (right), assuming $\delta\Delta\theta$=25 μrad; the RMS values correspond to the path length jitter $\delta\Delta L$.

6.3.3   Phase Drift

Phase fluctuation consists of not only fast jitters but also slow drifts. The two types of components may be hard to distinguish within the short time scale of a single fringe scan. The effect on M_{meas} depends on the ratio of jitters to drifts, as well as on the time structure (determined by N_{av}) of the scan. These are studied in detail in Sec.7.5.

   Figure 6.4 shows the drift of the fitted initial phase during several sets of continuous fringe scans. Over a linear range, phase drift is typically about 50 mrad/min. A relatively bad case is about 80 mrad/min. The overall phase shift throughout the entire set of about 10 scans is typically < 1 rad. Phase drift is the convolution of the drift of laser and beam position, both of which are affected by changes in environmental temperature. When phase drift is detected by a sudden decrease in Compton signal intensity, the laser is realigned to the beam by scanning the mirror actuators.

   Simulation of fringe scans was conducted to evaluate the effect of linear phase drift on M_{meas} with the following input conditions: M_0=0.636 ($\sigma_{y0} = 40$ nm for 174 deg mode), and a typical signal jitter of 23% w.r.t. E_{avg}. Figure 6.5 shows the M reduction due to a linear phase drift for $N_{av} = 10$, 50, and 100. The larger N_{av} scans are more affected because they take a longer time. Within a realistic drift range of 30-80 mrad/min, the M reduction factor C_{drift} for is >0.97 for $N_{av} = 100$, > 0.99 for $N_{av} = 50$ and $N_{av} = 10$.
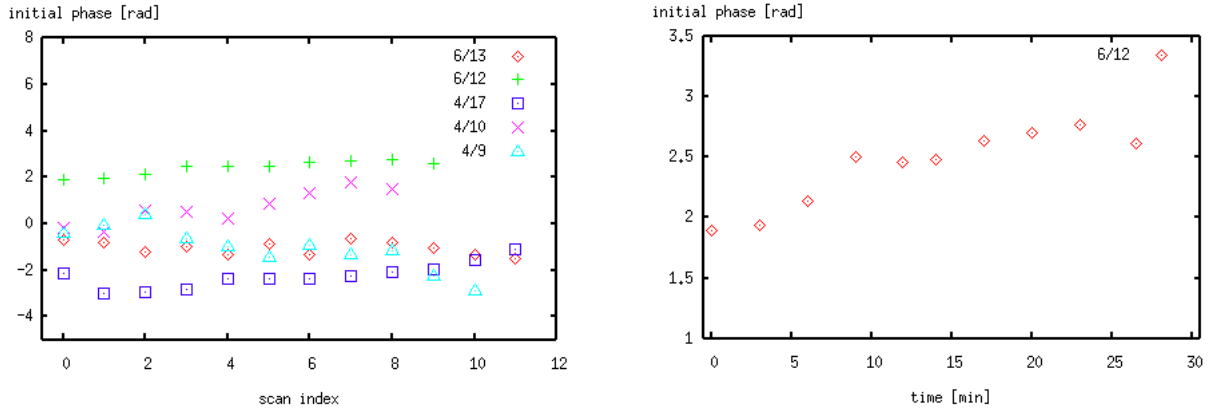

Figure 6.4: (left) The drift of the initial phase obtained by fitting the measured M spectrum during several sets of continuous fringe scans from Apr-Jun 2014. (right) The drift of the initial phase for one particular set of continuous scans on Jun. 12, plotted as a function of time. Here, the phase drift is about 30-35 mrad/min over the entire period.
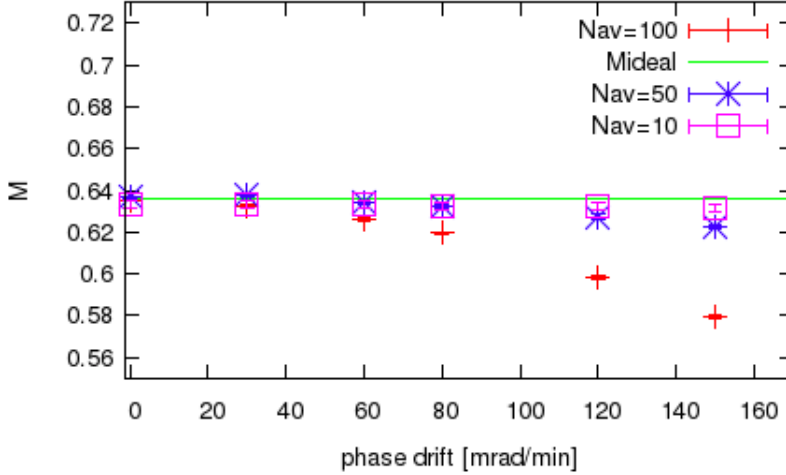
Figure 6.5: Simulated M reduction due to a linear phase drift for $N_{av} = 10, 50,$ and 100. Shown here are the results of 100 pseudo experiments assuming $M_0{=}0.636$ and a signal jitter of 23% w.r.t. E_{avg}. Within a realistic range of phase drift 30-80 mrad/min, M reduction is $< 1\%$ for both $N_{av} = 10$ and $N_{av} = 50$, and $<2.7\%$ for $N_{av} = 100$.

6.4 Fringe Rotation

The mismatch between the e^- beam and the axis of the laser fringes leads to rotated fringe in the form of "tilt" and "pitch" in the transverse (xy) plane and longitudinal direction, respectively. Figure 6.6 show the schematics. Fringe tilt $\Delta\Phi_{tilt}$ affects $\sigma_{y,meas}$ approximately as Eq. 6.9, and depends on σ_x. Fringe pitch $\Delta\Phi_{pitch}$ affects $\sigma_{y,meas}$ approximately as Eq. 6.10, and depends on the longitudinal laser spot size $\sigma_{z,laser}$.

$$\sigma_{y,meas}^2 \simeq \sigma_{y0}^2 + \sigma_x^2 \cdot \Delta\Phi_{tilt}^2 \tag{6.9}$$

$$\sigma_{y,meas}^2 \simeq \sigma_{y0}^2 + \sigma_{z,laser}^2 \cdot \Delta\Phi_{pitch}^2 \tag{6.10}$$

Both $\sigma_{z,laser}$ and σ_x are typically around 10 μm. For example, a rotation of 5 mrad would cause a nominal $\sigma_y = 40$ nm to be over-evaluated by about 25 nm. Laser fringe rotation is caused by the offset of laser spot on the lens w.r.t the lens center. Although this can be prevented by careful alignment prior to beam time, the laser spot position may drift over time. Furthermore, the e^- beam itself may be rotated in the transverse plane. Therefore fringe rotation is corrected using the e^- beam as a reference by conducting "tilt scans" and "pitch scans" in the final stage of beam tuning in the 174 deg mode. Figure 6.7 shows the online plot of pitch and roll scans. M is measured while deliberately rotating the laser fringes by manipulating intermediate mirrors in the lower path. M3 in Fig. 3.18 is rotated in x and y to generate tilt and pitch, respectively, while M174L is moved simultaneously with the same stroke to compensate for the variation in injection angle into the focal lens. In the end, the mirror actuators are set to values that yield the peak in the measured M response.

In Fig. 6.6, the offset of upper (lower) laser w.r.t. lens center is represented by $X_{U(L)}$. The longitudinal distance from the vertical table is represented by $Z_{U(L)}$. Using these, tilt and pitch are expressed as Eq. 6.11 and Eq. 6.12, respectively.

$$\Delta\Phi_{tilt} = \frac{1}{2}\left(\text{Arctan}\left(\frac{X_U + X_L}{f}\right)\right) \simeq \frac{X_U + X_L}{2f} \tag{6.11}$$

106

$$\Delta\Phi_{pitch} = \frac{1}{2}\left(\text{Arctan}\left(\frac{Z_U - Y_L}{f\sin\left(\theta/2\right)}\right)\right) \simeq \frac{Z_U - Z_L}{2f\sin\left(\theta/2\right)} \tag{6.12}$$

Here, f is the focal length of the lens, and θ is the crossing angle. For example, in Fig. 6.7 (bottom), the M3Y actuator was moved by 0.05 mm from 0 mm to -0.05 mm. This rotates the laser by $2\times$ 0.05 mm / 61.9 mm = 1.6 mrad. Given the distance of 625 mm between M3 and M174L, this resulted in a longitudinal offset of $\Delta Z \simeq 1.0$ mm. Using Eq. 6.12, the original fringe pitch error was about 2 mrad. Similarly, for the tilt in in Fig. 6.7 (top), the M3X stroke of 0.012 mm moved the laser on the lens by $2\times$ 0.012 mm $\times$ 625 mm/ 61.9 mm = 0.24 mm. Using Eq. 6.11, the original fringe tilt error was about 0.5 mrad. These calculations are consistent with the observed change in the measured M in Fig. 6.7.

The M reduction factor due to tilt and pitch are expressed approximately as Eq. 6.13 and Eq. 6.14, respectively, assuming a Gaussian laser profile.

$$C_{tilt} \simeq exp\left(-2\cdot k_y^2 \frac{\sigma_x^2}{1 + \sigma_x^2\sin^2\left(\theta/2\right)/\sigma_{t,laser}^2}\cdot\Delta\Phi_{tilt}^2\right) \tag{6.13}$$

$$C_{pitch} \simeq exp\left(-2\cdot k_y^2\sigma_{z,laser}^2\cdot\Delta\Phi_{pitch}^2\right) \tag{6.14}$$

The detailed calculations, found in [22] [30], assume $\Delta\Phi_{tilt}$, $\Delta\Phi_{pitch} \ll 1$, $\sigma_y \ll \sigma_x$, and $\sigma_y \ll \sigma_{t,laser}$, $\sigma_{z,laser}$, which is in valid for measuring $\sigma_y < 100$ nm since $\sigma_x \sim \sigma_{t,laser} \sim \sigma_{z,laser} \simeq 10$ μm. From the precision in determining the optimum mirror actuator setting by the fit shown in Fig. 6.7, the residual M reduction factors after performing tilt and pitch scans are $C_{tilt} > 0.999$, and $C_{pitch} > 0.989$, respectively.

---

[30]Equation 6.9 had assumed $\sigma_y \ll \sigma_x$ and $\sigma_x\sin\left(\theta/2\right) \ll \sigma_{t,laser}$. The latter does not necessarily stand for 174 deg mode since typically $\sigma_x \approx \sigma_{t,laser} \simeq 10\mu$m, thus $\sigma_x\sin\left(174^o/2\right) \simeq \sigma_{t,laser}$. In this case, the precise expression in Eq. 6.14 must be used.
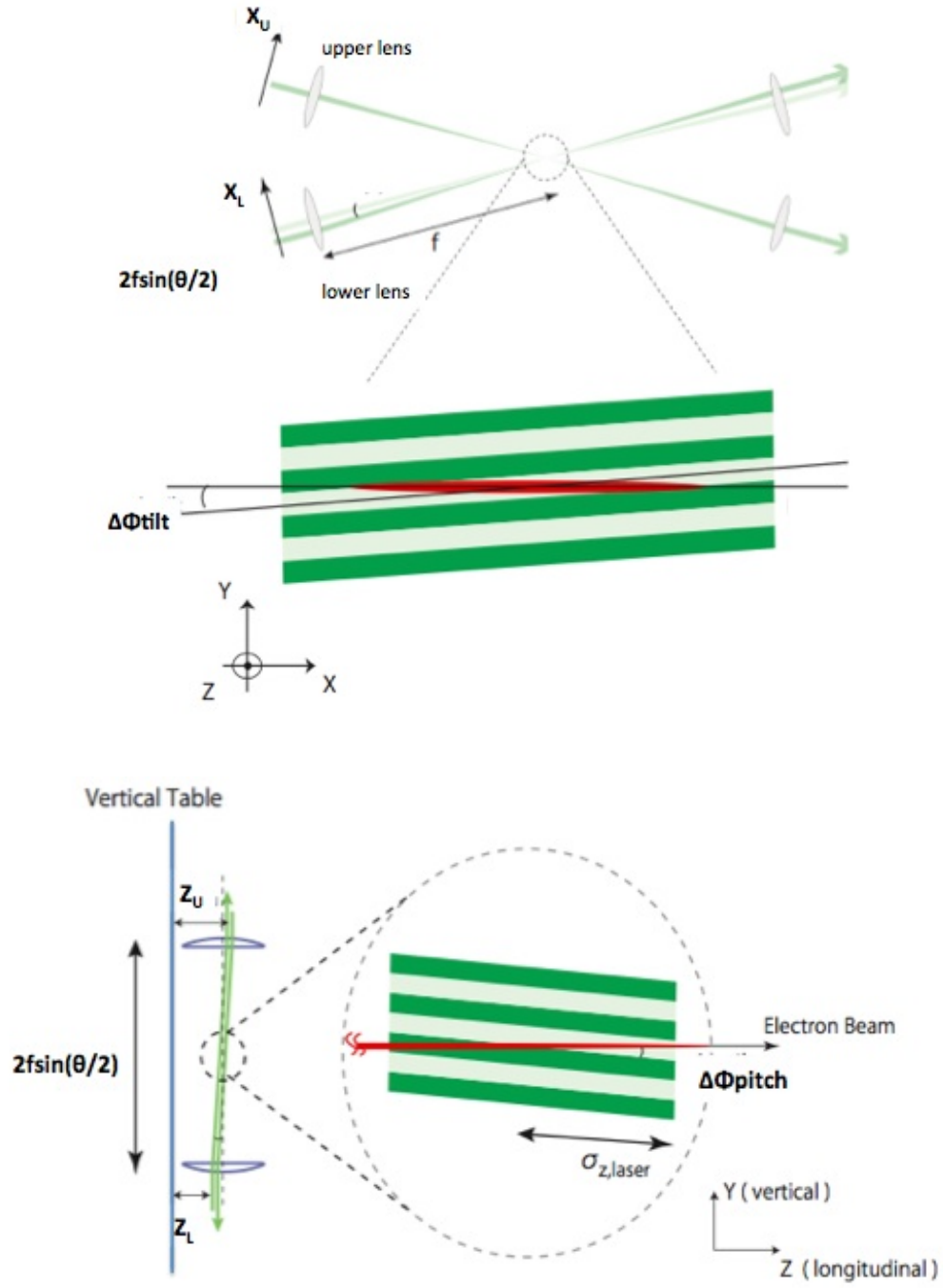
Figure 6.6: The schematics for fringe tilt (top) and fringe pitch (bottom) (figure modified from [25]).
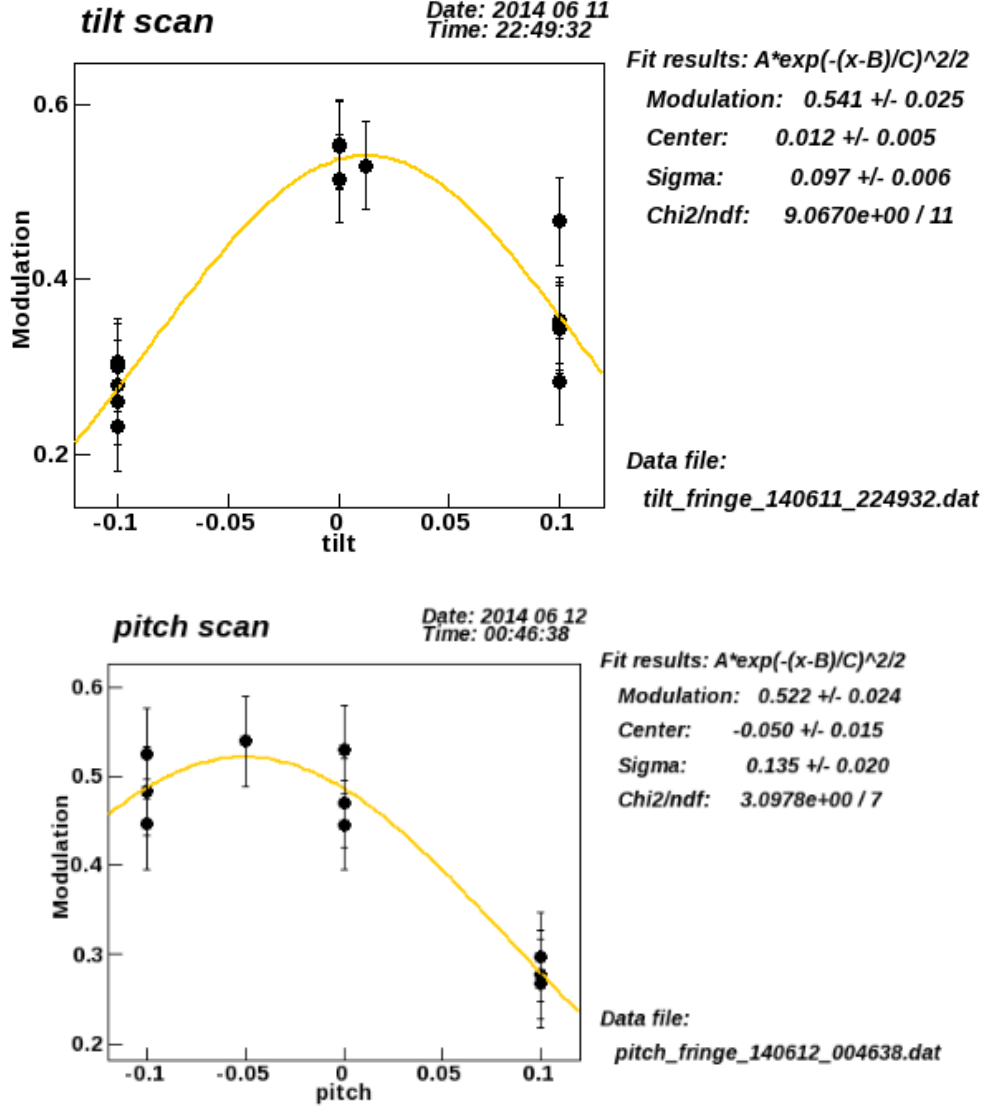
Figure 6.7: Example of the online plots made during ATF2 beam time (June 2014) for "tilt scan" (top) and "pitch scan" (bottom). The horizontal axis is the stroke of the mirror M3 actuator being scanned.

6.5 Laser Polarization

Section 5.4 explained that because the half mirror by specification has 50% reflectivity for S polarized light, any "contamination" from elliptical P polarized components will lead to intensity imbalance between the upper and lower laser paths. The resulting M reduction factor is expressed as [22]:

$$C_{pol} = \sqrt{(A - B\cos\phi\tan\theta)^2 + (C\sin\phi\tan\theta)^2} \tag{6.15}$$

$$A = 2\frac{\sqrt{R_s\left(1 - R_s\right)}P_s + \sqrt{R_p\left(1 - R_p\right)}P_p}{P_{tot}} = 2\frac{\sqrt{R_s\left(1 - R_s\right)} + \sqrt{R_p\left(1 - R_p\right)}R_{p/s}}{R_{p/s} + 1}$$

$$B = 2\frac{\left(\sqrt{R_s\left(1 - R_p\right)} - \sqrt{R_p\left(1 - R_s\right)}\right)\sqrt{P_s P_p}}{P_{tot}} = 2\frac{\left(\sqrt{R_s\left(1 - R_p\right)} - \sqrt{R_p\left(1 - R_s\right)}\right)\sqrt{R_{p/s}}}{R_{p/s} + 1}$$

$$C = 2\frac{\left(\sqrt{R_s\left(1-R_p\right)} + \sqrt{R_p\left(1-R_s\right)}\right)\sqrt{P_sP_p}}{P_{tot}} = 2\frac{\left(\sqrt{R_s\left(1-R_p\right)} + \sqrt{R_p\left(1-R_s\right)}\right)\sqrt{R_{p/s}}}{R_{p/s}+1}$$

Here, for S and P polarized light, R_s and R_p are the reflectivities of the half mirror, respectively. "P contamination" $R_{p/s}$ is defined as P_p/P_s, where P_s and P_p are the power entering the half mirror. If the half mirror were perfect i.e. $R_s = 1 - R_p = 50\%$, Eq. 6.15 would be rewritten as:

$$C'_{pol} = \sqrt{1 + \left(\frac{2\sqrt{P_sP_p}}{P_{tot}}\sin\phi\right)^2 \tan^2\theta} = \sqrt{1 + \sin^2 2\chi \tan^2\theta} \tag{6.16}$$

R_s and R_p were measured to be 50.3% and 20.1%, respectively. From Eq. 6.16, the fringe contrast can be written as $\cos\theta \cdot C'_{pol} = \sqrt{\cos^2\theta + \sin^2 2\chi \sin^2\theta}$. Although circular polarization ($\chi = 45^o$) maximizes contrast, elliptical components may mix in after reflection by several mirrors. Thus the linear polarization, which is easier to handle, is selected for the Shintake Monitor laser.

The polarization measurement results in Table 5.2 showed very little P contamination. Inserting those results into Eq. 6.15 yields negligible M reduction factors due to polarization: $C_{pol}(174^o)$ = 0.999 for 174 deg and $C_{pol}(30^o)$ = 0.998 for 30 deg. Furthermore, by optimizing the $\lambda/2$ plate angle to the "S peaks" (see Sec. 5.4), any residual P components are prevented from entering the half mirror, thus $C_{pol} \simeq 100\%$. During beam time, these "S peaks" were confirmed to yield the maximum M by conducting fringe scans as a function of the $\lambda/2$ plate angle scanned over a wide range ($>180^o$)[40]. This is consistent with the fact that these angles also yield the best power balance between the upper and lower paths as demonstrated in Sec. 5.4.

6.6 Power Imbalance

The calculations in Sec. 2.2 had assumed equal magnetic field amplitudes for both laser paths i.e. $B_1 = B_2$ ($B_{1(2)} \equiv \left|\overrightarrow{B_{1(2)}}\right|$). In order to represent the case of power imbalance i.e. $B_1 \neq B_2$, the magnetic fields are rewritten as :

$$\overrightarrow{B_1} = B_1\left(\sin\left(\theta/2\right), -\cos\left(\theta/2\right), 0\right)\cos\left(\omega t - \overrightarrow{k_1}\cdot\overrightarrow{x} - \frac{\alpha}{2}\right)$$

$$\overrightarrow{B_2} = B_2\left(-\sin\left(\theta/2\right), -\cos\left(\theta/2\right), 0\right)\cos\left(\omega t - \overrightarrow{k_2}\cdot\overrightarrow{x} + \frac{\alpha}{2}\right) \tag{6.17}$$

Consequently, the field intensity in Eq. 2.4 is modified to Eq. 6.18 and M is reduced as in Eq. 6.19:

$$\overline{\left|\overrightarrow{B_1}+\overrightarrow{B_2}\right|^2} = \frac{B_1^2+B_2^2}{2}\left(1 + \frac{2B_1B_2}{B_1^2+B_2^2}\cos\left(2k_yy+\alpha\right)\cos\theta\right) \tag{6.18}$$

$$M_{red} = \frac{2B_1B_2}{B_1^2+B_2^2}\left|\cos\theta\right|\exp\left[-2\left(k_y\sigma_y\right)^2\right] = \frac{2B_1B_2}{B_1^2+B_2^2}\cdot M \tag{6.19}$$

From Eq. 6.19, the M reduction factor due to power imbalance is expressed as :

$$C_{power} = \frac{2B_1B_2}{B_1^2+B_2^2} = \frac{2\sqrt{P_1/P_2}}{1+P_1/P_2} = \frac{2\sqrt{R_{12}}}{1+R_{12}} \quad \left(P_{1(2)} \equiv \left|\overrightarrow{B_{1(2)}}\right|^2; \quad R_{12} \equiv P_1/P_2\right) \tag{6.20}$$

6.6.1 Static Factors for Power Imbalance

The static factors that contribute to power imbalance are:

- the non-zero reflectance of lenses and prisms, the deviation from the ideally 100% reflectance of mirrors ($> 99\%$ by design), and the deviation from the ideally 50% reflectance of the half mirror for S polarized light (< 0.5 % from both catalogue and measurement). There are nearly the same number of optical components in each path, thus these small factors should not cause a significant M reduction.

- incoherent misalignment of each laser path downstream of the half mirror.

From Sec. 5.5, power imbalance was directly measured to be about 95% on Apr 30, 2014. This gives a negligible $C_{power} > 0.999$. Figure 5.11 shows another example of well balanced power provided the $\lambda/2$ plate is set as to allow only S polarized light to enter the half mirror.

6.6.2 Power Imbalance Due to Incoherent Power Jitter

Apart from static power imbalance, if the power of each laser path jitters independently shot-by-shot, the incoherent effect can also lead to power imbalance. This effect is studied using simulation as follows. Here, fringe scans of $N_{av} = 10$ and nominal $M_0 = 0.636$ are generated for 1000 pseudo experiments. The only input jitter is the power jitter $\delta P_{1(2)}$ applied in a random Gaussian distribution to the upper (lower) laser path. For $(\delta P_1, \delta P_2) = (10\%, 10\%), (20\%, 20\%), (30\%, 30\%), (5\%, 10\%), (10\%, 20\%), (10\%, 30\%)$. Table 6.2 shows C_{power} (defined in Eq. 6.20) as the statistical results of the 1000 pseudo experiments. Figure 6.8 shows the simulation results of the measured modulation M_{meas} for the first 100 pseudo experiments.

power jitter $(\delta P_1, \delta P_2)$	C_{power}
(5%, 10%)	0.998±0.000
(10%, 10%)	0.997±0.000
(10%, 20%)	0.993±0.000
(10%, 30%)	0.985±0.001
(20%, 20%)	0.989±0.001
(30%, 30%)	0.972±0.002

Table 6.2: C_{power} (defined in Eq. 6.20) as the statistical results of the 1000 pseudo experiments, for random power jitter $(\delta P_1, \delta P_2) = (10\%, 10\%), (20\%, 20\%), (30\%, 30\%), (5\%, 10\%), (10\%, 20\%), (10\%, 30\%)$ applied to the upper (1) and lower (2) paths.

The following observations are made:

- A larger power jitter in either path apparently leads to greater M reduction (from the mean of M_{meas} and/or C_{power}) and a larger fluctuation in M_{meas}.

- The M reduction due to incoherent power jitter is in general worse beyond the statistical error ranges than that predicted from static power imbalance using Eq. 6.20. For instance, a static $P_1/P_2 = 20\%$ gives $C_{power} = 0.994$, while the jitter simulation for $(\delta P_1, \delta P_2) = (20\%, 20\%)$ gives 0.989±0.001; a static $P_1/P_2 = 30\%$ gives $C_{power} = 0.984$, while the jitter simulation for $(\delta P_1, \delta P_2) = (30\%, 30\%)$ gives 0.972±0.002.

Some possible causes for incoherent power jitter are:

- The higher order effects from timing jitters, including the fine O(10) ps components seen in the temporal profile, may affect the position /angle of the laser pulses when entering into the half mirror. This in turn may lead to incoherent angular jitters when entering the focal lenses in each path, and thus power imbalance at the IP.

- The turbulence from air flow and the vibration of the mirrors in each path.

However, the power measurement in Sec. 5.5 indicates that the power jitter for each laser path is $< 1\%$. Therefore, based on the above-mentioned simulation results, the M reduction due to power jitter is confirmed to be negligible.
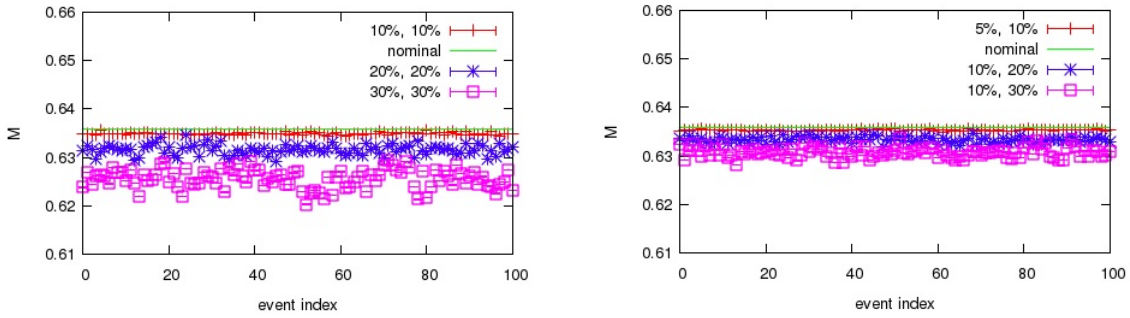

Figure 6.8: The simulation results of M_{meas} (for the first 100 events out of 1000 pseudo experiments) for the random power jitter $\delta P_{1(2)}$ applied to each of upper (lower) laser paths. The left columns are for equal jitter applied to both paths: $(\delta P_1, \delta P_2) = (10\%, 10\%), (20\%, 20\%), (30\%, 30\%)$. The right columns show the same for different jitter applied to each path: $(\delta P_1, \delta P_2) = (5\%, 10\%), (10\%, 20\%), (10\%, 30\%)$.

6.7 Laser Path Misalignment

The misalignment of the laser position at the IP leads to fringe contrast bias i.e. the reduction of M_{meas}. The consequence can be classified as follows:

1. The precision of the laser position w.r.t. the e$^-$ beam center position at the IP during collision is affected.

2. The overlap of the two laser beams at the IP is affected, leading to profile imbalance (i.e. σ_{laser} imbalance). Some other possible causes for profile imbalance are the divergence of the laser beam after emerging from the reducer, and the misalignment of the focal lens. Section 4.2.3 explained the lens adjustment for optimizing laser focusing.

The crossing of the laser paths is maintained well aligned to the e$^-$ beam at the IP by adjusting mirror angles using actuators (see Sec. 4.2.1). As position precision is generally better than 10% of the laser spot size (σ_{laser}), misalignment should not be a major issue. However, the realistic laser profile has a certain degree of laser pointing jitter, as seen from the shot-by-shot fluctuation of the laser profiles monitored by CCD cameras (see Sections 5.2 and 5.3). The bias from relative position misalignment is worse for a smaller σ_{laser} w.r.t. the horizontal e$^-$ beam size. Also, either the laser or beam position may drift over time before alignment is repeated. These non-static factors could lead to unexpected M reduction.

The following subsections evaluate the M reduction due to misalignment. First, the inter-correlated effects of relative position offset and profile imbalance will be considered, then the two factors will be separated. The calculations assume a Gaussian laser profile (as seen in Fig. 5.5), equal total laser power for the two paths, and $\sigma_y \ll \sigma_{t,laser}$.

6.7.1 Description of Laser Profile

In Sec. 2.2, the Compton signal intensity is calculated by the integration of the e$^-$ beam profile over the laser fringe intensity which is calculated as $\left|\overrightarrow{B_1} + \overrightarrow{B_2}\right|^2$ i.e. the magnetic field averaged over time in the lab frame. Here, Eq. 2.2 will be rewritten as Eq. 6.21 assuming Gaussian laser profiles $P_{t,laser}(x,y)$ and $P_{z,laser}(z)$ in the transverse and longitudinal dimensions, respectively.

$$\overrightarrow{B_1} = B\left(\sin(\theta/2), -\cos(\theta/2), 0\right)\sqrt{P_{1z,laser}(z)P_{1t,laser}(x,y)}\cos\left(\omega t - \overrightarrow{k_1}\cdot\overrightarrow{x} - \frac{\alpha}{2}\right)$$

$$\overrightarrow{B_2} = B\left(-\sin(\theta/2), -\cos(\theta/2), 0\right)\sqrt{P_{2z,laser}(z)P_{2t,laser}(x,y)}\cos\left(\omega t - \overrightarrow{k_2}\cdot\overrightarrow{x} + \frac{\alpha}{2}\right) \quad (6.21)$$

The schematics of transverse and longitudinal position misalignment were shown in Figures 4.4 and 4.5, respectively. When there is a transverse offset of l_1 and l_2 from the e$^-$ beam center (defined here at (0, 0, 0)), the transverse distances from the laser beam center to coordinate (x,y) can be expressed as $t_1 = \left|x\sin\frac{\theta}{2} - y\cos\frac{\theta}{2} + l_1\right|$ and $t_2 = \left|x\sin\frac{\theta}{2} + y\cos\frac{\theta}{2} + l_2\right|$[31]. Using these, the transverse laser profiles $P_{it,laser}(zx,y)$ (i = 1 (2): upper (lower)) are expressed as:

$$P_{1t,laser}(x,y) = \frac{\exp\left(-\frac{t_1^2}{2\sigma_{1t,,laser}^2}\right)}{\sqrt{2\pi\sigma_{1t,laser}^2}} \qquad P_{2t,laser}(x,y) = \frac{\exp\left(-\frac{t_2^2}{2\sigma_{2t,laser}^2}\right)}{\sqrt{2\pi\sigma_{2t,laser}^2}} \quad (6.22)$$

Similarly, for a longitudinal offset of Δz between the two laser beams at the IP, the longitudinal laser profiles $P_{iz,laser}(z)$ (i = 1 (2)) are expressed as:

$$P_{1z,laser}(z) = \frac{\exp\left(-\frac{(z-\Delta z/2)^2}{2\sigma_{1z,laser}^2}\right)}{\sqrt{2\pi\sigma_{1z,laser}^2}} \qquad P_{2z,laser}(z) = \frac{\exp\left(-\frac{(z+\Delta z/2)^2}{2\sigma_{2z,laser}^2}\right)}{\sqrt{2\pi\sigma_{2z,laser}^2}} \quad (6.23)$$

6.7.2 Longitudinal Misalignment

The M reduction factor due to longitudinal position misalignment and profile is [22]:

$$C_{z,align} = \sqrt{\frac{2\sigma_{1z,laser}\sigma_{2z,laser}}{\sigma_{1z,laser}^2 + \sigma_{2z,laser}^2}}exp\left(-\frac{z_0^2}{4\left(\sigma_{1z,laser}^2 + \sigma_{2z,laser}^2\right)}\right) \quad (6.24)$$

This is equivalent to the multiplication of two M reduction factors: $C_{z,pos}$ due to a longitudinal offset Δz between the two laser paths (Eq. 6.25) and $C_{z,pro}$ due to profile imbalance (Eq. 6.26).

$$C_{z,pos} = \exp\left(-\frac{\Delta z^2}{8\sigma_{z,laser}^2}\right) \quad (6.25)$$

---

[31]l_1 and l_2 have the same sign if offset is in the same direction, and vice versa

$$C_{z,pro} = \sqrt{\frac{2\sigma_{1z,laser}\sigma_{2z,laser}}{\sigma_{1z,laser}^2 + \sigma_{2z,laser}^2}} \qquad (6.26)$$

6.7.3 Transverse Misalignment

In evaluating laser path misalignment in the transverse plane, we will assume that $\sigma_y \cos(\theta/2) \ll \sigma_{t,laser}$ [32], and $l_2 = 0$ (since only the relative offset $|l_1 - l_2|$ is meaningful). The corresponding M reduction factor is [22] :

$$C_{t,align} = \frac{2\exp(A_t)/\sqrt{\sigma_{1t,laser}\sigma_{2t,laser}}}{\exp\left[-\frac{1}{2}\left(\frac{l_1}{\sigma_{1t,rel}}\right)^2\right]/\sigma_{1,t,rel} + 1/\sigma_{2,t,rel}} \sqrt{\frac{1}{1+\left(\frac{\sigma_x sin(\theta/2)}{\sigma_{t,l}}\right)^2}} \qquad (6.27)$$

$$A_t = -\frac{l_1^2\left(2\sigma_{2,t,laser}^2 + \sigma_x^2\sin^2(\theta/2)\right)}{8\sigma_{1t,laser}^2\sigma_{2t,laser}^2\left(1+\left(\frac{\sigma_x\sin(\theta/2)}{\sigma_{t,l}}\right)^2\right)}$$

Here, the following notation is used: $\sigma_{t,l} \equiv \sqrt{2}\left(1/\sigma_{1,t,laser}^2 + 1/\sigma_{2,t,laser}^2\right)^{-1/2}$ and $\sigma_{i,t,rel} \equiv \sqrt{\sigma_{i,t,laser}^2 + \sigma_x^2\sin^2(\theta/2) + \sigma_y^2\cos(\theta/2)}$ ($i =$ 1, 2). Equation 6.27 represents the coupled effects of profile and position. On the other hand, they can be evaluated separately under certain assumptions. If we assume no position misalignment i.e. $|l_1 - l_2|=0$, the M reduction factor due to profile imbalance only is expressed as:

$$C_{t,pro} = \frac{2/\sqrt{\sigma_{1t,laser}\sigma_{2t,laser}}}{1/\sigma_{1,t,rel} + 1/\sigma_{2,t,rel}} \sqrt{\frac{1}{1+\left(\frac{\sigma_x\sin(\theta/2)}{\sigma_{t,l}}\right)^2}} \qquad (6.28)$$

If we assume a perfectly balanced profile i.e. $\sigma_{1t,laser} = \sigma_{2t,laser}$, the M reduction factor due to transverse position alignment only is expressed as:

$$C_{t,pos} = \frac{2\exp(A_t)/\sigma_{1,t,laser}}{\left(1+exp\left[-\frac{1}{2}\left(\frac{l_1}{\sigma_{1t,rel}}\right)^2\right]\right)/\sigma_{1,t,rel}} \sqrt{\frac{1}{1+\left(\frac{\sigma_x sin(\theta/2)}{\sigma_{1t,laser}}\right)^2}} \qquad (6.29)$$

$$A_t = -\frac{l_1^2\left(2\sigma_{1,t,laser}^2 + \sigma_x^2\sin^2(\theta/2)\right)}{8\sigma_{1t,laser}^4\left(1+\left(\frac{\sigma_x\sin(\theta/2)}{\sigma_{1t,laser}}\right)^2\right)}$$

Figure 6.9 compares the M reduction for $C_{t,align}$ (Eq. 6.27) and for the multiple of the two individual factors $C_{t,pro} \cdot C_{t,pos}$. The non-zero discrepancy is an indication of the coupled effect between the two factors. However, this discrepancy is a negligible level of $< 1\%$.

simplified version

If $\sigma_y \ll \sigma_{t,laser}$ and $\sigma_x \sin(\theta/2) \ll \sigma_{t,laser}$ can be assumed, Eq. 6.27 can be simplified to:

---
[32]This is valid since the σ_y at interest < 100 nm, and $\sigma_{t,laser}$ is typically about $10\mu m$

$$C_{t,align} \simeq \frac{2\sqrt{\sigma_{1t,laser}\sigma_{2t,laser}}}{\sigma_{2t,laser}exp\left[-\frac{1}{2}\left(\frac{l_1}{\sigma_{1t,laser}}\right)^2\right] + \sigma_{1t,laser}exp\left[\left(\frac{l_1}{2\sigma_{1t,laser}}\right)^2\right]} \tag{6.30}$$

However, since $\sigma_x \simeq \sigma_{t,laser} \simeq 10-15\,\mu$m for recent ATF2 operation, the assumption $\sigma_x \sin(\theta/2) \ll \sigma_{t,laser}$ is not valid for θ=174 deg mode. In this case, the precise expression in Eq. 6.27 must be used.

6.7.4   Evaluation of Misalignment

Regarding profile imbalance, only the transverse profile $\sigma_{t,laser}$ can be inferred separately for each laser path, from laser wire scans. As for the longitudinal profile, the same ratio in $\sigma_{z,laser}$ between the two paths is assumed as that for $\sigma_{t,laser}$. The worst limits for $C_{t,align}$ and $C_{z,align}$ are estimated assuming the following typical conditions (according to observations): $\sigma_{t(z),laser} \simeq 15\,\mu$m, $\sigma_x \simeq 12\,\mu$m, position alignment precision better than 10% of $\sigma_{t(z),laser}$, profile balance better than 10:7. These give $C_{t,align} > 98.7\%$ and $C_{z,align} > 96.8\%$. The total M reduction factor due to position misalignment is expressed as $C_{align} = C_{t,align} \cdot C_{z,align} > 95.5\%$.
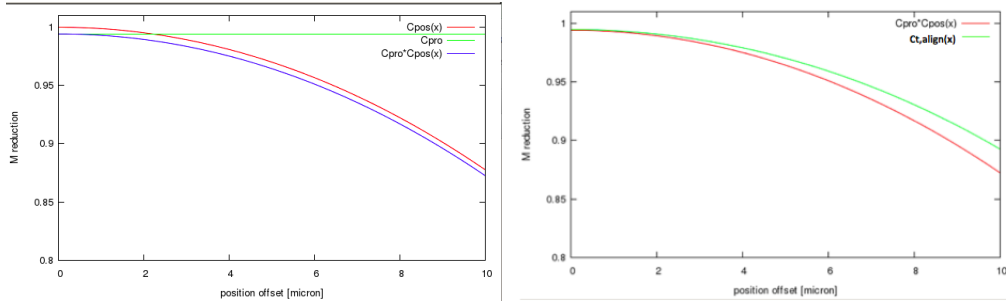

Figure 6.9: (left) The M reduction due to transverse position misalignment ($C_{t,pos}$: red) and profile imbalance ($C_{t,pro}$: green) , as well as the multiple of the two uncoupled factors ($C_{t,pos} \cdot C_{t,pro}$: blue). (right) The comparison of $C_{t,pos} \cdot C_{t,pro}$ with the M reduction calculated using the precise expression for $C_{t,align}$ in Eq. 6.27.

6.8   Spherical Wavefront Effects

The calculations in Sec. 2.2 used plane wave assumption for the laser colliding with the e$^-$ beam. However, realistically the laser has the spherical wavefronts characteristic of a Gaussian-like beam. The plane wave approximation is valid only at the focal point where the curvature radius is infinite. If the location of laser crossing and/or laser-beam collision is deviated from the laser focal point, the e$^-$ beam would interact with "distorted" fringes due to spherical wave-front effects (Fig. 6.10). This leads to M reduction calculated as follows[22]: Here, it is assumed that two Gaussian laser beams propagate in y, and that the laser-beam collision is offset by Δy w.r.t. the laser focal point (= crossing point) defined at (0,0,0). Defining $\delta y \equiv \Delta y/z_R$ to be the relative offset w.r.t. the Rayleigh length z_R, the resulting M reduction factor is:

$$C_{sphere} = \left(1 + \delta y^2\right)^{-1/4}\left[1 + \frac{\delta y^2}{\left(1 + z_R\frac{1+\delta y^2}{2k\sigma_x^2}\right)^2}\right]^{-1/4} \tag{6.31}$$

In recent operation, the horizontal e⁻ beam size σ_x is typically 12 μm, and z_R is measured to be 2.6 mm (see Sec. 5.1.2). Figure 6.11 shows the dependence of C_{sphere} on lens alignment precision for (left) z_R = 2, 3.5, 5.1 mm, assuming σ_x= 12 μm and (right) for σ_x= 20, 12, 2.2 μm, assuming z_R = 2.6 mm. It can be seen that the tolerance for lens misalignment is looser for a longer z_R and/or a smaller σ_x. The measured z_R = 2.6 mm and lens alignment precision of typically better than 0.5 mm gives $\delta y < 19\%$. Inserting these into Eq. 6.31, C_{sphere} is estimated to be > 98.8%. This effect is a concern only for measuring the smallest σ_y using the 174 deg mode.
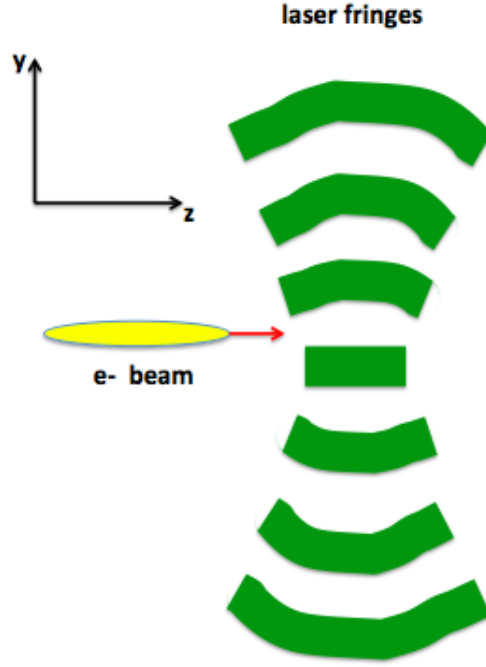

Figure 6.10: The schematics of the effect of Gaussian spherical wavefronts when the collision of laser and e⁻ beam is offset from the laser waist.
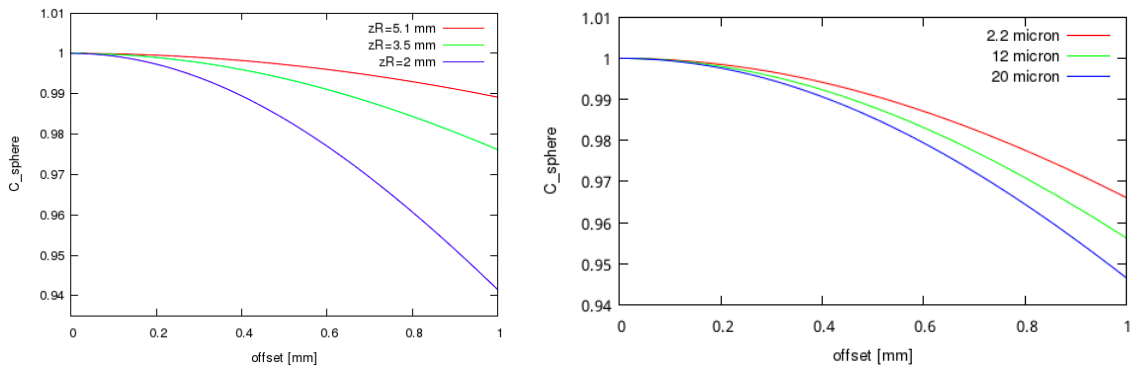

Figure 6.11: The dependence of C_{sphere} on lens alignment precision shown for (left) Rayleigh length z_R = 2, 3.5, 5.1 mm, assuming σ_x= 12 μm and (right) for σ_x= 20, 12, 2.2 μm , assuming z_R = 2.6 mm.

6.9 Change of the Beam Size within the Laser Fringes

The sudden strongly focusing of σ_y to O(10) nm requires the beam to have a large divergence angle at the IP (i.e. a short curvature radius). Therefore, the growth in σ_y within the finite longitudinal length of the laser fringes needs to be taken into account (see Fig. 6.12). The "effective beam size" $\sigma_{y,eff}$ can be written as a function of the longitudinal coordinate (z) on the laser fringe as:

$$\sigma_{y,eff}(z) = \sqrt{\sigma_y^2(0) + \frac{\varepsilon_y}{\beta_y^*}z^2} \tag{6.32}$$

This shows the dependence on the beam divergence angle $\sqrt{\varepsilon_y/\beta_y^*}$, which is determined by the emittance ε_y and the IP beta function β_y^*. Here, $\sigma_y(0) = \sqrt{\varepsilon_y\beta_y^*}$ is the nominal beam size, assuming all chromatic aberrations have been corrected. Since the laser Rayleigh length ($\simeq 5$ mm) is much longer than σ_y, the e$^-$ beam is assumed to interact with laser fringes that stretch homogeneously in y. On the other hand, in the longitudinal (z) direction, a finite spread of about $\sigma_{z,laser}$ affects fringe intensity as : $1 + \cos\theta\cos(2k_yy + \alpha) \rightarrow \exp\left(-\frac{z^2}{2\sigma_{z,laser}}\right)\{1 + \cos\theta\cos(2k_yy + \alpha)\}$. The M reduction from this effect is[22]:

$$C_{growth} = \frac{1}{\sqrt{1 + 4k_y^2\sigma_{z,laser}^2\frac{\varepsilon_y}{\beta_y^*}}} \tag{6.33}$$

Assuming a typical $\sigma_{z,laser} \simeq 10$ μm, $C_{growth} > 99.7\%$. This corresponds to a negligible beam size growth of < 0.2 nm for $\sigma_y = 37$ nm. This factor is nearly equally negligible for all modes, with exception of the 174 deg mode, which receives the heaviest impact relative to the minuscule σ_y.
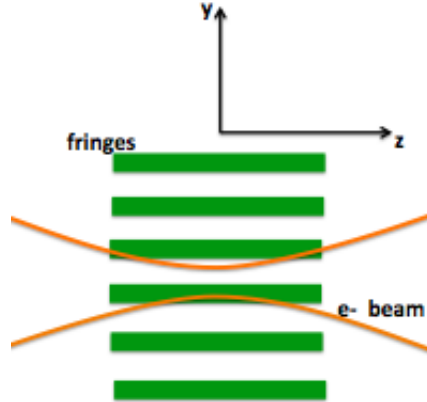

Figure 6.12: The schematics of the change of beam size inside the longitudinal spread of the laser fringes.

7 Study of Signal Jitters and Drifts

The previous Chap. 6 described the M reduction factors affecting beam size measurements. The most important M reduction factor is phase jitter. The purpose of this chapter is to provide the understanding of the other signal jitter sources which is necessary for the analysis of phase jitter. The most important sections are Sections 7.4 - 7.7, where simulation assuming realistic ATF2 experiment conditions is used to demonstrate the extraction of phase jitter from fringe scan data. An original method was developed for this purpose. Finally Sec. 7.8.1 evaluates phase jitter from actual beam time data.

7.1 Signal Jitter Sources

This section describes the individual signal jitter sources (also see [40][41]). Out of these, phase jitter was first brought up in Sec. 6.3 as a M reduction factor, while the other jitter sources are necessary for its understanding.

Fast signal jitter sources that vary shot-by-shot cause fluctuations of the measured signal energy and consequently degrade beam size measurement precision and beam tuning efficiency. Detection of smaller M values may even become impossible under very heavy jitters comparable in scale to the signal modulation itself. At the low e^- bunch charge ($\lesssim 1 \times 10^9$) used for small σ_y measurements during recent ATF2 operation, the relative signal jitter (w.r.t to E_{avg}) is typically observed to be 15-25 % at peaks and bottom phases of fringe scans and and 25-35% at mid-points phases. This varies depending on the conditions of the laser and/or the e^- beam. Individual jitter sources are assessed by improving hardware or offline data correction.

7.1.1 Phase Jitter (Vertical Relative Position Jitter)

Section 6.3 introduced phase jitter (σ_φ), or equivalently vertical relative position jitter ($\delta\Delta y$) as one of the dominant M reduction factors. The signal jitter caused by σ_φ depends on M and fringe scan phase φ, and can be expressed as :

$$\Delta E_p = \sqrt{\overline{\left(E\left(\varphi\right) - \overline{E\left(\varphi\right)}\right)^2}} = \sqrt{\overline{E\left(\varphi\right)^2} - \left(\overline{E\left(\varphi\right)}\right)^2} \tag{7.1}$$

$$= E_{avg} M \sqrt{\frac{1}{2}\left[1 - 2\cos^2\left(\varphi\right)\exp\left(-\sigma_\varphi^2\right) + \cos\left(2\varphi\right)\exp\left(-2\sigma_\varphi^2\right)\right]}$$

Here, $\overline{E\left(\varphi\right)}$ and $\overline{E\left(\varphi\right)^2}$ are expressed using the modulation already reduced by σ_φ : $M_{red} = M \cdot \exp\left(-\sigma_\varphi^2/2\right)$ as:

$$\overline{E\left(\varphi\right)} = \int \exp\left(-\frac{\varphi'^2}{2\sigma_\varphi^2}\right) E_{avg}\left[1 + M\cos\left(\varphi + \varphi'\right)\right] d\varphi' = E_{avg}\left(1 + M_{red}\cos\varphi\right) \tag{7.2}$$

$$\overline{E\left(\varphi\right)^2} = \int \exp\left(-\frac{\varphi'^2}{2\sigma_\varphi^2}\right) \left\{E_{avg}\left[1 + M\cos\left(\varphi + \varphi'\right)\right]\right\}^2 d\varphi' \tag{7.3}$$

$$= E_{avg}^2 \left\{1 + 2M_{red}\cos\varphi + M_{red}^2/2 \cdot \left[\exp\left(\sigma_\varphi^2\right) + \cos\left(2\varphi\right)\exp\left(-\sigma_\varphi^2\right)\right]\right\}$$

Using a method described in Sec. 7.4, the σ_φ extracted by fitting fringe scan data is typically 400 - 750 mrad for the 174 deg mode. For example, when measuring a nominal σ_y of 45 nm ($M_0=$ 0.56 for 174 deg mode), a σ_φ of 500 mrad ($\delta\Delta y \simeq 21$ nm) causes signal jitter w.r.t E_{avg} of about 9% at the fringe peak or bottom, and about 25% at the mid-point.

7.1.2 Statistical Fluctuation

Section 3.6 gave the evaluation of the statistical fluctuation of the measured E_{sig}, which is the combined effect of Compton photon statistics and detector response. It was shown that the contribution to relative signal jitter is $< 1\%$ from the fluctuation of the number of photo-electrons ($N_{pe} > 10000$) output from the PMT photocathodes, 5-10% from the statistical fluctuation of the number of Compton photons per bunch (N_{sig}=100-350), and 14-27% from the fluctuation of shower development. Section 3.6.3 took into account the small effect ($\lesssim 1\%$) from photon angular jitter and the signal reduction due to the possible misalignment of the movable collimator. From all of the above, the statistical signal fluctuation is estimated to be about 15-28% [33].

7.1.3 Background Energy Fluctuation

The Compton signal energy is measured using the "ON/OFF" method (see Sec. 3.5.4), for which the signal energy (E_{sig}) is calculated by subtracting "OFF events" (E_{OFF}) from "ON events" (E_{ON}: signal+BG) as $E_{sig} = E_{ON} - E_{OFF}$. Variations in BG conditions may arise from an enhancement in the interaction between the beam halo and beam pipe triggered by beam orbit instability. Given the sufficiently high S/N ratio of $\gtrsim$50 in recent operation, the relative signal jitter due to BG energy jitter is $< 5\%$ w.r.t. E_{avg} and not problematic.

7.1.4 Laser Timing Jitter

Sections 3.4.2 and 4.2.5 described the mechanism of laser timing adjustment. Laser timing and e^- beam timing are monitored using the signals from PIN-PDs and strip-line BPMs, respectively. Sub-ns precision matching is carried out during beam time by scanning laser Q-switch timing using digital modules. The design FWHM laser pulse width is 8 ns, while the e^- beam pulse width is about 20 ps. Therefore, relative timing jitter (dominated by laser timing jitter) on the order of O(1 ns) would affect the intensity of the laser colliding with the e^- beam pulse by pulse. This results in signal jitters expressed as:

$$\frac{\Delta E_{timing}}{E_{avg}} = 1 - \frac{\frac{1}{\sqrt{2\pi\sigma_{\Delta t}^2}} \int dt \exp\left(-\frac{t^2}{2\sigma_{\Delta t}^2}\right) P_{laser}(t)}{\int dt \delta(t) P_{laser}(t)} \tag{7.4}$$

$$= 1 - \sqrt{\frac{\sigma_{t,rms}^2}{\sigma_{t,rms}^2 + \sigma_{\Delta t}^2}} \approx \frac{1}{2}\left(\frac{\sigma_{\Delta t}}{\sigma_{t,rms}}\right)^2$$

Here, t represents the relative timing between the laser and the e^- beam, and $\sigma_{\Delta t}$ its jitter. $P_{laser}(t) \propto \exp\left(-\frac{t^2}{2\sigma_{t,rms}^2}\right)$ is the laser temporal profile with a design RMS pulse width of $\sigma_{t,rms}$ = 3.4 ns. In order to maintain signal jitters to $< 5\%$, $\sigma_{\Delta t}$ should be suppressed to $\lesssim 1$ ns. The horizontal fluctuation of the laser temporal profile observed using an oscilloscope (see Fig. 3.24) indicates laser timing jitter to be about 1 ns (RMS)[34]. From Eq. 7.4, this leads to a signal jitter of about 4.3%.

---

[33]The evaluation of statistical fluctuations here does not take into account the effect from other energy jitter sources e.g. phase jitter or horizontal relative position jitter. These are mentioned separately in the following subsections.

[34]There are finer structures of O(10) ps order observed in the temporal profile that could also possibly affect the intensity of collision with the e^- beam pulse with has a similar time scale. However this is beyond the resolution of the PIN-PD.

7.1.5 Total Laser Power Jitter

The signal jitter due to the total power jitter $\Delta P / P$ is:

$$\frac{\Delta E_{power}}{E_{avg}} = \frac{\Delta P}{P} \tag{7.5}$$

The power measurements in Sec. 5.5 show total laser power jitter to be $\lesssim 1\%$. The contribution to signal jitters is negligible compared to the change in laser intensity during collision with the e$^-$ beam such as due to position offset at the IP.

7.1.6 Horizontal Relative Position Jitter

Laser pointing jitter and/or horizontal e$^-$ beam position jitter leads to fluctuation in the laser intensity intercepted by the e$^-$beam. Jitter conditions can change over time depending on the stability of the laser and the e$^-$ beam. The estimated laser pointing jitter in Sec. 5.3 is approximately consistent with the laser profile fluctuation ($< 5\%$ of the laser spot diameter) observed using CCD cameras. Here, relative position and its jitter will be denoted as Δx and $\sigma_{\Delta x}$, respectively. The signal jitter due to $\sigma_{\Delta x}$ can be expressed as:

$$\frac{\Delta E_{rel}}{E_{avg}} = 1 - \frac{\frac{1}{\sqrt{2\pi\sigma_{\Delta x}^2}} \int d\Delta x \exp\left(-\frac{\Delta x^2}{2\pi\sigma_{\Delta x}^2}\right) P_{pos}\left(\Delta x\right)}{\int d\Delta x \delta\left(\Delta x\right) P_{pos}\left(\Delta x\right)} \tag{7.6}$$

$$= 1 - \sqrt{\frac{\sigma_{lw}^2}{\sigma_{lw}^2 + \sigma_{\Delta x}^2}}$$

Here, $P_{pos}\left(\Delta x\right) \propto \exp\left(-\frac{\Delta x^2}{2\sigma_{lw}^2}\right)$ is the Gaussian profile based on relative position, whose width σ_{lw} is the fitted sigma in a laser wire scan. In Sec. 5.3, $\sigma_{\Delta x}$ is evaluated using a laser wire scan to be $16\pm5\%$ of σ_{lw}. Using Eq. 7.6, this causes $1.3\pm0.9\%$ in signal jitters.

7.1.7 Electron Beam Intensity Jitter

The jitter of the e$^-$ beam intensity directly leads to jitters in the Compton signal energy. To suppress this, the measured signal energy is normalized pulse by pulse by the beam bunch charge (N_e) measured by the "ICT monitor" introduced in Sec. 3.5.4 (Fig. 3.34). Figure 7.1 shows the N_e measured during a single fringe scan. The beam intensity jitter $\delta N_e/N_e$ is typically 5-10%. This "ICT correction" process can reduce the signal jitter due to $\delta N_e/N_e$ down to the the resolution of the ICT monitor, which was evaluated to be about 2 %[22]. However its resolution may become degraded due to surrounding electronics noise. Typically, a jitter reduction of $\lesssim 2\%$ is observed after ICT correction.
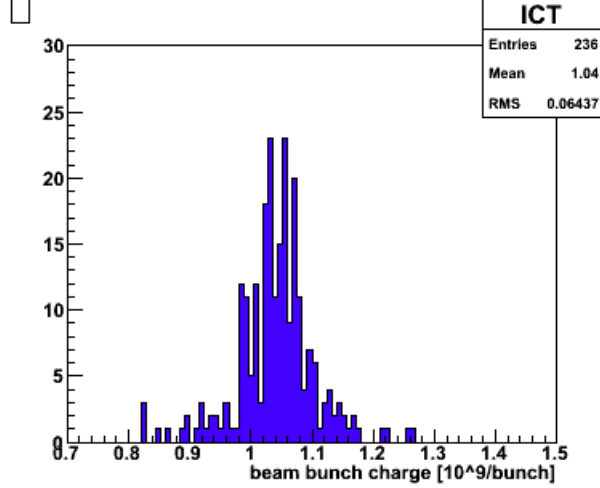
Figure 7.1: A histogram of the e$^-$ beam bunch charge (unit: 10^9/ bunch) measured by the ICT monitor during a single fringe scan. Here, the beam intensity jitter is about 6%.

7.2 Modeling of Signal Jitters

The signal jitter (ΔE) in a fringe scan is defined as the standard deviation of N_{av} (= number of pulses) events of energy measured at each phase. Total signal jitter can be expressed approximately as a convolution of vertical jitter (ΔE_V) and the jitter due to phase jitter (ΔE_p) as :

$$\triangle E = \sqrt{\triangle E_V^2 + \triangle E_p^2} \tag{7.7}$$

The expression for ΔE_p was given in Eq. 7.1. Vertical jitter is expressed as :

$$\Delta E_V = \sqrt{C_{const}^2 + \left(C_{stat}\sqrt{E}\right)^2 + (C_{linear}E)^2} \tag{7.8}$$

Each jitter component is assumed to follow a Gaussian distribution. C_{const} is mainly related to electrical noise of the detector [35]. C_{linear} is related to laser related instabilities e.g. timing, power, and position, as well as e$^-$ beam intensity jitter. The stochastic term C_{stat} represents the statistical signal fluctuations, which depends on the fluctuation of the number of Compton signal photons reaching the detector as well as detector response. Typically, the C_{stat} term is dominant over the terms C_{const} and C_{linear}. The C_{linear} term may vary over time, while the terms C_{stat} and C_{const} remain relatively stable.

7.3 Calibration of Detector Response

The following calibration was performed to evaluate the linearity and the fluctuation related to the response of the gamma detector response. Beam bunch charge (N_e) was changed in steps while recording E and ΔE, defined as mean and standard deviation, respectively, of the measured signal energy for each N_e. Only the upper laser path was made to collide with the e$^-$ beam by setting its position to the peak of a laser wire scan.

---

[35] For the analysis of phase jitters, BG fluctuation is subtracted from the signal jitters. Thus the effect of BG fluctuation should not be included in the term C_{const}

Figure 7.2 shows good linearity of E w.r.t. a wide intensity range from $N_e \sim 0.5 \times 10^9$ to $N_e \sim 3.5 \times 10^9$ [36]. Figure 7.3 shows ΔE plotted as a function of E, and fitted with Eq. 7.9 with 3 free parameters C_{const}, C_{stat}, and C_2.

$$\Delta E = \sqrt{C_{const}^2 + \left(C_{stat}\sqrt{E}\right)^2 + (C_2 E)^2} \tag{7.9}$$

Here, C_2 is mainly caused by the intensity fluctuation of the e^- beam and the laser at the IP. The terms C_{const} and C_{stat} are approximately consistent with those in Eq. 7.8 for the same detector condition. The fitted result gives $C_{stat} = 6.2 \cdot \sqrt{\text{unit of } E}$. The stochastic term contributes to relative signal jitter as $C_{stat}/\sqrt{E}$: about 17% (w.r.t. E_{avg}) for low E corresponding to $N_e = 1 \times 10^9$, and about 10% for a higher E corresponding to $N_e = 3 \times 10^9$. The relationship between N_e and E are derived using the linearity plot in Fig. 7.2. The C_{stat} derived for each N_e is used for σ_φ analysis in Sec. 7.8.1.
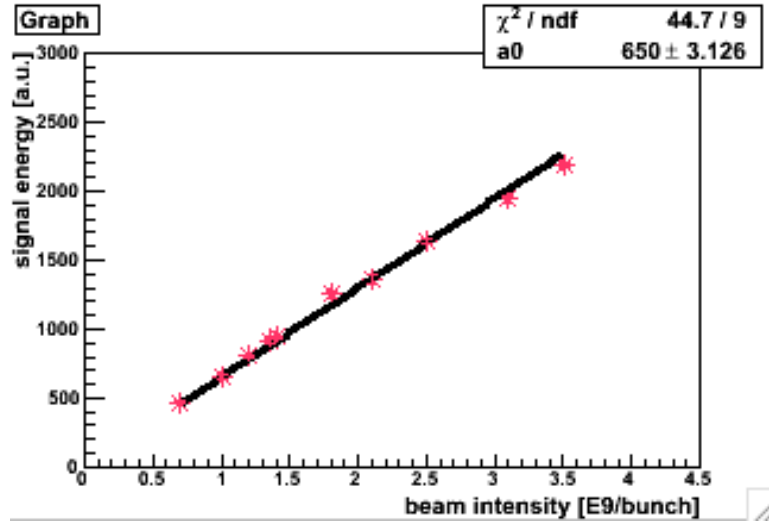
Figure 7.2: The linearity of the gamma-ray detector response is demonstrated by plotting energy measured as a function of e^- beam bunch charge (N_e [10^9]) . The fitted result is : E [a.u] $= 650 \times N_e$.

---

[36] In fact, the same linearity and slope was obtained when this measurement was conducted one month later, despite that the e^- beam orbit conditions were different from this measurement.
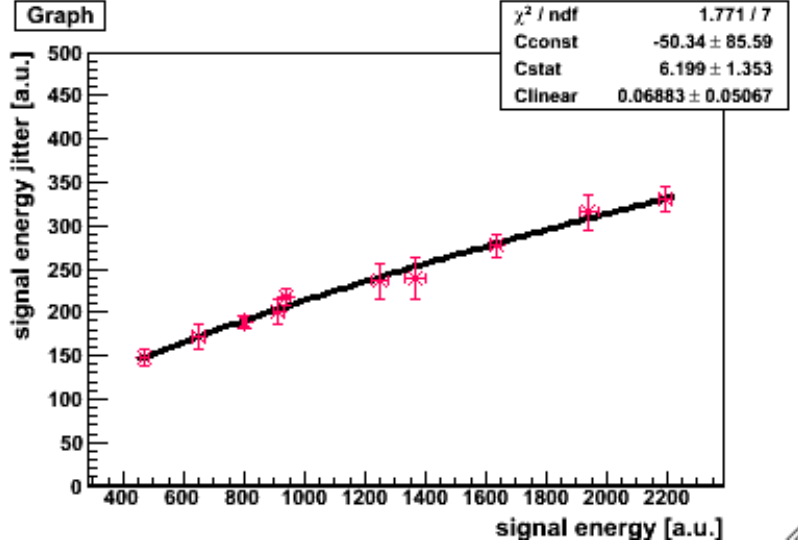
Figure 7.3: The calibration of the fluctuation related to detector response: energy jitter is plotted as a function of energy, and fitted with Eq. 7.9. Here, energy is shown in the form of the sum of ADC counts of the front four detector layers, which is the usual case for fringe scan analysis.

7.4 Method for Deriving Phase Jitter

An original analysis method has been developed for the purpose of extracting phase jitter σ_φ from fringe scan data; it is the first ever to be able to do so. In this section, this method will be explained using the Monte Carlo simulation plots in Fig. 7.4; here Compton signal energy E is generated according to:

$$E = E_{avg} \{1 + M \cdot \cos(\varphi + \varphi_0)\} \tag{7.10}$$

In Eq. 7.10, the phase φ is jittered according to a certain distribution. In Sec. 7.5, both Gaussian-like phase jitters and complex non-Gaussian phase jitters are tested. Furthermore, vertical jitters are implemented as Eq. 7.8 according to a random Gaussian distribution. The phase jitter extraction method comprises of the following two steps:

Step1: Figure 7.4 (top): the fitting of the M spectrum in a fringe scan with Eq. 2.10 to obtain M_{meas}, E_{avg} and φ_0; here the measured signal energy is plotted as a function of φ.

Step2: Figure 7.4 (bottom): the fitting of the "signal jitter plot" by Eq. 7.7 to obtain σ_φ; here the measured signal energy jitter (defined as the S.D. of the N_{av} events at each φ) is plotted as a function of φ.

The Eq. 7.7 $\triangle E = \sqrt{\triangle E_V^2 + \triangle E_p^2}$ used in Step 2., as explained in Sec. 7.2, assumes a convolution of Gaussian distributed jitters comprised of phase jitters and vertical jitters. The signal jitter due to σ_φ (ΔE_p) is given by Eq. 7.1. Vertical jitters (ΔE_V) is written as [42]:

$$\Delta E_V = \sqrt{C_{const}^2 + C_{stat}^2 \overline{E(\varphi)} + C_{linear}^2 \overline{E(\varphi)^2}} \tag{7.11}$$

In this model, $\overline{E(\varphi)}$ (Eq. **??**) and $\overline{E(\varphi)^2}$ (Eq. **??**) take into account the effect of σ_φ on the measured energy. The free parameters extracted from fitting are σ_φ and C_{linear}. The fixed

parameters are the M_{meas}, E_{avg} and φ_0 obtained in Step 1, as well as the estimated values of the relatively time stable terms C_{const} and C_{stat}. The dominant C_{stat} term is estimated using the detector calibration results in Sec. 7.3 according to the e$^-$ beam bunch charge of each scan; the effect of the uncertainty of C_{stat} is shown in Sec. 7.6. The C_{const} term, whose effect is small, is fixed to a pessimistic value of 5% w.r.t. E_{avg} [37].

The fitting of the measured energy jitters in Step 2 is carried out by χ^2 minimization. The statistical error of a variance value "σ" (ΔE in this case) is estimated as follows [43]: Taking s to be the estimation of σ, the test statistic ns^2/σ^2 follows $\chi^2_{n-1}(\alpha)$, based on a χ^2 distribution with $n - 1$ degrees of freedom and probability α. Defining the statistical error as 1 standard deviation (68% C.L.), the probabilities 0.84 and 0.16 will be used in calculating the upper and lower limits of $\sigma^2/s^2 = n/\chi^2_{n-1}(\alpha)$ as (in this case $n \iff N_{av}$):

$$\frac{\sigma^{(-)}}{s} = \sqrt{\frac{N_{av}}{\chi^2_{N_{av}-1}(0.16)}} \qquad \frac{\sigma^{(+)}}{s} = \sqrt{\frac{N_{av}}{\chi^2_{N_{av}-1}(0.84)}} \tag{7.12}$$

Therefore, the error bars for each point of the "signal jitter plot" are expressed as:

$$\left[s - s \cdot \sqrt{\frac{N_{av}}{\chi^2_{N_{av}-1}(0.16)}}, \quad s + s \cdot \sqrt{\frac{N_{av}}{\chi^2_{N_{av}-1}(0.84)}} \right] \tag{7.13}$$

For a larger sample size (N_{av}), because the $\chi^2_n(\alpha)$ distribution approaches a standard distribution, the error bars are more symmetrical. On the other hand, the errorbars are more asymmetrical for a smaller sample size. For example, Eq. 7.13 gives $[0.0059 \cdot s, \quad 0.084 \cdot s]$ for N_{av}=100, as opposed to $[0.875 \cdot s, \quad 1.42 \cdot s]$ for N_{av}=10. In Sec. 7.8.1, where this method is applied to data analysis, Fig. 7.6 shows a fitted jitter plot for an actual fringe scan.

---

[37]It has been confirmed that the difference in the fitted result of σ_φ is $\lesssim 1$ % when C_{const} is fixed to 0, as opposed to 5%.
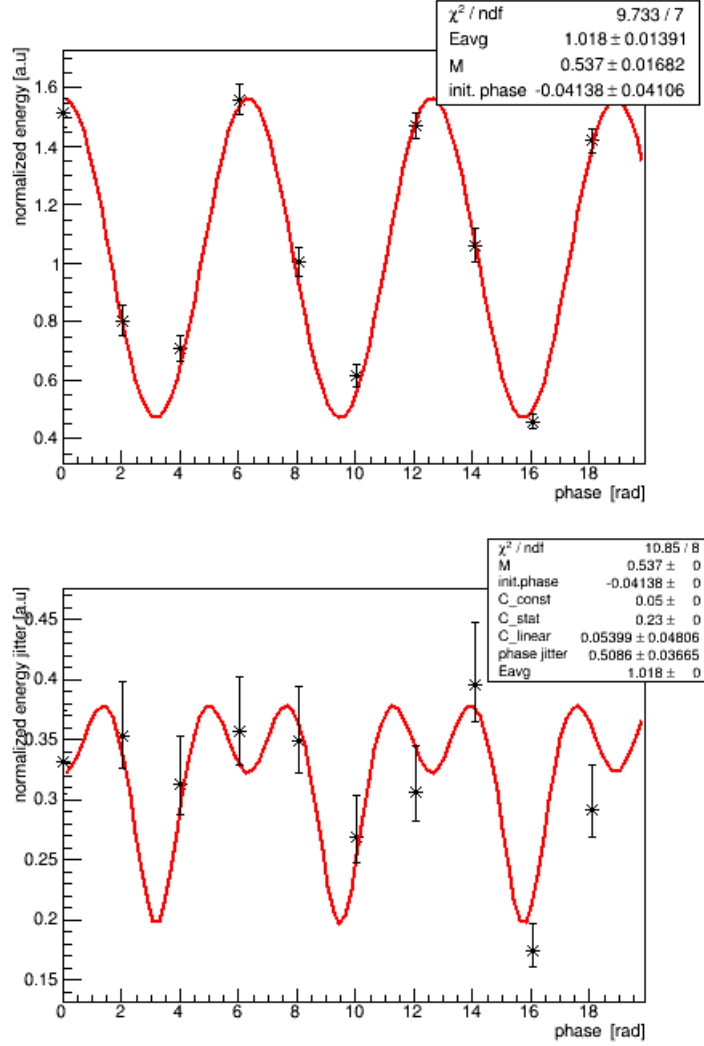
Figure 7.4: The schematics of phase jitter extraction using a two step process: (top) Step 1: the measured M spectrum is fitted with Eq. 2.10 in order to obtain M_{meas}, E_{avg} and φ_0. (bottom) Step 2: the energy jitter (S.D. of the N_{av} events) of the same scan is plotted as a function of φ, then fitted with Eq. 7.7 to extract σ_φ and C_{linear}. The fixed parameters are M_{meas}, E_{avg} and φ_0 obtained in Step 1 and the estimated values of the relatively time stable C_{const} and C_{stat}.

7.5 Simulation Test of Phase Jitter Extraction Method

This section uses simulation tests to demonstrate the precision of extracting σ_φ using the method described in Sec. 7.4, and using it to correct the measured M. This is important for precise σ_y evaluation since σ_φ is one of the dominant systematic errors. In the simulations, fringe scans are generated assuming nominal modulation M_0= 0.636, corresponding to σ_{y0}=40 nm for the 174 deg mode, and a realistic scenario of vertical jitter and phase instabilities.

7.5.1 Gaussian-like Phase Jitters

In this section, fringe scans are generated with the following input conditions:

- Phase jitter σ_φ is input into the Compton signal energy according to a random Gaussian distribution as: $E(\varphi, \sigma_\varphi) = E_{avg}\{1 + M \cdot \cos{(\varphi + \varphi_0 + Gaus(0, \sigma_\varphi))}\}$. The input σ_φ ($\sigma_{\varphi,in}$)

covers a wide range of $\{0, 0.23, 0.47, 0.71, 0.94\}$ rad. For the 174 deg mode, this corresponds to relative position jitter $\delta\Delta y$ of $\{0, 10, 20, 30, 40\}$ nm.

- Vertical jitter is input according to Eq. 7.8, consisting of $(5\%, 20\%, 10\%)$ w.r.t. E_{avg} from $(C_{const}, C_{stat}, C_{linear})$, each following a random Gaussian distribution [38]. This gives a typical total vertical jitter of about 23% at the mid-point fringe scan phases (where $E = E_{avg}$).

The fitting process described in Sec. 7.4 is used to extract σ_φ. Then, the extracted $\sigma_{\varphi,out}$ is used to correct the reduced M_{meas} back towards M_0 as Eq. 6.7. Figure 7.5 shows the simulation results as the mean and statistical error of 1000 pseudo experiments for $N_{av}=50$ and $N_{av}=10$; the precision of $\sigma_{\varphi,out}$ and M_{corr} is generally within tolerable ranges; The systematic bias intrinsic to this method are observed as follows:

- The relative deviation of M_{corr} w.r.t. M_0 is $\lesssim 1\%$ for $N_{av}=50$, and $< 4.5\%$ for $N_{av}=10$.

- The deviation of $\sigma_{\varphi,out}$ w.r.t. $\sigma_{\varphi,in}$ is < 15 mrad for $N_{av}=50$, and < 55 mrad for $N_{av}=10$ (with exception of zero-$\sigma_{\varphi,in}$).

- For smaller N_{av}, M is not reduced as much as the theoretic expectation $M_{meas} = M_0 \cdot \exp\left(-\sigma_\varphi^2/2\right)$ (pink curve). This will be explained in Sec. 7.5.3.
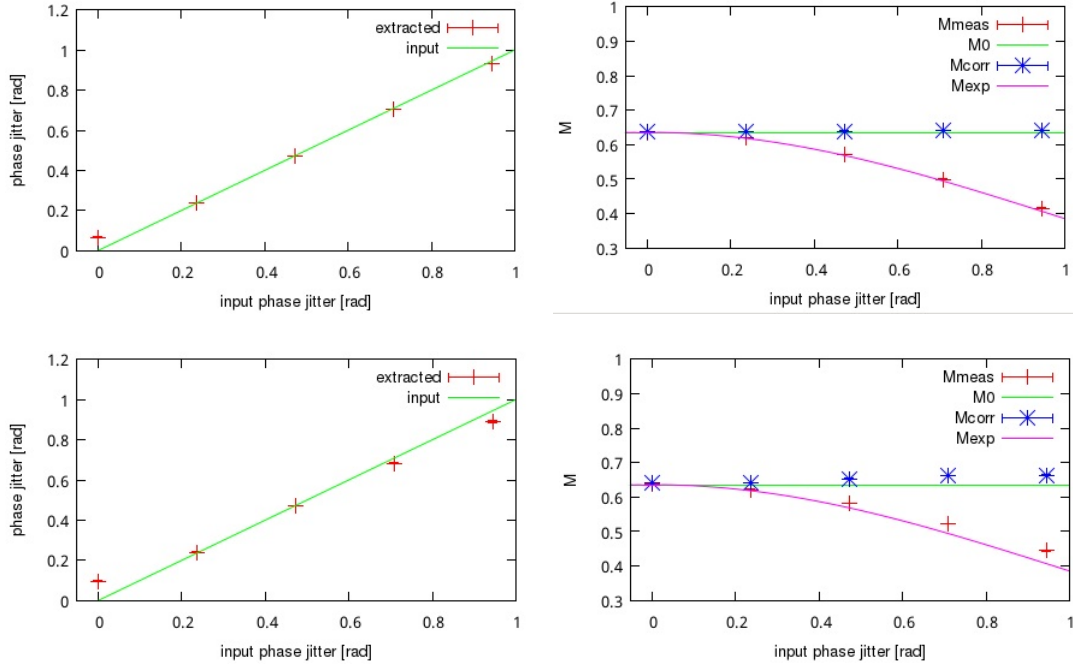
Figure 7.5: Fringe scan simulation with input of Gaussian-like σ_φ ($\sigma_{\varphi,in} = 0, 0.23, 0.47, 0.71, 0.94$ rad), and realistic vertical jitters totalling to about 23% w.r.t. E_{avg}. Shown here are the statistical results of 1000 pseudo experiments for $N_{av}= 50$ (top row) and $N_{av}= 10$ (bottom row). The left plots show the extraction precision for $\sigma_{\varphi,out}$ (red) w.r.t. the input $\sigma_{\varphi,in}$ (green). The right plots show the reduction of M_{meas} by $\sigma_{\varphi,in}$, and its correction (M_{corr}) using the $\sigma_{\varphi,out}$ extracted in the left plots.

---

[38] At the mid point of a fringe scan, relative vertical signal jitter is expressed as $\Delta E_V/E_{avg} = \sqrt{(C_{const}/E_{avg})^2 + (C_{stat}/\sqrt{E_{avg}})^2 + C_{linear}^2}$. Therefore, a more strict expression would be "5% w.r.t. E_{avg} from C_{const}, 20% w.r.t. $\sqrt{E_{avg}}$ from C_{stat}, and 10% from C_{linear}". In this thesis, the expression will be simplified by referring to all terms as "w.r.t. E_{avg}".

7.5.2 Complex Phase Fluctuations

The aim of this section is to study the effect of a more complex and realistic non-Gaussian phase fluctuation. The fringe phase variation for a previous laser was measured by T.Yamanaka in 2009 [32] using a phase monitor which used to be installed on the vertical table. This took place during beam off time, thus excludes e^- beam jitters. Figure 7.6 shows the reproduced version of this phase pattern, whose amplitude has an RMS of about 0.45 rad. The original amplitude of the phase pattern is multiplied by a factor of $\{0, 0.5, 1, 1.5, 2\}$, and input into fringe scan simulation similar to that in Sec. 7.5.1, assuming M_0=0.636 and vertical jitter comprised of (5%, 20%, 10%) w.r.t. E_{avg} from $(C_{const}, C_{stat}, C_{linear})$. The purpose is to observe the precision of $\sigma_{\varphi,out}$ and M_{corr} i.e. the correction of M_{meas} using $\sigma_{\varphi,out}$ as in Eq. 6.7. Two types of simulations are conducted; keeping all other conditions (e.g. vertical jitters) the same, their difference lies in the input phase, explained as follows:

1. Just the measured phase variation in Fig. 7.6 alone. Figure 7.7 shows the precision of $\sigma_{\varphi,out}$ and M_{corr} for N_{av}=50 and N_{av}=10.

2. The measured phase variation in Fig 7.6 as well as the following additional input phase instabilities: a linear phase drift of 80 mrad/min (worse than typical), and a 0.7 rad jump at φ=11 rad. Figure 7.8 shows the precision of $\sigma_{\varphi,out}$ and M_{corr} for N_{av}=50 and N_{av}=10.
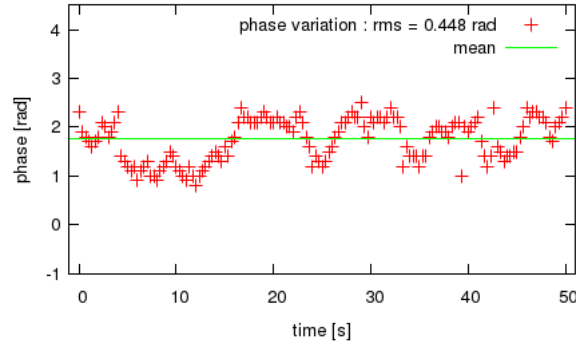
Figure 7.6: The measured phase variation of the laser fringes reproduced for 150 pulses in 3 Hz intervals.
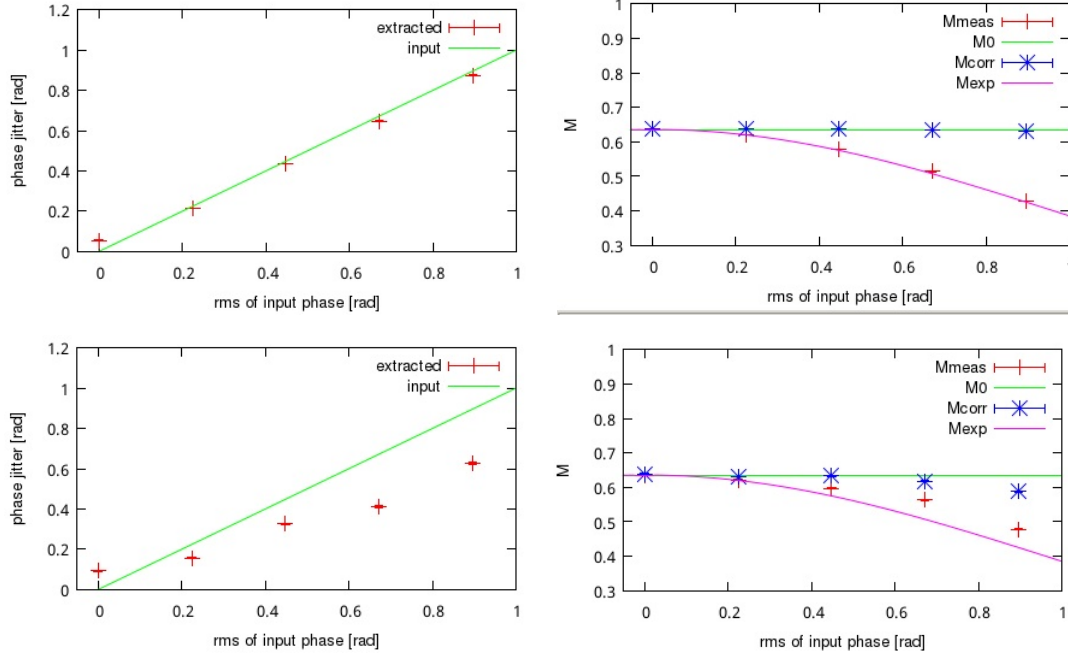
Figure 7.7: Fringe scan simulation using various amplitudes of the phase variation in Fig. 7.6 and realistic vertical jitters totaling to about 23% w.r.t. E_{avg}. Shown here are the simulation results for 1000 pseudo experiments for $N_{av} = 50$ (top) and $N_{av} = 10$ (bottom).

The plots on the left show the extraction precision of $\sigma_{\varphi,out}$ w.r.t. the input (green). The plots on the right show the M_{meas} reduced by $\sigma_{\varphi,in}$, and the precision of its correction using the $\sigma_{\varphi,out}$ extracted in the left plots.
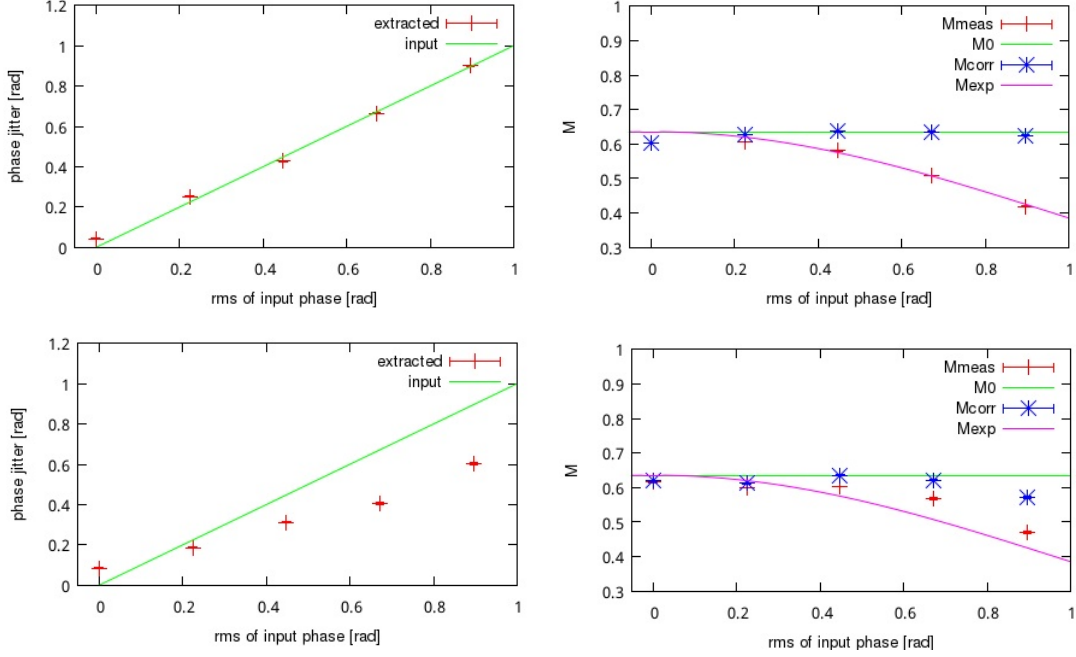
Figure 7.8: Fringe scan simulation with the same input conditions as in Fig. 7.7, as well as the following additional phase instabilities: a linear phase drift of 80 mrad/min, and a 0.7 rad jump at the fringe phase $\varphi=11$ rad. Shown here are the simulation results for 1000 pseudo experiments for $N_{av} = 50$ (top) and $N_{av} = 10$ (bottom).

The plots on the left show the extraction precision of $\sigma_{\varphi,out}$ w.r.t. the input (green). The plots on the right show the M_{meas} reduced by $\sigma_{\varphi,in}$, and the precision of its correction using the $\sigma_{\varphi,out}$ extracted in the left plots.

Regarding the case of the original phase RMS $\simeq 0.45$ rad in 2., results are compared between N_{av}=10, 20, 50, and 100 in Table 7.1 and Fig. 7.9. Here, $\Delta M_{corr} \equiv M_{corr} - M_0$ is the error of M_{corr}, ΔM_{meas} is the deviation of M_{meas} w.r.t. the expected value i.e. $M_0 \cdot \exp\left(-\sigma_\varphi^2/2\right)$, and ΔC_φ is the deviation of the correction factor $C_\varphi = \exp\left(-\sigma_{\varphi,out}^2/2\right)$ (using $\sigma_{\varphi,out}$) from the ideal $\exp\left(-\sigma_{\varphi,in}^2/2\right)$ (using $\sigma_{\varphi,in}$).

N_{av}	$\Delta M_{corr}/M_0$	$\Delta M_{meas}/M_{exp}$	$\Delta C_\varphi/C_{\varphi,exp}$
10	- 0.1%	4.8%	5.3%
20	- 2.1%	1.5%	4.0%
50	$\sim$ 0%	0.9%	0.9%
100	0.3%	0.9%	0.6%

Table 7.1: The comparison of results between N_{av}=10, 20, 50, and 100, for M_{corr} w.r.t. M_0, and M_{meas} and C_φ w.r.t. their values expected from a Gaussian model. These are from simulation using the particular input of phase amplitude RMS $\simeq 0.45$ rad, with all other input conditions same as in Fig. 7.8.
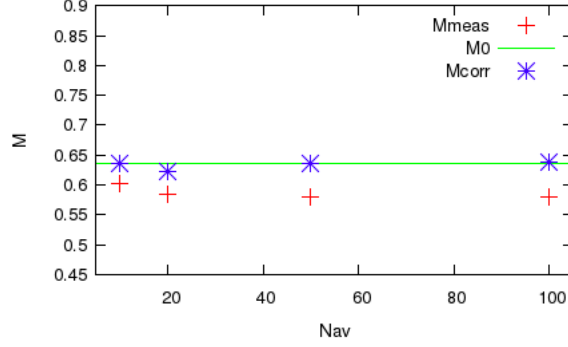
129

Figure 7.9: The measured phase variation in Fig. 7.6 with an amplitude RMS of about 0.45 rad is input into fringe scan simulation along with a linear phase drift of 80 mrad/min, a 0.7 rad jump at the fringe phase φ=11 rad, and realistic vertical jitters totaling to about 23% w.r.t. E_{avg}. Shown here are the simulation results for 1000 pseudo experiments of the effect on M_{meas} and M_{corr} (corrected using $\sigma_{\varphi,out}$) for N_{av} =10, 20, 50, and 100.

Interpretations:

The precision of $\sigma_{\varphi,out}$ (w.r.t. the RMS of $\sigma_{\varphi,in}$) and the precision of M_{corr} (w.r.t. M_0) is better for a larger N_{av}. These are explained as follows:

1. The realistic phase fluctuation is a combination of jitters and slower drifts. Its systematic effect on M_{meas} depends on the time structure of the scan, which in turn depends on N_{av} i.e. the time spent at each phase. The same phase variation (σ_φ) behaves more like Gaussian-like jitters for a large N_{av} and more like slow drifts for a small N_{av}. Therefore, a large N_{av} is more suited to the Gaussian model used for σ_φ extraction.

2. Just as for the Gaussian jitters in Fig. 7.5, for a large N_{av}, M_{meas} reduction is more in accordance with the expected $M_0 \cdot \exp\left(-\sigma_\varphi^2/2\right)$. This will be explained in Sec. 7.5.3. Both this and 1. explain the fact that the precision of M_{corr} (obtained using Eq. 6.7) is better for a large N_{av}.

Regarding the most complex phase variation in Fig. 7.8, for N_{av}=50, good precision is observed regardless of the amplitude of $\sigma_{\varphi,in}$ [39]:

- The deviation of $\sigma_{\varphi,out}$ (w.r.t. the RMS of $\sigma_{\varphi,in}$) is < 30 mrad,

- The relative deviation of M_{corr} (w.r.t. M_0) is < 2 %.

For a smaller N_{av}=10, the $\sigma_{\varphi,out}$ extracted using a Gaussian jitter model tend to be under-evaluated w.r.t. the RMS of $\sigma_{\varphi,in}$. This is due to the effect of drift components over-taking the effect of jitter components since less time is taken at each phase. However, the reduction of M_{meas} itself tends to be less apparent than that theoretically expected from a Gaussian model. Because the outcomes of the two factors $\sigma_{\varphi,out}$ and M_{meas} partially cancel each other out, the relative deviation of M_{corr} for N_{av}=10 is still better than 4% for all inputs except the largest $\sigma_{\varphi,in}$=0.89 rad, for which it is better than 10%. Note that ultimately, M_{corr} is the factor important for precise beam size evaluation.

---

[39] The discussions here are made with exception of the unrealistic case of zero-$\sigma_{\varphi,in}$. At zero input $\sigma_{\varphi,in}$, there is a "fake $\sigma_{\varphi,out}$" of about 48 mrad, due to the coupling to vertical jitters, to be explained in Sec. 7.6.

From Table 7.1 and Fig. 7.9, M_{corr} precision is best for N_{av}=100 and N_{av}=50. Although the former has a larger N_{av}, the more time consuming scan receives more M reduction from the significant input linear drift of 80 mrad/min, whereas the M correction only compensates for Gaussian-like phase jitters. Similarly when comparing Figures 7.7 and 7.8, a slight difference can be seen for the N_{av}=50 case, due to the effect of the linear phase drift.

The extraction precision of C_{linear}, as well as the values extracted from actual fringe scan data are given in Appendix E.

7.5.3 Interpretations of Modulation Reduction due to Phase Fluctuation

This section explains why the M reduction due to σ_φ is more in accordance with the theoretical curve $M_{meas} = M_0 \exp\left(-\sigma_\varphi^2/2\right)$ for a larger N_{av} scan, and less apparent for a smaller N_{av} scan [42]. Modulation is obtained by fitting the fringe scan data with the function (Eq. 2.10) $f\left(\varphi, E_{avg}, M, \varphi_0\right) = E_{avg}\left(1 + M\cos\left(\varphi + \varphi_0\right)\right)$, based on the minimization of

$$\chi^2 = \sum_i^N \frac{\{E\left(\varphi_i\right) - f\left(\varphi_i, E_{avg}, M, \varphi_0\right)\}^2}{\sigma_{E,i}^2} \tag{7.14}$$

The error bar $\left(\sigma_{E,i}\right)$ at each phase φ_i (i=1, 2,..., N: N = number of steps) is defined as the standard deviation of the N_{av} measured energy events divided by $\sqrt{N_{av} - 1}$.

Here we shall observe the distribution of $\cos\left(\phi\right)$, where the set phase $\phi \equiv \varphi + \varphi_0$ follows a Gaussian distribution with sigma σ_ϕ (= phase jitter). Figure 7.10 (top) shows the simulation results for 1000 events assuming σ_ϕ=0.7 rad at the fringe peak phase (mean ϕ=0), mid-point phase (mean $\phi = \pi/2$), and bottom phase (mean $\phi = \pi$).

The mean and standard deviation of $\cos\left(\phi\right)$ for N_{av} events will be denoted as a and s, respectively. Figure 7.11 shows the correlation between a and s at peak, mid-point, and bottom fringe phases, for 1000 pseudo experiments. At peak phase, the negative correlation between a and s indicates that the larger the mean of the measured energy $\left(\overline{E\left(\phi\right)}\right)$ is, the smaller its standard deviation σ_E will be. In contrast, at bottom phase, the positive correlation between a and s indicates that the smaller $\overline{E\left(\phi\right)}$ is, the smaller σ_E will be. In other words, the weight in Eq. 7.14 is "larger for larger energy data" at fringe peaks and "larger for smaller energy data" at fringe valleys. Furthermore, the comparison between N_{av}=10 and N_{av}=100 in Fig. 7.11 shows that this correlation trend is more significant for a smaller N_{av}. In conclusion, due to the enhancement in opposite directions at fringe peaks and valleys, for the same amount of phase jitter, a smaller N_{av} scan tends to result in a larger fitted M_{meas} than the theoretical value $M_0 \exp\left(-\sigma_\varphi^2/2\right)$. Figure 7.12 shows the difference in M reduction between $N_{av} = 10$, 50, and 100 with the same simulation input conditions as in Sec. 7.5.
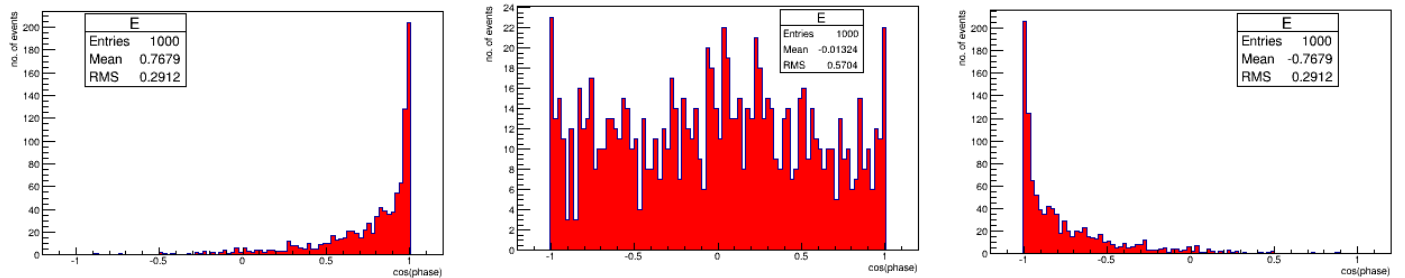

Figure 7.10: The distribution of 1000 events of $\cos\left(\phi\right)$, where ϕ is given a random Gaussian distribution with sigma=0.7 rad. From left to right: the distribution at the fringe peak phase i.e. mean ϕ=0, mid-point phase i.e. mean $\phi = \pi/2$, and bottom phase i.e. mean $\phi = \pi$.
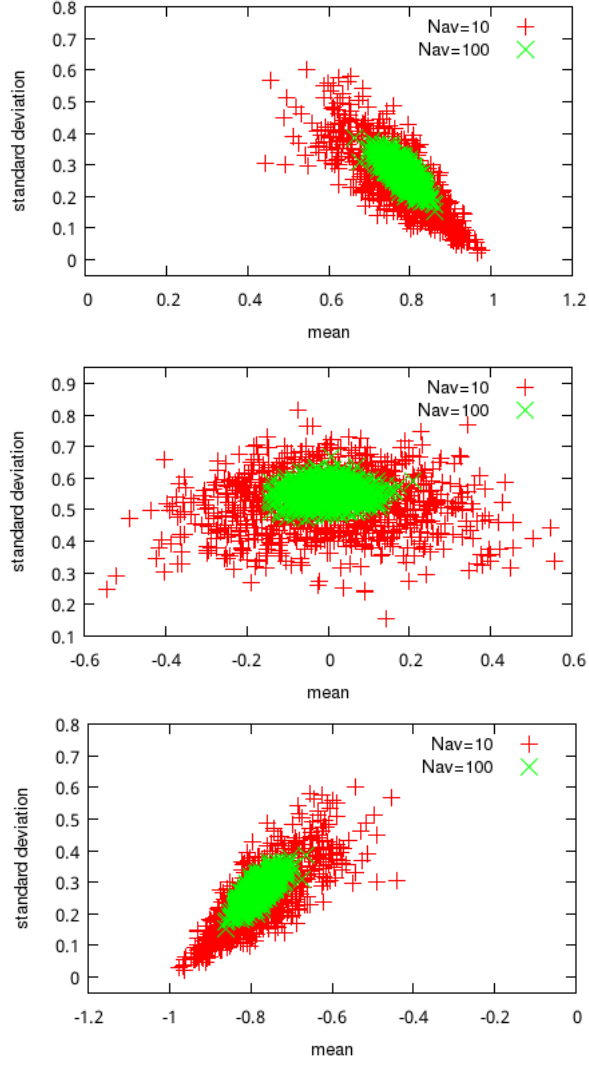
Figure 7.11: The correlation between the average and standard deviation of N_{av} events of $\cos(\phi)$, where ϕ has a Gaussian distribution with sigma=0.7 rad. The red and green represent N_{av}=10 and 100, respectively. (top) at fringe peak phase i.e. mean ϕ=0 (middle) at mid-point phase i.e. mean $\phi = \pi/2$ (bottom) at bottom phase i.e. mean $\phi = \pi$.
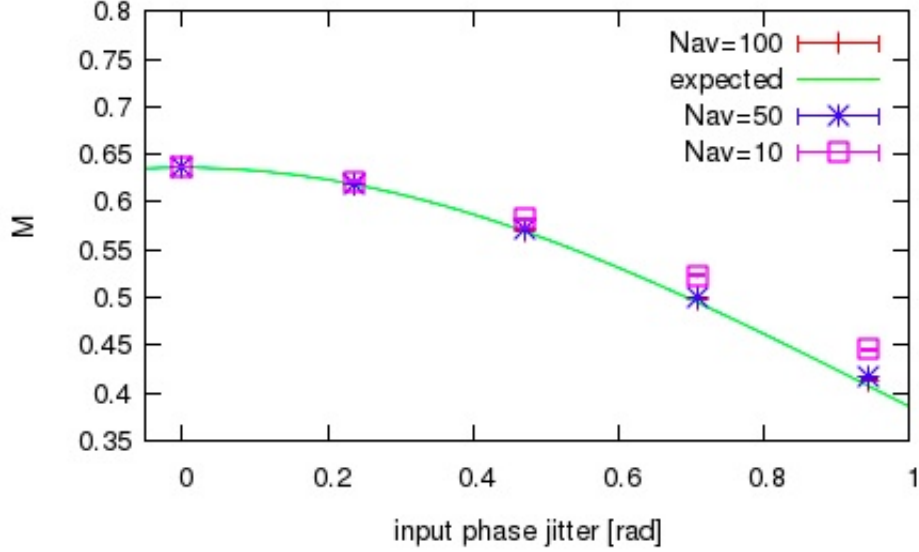
Figure 7.12: Simulation of M reduction due to a Gaussian-like σ_φ inputs ($\sigma_{\varphi,in}$ =0, 0.23, 0.47, 0.71, 0.94 rad) and the same input conditions as in Fig. 7.5. Shown here for N_{av}= 10, 50, and 100 are the statistical results of 1000 pseudo experiments.

7.6   Effect of Vertical Jitters

This section uses simulation to evaluate the effect of vertical jitters on the measured M_{meas} and on the extraction and compensation of σ_φ. In this section, the vertical jitter terms C_{const}, C_{stat}, and C_{linear} in Eq. 7.8 are defined as the contribution to relative signal jitter w.r.t. E_{avg} in a fringe scan.

7.6.1   Effect on Modulation

Fringe scan simulation was conducted as follows: vertical jitter was varied by changing only the most dominant term C_{stat} from 0% to 30%; $\sigma_{\varphi,in}$ and the terms C_{const} and C_{linear} are kept to 0. Results are shown as the statistical results of 1000 pseudo experiments. Figure 7.13 (left) shows the effect of vertical jitter on M_{meas} for N_{av}=50 and N_{av}=10. It can be concluded that vertical jitters do not cause apparent M reduction. Figure 7.13 (right) shows the relative error of M_{meas}, defined as the standard deviation of 1000 events divided by their average; the standard deviation increases with vertical jitters, and is larger for a smaller N_{av} by a factor of approximately $\sqrt{N_{av}}$. It has been confirmed that similar results are obtained when C_{const} or C_{linear} are changed.
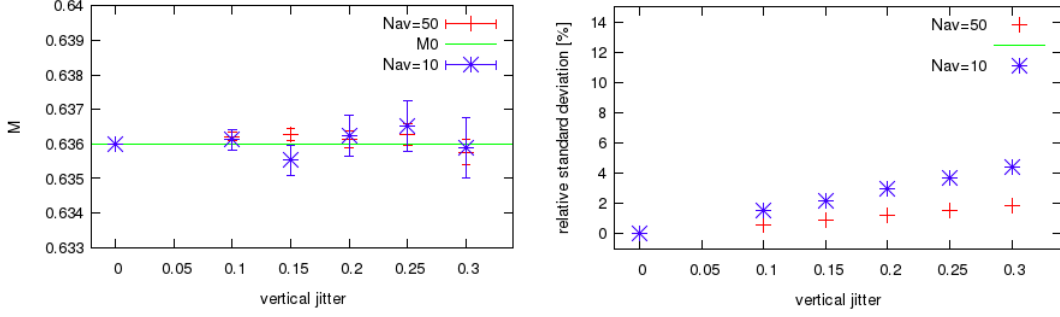
Figure 7.13: Simulation of the effect of vertical jitter on M_{meas} shown for fringe scans of N_{av}=50 (red) and N_{av}=10 (blue); input conditions are: $M_0 = 0.636$, $(C_{const}, C_{linear}) = (0\%, 0\%)$, $\sigma_{\varphi,in} = 0$ rad, and C_{stat} changed in steps from 0% to 30% w.r.t. E_{avg}. Shown here are the statistical results of 1000 pseudo experiments as a function of vertical jitter (C_{stat}): (left) M_{meas} and (right) the standard deviation of 1000 events of M_{meas} divided by their average.

7.6.2   Effect on Phase Jitter Extraction and Compensation

For the same simulation as in Fig. 7.13, keeping in mind that the input $\sigma_{\varphi,in}$ is zero, Fig. 7.14 shows the "fake $\sigma_{\varphi,out}$", defined as the non-zero $\sigma_{\varphi,out}$ extracted from fitting by the method in Sec. 7.4. This indicates the bias of $\sigma_{\varphi,out}$ determination attributed to the coupling from vertical jitters [40]. For a typical $C_{stat} = 15\%$, the fake σ_φ is about 30 mrad and 55 mrad for $N_{av} = 50$ and $N_{av} = 10$, respectively.
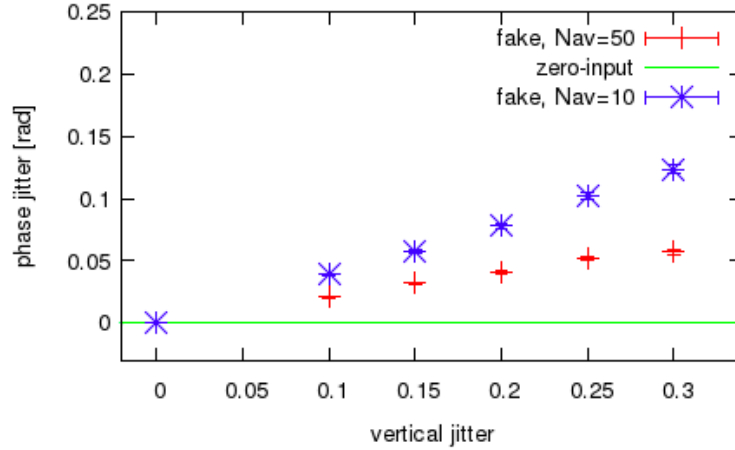
Figure 7.14: For the same simulation as in Fig. 7.13 with zero input $\sigma_{\varphi,in}$, the "fake $\sigma_{\varphi,out}$" extracted from fitting is plotted as a function of the input vertical jitter.

Uncertainty of Vertical Jitter Estimation

The accuracy of $\sigma_{\varphi,out}$ is affected by the precision of the value of C_{stat} fixed during the σ_φ extraction process ($C_{stat,fix}$). From the calibration results in Fig. 7.3, $C_{stat,fix}$ is estimated with a

---

[40]Here, the bias of $\sigma_{\varphi,out}$ is based on the average output value of the pseudo experiments in the simulation.

relative precision of about 20% [41]. For bunch charge 1×10^9, C_{stat} is estimated as 17.2±3.8% i.e. ΔC_{stat}=±3.8%. Here, $\Delta C_{stat} \equiv C_{stat,fix} - C_{stat}$ is the absolute error of $C_{stat,fix}$ (i.e. the deviation from the true C_{stat}).

Fringe scan simulation was conducted in order to evaluate the effect of the uncertainty of $C_{stat,fix}$ on the extraction and compensation of σ_φ. The input conditions are: $M_0 = 0.636$, $\sigma_{\varphi,in} = 0.47$ rad (Gaussian), and $(C_{stat}, C_{const}, C_{linear}) = (17\%, 5\%, 10\%)$. While the true C_{stat} (input) is 17%, $C_{stat,fix}$ is changed as {12%, 13.5%, 17%, 20.5%, 22%} in the fitting process to extract $\sigma_{\varphi,out}$. The extracted $\sigma_{\varphi,out}$ is then used to correct M_{meas} as in Eq. 6.7. Table 7.2 lists the results for the particular cases of $\Delta C_{stat} = 0\%$, 3.5%, and -3.5%, for $N_{av} = 50$ and $N_{av} = 10$:

- The relative error of $\sigma_{\varphi,out}$ ($|\delta\sigma_{\varphi,out}/\sigma_{\varphi,in}|$) is < 6.5% for $N_{av} = 50$, and $\lesssim$ 7.5% for $N_{av} = 10$.

- The relative error of M_{corr} ($|\delta M_{corr}/M_0|$) is < 1.5% for $N_{av} = 50$, and < 4% for $N_{av} = 10$.

Figure 7.15 shows the simulation results as a function of $C_{stat,fix}$. It can be seen that the under-estimation of $C_{stat,fix}$ leads to the over-evaluation of $\sigma_{\varphi,out}$ and thus the over-correction of M_{meas}; and vice versa, the over-estimation of $C_{stat,fix}$ leads to the under-evaluation of $\sigma_{\varphi,out}$ and thus the under-correction of M_{meas}. This can contribute to the systematic error of σ_φ extraction and compensation.

		$\Delta C_{stat} = -3.5\%$	$\Delta C_{stat} = 0\%$	$\Delta C_{stat} = 3.5\%$
$N_{av} = 50$	$\delta\sigma_{\varphi,out}/\sigma_{\varphi,in}$	4.9%	$\sim 0\%$	- 6.4%
	$\delta M_{corr}/M_0$	1.5%	0.5%	- 0.9%
$N_{av} = 10$	$\delta\sigma_{\varphi,out}/\sigma_{\varphi,in}$	4.7%	- 0.2%	- 7.4%
	$\delta M_{corr}/M_0$	3.8%	2.6%	1.0%

Table 7.2: Relative systematic errors ($\delta\sigma_{\varphi,out}/\sigma_{\varphi,in}$ and $\delta M_{corr}/M_0$) due to the under/over-estimation of the C_{stat} value fixed in the σ_φ fitting process; these result from fringe scan simulation for 1000 pseudo experiments. Input conditions are: $M_0 = 0.636$, $(C_{stat}, C_{const}, C_{linear}) = (17\%, 5\%, 10\%)$ w.r.t. E_{avg}, and $\sigma_{\varphi,in}= 0.47$ rad.
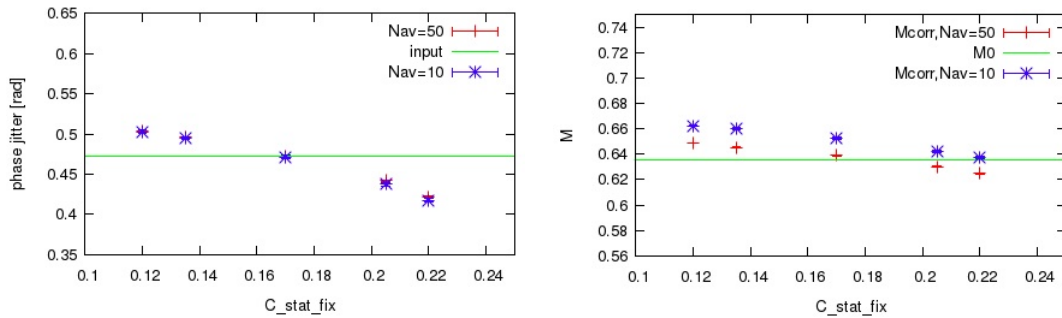

Figure 7.15: From the same fringe scan simulation as as in Table 7.2: $\sigma_{\varphi,out}$ (left) and M_{corr} (right) as a function of the fixed value of C_{stat}. Results are shown as the statistical results of 1000 pseudo experiments for $N_{av} = 50$ (red) and $N_{av} = 10$ (blue).

---

[41]This evaluation takes into account the uncertainty of the relationship between bunch charge and energy in Fig. 7.2 as well as the fitting precision of C_{stat} in Fig. 7.3.

7.7 Conclusion on the Precision of Correction for Phase Fluctuation

This section draws a conclusion on the precision of the evaluation of systematic errors due to phase fluctuation [42]. This was studied using simulation in Sections 7.5 and 7.6.

For a Gaussian-like phase jitter (Sec. 7.5.1):

- The relative deviation of M_{corr} w.r.t. M_0 ($|\delta M_{corr}/M_0|$) is $\lesssim 1\%$ for $N_{av}=50$, and $< 4.5\%$ for $N_{av}=10$.

- The deviation of $\sigma_{\varphi,out}$ w.r.t. $\sigma_{\varphi,in}$ ($|\sigma_{\varphi,out} - \sigma_{\varphi,in}|$) is < 15 mrad for $N_{av}=50$, and < 55 mrad for $N_{av}=10$.

On the other hand, the more realistic and complex phase variation (Sec. 7.5.2) is a combination of Gaussian-like jitters and slow drift components. In this case, it is more meaningful to focus on the precision of M_{corr}, rather than the value of the extracted $\sigma_{\varphi,out}$ itself. Ultimately, M_{corr} is the important factor for precise σ_y evaluation. For the same phase variation pattern, both the extracted $\sigma_{\varphi,out}$ and the reduction of M_{meas} are dependent on N_{av}. Therefore the outcome of M_{corr} ($= M_{meas}/\exp\left(-\sigma_{\varphi,out}^2/2\right)$ as in Eq. 6.7) is the combined result of the two. This was explained in Sec. 7.5.3. The relative deviation of M_{corr} w.r.t. M_0 is observed as follows:

- For $N_{av}=50$, $|\delta M_{corr}/M_0|$ is $\lesssim 2\%$

- For $N_{av}=10$, out of the $\sigma_{\varphi,in}$ RMS values tested, $|\delta M_{corr}/M_0|$ is $\lesssim 4\%$ for the realistic $\sigma_{\varphi,in}$ of 0.22 rad, 0.45 rad, 0.67 rad, and $\lesssim 10\%$ for the extraordinarily large 0.89 rad.

- Especially good precision was demonstrated for the $\sigma_{\varphi,in}$ RMS of 0.45 rad, which is close to that extracted from the most important beam time data in June 2014; $|\delta M_{corr}/M_0|$ is less than 1% for both $N_{av}=50$ and $N_{av}=10$.

The above assumed the C_{stat} term being fixed accurately to its true value during the fitting process to extract $\sigma_{\varphi,out}$. Section 7.6.2 showed that for the typical uncertainty of $C_{stat,fix}$ and assuming a $\sigma_{\varphi,in}$ of 0.47 rad, the additional relative error of M_{corr} is $< 1.5\%$ for $N_{av} = 50$, and $< 4\%$ for $N_{av} = 10$.

In conclusion, for the realistic phase variation amplitude of approximately 0.2-0.7 rad, the precision of M_{corr} w.r.t. M_0 is estimated to be better than 2.5% for $N_{av}=50$ and better than 5.7% for $N_{av}=10$. This takes into consideration both the complexity of a realistic phase pattern and the uncertainty of $C_{stat,fix}$. This conclusion will be applied to the evaluation of systematic errors for the most important beam size measurements in Sec. 8.1.2.

7.8 Extraction of Phase Jitter from Beam Time Data

7.8.1 Evaluation of Phase Jitter in Fringe Scans

In this section, the phase jitter (σ_φ) in actual beam size measurements is evaluated using the method given and verified in Sections 7.4 - 7.7. Figure 7.16 shows an example for a 174 deg mode $N_{av}=50$ fringe scan in May, 2014, where the extracted $\sigma_\varphi=0.73\pm0.03$ rad corresponds to relative vertical position jitter $\delta\Delta y = 30.9\pm1.4$ nm. This causes a $\sigma_{y,meas}$ over-evaluation of approximately 9.5 - 12.5 nm. Figure 7.17 shows the history of the estimated σ_φ in fringe scans sampled from April to June of 2014. For the smallest σ_y measured in the 174 deg mode in June 2014, the typical σ_φ is 0.4-0.7 rad, corresponding to $\delta\Delta y$ of about 15-30 nm. For the 30 deg mode, σ_φ is smaller, typically < 300 mrad. The mode dependence of σ_φ can also be inferred from the simulation in Sec. 6.3.1 and the data analysis in Table 6.1, and can be explained as follows:

---

[42]The discussions here are made with exception of the unrealistic case of zero-$\sigma_{\varphi,in}$

1. The path length after the half mirror is longer for the 174 deg mode than that of the 30 deg mode by a factor of 2; therefore laser pointing jitter leads to more path length variation and consequently larger σ_φ for the 174 deg mode.

2. The 174 deg mode is more sensitive to e^- beam jitter by about a factor of 4; relative position jitter is related to phase jitter as $\sigma_\varphi = 2k_y \cdot \delta\Delta y$. The factor $2k_y = 2\pi/d$ is 0.0236 nm^{-1} for the 174 deg mode, as opposed to 0.00611nm^{-1} for the 30 deg mode. For example, $\delta\Delta y$= 20 nm would cause $\sigma_\varphi = 0.47$ rad for the former and only $\sigma_\varphi = 0.12$ rad for the latter.
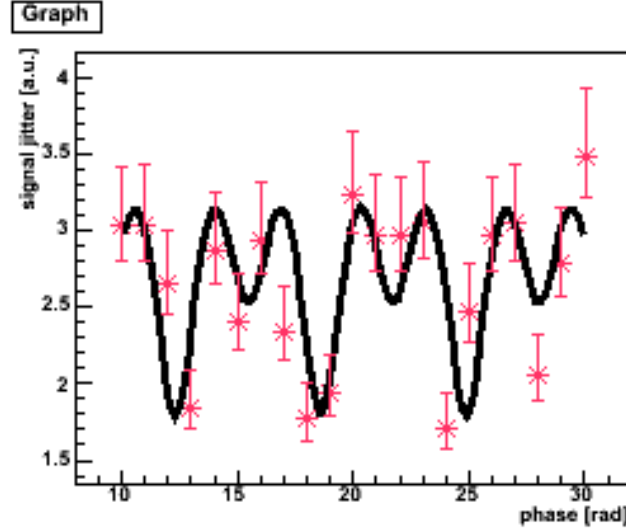
Figure 7.16: An example of σ_φ extraction for a 174 deg mode N_{av}=50 fringe scan. Here, the signal jitter (standard deviation of N_{av} events measured at each phase) is plotted as a function of phase, and σ_φ is obtained by fitting. For this scan, σ_φ is estimated to be 0.74±0.03 rad.
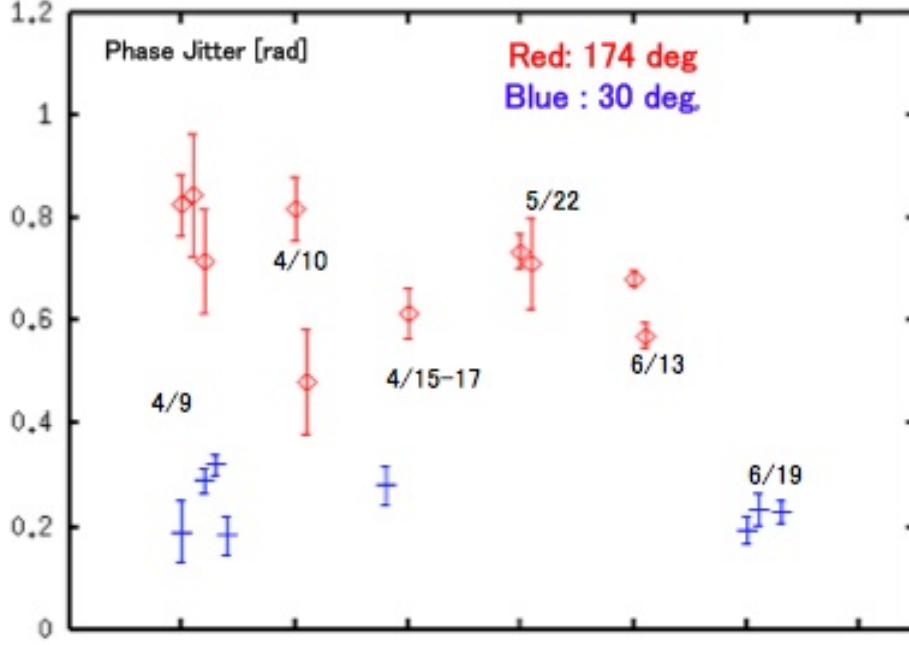
Figure 7.17: The history of σ_φ extracted from randomly sampled single fringe scans in April - June of 2014. The red points and blue points represent the 174 deg and 30 deg modes, respectively. Both modes are a mixture of N_{av}=50 and N_{av}=10. The error bars are the fitting errors. The horizontal axis represents time.

7.8.2 Modulation Correction using the Extracted Phase Jitter

Using the extracted $\sigma_{\varphi,out}$, the measured M_{meas} can be corrected as $M_{corr} = M_{meas}/\exp(-\sigma_\varphi^2/2)$ (Eq. 6.7). The precision was demonstrated in Sections 7.5 - 7.7 to be better than a few %.

Modulation correction in consistent scans

Table 7.3 lists the M_{meas}, $\sigma_{\varphi,out}$, and M_{corr} as the statistical results of a few sets of "continuous scans" recorded in spring of 2014. These consist of consecutive N_{av}=10 (or 20) scans, with 1 or more N_{av}=50 scans within the same time slot, under assumedly the same e^- beam conditions. As explained in Sec. 7.5.2, the realistic phase variation is a combination of jitters and drifts. Thus, both its effect on M_{meas} and the extracted value of $\sigma_{\varphi,out}$ depend on the time structure (N_{av}) of the fringe scan. Therefore M correction needs to be conducted for each individual scan within each N_{av} group.

Figure 7.18 compares the results of M_{meas}, M_{corr}, $\sigma_{\varphi,out}$, and $\delta\Delta y$ (converted as $\delta\Delta y = \sigma_{\varphi,out}/(2k_y)$) between small N_{av} (10 or 20) and large N_{av} (50) from May-June of 2014. Based on these, the following observations are made:

1. After correcting each individual scan using its $\sigma_{\varphi,out}$, the values of M_{corr} are closer between N_{av}=10 and N_{av}=50 within the same group than the values of M_{meas} before correction.

2. The relative position jitter $\delta\Delta y$ is in general between 50-70% of $\sigma_{y,corr}$ i.e. the "true" beam size.

Modulation Correction for Wakefield Studies

Stable measurements by the Shintake Monitor play an essential role in the study of e^- beam factors which impose limitations on small σ_y focusing. A possibly dominant factor is the wakefield effect due to the interaction of the beam with the electromagnetic fields generated at discontinuities in the beam line (see [18] and Appendix G). Because wakefield effects cause σ_y to increase with bunch charge (N_e), they can be studied by measuring M while changing N_e in steps. An example is given in Fig. 7.19, where M_{meas} is plotted as a function of N_e. Plotted together here is the M_{corr} calculated by inserting the $\sigma_{\varphi,out}$ extracted for each scan into Eq. 6.7. These are then fitted with an exponential function. The consistency of the fitted sigma between M_{meas} and M_{corr} is another indication of the reliability of σ_φ extraction and compensation: 2.48±0.11 for M_{meas} and 2.64±0.12 for M_{corr}. These indicate the growth of σ_y w.r.t. N_e to be about 17 nm/10^9.
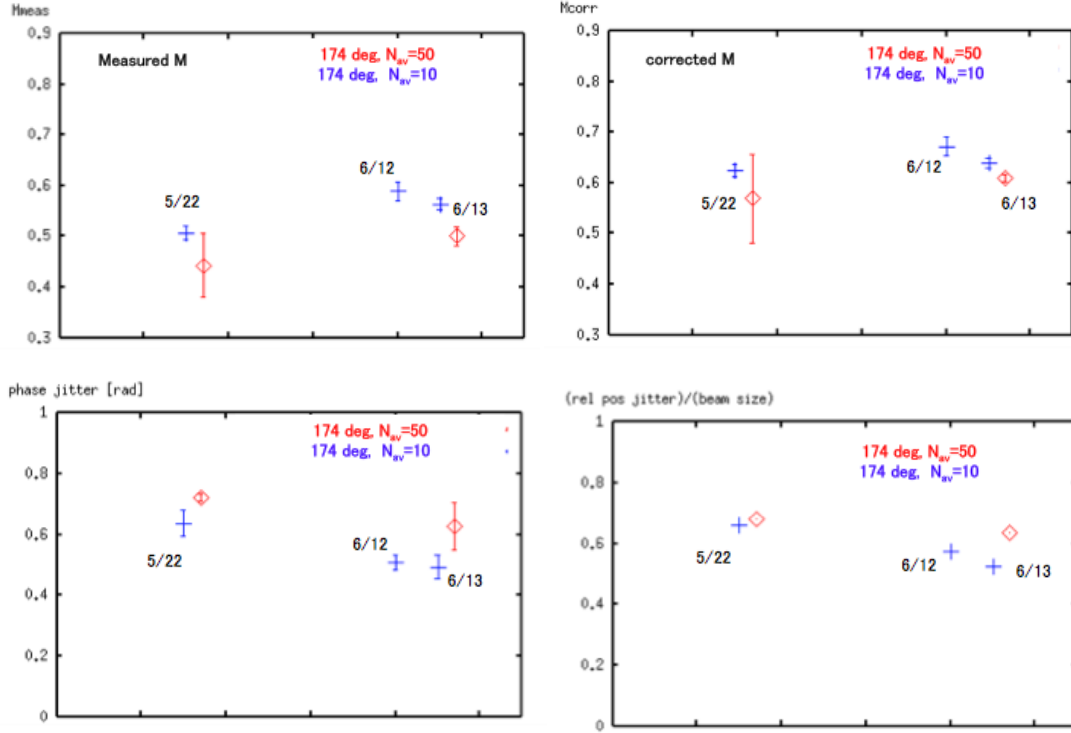
Figure 7.18: [top] The measured M (left) and the M corrected using the extracted σ_φ (right) for representative 174 deg mode "continuous scans" in May-June of 2014. Red and blue represent large N_{av} (50) and small N_{av} (10), respectively. The data points and their error bars show the mean and standard deviation divided by $\sqrt{N-1}$ (N = the number of scans), respectively, of the scans in each set. The horizontal axis represents time.
[bottom] The σ_φ extracted for the same continuous scans as the top plots (left) and the ratio of relative position jitter $\delta\Delta y$ ($= \sigma_\varphi/(2k_y)$) w.r.t. $\sigma_{y,corr}$ (right).
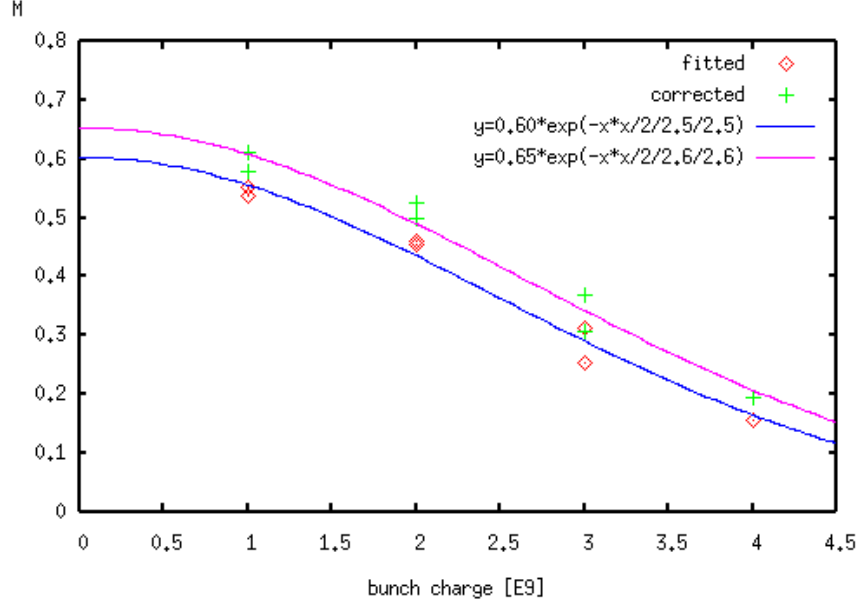
Figure 7.19: A "beam intensity scan" (for ATF2 wakefield study) showing M_{meas} as a function of beam bunch charge. Plotted together is M_{corr} corrected using the σ_φ extracted for each scan. The sigmas of the fitted exponential functions are approximately consistent between M_{meas} and M_{corr}. These indicate that the beam size growth w.r.t. the beam bunch charge is about 17 nm/10^9.

date (in 2014)	Apr. 9	Apr. 10	Apr. 17	May 22	June 13
bunch charge [10^9]	0.7	0.55	0.53	0.6	1.1
small N_{av} scans					
(N_{av}, no. of scans)	(10, 8)	(20, 6)	(20, 10)	(10, 10)	(10, 12)
M_{meas}	0.297±0.019	0.333±0.012	0.401±0.010	0.507±0.013	0.563±0.011
$\sigma_{y,meas}$ [nm]	66.1±1.8	62.6±1.0	57.1±0.8	49.2±0.6	45.1±0.8
σ_φ [rad]	0.545±0.120	0.720±0.064	0.550±0.050	0.637±0.043	0.492±0.039
M_{corr}	0.361±0.027	0.435±0.010	0.471±0.017	0.625±0.012	0.640±0.009
$\sigma_{y,corr}$ [nm]	60.5±2.2	54.5±0.8	51.8±1.3	40.8±0.9	39.7±0.6
$\Delta\sigma_y$ [nm]	5.6±2.8	8.1±1.3	5.3±1.5	8.4±1.1	5.4±1.4
large N_{av} scans					
(N_{av}, no. of scans)	(50, 3)	(50, 2)	(50, 2)	(50, 2)	(50, 2)
M_{meas}	0.285±0.025	0.352±0.029	0.394±0.018	0.443±0.064	0.500±0.018
$\sigma_{y,meas}$ [nm]	66.9±2.3	61.1±2.4	57.7±1.4	53.9±4.8	49.7±1.3
σ_φ [rad]	0.792±0.047	0.651±0.238	0.649±0.047	0.722±0.012	0.628±0.078
M_{corr}	0.419±0.037	0.440±0.032	0.465±0.067	0.569±0.088	0.610±0.008
$\sigma_{y,corr}$ [nm]	55.6±1.8	54.0±2.4	52.3±4.9	44.8±5.6	41.9±0.5
$\Delta\sigma_y$ [nm]	11.3±2.9	7.1±3.4	5.4±5.1	9.1±7.4	7.8±1.4

Table 7.3: The comparison between consecutive scans of small N_{av} (10 or 20) and large N_{av} (50), of the following: the measured M_{meas} and $\sigma_{y,meas}$, the extracted phase variation ($\sigma_{\varphi,out}$), and the M_{corr} and $\sigma_{y,corr}$ corrected using the $\sigma_{\varphi,out}$ for each scan. The statistical errors are defined as the standard deviation of the scans divided by $\sqrt{N-1}$, where N is the number of scans. $\Delta\sigma_y$ is the contribution to σ_y growth from σ_φ.

7.8.3 Comments about Electron Beam Jitter

The direct measurement of vertical e$^-$ beam jitter ($\delta\Delta y_e$) at the IP is not available yet since the IPBPM is still under commissioning for electronics and alignment at ATF2. As a support for the ATF2 Goal 1, the IPBPM aims to achieve a resolution of 10-20 nm with 30 μm dynamic range, which contributes 1.3 - 4.7 nm to $\sigma_y \simeq$40 nm. This corresponds to a σ_φ which is within the range that can be extracted precisely from fringe scans using the method given in Sec. 7.4.

The information from BPMs in the upstream sections of the FFS beam line indicate that $\delta\Delta y_e$, mostly due to the vibration of quadrupole magnets, is generally about 15% of σ_y [38]. The $\delta\Delta y_e$ at the IP is thought to the convolution of this and a significant additional jitter caused by the vibration of the final doublet (FD) quadrupoles, QD0 and QF1 [30]. In the table below, the first column lists the measured vertical vibrations ($\delta\Delta y_{mag}$) of QD0 and QF1[22]. The second column lists the $\delta\Delta y_e$ at the IP translated from $\delta\Delta y_{mag}$. The third column lists the corresponding phase jitter in fringe scans σ_φ (estimated as $2k_y \cdot \delta\Delta y_e$). The fourth column lists the contribution to the growth of a nominal σ_y= 40 nm. The first two rows are for each of QD0 and QF1, while the third row combines them as the FD, assuming they are non-correlated. The last row convolutes the FD vibration with the $\delta\Delta y_e$ (assumedly 15% of σ_y= 40 nm) coming in from upstream.

	δy_{mag}	$\delta\Delta y_e$	σ_φ	$\Delta\sigma_y$
QD0	4.8 nm	7.3 nm	0.17 rad	0.7 nm
QF1	30 nm	12.6 nm	0.30 rad	1.9 nm
FD		14.6 nm	0.35 rad	2.6 nm
total (FD+upstream)		15.8 nm	0.37 rad	3.0 nm

The smallest σ_y measured in June 2014 are close to 40 nm. For the case of σ_y=40 nm, the total $\delta\Delta y_e$ of about 16 nm is about 40% of σ_y. Assuming a total σ_φ of 0.5 rad (typical for June 2014), the subtraction of the contribution from $\delta\Delta y_e$ (0.37 rad) in quadrature would leave the contribution from the Shintake Monitor to be about 0.34 rad. This indicates that the contribution to the total phase jitter (relative position jitter) is about equal between the laser and the e$^-$ beam. The estimated contribution from the laser is comparable in scale to (a) the laser-only phase jitter measured by T.Yamanaka (RMS~0.45 rad) for a previous laser, and (b) the simulation results in Sec. 6.3.2 which assumed a pessimistic value for laser pointing jitter.

7.9 Status of Signal Jitter in Fringe Scans

This section describes the status of signal jitters observed in actual fringe scans. The following notations are used:

- $\Delta E(\varphi)$: signal jitter i.e. standard deviation of the N_{av} measured energy events at each phase.

- $E(\varphi)$: mean of the N_{av} measured energy events at each phase.

- $\Delta E_{rel}(\varphi)$: "relative signal jitter" i.e. $\Delta E(\varphi)$ divided by $E(\varphi)$ at each phase.

The number of signal photons per bunch is estimated in Sec. 3.6.1 to be O(10^2); thus the total energy deposit per bunch in the detector is expected to have a Gaussian-like distribution. Figures 7.20 and 7.21 show the distribution of energy measured at a single fixed phase of a N_{av}= 50 fringe scan. Figure 7.20 shows the sum of energy deposit in the front four detector layers. Figure 7.21 shows the energy deposit in each of the eight PMTs. These distribution shapes and ΔE_{rel} from the real data are comparable to those from simulation such as shown in Fig. 7.22. For the same scan, $\Delta E_{rel}(\varphi)$ and

the M spectrum ($E(\varphi)$) are plotted together in Fig. 7.23 (left). $\Delta E(\varphi) = \sqrt{\Delta E_p^2(\varphi) + \Delta E_p^2(\varphi)}$ and its two components, $\Delta E_p(\varphi)$ and $\Delta E_V(\varphi)$, are plotted together with the M spectrum in Fig. 7.23 (right). Both $\Delta E_{rel}(\varphi)$ and ΔE_p are minimum at the fringe peaks and maximum at the mid-points. $\Delta E_V(\varphi)$, which scales with energy $E(\varphi)$, is in phase with the M spectrum.

Relative signal jitter ΔE_{rel} in a fringe scan is typically 15-25% at fringe peaks, and 25-35% at fringe mid-points. Table 7.4 lists the contribution from the individual signal jitter sources described in Sec. 7.1. Adding each component in quadrature yields a total approximately consistent with the ΔE_{rel} observed in actual fringe scans at mid point phases for the similar beam bunch charge of 10^9.
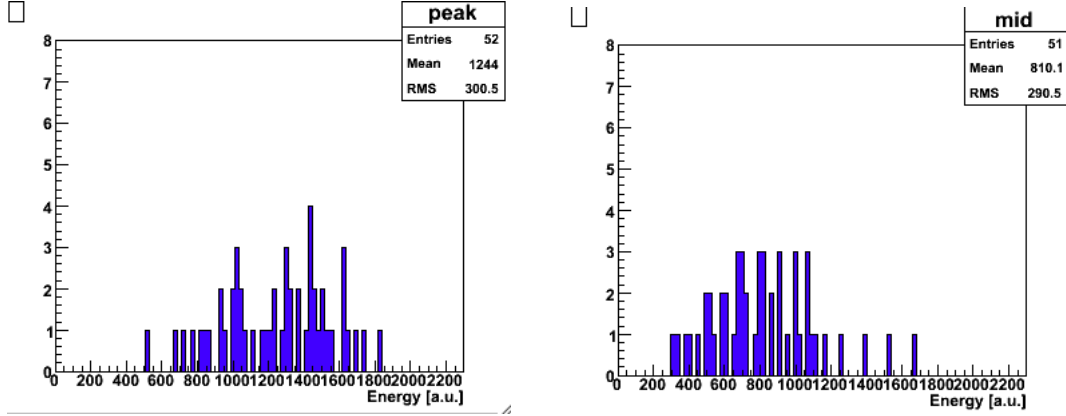
Figure 7.20: The distribution of energy events measured at a particular single phase in a N_{av}=50 fringe scan. (left) at peak (right) at mid-point. Here, signal jitter (= RMS/mean) is 22% and 33% at the peak and mid-point phases, respectively.
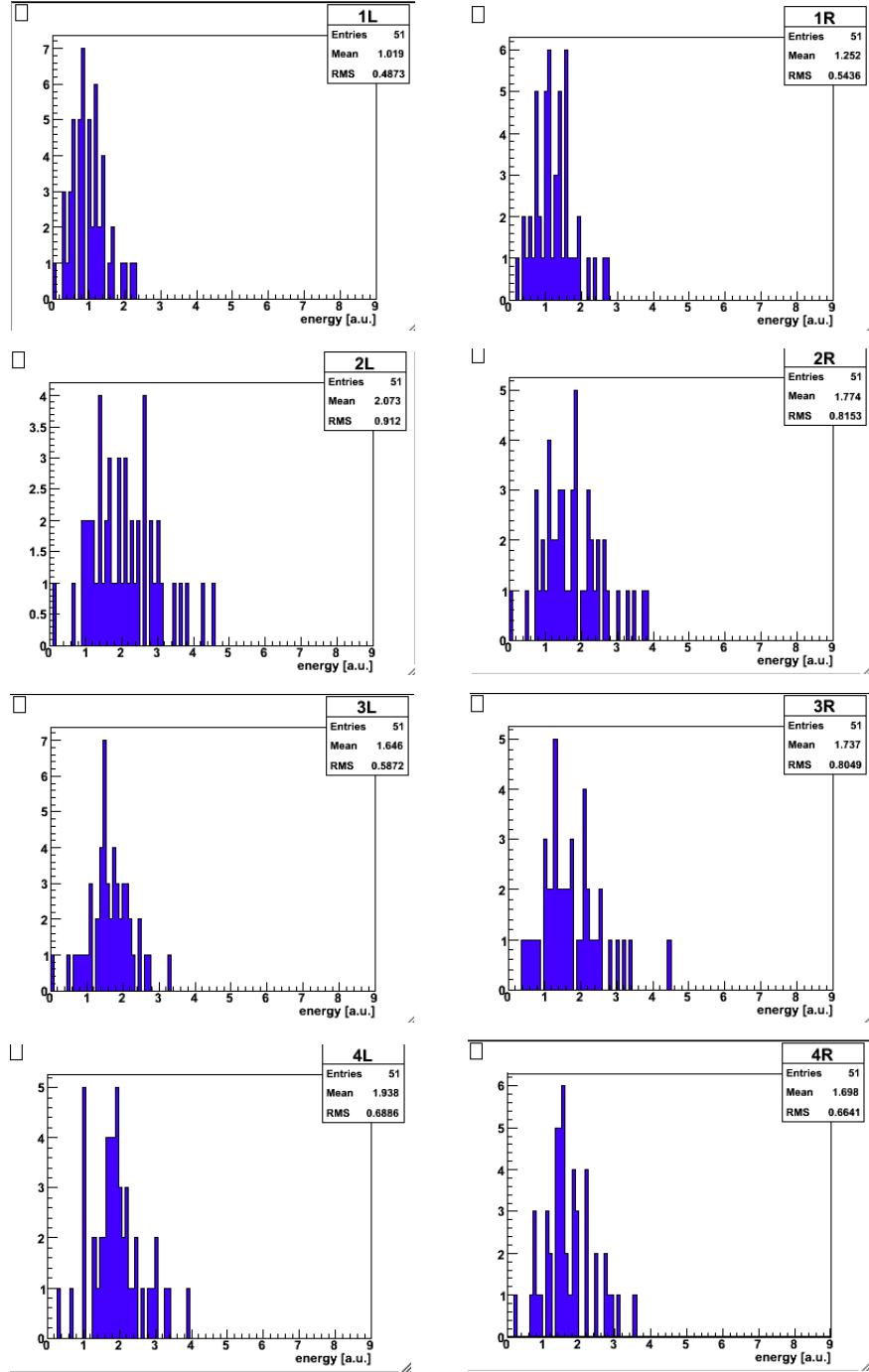
Figure 7.21: The distribution of energy deposit measured by each of the eight PMTs of the front four detector layers, at one of the mid points in the same N_{av}=50 fringe scan as in Fig. 7.20.
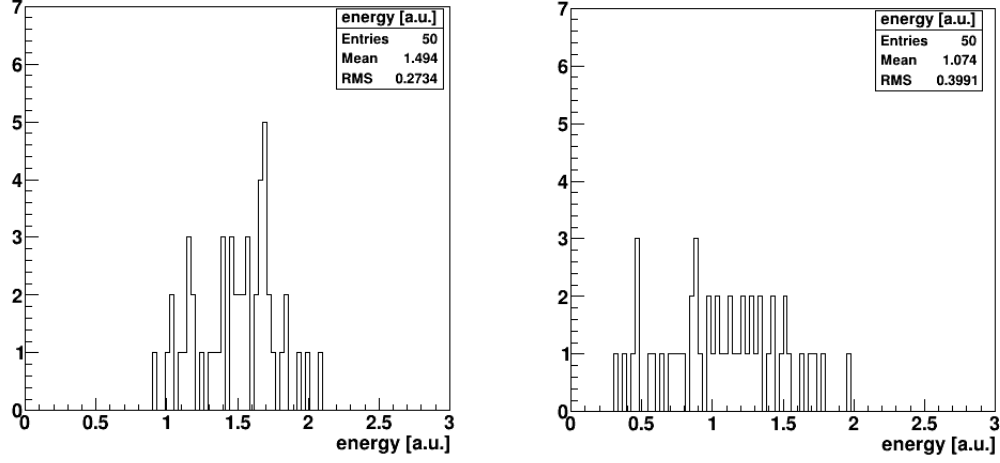
Figure 7.22: The distribution of Compton signal energy from the simulation of a N_{av}=50 fringe scan assuming M_0=0.636, σ_φ=0.59 rad, and vertical jitters consisting of (5%, 15%, 10%) w.r.t. E_{avg} from (C_{const}, C_{stat}, C_{linear}); (left) at a single peak phase; (right) at a mid-point phase. Here, signal jitter (= RMS/mean) is 18% and 37% at peak and mid-point, respectively.
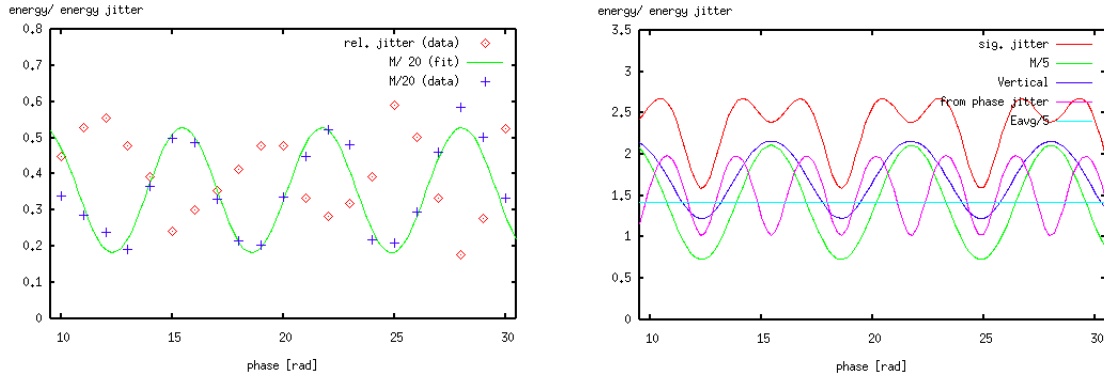
Figure 7.23: For the same N_{av}=50 scan as in Fig. 7.20: (left) The M spectrum and the relative signal jitter $\Delta E_{rel}(\varphi)$ are plotted together as a function of phase φ. (right) Total signal jitter $\Delta E(\varphi)$ and its two components $\Delta E_p(\varphi)$ and $\Delta E_V(\varphi)$, are plotted together with the M spectrum as a function of phase φ. The dots and the solid curves are the real data and the fitted results, respectively.

144

source	$\Delta E/E_{avg}$	comments
phase jitter (vertical relative position jitter)	28%	assume σ_φ= 500 mrad
relative timing jitter	$\lesssim 5\ \%$	see Sec. 7.1.4
total laser power jitter	$\lesssim 1\%$	see Sections 5.5 and 7.1.5
horizontal relative position jitter	$\lesssim 2\ \%$	see Sections 7.1.6 and 5.2
BG fluctuation	$< 5\%$	see Sec. 7.1.3
statistical fluctuations	$\lesssim 20\%$	see Sec. 3.6
ICT monitor resolution	$\sim 2\%$	see Sec. 7.1.7
total	$\lesssim 35\%$	at fringe mid-point

Table 7.4: The contribution from individual sources to the signal jitter w.r.t. E_{avg} in a fringe scan. The estimation here assume e$^-$ bunch charge of 10^9, N_{sig}=200 entering the detector, and $\sigma_y = 40$ nm.

8 Summary

8.1 Beam Time Performance

By June 2014, the Shintake Monitor has been stably measuring a world record σ_y of below 45 nm [19]. This section gives the full σ_y evaluation based on the systematic error studies in Chapters 6 and 7. The results demonstrate that the ATF2 Goal 1 σ_y of 37 nm has been achieved.

8.1.1 Evaluation of Measurement Stability

Section 4.1 described the factors that contributed to the ATF2 beam focusing progress, focusing mainly on the improvements of the accelerator beam line and e^- beam stability [43]. As for the Shintake Monitor system, the following improvements are thought to have contributed significantly to the measurement of small σ_y in 2014 spring:

1. The reduction of signal jitters by (a) the tuning of the laser profile and (b) adjustment of the injection seed laser to stablize the laser Q-switch timing.

2. The speeding up of the Shintake Monitor control software from about 1 Hz to about 3 Hz; this may have reduced effect from drifts in the position of the laser and / or the e^- beam.

3. The reinforcement of the detector shielding by adding Pb blocks against bremstrahlung BG and paraffin plates against neutron BG.

These efforts realized efficient beam tuning using the Shintake Monitor with a measurement stability of as good as about 5%. Table 8.1 and Fig. 8.1 show the results for two representative sets of continuous N_{av}=10 scans conducted at the 174 deg mode under stable beam condition and a beam bunch charge $\simeq 1 \times 10^9$. On June 12, 10 scans were taken within about 30 min. Just about 24 hrs later, on June 13, 12 scans were taken within about 50 min [44]. These are the results before correcting for systematic errors, and are shown in the form of the mean and standard deviation (S.D.) of the scans in each set. The results of some other consecutive scans from 2014 spring were shown in Table 7.3.

Figure 8.2 shows two examples of single fringe scans from the June 12 set in Fig. 8.1 (left). Without correction for σ_φ, nor taking into account any other systematic errors, the results are: (left) $M_{meas} = 0.660 \pm 0.021(stat.)$, $\sigma_{meas} = 38.3 \pm 1.5(stat.)$ nm; (right) about 17 min later: $M_{meas} = 0.678 \pm 0.020(stat.)$, $\sigma_{meas} = 37.1^{+1.4}_{-1.5}(stat.)$ nm. For each fringe scan, at a single phase, 10 pulses (N_{av}=10) are measured with the laser colliding with the e^- beam (E_{ON} in Sec. 3.5.4) and 1 pulse is measured without collision as the BG energy (E_{OFF} in Sec. 3.5.4). This is repeated for each of the 20 phases in the scan. Then the mean of the 10 pulses of Compton signal energy $E_{sig} = E_{ON} - E_{OFF}$ is plotted as a function of phase, with the errorbars being the standard deviation divided by $\sqrt{N_{av} - 1}$. This cosine-like curve is fitted with Eq. 2.10 to obtain the M_{meas} shown in the histograms in Fig 8.1.

Before each of the two continuous scan sets was conducted, the multi-knob tuning described in Sec. 4.1 was carried out in order to focus the beam size. In addition, out of the setup procedures in Sec. 4.2, the factors that could change over time were reoptimized: transverse and longitudinal position alignment of the laser w.r.t. the e^- beam, and laser timing adjustment.

---

[43]Because the e^- beam orbit feedback ceases to function below the threshold beam bunch charge of 0.8×10^9, some measurements conducted at a bunch charge lower than that may have been affected by beam instability. However this could not be confirmed since the BPMs cannot record reliable beam orbit information at such low beam intensity.

[44]Between the set on June 12 and the set on June 13, the position of the OTR monitors in the extraction line were scanned and moved for the purpose of wakefield studies. It is not certain where this may have caused some slight changes in the e^- beam orbit.

date	M_{meas}	$\sigma_{y,meas}$ [nm]	stability [45]
June 12 (10 scans)	0.589 ± 0.050 (S.D.)	43.3 ± 3.7 (S.D.)	8.5%
June 13 (12 scans)	0.563 ± 0.036 (S.D.)	45.1 ± 2.7 (S.D.)	6.4%

Table 8.1: The results of two representative sets of continuous N_{av}=10 scans conducted in the 174 deg mode, before correcting for systematic errors, shown as the mean and standard deviation (S.D.) of the scans in each set. The common conditions are: N_{av}=10, beam bunch charge $\simeq 1 \times 10^9$, and the normalization of the measured energy by the measured bunch charge pulse-by-pulse.
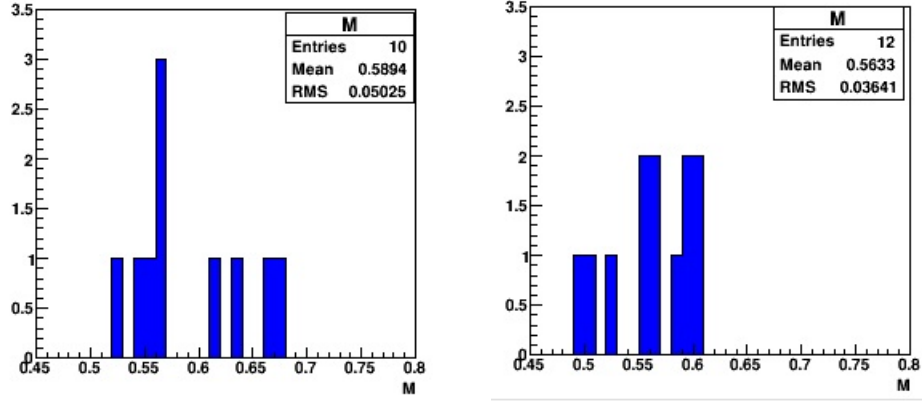
Figure 8.1: The two sets of continuous scans in the 174 deg mode, whose results before the correction for systematic errors are shown in Table 8.1.
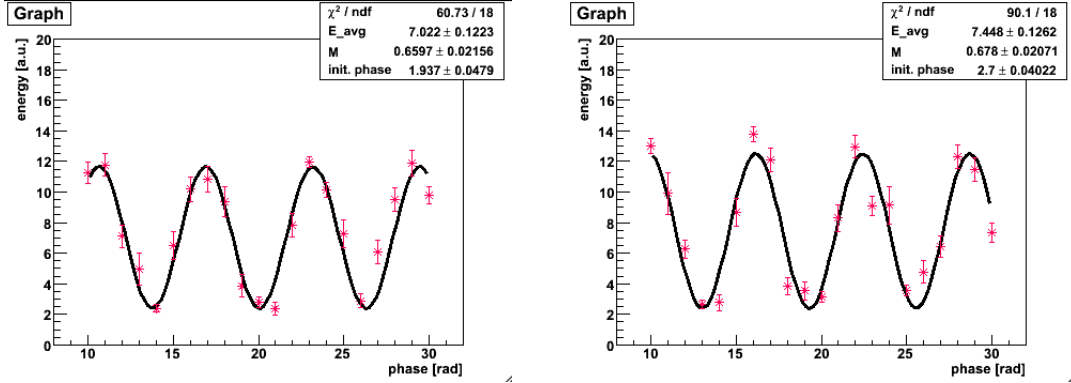
Figure 8.2: Examples of the high M measured in the 174 deg mode as part of the "consistency scan" shown in Fig. 8.1. The results before correction for systematic errors are (left) $M_{meas} = 0.660 \pm 0.021(stat.)$, $\sigma_{meas} = 38.3 \pm 1.5(stat.)$ nm. (right) about 17 min later: $M_{meas} = 0.678 \pm 0.020(stat.)$, $\sigma_{meas} = 37.1^{+1.4}_{-1.5}(stat.)$ nm.

147
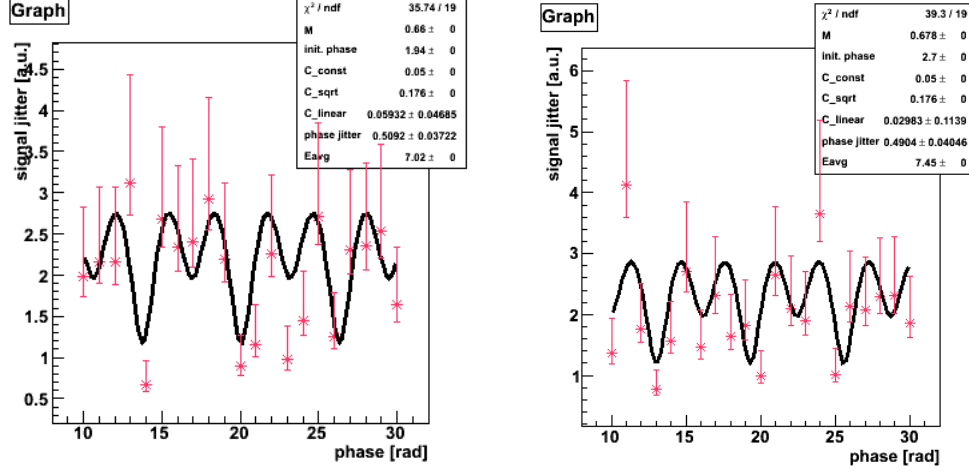
Figure 8.3: The plots for the extraction of phase jitter corresponding to each of the N_{av}=10 scans shown in Fig. 8.2. The extracted phase jitter values are (left) $\sigma_\varphi = 0.509 \pm 0.037(stat.)$ rad, and (right) $\sigma_\varphi = 0.490 \pm 0.040(stat.)$ rad.

As the counterparts of Table 8.1 and Fig. 8.1, Table 8.2 and Fig. 8.4 show the results after correcting each individual scan for its σ_φ extracted using the method described in Sec. 7.4. The extracted σ_φ is 0.509±0.023 rad and 0.492±0.039 rad for June 12 and June 13, respectively. The corresponding relative position jitter $\delta\Delta y$ ($\delta\Delta y/\sigma_{y,corr}$) is 21.5±1.0 nm (57.3±7.8 %) and 20.8±1.7 nm (52.4±6.7 %), for June 12 and June 13, respectively.

date	M_{corr}	$\sigma_{y,corr}$ [nm]	stability
June 12 (10 scans)	0.672 ± 0.051 (S.D.)	37.5 ± 3.9 (S.D.)	7.6%
June 13 (12 scans)	0.640 ± 0.029 (S.D.)	39.7 ± 2.1 (S.D.)	4.5%

Table 8.2: The results of the two sets of continuous scans shown in Table 8.1 and Fig. 8.1, after correction using the σ_φ extracted for each individual scan.
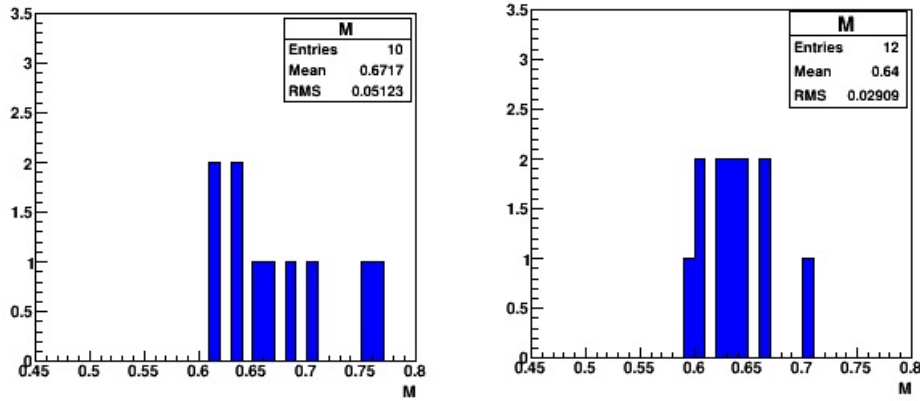
Figure 8.4: The two sets of continuous scans shown in Fig. 8.1, after correction using the σ_φ extracted for each individual scan: The corrected results are shown in Table 8.2.

8.1.2 Evaluation of the Smallest Beam Sizes

Table 8.3 summarizes the M reduction factors evaluated for the smallest σ_y measured in the two sets of continuous scans mentioned in Sec. 8.1.1. If the correction for phase jitter σ_φ (as in Table 8.2 and Fig. 8.4) is not carried out, the systematic errors on the measured σ_y are evaluated based on all of the M reduction factors i.e. C_{total} in Table 8.3; in this case, the smallest beam sizes measured in continuous scans by the Shintake Monitor are:

$$43.3 \pm 1.2(stat.)^{+0.0}_{-13.9}(syst.) \text{ nm} \tag{8.1}$$

$$45.1 \pm 0.8(stat.)^{+0.0}_{-8.0}(syst.) \text{ nm} \tag{8.2}$$

However, the full evaluation of M_{meas} ($\sigma_{y,meas}$) will be carried out after correcting for the extracted phase fluctuation σ_φ for each scan. As explained in Sections 7.5 - 7.7, the precision of M_{corr} is a combined effect of the extraction precision of σ_φ as well as its effect on M_{meas}. Section 7.7 concluded from simulation test results that when the phase variation amplitude is within the realistic range of 0.2-0.7 rad, the precision of M_{corr} (w.r.t. the true M_0) is better than 2.5% for N_{av}=50 and better than 5.7% for N_{av}=10. The propagation to $\sigma_{y,corr}$ can be evaluated using Eq. 2.11. For the σ_y=39.7 nm measured on June 13 (see Table 8.2), this corresponds to an uncertainty of at most 2.6 nm, which is about 6.5% of σ_y. Below, this uncertainty of correction for σ_φ i.e. $\Delta\sigma_{y,corr}$= 6.5% $\times\sigma_y$ is taken into account when evaluating systematic errors. In this case, the smallest beam sizes measured in continuous scans by the Shintake Monitor are:

$$37.5 \pm 1.3(stat.)^{+2.7}_{-8.7}(syst.) \text{ nm} \tag{8.3}$$

$$39.7 \pm 0.6(stat.)^{+2.6}_{-4.0}(syst.) \text{ nm} \tag{8.4}$$

For the systematic errors in Equations 8.3 and 8.4, the upper limit (+) is from $\Delta\sigma_{y,corr}$. The lower limit (-) is the convolution of $\Delta\sigma_{y,corr}$ and the other factors in Table 8.3 excluding C_φ i.e. $C'_{total} = C_{total}/C_\varphi$, which is 0.858 and 0.938 for June 12 and June 13, respectively.

The final results in Equations 8.3 and 8.4 indicate that the ATF2 Goal 1 has been achieved within the range of the evaluated errors. The measurement resolution of the Shintake Monitor for σ_y= 39.7 nm is evaluated to be about 10%. Table 8.4 summarizes the full evaluation of the two sets of continuous scans. More details are given in Appendix F.

date	June 12 (10 scans)	June 13 (12 scans)
C_φ	0.879	0.886
$C_{t,align}$	> 0.965	> 0.991
$C_{z,align}$	> 0.915	> 0.974
C_{tilt}	> 0.999	> 0.999
C_{pitch}	> 0.989	> 0.989
C_{sphere}	> 0.988	> 0.988
C_{growth}	> 0.997	> 0.997
C_{drift}	> 0.999	> 0.999
C_{power}	> 0.999	> 0.999
C_{pol}	1.000	1.000
C_{total}	> 0.754	> 0.831

Table 8.3: The summary of M reduction factors evaluated for the two record sets of continuous N_{av}=10 fringe scans on June 12 and June 13 mentioned in Sec. 8.1.1.

date	M	σ_y [nm]
June 12 (10 scans)	$0.672 \pm 0.017(stat.)^{+0.118}_{-0.038}(syst.)$	$37.5 \pm 1.3(stat.)^{+2.7}_{-8.37}(syst.)$ nm
June 13 (12 scans)	$0.640 \pm 0.009(stat.)^{+0.056}_{-0.036}(syst.)$	$39.7 \pm 0.6(stat.)^{+2.6}_{-4.0}(syst.)$ nm

Table 8.4: The full evaluation of the two record sets of continuous fringe scans on June 12 and June 13. Correction is carried out for the phase jitter extracted using the method described in Chap. 7. The systematic errors take into account the M reduction factors in Table 8.3.

8.2 Future Goals

8.2.1 Remaining Issues

The full evaluation of the smallest σ_y stably and continuously measured in June 2014 (Table 8.4) indicate that the ATF2 Goal σ_y of 37 nm has been achieved. However, the "raw" measured values i.e. not taking into account the systematic errors, are still larger than the σ_y expected from the design values of the optics and the vertical emittance. Some possible explanations are:

1. The systematic errors related to the Shintake Monitor laser; these are discussed extensively in Chapters 6 and 7. Various efforts have been ongoing to further improve the stability of the laser.

2. The jitter and drift of the e^- beam orbit at the IP.

3. Residual beam size growth due to wakefield effects. The smallest beam sizes were measured at very low beam intensity in order to minimize the effect from wake fields. This issue is discussed in Appendix G and in references [20, 18, 19].

4. Measurements of the beam optics and the emittance may have some ambiguities. See [19, 18] for details.

Regarding 2., the possible effects of e^- beam instability can be further grouped as the following:

- Contribute to phase jitter and drift, which are among the most dominant systematic errors.

- Cause actual σ_y growth.

- Degrade the effectiveness of beam tuning. For example, the orbit drift of the e^- beam may change its position at sextupole magnets and thus affect the correction of chromaticity and higher order aberrations.

The stabilization of e^- beam position at the IP is important for both achievement of Goal 2 and for the reproductivity of the Goal 1 beam size. The O(nm) resolution cavity BPMs "IPBPMs" currently under commissioning at ATF2 will be useful for measuring the beam orbit jitters and drifts.

The results of the error studies reported in this thesis indicate that the measured M can be corrected, provided precise measurement of phase jitter, thus suppressing systematic errors down to only the contribution from the other factors, which have been confirmed to be less serious than phase jitter. The method for compensating phase jitter can be verified even better if its precision when applied to actual data could be directly confirmed. One possible way is to deliberately jitter the piezo controller which shifts the phase during a fringe scan, described as follows:

1. First, measure M before jittering the piezo controller.

2. Deliberately jitter the piezo controller by a known amount so as to create phase jitter. The e^- beam condition needs to be kept stable.

3. Extract the phase jitter from the fringe scan using the method described in Sec. 7.4, and use the result to correct the M_{meas} in 2..

4. Compare M_{corr} to the M_{meas} in 1. i.e. before jittering the piezo controller. The extracted phase jitter can also be compared to the monitored value of the piezo controller jitter.

Furthermore, the precision of evaluating and correcting for phase jitter can be improved by its direct measurement using the IPBPMs for the e$^-$ beam jitter at the IP, as well as a phase monitor for the laser fringes. This would allow the precise measurement of even smaller σ_y .

8.2.2 Possibility of Using the Shintake Monitor at the ILC

In recent years, international collaborations have been joining forces to realize the construction of the ILC. This section gives my personal views on the prospects of using the Shintake Monitor at the ILC in the future. There will be no space in the IP area of the ILC for the Shintake Monitor during normal operation because physics detectors are installed there. However, a beam size monitor with O(10) nm resolution is necessary for confirming that the e$^-$ and e$^+$ beams can be sufficiently focused at the IP to achieve the design luminosity. One candidate for this is the pair monitor[44]. However, there has been little development carried out on the pair monitor hardware. In contrast, the Shintake Monitor has been proven capable of stable measurement of O(10) nm beam sizes at both ATF2 and SLAC. Therefore it is possible to upgrade the Shintake Monitor for initial commissioning of the ILC beam line before detector installation. When the pair monitor hardware has been sufficiently developed, it may replace the Shintake Monitor when beam-beam collision actually commences.

As described throughout this thesis, the world record beam size measurements by the Shintake Monitor has played an essential role in successfully verifying the FFS design featuring the Local Chromaticity Correction Scheme for the ILC. The next step is to enable the Shintake Monitor to be the utilized at the ILC by resolving the following issues intrinsic to the higher beam energy and the smaller design σ_y at the ILC.

Related to higher beam energy

- The total Compton scattering cross section decreases as beam energy increases. This can be seen from Eq. 2.8 and Fig. 8.5. Here, σ_{total} is expressed as a function of the parameter $q = \gamma k/m$, which is scales linearly with both beam energy (γ) and incident laser photon energy (k). For ATF, $q = 0.0116$, assuming beam energy 1.3 GeV and λ=532 nm. For ILC, $q = 2.23$, assuming beam energy 250 GeV and also λ=532 nm . From Fig. 8.5, the σ_{total} for ILC would be reduced to about 1/3 of that for ATF, which imposes a limit on signal statistics i.e. the number of Compton scattering photons. Although this could be compensated by increasing the laser energy, additional effort is needed in order to stabilize a more intense laser.

- Both the signal and BG energy spectrum will be changed. Since the signal energy will be higher and may approach that of bremstrahlung BG, some changes may be required for the design of the gamma-ray detector and/or analysis methods for separating signal and BG.

- The much higher radiation levels at ILC demands reinforced shielding of the Shintake Monitor components to be placed inside the accelerator tunnel e.g. the laser optics, gamma-ray detector, and controllers.

Related to smaller design beam size

- Laser wavelength $\lambda \lesssim 250$ nm is required for producing the fringe pitches narrow enough for measuring the $\sigma_y < 10$ nm at the ILC. For example, $M = 0.95$ at 174 deg mode yields σ_y=12.8

nm for (d, λ) = (266 nm, 532 nm), while halving the wavelength to (d, λ) = (133 nm, 266 nm) yields σ_y = 6.4 nm. One option is to use 4th harmonics generation. Another option is to change to UV lasers (e.g. ArF excimer lasers (λ =193 nm) or F_2 excimer lasers (λ = 157 nm)). However, these lasers outside the visible range are impractical in terms of alignment and stability control. For example, the essential process of overlapping the laser and the e$^-$ beam on the current screen monitor would become difficult. The practical usage of the Shintake Monitor during the initial beam line commissioning may be to measure $\sigma_y \simeq$ 20 nm with a laser of λ =532 nm at a location slightly upstream of the IP, then use the results to estimate the achievable σ_y at the IP based on beam focusing optics design.

- Systematic errors need to be suppressed further to measure the smaller σ_y at the ILC with satisfactory resolution. Without correcting for phase jitter, the systematic error for $\sigma_{y,meas} \simeq$ 45 nm at ATF2 is about 8 nm (see Eq. 8.2), which corresponds to a measurement resolution of about 20%. Assuming $\sigma_y \simeq$ 20 nm at the ILC, the error needs to be suppressed below 4 nm to achieve a resolution better than for instance 20%. The suppression of the dominant phase jitter i.e. relative position jitter calls for reinforced stabilization of both the e$^-$ beam and the laser (e.g. laser pointing jitter and profile fluctuation). Residual phase jitter can be compensated for by applying the phase jitter correction method described in this thesis. Howerer, precison can be improved by the direct measurement of both e$^-$ beam jitter and laser fringe phase jitter. These emphasize the importance of the development of O(nm) resolution BPMs and laser fringe phase monitors.

Furthermore, the operation of the Shintake Monitor needs to be adapted to the higher repetition rate of 5 Hz and the multi-bunch operation at the ILC, as opposed to the single bunch 3 Hz operation at ATF2. The O(10) ms time resolution of the Shintake Monitor piezoelectric stage for fringe phase control satisfies the demand from the higher repetition rate. On the other hand, multi-bunch operation calls for a more speedy beam size measurement methods than that for single bunch operation. The R&D of multi-bunch operation is ongoing at ATF.
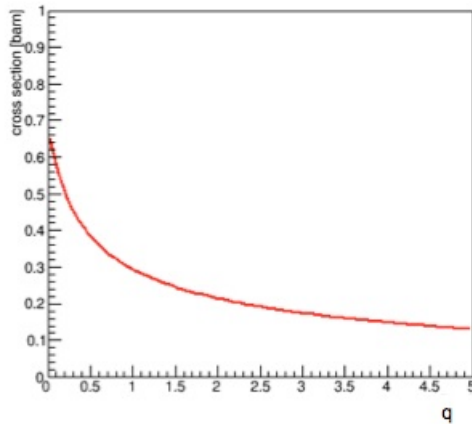
Figure 8.5: The dependence of total Compton scattering cross section σ_{total} on $q = \gamma k/m$ (m:e$^-$ rest mass; k : incident laser photon energy), shown here in a wider range of q = 0 - 5 (as opposed to the narrow range in Fig. 2.9).

8.3 Conclusion

At the International Linear Collider (ILC), the high luminosity of about 2×10^{34} cm^{-2}s^{-1} required for its physics program calls for the focusing of its e$^-$ and e$^+$ beams to nanometer sizes at the interaction

point (IP). The Accelerator Test Facility 2 (ATF2) was constructed at KEK as a realistic scaled down test prototype of the final focus system (FFS) of the ILC. The Goal 1 of ATF2 is to focus the vertical e$^-$ beam size (σ_y) to 37 nm, scaled by energy from the ILC design σ_y of 5.9 nm and by doing so, demonstrate the design of a FFS that is to be used at the ILC. This FFS design features a beam focusing method called the Local Chromaticity Correction scheme, which realizes a shorter FFS beam line and less beam halo than preceding designs.

The Shintake Monitor is a beam size monitor installed at the virtual IP of ATF2 for the purpose of measuring its O(10) nm σ_y. Featuring a technique of using laser interference fringes as a probe to scan the e$^-$ beam, the Shintake Monitor is the only existing device that has demonstrated measurement of σ_y below 100 nm. Its measurement scheme is as follows: a pulsed Q-switch Nd:YAG laser beam is split into upper and lower paths which cross at the IP to form laser interference fringes. The collision of the e$^-$ beam against the fringes release photons from inverse Compton scattering. By scanning the fringe phase with respect to the e$^-$ beam using a piezo-electric stage, a modulation pattern is produced in the photon energy measured by a downstream calorimeter-type gamma-ray detector. The σ_y is calculated from this modulation (M). The laser optics are designed to accommodate a wide range of σ_y from about 25 nm to a few μm with better than 10% accuracy. A series of hardware improvements stabilized the timing, profile, and position of the laser. The effective beam tuning using the Shintake Monitor contributed essentially to the ATF2 beam focusing progress; by June 2014, the focusing of σ_y to below 45 nm has been demonstrated on repeated occasions with a measurement stability of about 5%.

The most important of my personal contributions to the development and performance evaluation of the Shintake Monitor is an extensive study of various systematic errors. These are called "M reduction factors" because they cause under-evaluation of M i.e. over-evaluation of σ_y. The dominant M reduction factor is found to be the fluctuation of the relative phase between the laser and the e$^-$ beam. An original method was developed for the extraction and correction of phase jitter. The reliability of this method was demonstrated using simulation assuming realistic ATF2 conditions; the M correcetd using the extracted phase jitter was shown to have a precision corresponding to better than 6.5% of the beam size. Based on various measurements of the laser and the gamma-ray detector response, systematic errors were evaluated for beam time data collected in 2014 spring. The full beam size evaluation for a set of world record continuous σ_y measurements in June 2014 is $\sigma_y = 39.7 \pm 0.6(stat.)^{+2.6}_{-4.0}(syst.)$ nm; the beam size resolution is about 10%. These studies enabled the precise evaluation of σ_y, and their results indicate that the ATF2 Goal 1 has been achieved within error ranges.

Because the ATF2 is a scaled prototype of the ILC FFS with similar difficulties in beam tuning, various technologies verified at ATF2 are applicable to the ILC. Therefore, the above-mentioned precise σ_y evaluation was a large step towards demonstrating the feasibility of realizing the ILC. By resolving several issues in performance and design, the Shintake Monitor is also a promising candidate for the O(nm) resolution beam size monitor necessary for the beam line commissioning at the actual ILC. Furthermore, the results of the error studies reported in this thesis indicate that it would be possible to suppress systematic errors so as to allow the measurement of the smaller O(nm) σ_y at the ILC in the future, provided precise measurement of phase jitter using O(nm) precision BPMs and laser fringe phase monitors.

9 Acknowledgment

10 Appendix

A   Laser Cavity

Figure A.1 shows the layout of the laser head of a PRO-Series laser manufactured by Spectra Physics[24]. The Shintake Monitor uses the Quanta-Ray PRO-350 laser. The major components are described as the following. There are vertical and horizontal controls in various locations which allow adjustment of the routing of the beam.

Oscillator section:

The components here make up the laser cavity where the initial laser beam is generated. The alignment of the oscillator cavity and the optimization of output power and mode quality are conducted through vertical and horizontal controls, which are accessible when the head cover is removed.

- Rear mirror ("high reflector") M1: one of the two oscillator cavity end mirrors. M1 reflects all laser light back into the cavity.

- Output coupler M2: the other cavity end mirror. M2 allows a part of the light to pass through as the output laser beam.

Q-switch system:

The Q-switch system is used for producing laser pulses of high intensity and short pulses. It is comprised of a quarter-wave plate, a polarizer, and a Pockels cell.

- Quarter-wave plate: rotates the polarized cavity light by 90 deg. It suppresses laser oscillation until the Q-switch is fired.

- Pockels cell: a crystal used as a high-speed optical shutter for Q-switch pulses. It is opaque (blocks light) until a voltage is applied to it. The Marx bank provides the power to drive the Pockels cell and uses a TTL trigger source to turn the cell on and off.

- Polarizer: a coated optical component that allows only light with a selected polarization to pass through

Amplifier section:

Two rectangular pump chambers add energy to the laser beam from the oscillator section. This amplified beam becomes the laser output. The pump chamber has a flash lamp at one focus point and a YAG rod i.e. the lasing media at the other. The YAG rod is pumped by the flash lamp. Fold mirrors route the laser beam from the oscillator to the amplifier section.

Injection seeder:

The injection seeder provides a small amount of single-frequency laser light (wavelength (λ)=1064 nm) to stimulate emission at a single longitudinal mode in the host laser oscillator once the proper threshold for lasing is reached in the rod. Its controls are provided on one of the laser side panels.

Second harmonic generator (SHG):

Crystals arranged in a particular sequence and orientation generate second harmonics from the primary λ of 1064 nm to 532 nm. The dichroic mirror DM1 reflects and routes light of λ= 532 nm to DM2 while transmitting the residual λ= 1064 nm light to the beam dump. A temperature controller stabilizes the temperature of the SHG crystals, thus maintaining stable output regardless of changes in ambient temperature.

Beamlok:

The Beamlok is a device for position stabilization. The dichroic mirror DM2 mounted on an x-y piezo servo routes the output beam through the BeamLok sensor and out of the laser head. The BeamLok pointing sensor detects the far field beam position and provides feedback to the controller for stable beam-pointing output. This controller then controls the piezo servo carrying DM2.
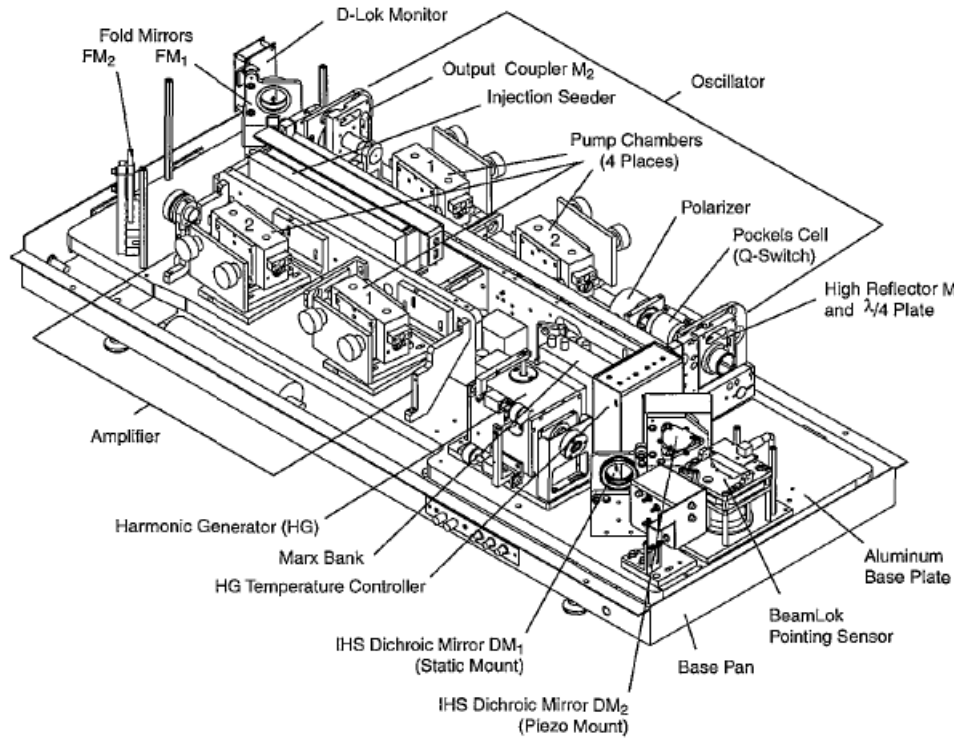

Figure A.1: The layout of the laser head of a PRO-Series laser manufactured by Spectra Physics Inc. [23]

B   Gauss Beam Focusing

B.1   Properties of an Ideal Gaussian Beam

Most of the discussion pertaining to laser beam propagation and focusing in this thesis are based on a model based on Gaussian beam physics. A Gaussian beam is the fundamental mode of a coherent laser beam. For the realistic laser, there is a certain amount of deviation from Gaussian (see Sec. 5.2). Figure shows the schematics of the focusing of a Gaussian laser beam[45].

The electric field of the Gaussian beam has a radially symmetric distribution, and can be expressed as:

$$E(z,r) = E(z,0) \exp\left(-\frac{r^2}{\omega^2(z)}\right) \tag{B.1}$$

The intensity distribution of a Gaussian beam is also Gaussian, and can be expressed as:

$$I(z,r) = I(z,0) \exp\left(-\frac{2r^2}{\omega^2(z)}\right) \tag{B.2}$$

Here, z is the direction of beam propagation, r is the radial direction. $E(z,0)$ is the field amplitude on the axis (r=0). The beam radius $w(z)$ is defined as the radius at which the intensity decrease to $1/e^2$ of $I(z,0) = |E(s,0)|^2$, the intensity on axis. $w(z)$ can be expressed as a function of z, the propagation distance w.r.t. the waist position (z_0), and waist size w_0 as:

$$\omega(z) = \omega_0 \sqrt{1 + \left\{\frac{\lambda(z-z_0)}{\pi\omega_0^2}\right\}^2} = \omega_0 \sqrt{1 + \left(\frac{z-z_0}{z_R}\right)^2} \tag{B.3}$$

The Rayleigh length z_R is defined as the distance over which the laser waist is increased by $\sqrt{2}$ times, and can be expressed as:

$$z_R \equiv \frac{\pi\omega_0^2}{\lambda} \tag{B.4}$$

The curvature radius $R(z)$ can be expressed as:

$$R(z) = |z-z_0| \left\{1 + \left(\frac{\pi\omega_0^2}{\lambda(z-z_0)}\right)^2\right\} \tag{B.5}$$

The beam divergence Θ is an important property in laser beam transportation, and can be expressed as:

$$\Theta = \tan^{-1}\left(\frac{\lambda}{\pi\omega_0}\right) \simeq \frac{\lambda}{\pi\omega_0} \qquad (\Theta \ll 1) \tag{B.6}$$

The approximation $\Theta \ll 1$ stands since λ=532 nm and ω_0 is about 20 μm. The waist radius ω_0 at the focal point can be expressed using ω_i, the radius injecting into the focal lens, and f, the focal length of the lens, as:

$$\omega_0 = \frac{\lambda f}{\pi\omega_i} \tag{B.7}$$

A larger ω_i injecting into the focal lens and a shorter f leads to a larger divergence angle. This can be understood by using Eq. B.7 and Eq. B.6 to rewrite beam divergence as:

$$\Theta = \tan^{-1}\left(\frac{\omega_i}{f}\right) \simeq \frac{\omega_i}{f} \tag{B.8}$$

Correction for a Non-Gaussian Beam The M^2 value serves as a beam quality factor which represents the degree of deviation from an idealistic Gaussian beam ($M^2 = 1$). The waist size achievable by focusing at the focal point depends on M^2. For the realistic beam, Eq. B.3 and Eq. B.7 are corrected as Eq. B.9 and Eq. B.10, respectively.

$$\omega\left(z\right) = \omega_0 \sqrt{1 + \left\{\frac{M^2 \lambda \left(z - z_0\right)}{\pi \omega_0^2}\right\}^2} = \omega_0 \sqrt{1 + \left(\frac{z - z_0}{z_R}\right)^2} \tag{B.9}$$

$$\omega_0 = \frac{\lambda f M^2}{\pi \omega_i} \tag{B.10}$$

This indicates that the ω_i injecting into the focal lens need to be made smaller by a factor of M^2 in order to achieve the same waist radius ω_0 at the focal point. A larger M^2 indicates a more sudden change in spot size as the beam propagates. This can be explained by that the beam divergence is magnified by a factor of M^2 as:

$$\Theta = \tan^{-1}\left(\frac{M^2 \lambda}{\pi \omega_0}\right) \simeq \frac{M^2 \lambda}{\pi \omega_0} \tag{B.11}$$

Accordingly, the Rayleigh length in Eq. B.4 and the curvature radius in Eq. B.5 are shortened by a factor of approximately M^2 as:

$$z_R \equiv \frac{\pi \omega_0^2}{M^2 \lambda} \tag{B.12}$$

$$R(z) = |z - z_0| \left\{1 + \left(\frac{\pi \omega_0^2}{M^2 \lambda \left(z - z_0\right)}\right)^2\right\} \tag{B.13}$$
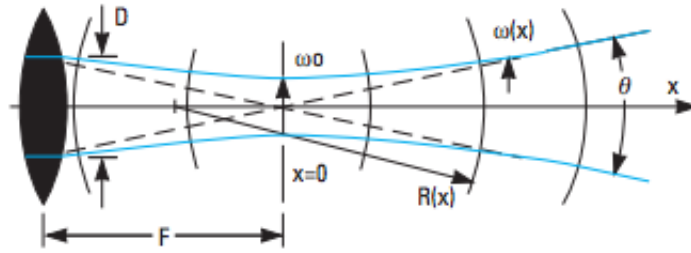

Figure B.1: The schematics of Gaussian beam focusing. [45]

C   Damage Threshold for Optical Components

In order to prevent damage by high intensity laser, it is necessary to ensure that the damage threshold for the optical components withstand the intensity of the laser beam in contact. This section gives a theoretical calculation of laser energy density, which scales with total laser energy and the inverse of laser spot area.

For the case of a Gaussian intensity profile, a two dimensional distribution is written as:

$$P(x,y) = \frac{1}{2\pi \sigma_{t,laser}^2} exp\left(-\frac{x^2}{2\sigma_{t,laser}^2} - \frac{y^2}{2\sigma_{t,laser}^2}\right) \tag{C.1}$$

Here, $\sigma_{t,laser}$ represents the transverse laser spot size radius on the surface of the component of interest. The peak energy density is expressed using total energy W as:

$$I_{peak}\left(W, \sigma_{t,laser}\right) = \frac{W}{2\pi\sigma_{t,laser}^2} \tag{C.2}$$

The design total energy of 1.4 J/pulse is cut by 60% to 0.56 J/pulse by a beamsplitter on the laser table to prevent damage of components. The typical $\sigma_{t,laser}$ is about 3 mm between the reducer and the focal lens on the vertical table (see Sec. 5.2). W=0.56 J/pulse and $\sigma_{t,laser} \simeq 3\,\mathrm{mm}$ gives $I_{peak} = 0.3\,\mathrm{J/cm^2}$.

In the past, some mirrors in the full power beam line that had damage threshold $I_{th} = 10\,\mathrm{J/cm^2}$ had been replaced with mirrors of $I_{th} = 20\,\mathrm{J/cm^2}$. Using Eq.C.2, the corresponding lower limit on laser spot size at a mirror is:

$$\sigma_{t,laser} > \sqrt{\frac{W}{2\pi I_{th}}} \simeq \begin{cases} 0.9\,\mathrm{mm} & (I_{th} = 10\,\mathrm{J/cm^2}) \\ 0.7\,\mathrm{mm} & (I_{th} = 20\,\mathrm{J/cm^2}) \end{cases} \tag{C.3}$$

However, the above-mentioned thresholds are defined for wavelength $\lambda = 1064$ nm and pulse width 10 ns (FWHM)[46], whereas the damage threshold scales with λ and the square root of time domain. Therefore when setting the safety margin for a laser of $\lambda = 532$ nm and pulse width = 8 nm (FWHM), I_{th} needs to be halved, then divided by $\sqrt{10\,\mathrm{ns}/8\,\mathrm{ns}} \simeq 1.25$. Thus Eq. C.3 becomes:

$$\sigma_{t,laser} > \sqrt{\frac{W}{2\pi\left(I_{th}/2/1.25\right)}} \simeq \begin{cases} 1.5\,\mathrm{mm} & (I_{th} = 10\,\mathrm{J/cm^2}) \\ 1.1\,\mathrm{mm} & (I_{th} = 20\,\mathrm{J/cm^2}) \end{cases} \tag{C.4}$$

Furthermore, for a pulse laser, there may be hot spots in the profile. This requires another safety margin of a factor of 2-3[48]. Taking this into account, the $\sigma_{t,laser} \simeq 3\,\mathrm{mm}$ on the vertical table barely meets the stricter version of safety margin for mirrors of $I_{th} = 20\,\mathrm{J/cm^2}$[46]. We must also keep in mind the possibility of sudden changes in focusing patterns, and that the discussion here is only on a theoretical basis.

For a CW laser, we think in terms of power density, which is simply written as (total power)/(beam spot area), where beam spot area = $\pi\sigma_{t,laser}^2$. For example, for the Nd:YAG CW laser (50 mW, 532 nm, diameter 0.8 mm) used for the alignment of optical components, the power density is (50 mW)/($\pi \cdot 0.4^2\,\mathrm{mm^2}$) = 9.95 W/cm^2.

D   Alternative Scenarios of Simulation Test for Phase Jitter Extraction

Section 7.5.2 demonstrated the results for the extraction and compensation of a complex and realistic non-Gaussian phase fluctuation. The purpose of this section is to show that similar precision for M_{corr} can be achieved for some alternative scenarios of complex phase instabilities. The inputs into these simulations are based on the same phase variation pattern (Fig. 7.6) and the same vertical jitter as in Sec. 7.5.2, whereas the following alterations are made upon the the order of the phase variation in Fig. 7.6, the linear drift, or the phase jump.

1. Figure: D.1: the first half and second half of the phase pattern in Fig. 7.6 are interchanged.

---

[46]Compared to a flat top distribution, a Gaussian intensity profile requires multiplying W by a factor of two to accommodate the peak power density at the center of the beam. The actual laser beam is in between a flat top distribution and the assumed Gaussian, thus the peak intensity is lower than a perfect Gaussian case, which slightly lowers restrictions.

2. Figure: D.2: the linear drift is input as 60 mrad / min for the interval of φ=0-10 rad, 0 mrad / min for φ=11-14 rad, and 80 mrad / min for φ=15-19 rad. The linear drift in Fig. 7.8 was a constant 80 mrad / min.

3. Figure: D.3: the location of the 0.7 rad phase jump is moved to φ= 6 rad (fringe peak) and φ=15 rad (fringe valley). The original location in Fig. 7.8 was at φ= 11 rad (fringe mid-point).

In the plots below, the results of M_{corr} (w.r.t. M_0) are compared with that in Fig. 7.8, and are shown for 1000 pseudo experiments for N_{av}=50 and N_{av}=10. For the smallest σ_y measurements in June 2014, σ_φ is approximately in the range of 0.4-0.7 rad. It can be seen that within this realistic σ_φ range, no significant difference can be seen in the precision of M_{corr} between Fig. 7.8 and the alternative scenarios. The only points with discrepancy beyond the range of the errorbars are for N_{av}=10 in Fig. D.3 and are only < 3.1%.
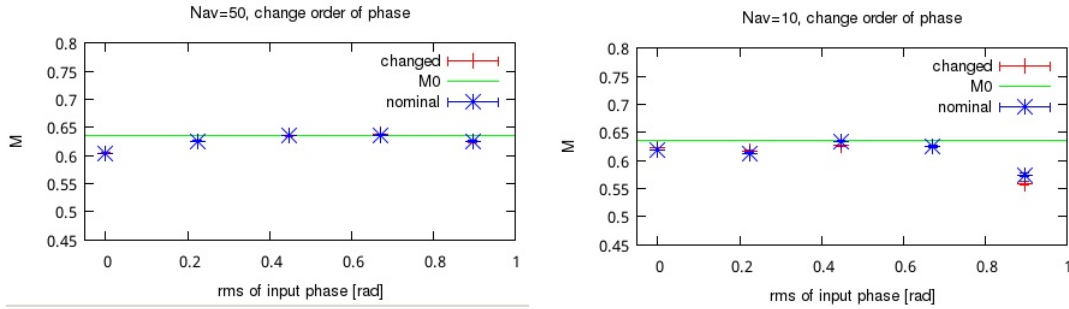

Figure D.1: The red points show the results of M_{corr} w.r.t. M_0 (green line) from an alternative version of the fringe scan simulation in Fig. 7.8; here the first half and the second half of the phase variation in Fig. 7.6 have been interchanged. The other input conditions are kept the same as in Fig. 7.8. For comparison, the blue points show the original results in Fig. 7.8. These are the results of 1000 pseudo experiments for $N_{av} = 50$ (left) and $N_{av} = 10$ (right).
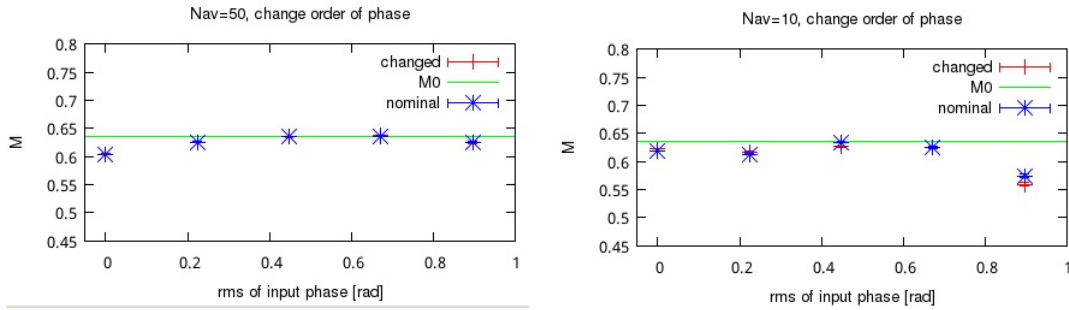

Figure D.2: The red points show the results of M_{corr} w.r.t. M_0 (green line) from an alternative version of the fringe scan simulation in Fig. 7.8; here the linear drift is input as 60 mrad / min for the interval of φ=0-10 rad, 0 mrad / min for φ=11-14 rad, and 80 mrad / min for φ=15-19 rad.The other input conditions are kept the same as in Fig. 7.8. For comparison, the blue points show the original results in Fig. 7.8, where the linear drift is a constant 80 mrad / min. These are the results of 1000 pseudo experiments for $N_{av} = 50$ (left) and $N_{av} = 10$ (right).
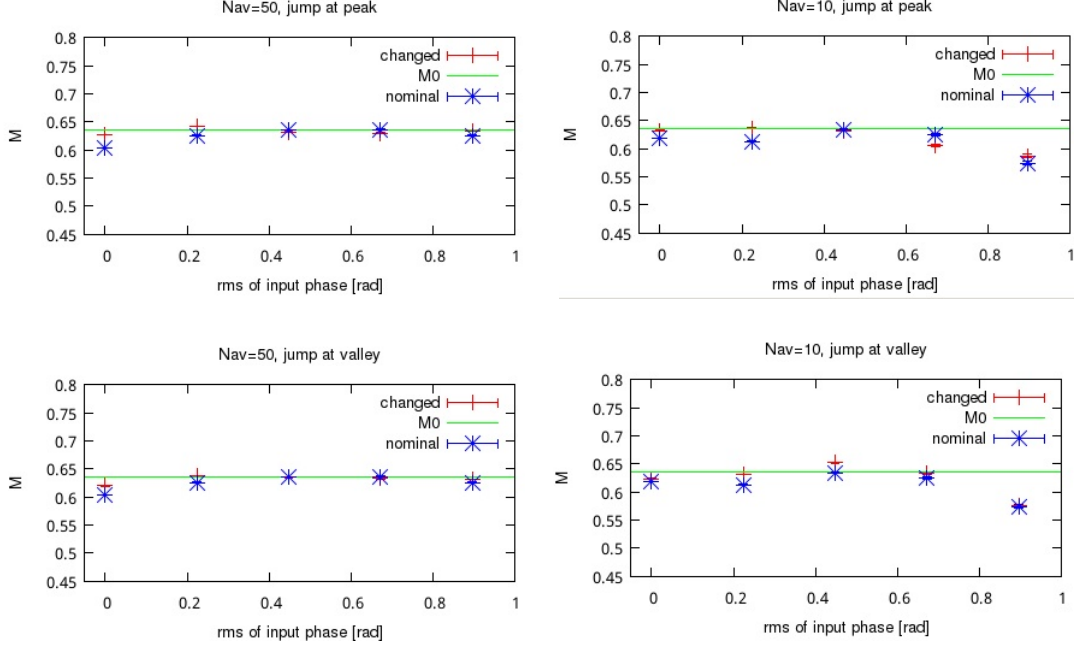
Figure D.3: The red points show the results of M_{corr} w.r.t. M_0 (green line) from an alternative version of the fringe scan simulation in Fig. 7.8; in the top row, the location of the 0.7 rad phase jump has been moved to $\varphi=$ 6 rad (fringe peak); in the bottom row, the phase jump has been moved to $\varphi=$15 rad (fringe valley). The other input conditions are kept the same as in Fig. 7.8. For comparison, the blue points show the original results in Fig. 7.8, for which the phase jump is at $\varphi=$ 11 rad (fringe mid-point). These are the results of 1000 pseudo experiments for $N_{av} = 50$ (left) and $N_{av} = 10$ (right).

E Extraction of C_{linear}

C_{linear} is the other free parameter extracted from fringe scan data alongside phase jitter σ_φ using the method given in Sec. 7.4. Figure E.1 demonstrates the extraction precision of C_{linear} for both the simulation of Gaussian-like σ_φ in Fig. 7.5 as well as the the simulation of realistic σ_φ in Figures 7.7 and 7.8.

Figure E.2 shows a history of C_{linear} extracted from fringe scan data in May-June 2014. The center of the data points are between 6-10% in general. The major factors contributing to C_{linear} are laser timing jitter ($\lesssim$ 5%), e$^-$ beam intensity jitter ($\sim$ 2% = ICT monitor resolution), and the reduction in the laser power interacting with the e$^-$ beam due to fluctuation of the laser profile at the IP ($<$ few %).
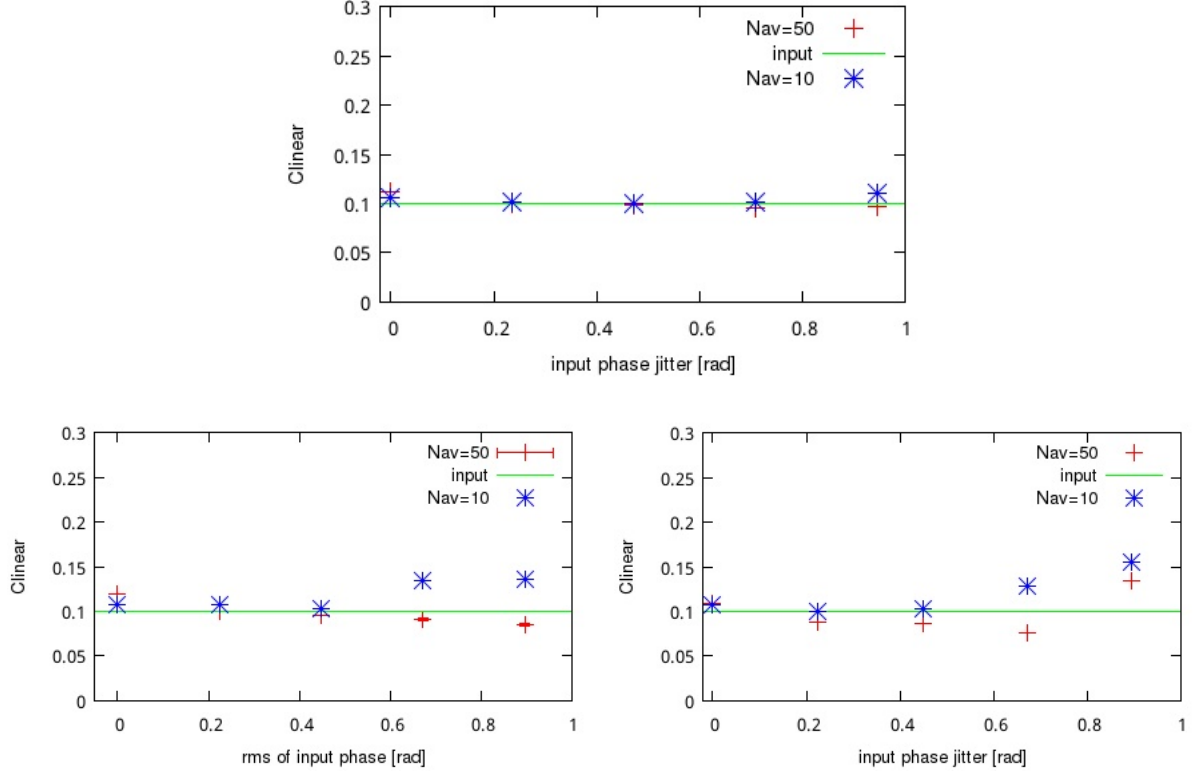
Figure E.1: The simulation results for the extraction of C_{linear}. The horizontal axis is the RMS of the input phase variation ($\sigma_{\varphi,in}$). The red and blue points are the extracted C_{linear} for $N_{av} = 50$ and $N_{av} = 10$, respectively, shown as the statistical results of 1000 pseudo experiments. The green line is the input C_{linear} (=10% w.r.t. E_{avg}). (top) From the simulation in Fig. 7.5; the absolute deviation of the extracted C_{linear} w.r.t. to the input is $< 1.5\%$ for any amplitude. (bottom left) From the simulation in Fig. 7.7. (bottom right) From the simulation in Fig. 7.8. With exception of the largest RMS $\sigma_{\varphi,in} = 0.90$ rad, the absolute deviation of the extracted C_{linear} w.r.t. to the input is $\lesssim 3\%$. For $\sigma_{\varphi,in} = 0.90$ rad, the deviation is $\lesssim 6\%$.
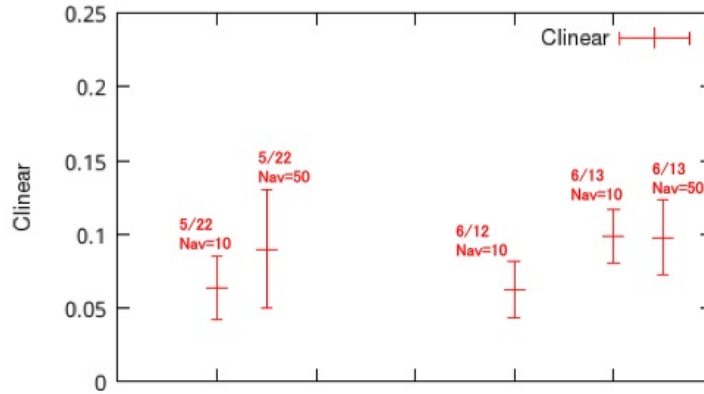

Figure E.2: A history of C_{linear} extracted from fringe scan data in May-June 2014. The center of the data points are between 6%-10% in general. Each data group is labeled by the date and N_{av}.

F Details of Beam Time Results

For the continuous scans on June 12 and June 13 mentioned in Sec. 8.1, Figures F.1, F.2 and F.3 show the results of M_{meas}, M_{corr}, and σ_φ respectively, as a function of time. For each scan, σ_φ is derived using the method described and verified in Sections 7.4 - 7.7, and M_{corr} is by correcting M_{meas} using the extracted σ_φ as in Eq. 6.7.
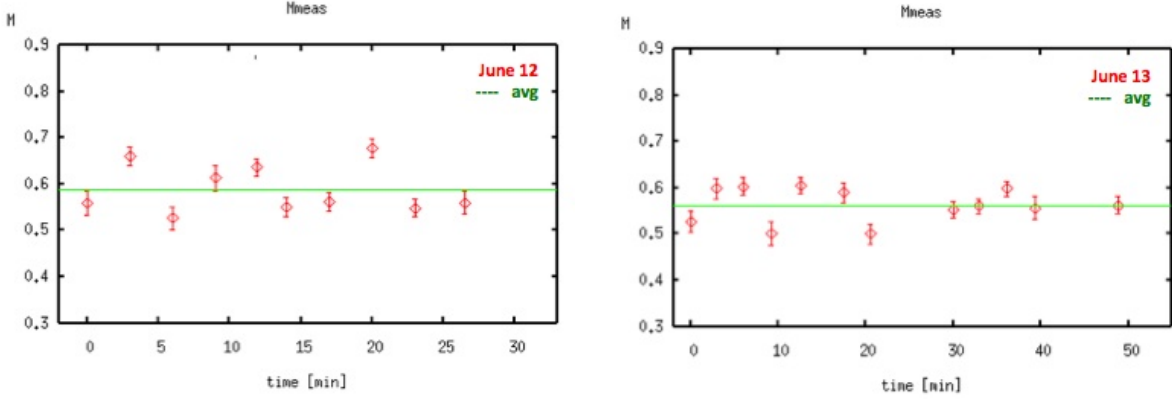

Figure F.1: M_{meas} shown as a function of time for the continuous fringe scans on June 12 (left) and June 13 (right), mentioned in Sec. 8.1. The errorbars are the fitting errors.
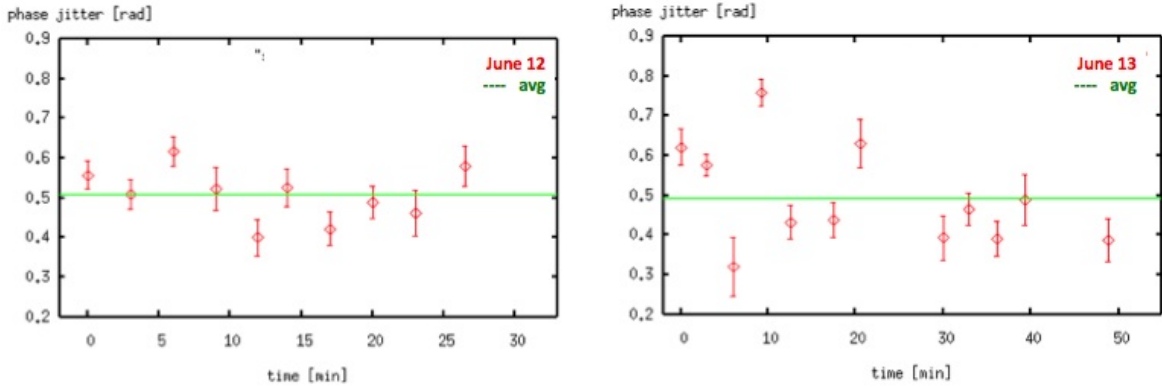

Figure F.2: σ_φ shown as a function of time for the continuous fringe scans on June 12 (left) and June 13 (right), mentioned in Sec. 8.1. The errorbars are the fitting errors.
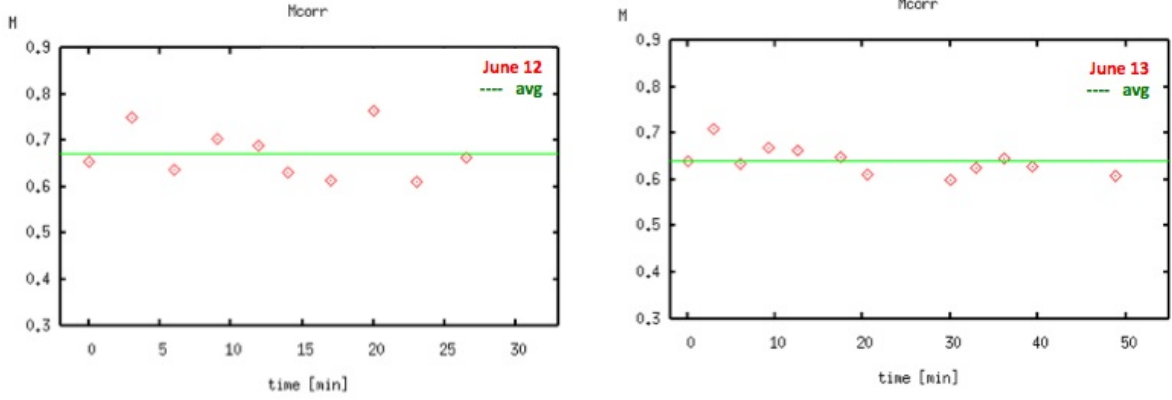
163

Figure F.3: M_{corr} shown as a function of time for the continuous fringe scans on June 12 (left) and June 13 (right), mentioned in Sec. 8.1.

G   Wake Field Effects

The small beam sizes achieved by ATF2 as mentioned in this thesis were measured with very low beam bunch charge ($\lesssim 1.0 \times 10^9$). The beam size (σ_y) is observed to depend strongly on bunch intensity. Figure G.2 shows examples of the intensity dependence measurement.

The most probable cause of the intensity dependence is wakefield in the final focus beam line. Figure G.1 shows the schematics of wakefield. Relativistic particles create electromagnetic fields behind them as they travel down the beam line. The particles in the later part of the bunch are kicked by the fields created by the preceding particles. In this way, wakefield causes particles to stray off course, thus leading to beam size blow up. In particular, when beam particles pass offset from the center of the beam pipe, they are kicked by the wakefield generated from unleveled locations in the beam line, where wake filed generation is enhanced.

Wakefield scales approximately inversely with beam energy when the distance between the beam and the beam pipe walls is much longer than the beam bunch length, and scales approximately linearly to bunch intensity and beta function. Beam size focusing is affected more by wakefield at ATF2 than at the ILC because of the lower ATF2 beam energy and the longer bunch length (6-8 mm for ATF2 as opposed to 300 μm for the ILC). Wakefield effect should be less serious at the ILC because of the higher beam energy, shorter bunch length, and better vacuum chamber material of Cu, as opposed to Al for ATF2 [47]. The effect of wakefield at ATF2 has been studied by simulation during its design stage (see ATF2 Proposal [4], pg 31) for cavities, bellows, and flanges (in the form of average kick angles per unit offset). However the significant intensity dependence observed in experiment is larger than the theoretical calculations.

The contribution of wakefield to the measured beam size is expressed as:

$$\sigma_y^2(q) = \sigma_y^2(0) + a^2 q^2 \tag{G.1}$$

Here, $\sigma_y(0)$is the beam size at zero-charge i.e. without wakefield effect, q is the bunch charge in nC, and a represents the wakefield contribution in nm $\cdot$ nC^{-1}. The contribution of wakefield to beam size growth has been measured to be 100-140 nm $\cdot$ nC^{-1}[19]. This is more significant than the effect calculated from only cavity BPMs. To minimize wakefield effect, ATF2 is usually operated in 2014 spring at a very low charge of 80-200 pC, which correspond to bunch population of 0.5-1.25$\times 10^9$.

---

[47]The ILC vacuum chamber is to be made of Cu for the purpose of resistive wall wake, which is not necessary at ATF2.

For example, using Eq.G.1, the typical bunch charge of 1.0×10^9 (160 pC) would cause a σ_y of 45 nm to be blown up by about 2.8 nm.

A large part of beam time in 2014 spring was dedicated to the investigation of the reason for the unexpectedly large effect on σ_y: identify the wakefield sources and engineer solutions to mitigate them. Most wake studies involve measuring M using the Shintake Monitor. When investigating intensity dependence, M is measured as a as a function of bunch intensity as in Fig.G.2. When investigating the source of wakefield, M is measured as a function of the scanned position of beam line components, which are placed on a mover for this purpose. Figure G.3 shows one example, where the vertical direction of one of the OTR monitors (OTR2) is scanned, while observing the effect on the measured M.

The various efforts to mitigate wakefield sources in the high beta region of the FFS line include:

- the shielding of bellows and vacuum ports

- the removal of some cavity BPMs, reference cavities, wire scanners, and some other components from a large beta section to a lower beta section

- the realignment of beam pipes

Owing to these prolonged efforts, the effect on σ_y is thought to have become weaker, however still remains one of the major limits in σ_y focusing. A clear conclusion is yet to be reached and the studies are still ongoing. The understanding of the bunch intensity dependence of σ_y and the wakefield effects are part of what is referred to as the "Goal 3" of ATF2. More detailed discussions and study results are found in the references [21, 18, 30, 19, 20].
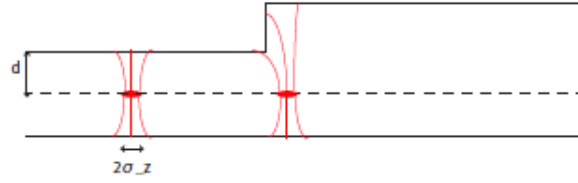

Figure G.1: The schematic diagram of wakefield in the beam line. Here, d is the distance between the e$^-$ beam and the beam pipe, and σ_z is the longitudinal bunch length. [25]
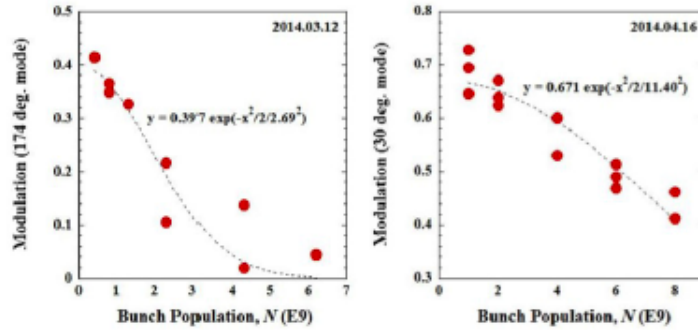

Figure G.2: Intensity dependence of the M measured by the Shintake Monitor [19, 18]: (left) using the 174 deg mode (right) using the 30 deg mode.
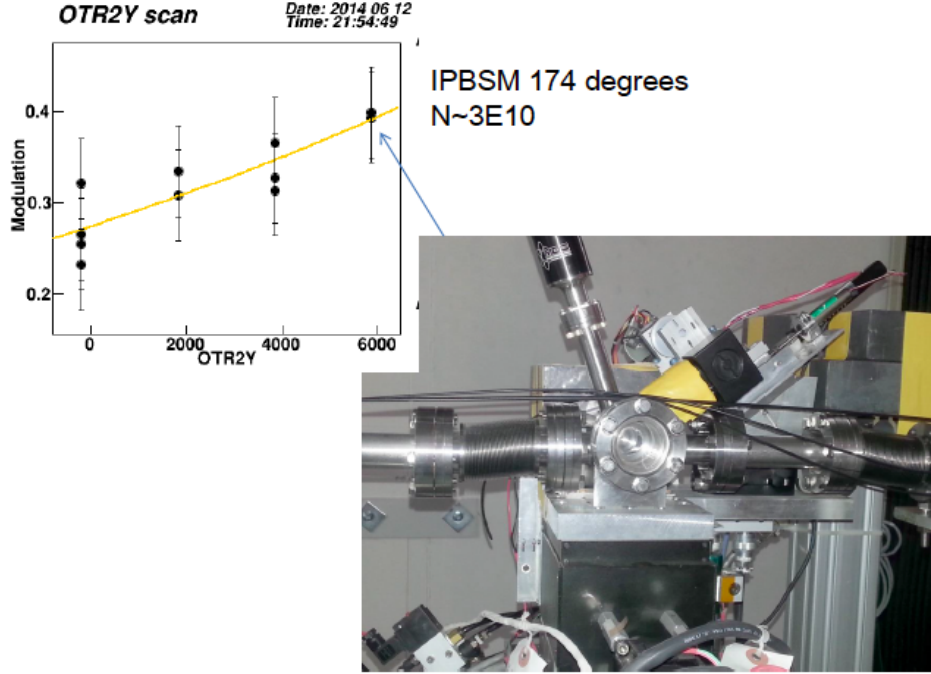
Figure G.3: A scan of the OTR2 vertical position in order to investigate the impact on the beam size from the wake field produced in this part of the beam line. The beam bunch intensity here is about 3×10^9. [21].

H Cross-check of Analysis Methods

As mentioned in Sec. 3.5.4, typically the sum of ADC counts in only the front 4 layers is used in analysis. This custom is meant for accommodating any S/N ratios since under high BG circumstances, the last bulk layer is dominated by BG. Some alternative methods are to use the ADC counts from all 5 layers, or to use the 2nd layer only, as it has the highest S/N ratio.

It has been confirmed that the fitted beam size is consistent within the fitting errors for the sum of the ADC counts of the following:

- the front 4 layers only (as typical)

- all five layers

- only the 2nd layer, which has the highest ratio of signal deposit

Figure H.1 shows an example of the above-mentioned three types of analysis results for the same fringe scan (from the ATF2 control room panel). It can be seen there is no significant difference in either the beam size, nor the signal fluctuation.
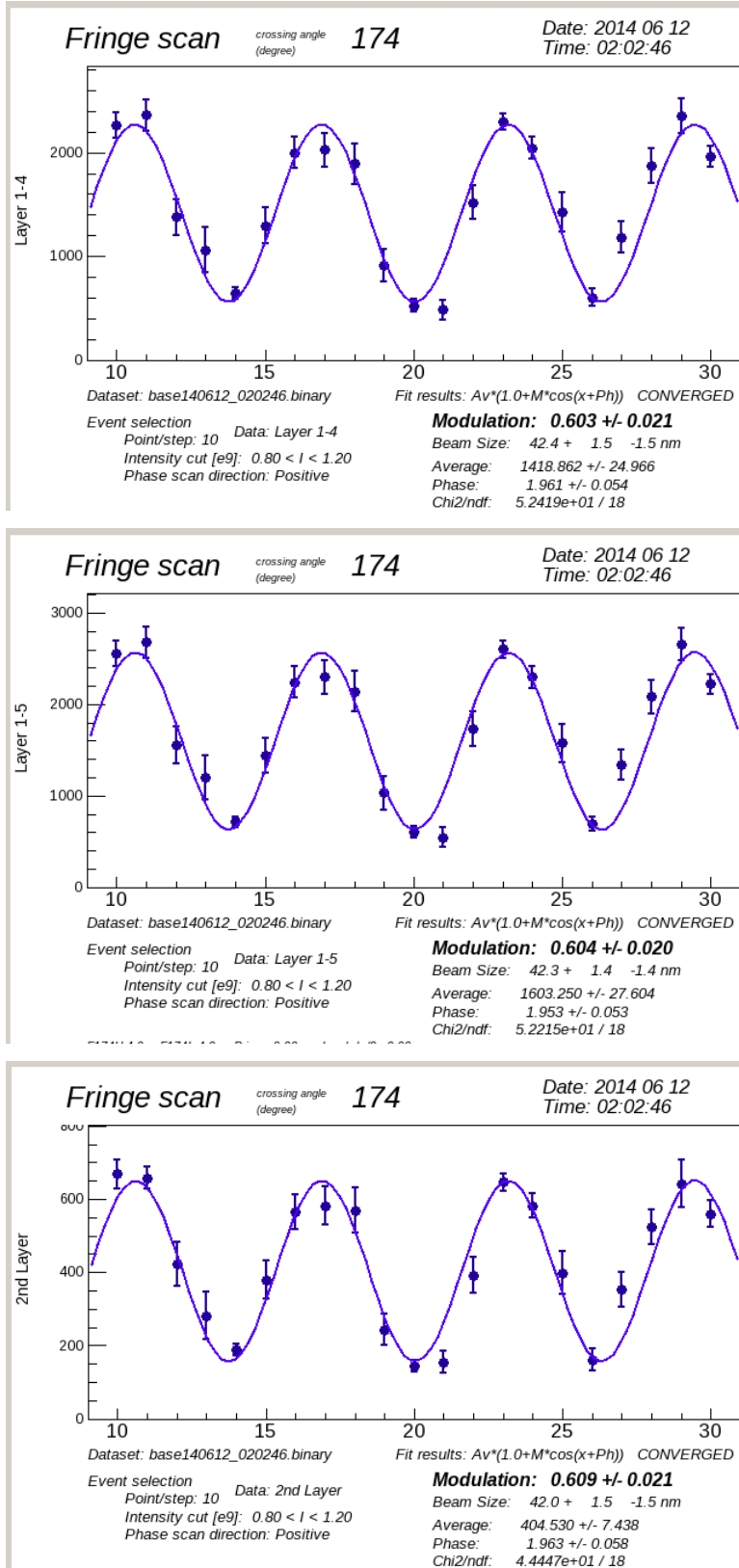
Figure H.1: The analysis results (from the ATF2 control panel) for the same fringe scan from June 2014 shows no significant difference in M or σ_y between alternative methods: (top) front 4 layers: $\sigma_y = 42.4 \pm 1.5$ nm (b) all five layers: $\sigma_y = 42.3 \pm 1.4$ nm (c) second layer only: $\sigma_y = 42.0 \pm 1.5$ nm.

I DAQ

The Shintake Monitor system is made up of many optical components and sub-monitors, their controllers, and digital modules. Furthermore, its operation requires experiment data and control data to be shared on a time synchronized basis with other ATF2 beam monitors. The control and data acquisition (DAQ) of the Shintake Monitor are performed on the EPICS (Experimental Physics and Industrial Control System)[49] platform. It is a software environment capable of linking together individually distributed control systems on a realtime basis. In EPICS, servers called Input/Output Controllers (IOCs) pass on information to individual PCs through a network protocol called Channel Access (CA).

Figure I.1 shows the schematics of the control system comprised of various devices each linked to the EPICS via an IOC. Information is exchanged based on a "record" with a "PV name". The e^- beam related database channels (EPICS PVs) are synchronized and updated by a beam repetition rate of 3.12 Hz. The EPICS IOC gather the status of the device (=DAQ), update the appropriate EPICS PV, and control the device through individual computers.

In the Shintake Monitor system, the main computers for control and DAQ are called "lxs-ip" and "ip-ccnet". These communicate with the EPICS.

lxp-ip: the EPICS IOC for most Shintake Monitor devices run on the lxp-ip. Each IOC acquires and exchanges information about the status of the device it's responsible for. Some examples are: (a) The linear stage on which mirrors are mounted receive commands from their controllers to move to the designated position in order to switch to a particular crossing angle mode. Its position status is acquired by the IOC and updated to the EPICS PV. (b) The position of the attenuator is monitored using a infrared ray sensor and read out by a PLC. The information of whether the attenuator is inserted or ejected is update it to an EPICS PV by the IOC. Other devices, such as the IP screen mounted on a mover, need to confirm the inserted state before they are allowed to move to their designated position to prevent damage by high intensity laser.

ip-ccnet: the ip-ccnet handles the DAQ and controls the synchronization of the VME modules: the charge sensitive ADCs: V005 (for the gamma-ray detector) and RPV171 (for the ICT monitor). It runs a reader process called "Event Collector" which gathers the ADC data from the VME modules and updates the EPICS PV called "IPBSM:AllData". This allows the measured Compton signal energy to be normalized precisely by the measured e^- beam intensity during fringe scan using synchronized data for both.

Another computer, referred to as the "Windows machine" specially handles the control of the mirror actuators.

These tasks (e.g. giving commands, acquiring information) can be done via PCs connected to the EPICS with permission to "read" or "write", such as through the control panels in the ATF control room.

Owing to the EPICS, the information of other ATF2 beam monitors such as the BPMs could be recorded within the fringe scan data set on a synchronized basis.
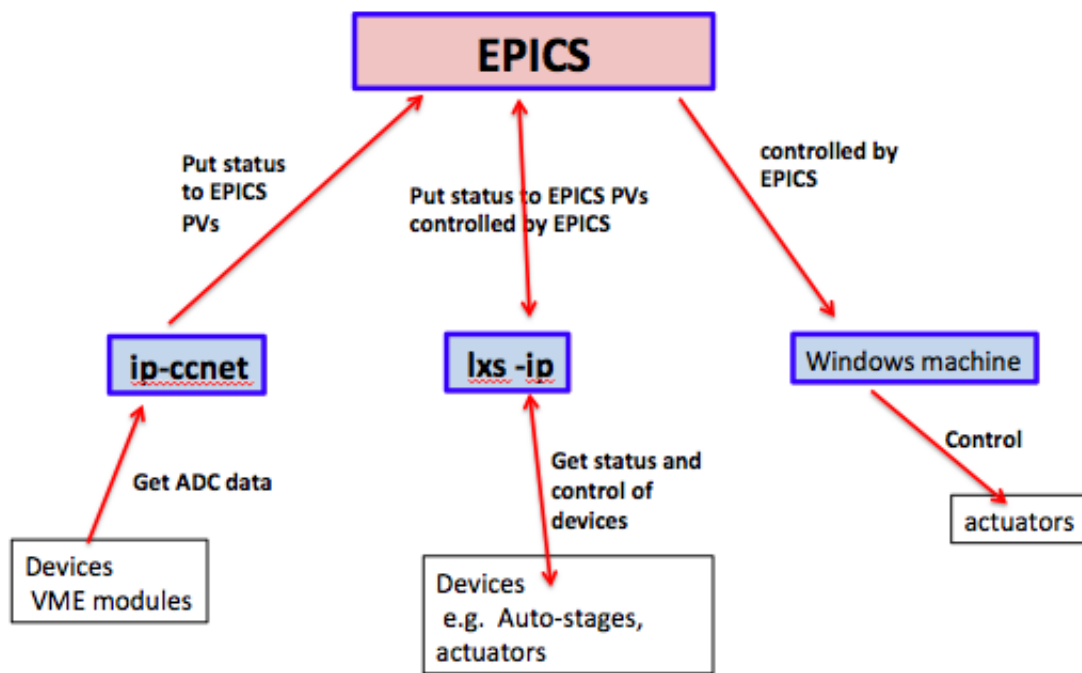
Figure I.1: The schematics of control and DAQ based on the EPICS platform. [25]

References

[1] Reference Design Report, August, 2007

[2] ILC Technical Design Report, June 2013

[3] K. Yokoya, presentation slides for ILC Summer Camp 2012

[4] ATF2 Collaboration, B.I.Grishanov et al, "ATF2 Proposal", 2005, pp.1-113 <in2p3-00025605>

[5] Pantaleo Raimondi and Andrei Seryi, "Novel Final Focus Design for Future Linear Colliders", Phys. Rev. Lett., 86:3779–3782, Apr 2001.

[6] K. Kubo, "Linear Collider Beam Dynamics", OHO-14 Lectures, 2014

[7] P.G.Tenebaum, "Expanded Studies of Linear Collider Final Focus Studies at the Final Focus Test Beam", SLAC Report-95-475 (1995)

[8] The ATF Collaboration: "Experimental Validation of a Novel Compact Focusing Scheme for Future Energy Frontier Linear Lepton Colliders", Phys. Rev. Lett. 112, 034802

[9] S. Jang et al, "The High Position Resolution Cavity BPM Development and Measurement for ILC Final Focus System", proceeding for IPAC14, Dresden, Germany, 2014

[10] Y. Inoue et al., "Development of a High Resolution Cavity Beam Position Monitor", Physical Review Special Topics, Accelerators and Beams, 11, 062801, 2008

[11] N. Blaskovic Kraljevic et al, "Development of a Low-latency, High-precision, Intra-train Beam Feedback System Based on Cavity Beam Position Monitors", proceedings for IPAC14, Dresden, Germany, 2014

[12] T.Okugi et al., "Linear and Second Order Optics Corrections for the KEK Accelerator Test Facility Final Focus Beam Line", PHYSICAL REVIEW SPECIAL TOPICS - ACCELERATORS AND BEAMS 17, 023501 (2014)

[13] T. Shintake, "Proposal of a Nanometer Beam Size Monitor for e+e- Linear Colliders", Nuclear Instruments and Methods in Physics Research Section A, 311(3):453 – 464, 1992.

[14] S. Weinburg, "The Quantum Theory of Fields", vol 2.

[15] OTR monitors : IBIC12 TUPB70

[16] PRST-AB 10, 042801(2007)

[17] ATF wiki

[18] K. Kubo and the ATF2 Collaboration: "Towards International Linear Collider: Experiments at ATF2", presentation slides and proceeding for the 5th International Particle Accelerator Conference (IPAC14), Dresden, Germany, 2014.

[19] S. Kuroda and the ATF2 Collaboration: "ATF2 for Final Focus test Beam for Future Linear Colliders", presentation slides and proceeding of ICHEP14.

[20] K. Kubo et al, "Wakefield Issues for the Linear Colliders" , ICFA Beam dynamics Newsletter. No. 61. (2013)

[21] K.Kubo, "Intensity dependence of Beam size at IP and Wakefield in ATF2", presentation of LCWS2014

[22] Y. Yamaguchi, Master thesis at Graduate School of Science, the University of Tokyo (2010)

[23] Spectra-Pysics Lasers, Injection Seeder, Model 6350, User's Manual

[24] Spectra-Pysics Lasers, Quanta-Ray PRO-Series, User's Manual

[25] M. Oroku, Doctoral thesis at Graduate School of science, The University of Tokyo (2012)

[26] Phisik Instrumente GmbH & Co. KG. web site

[27] Hamamatsu Photonics, R7400U data sheet

[28] H.Yoda, "Development of Gamma-ray Detector for the Shintake Beam Size Monitor", Master thesis at Graduate School of Science, the University of Tokyo, 2008.

[29] J. Yan, Master thesis at Graduate School of Science, The University of Tokyo (2011)

[30] T. Okugi, presentation at the LCWS14, TB Meeting

[31] T. Okugi, presentation slides at the ILC Summer Camp 2014

[32] T.Yamanaka. Master thesis at Graduate School of Science, The University of Tokyo (2009)

[33] Kagaku Gijutsu-sha, Scientific Products Buyer's Guide.

[34] J. Alabau-Gonzalvo et al., Proc. IPAC12, MOPPR044, 879, New Orleans, USA (2012)

[35] T. Okugi, "R&D: ATF2", slides for ATF2 TB & SGC Meeting, June 2012

[36] Helmut Wiedmann, "Particle Accelerator Physics"

[37] The Thorlab web site for Adaptive Optics Kits

[38] J. Pfingstner et al, "EXPERIMENTAL VERIFICATION TOWARDS FEED-FORWARD GROUND MOTION MITIGATION AT ATF2", MOPOL03, proceedings for LINAC14, 2014.

[39] Eugene Hecht and Alfred Zajac. Optics (Pie). Pearson, revised international ed edition, 2 2003.

[40] J.Yan et al, "Measurement of Nanometer Electron Beam Sizes with Laser Interference using Shinrtake Monitor", Nuclear Instruments and Methods in Physics Research Section A740 (2014) 131-137

[41] J.Yan et al, "Measurement of Nanometer Electron Beam Sizes Using Laser Interference by Shintake Monitor", Proceedings of Science

[42] Private communications with K.Kubo

[43] "Toukeigaku", S. Ikeda, K. Matsui, Y. Tomita, Y. Baba, 1991.

[44] K. Ito et al, "Beam Size Measurement with Pair Monitor and BeamCal", arXi :0901.4446v2, 2009

[45] Newport Japan Tutorial, Gaussian Beam Optics

[46] Newport web site, Laser damage Threshold

[47] Hanamura Optics Corp. web site, Laser Optics

[48] Website for Newport products

[49] EPICS homepage, Argonne National Laboratory